

Evolution of the Porosity and Adsorption
Properties of Pyrolytic Carbons
During Activation



Luca Cervini

This dissertation is submitted for the degree of Doctor of

Philosophy

June 2021

Department of Chemistry

Declaration

This thesis has not been submitted in support of an application for another degree at this or any other university. It is the result of my own work and includes nothing that is the outcome of work done in collaboration except where specifically indicated. Many of the ideas in this thesis were the product of discussion with my supervisor Dr. John M. Griffin.

Excerpts of this thesis have been published in the following conference manuscripts and academic publications:

L. Cervini, O. D. Lynes, G. R. Akien, A. Kerridge, N. S. Barrow, J. M. Griffin, *Energy Storage Mater.* **2019**, *21*, 335–346

L. Cervini, N. Barrow, J. Griffin, *Johnson Matthey Technol. Rev.* **2019**, *64*, 152–164

Lancaster University, UK

Abstract

Activated carbons are industrially relevant materials because of a broad range of applications, such as catalyst supports and supercapacitor electrode materials. The performance of supercapacitors depends on the properties of the carbon pores; that is the pore sizes, volumes, connectivity, and the ability to capture electrolyte species. The characterization of these aspects is a challenging task because no single technique can fully describe activated carbons. Despite sample-specific features, most activated carbons show distorted graphite-like features on the nanometre scale, the void between which constitutes the micropores. The macroscopic structure is amorphous. Pyrolytic PEEK-Derived Carbons (PDCs) generally contain a broad pore size distribution ranging from subnanometre pores up to a few nanometres, and the average pore size can easily be tuned during synthesis. This thesis aims to characterize PDCs by combining a range of complementary techniques, mainly NMR, XRD, and GS. Insight was gained into the nanometre scale structure of the pores, the macroscopic connectivity of the pores, and the electrolyte adsorption properties of those pores.

The influence on the appearance of the NMR spectrum of sample parameters such as the particle size, the burn-off and the spatial pore distribution, as well as solvent parameters such as viscosity and polarity, were investigated. The quantification by NMR of the ex-pore and in-pore populations can be biased by exchange-averaging of these two environments into a broad peak. This phenomenon was more pronounced in small particles because of shorter diffusion paths, in low viscosity and polar solvents because of weaker attraction to the hydrophobic pore surface, and in samples with higher degrees of activation due to faster diffusion kinetics in bigger pores.

Steam, CO₂ and KOH activation conditions were used at different temperatures (700 – 900 °C) and reaction times (minutes to hours) to assess the effect on the structure.

Lower temperatures yielded rougher and less stable pore walls. The pores were poorly connected, and the pore sizes inhomogeneously distributed within the particle, leading to distinct NMR environments. Conversely, activation at 900 °C provided a stable, homogeneous and well-connected structure.

The adsorption of water and alkali ions in solution constitutes the first NMR-based experimental insight into how pore properties affect the total adsorption strength of the carbon. Large pores were found to contain higher concentrations of ions than small pores, at equilibrium. The ratio of adsorbed ions relative to free ions depended on the nature of the ion and its solvation shell.

The adsorption mechanism of sodium was further characterized under an applied potential using a custom designed and 3D printed cell employed in an ex-situ electrode charging protocol, benchmarked against a commercial Swagelok cell. The self-discharge kinetics were quantified and found to consist of at least two contributions: a fast charge redistribution and a slow faradaic process. The in-pore population was then observed with NMR after ion-redistribution was complete, and found to qualitatively agree with the literature, although more experiments are required to identify sample specific features.

This thesis has shown the importance of multi-technique characterisation as well as careful control over activation conditions. The tunability of pore structures in carbon and subsequent interpretation of adsorbed ions in NMR spectra is relevant for many industrial fields. Demonstration of a 3D printed ex-situ electrochemical cell for NMR will help to accelerate studies of carbons in the area of battery materials.

Acknowledgements

My PhD was an amazing adventure that was made possible by many people and organizations. I would like to thank first my two supervisors, John Griffin and Nathan Barrow, for letting me take a glimpse at the very exciting world of scientific research. Several funding bodies have been of great support among which Johnson Matthey and the EPSRC through the iCASE studentship, thanks to which I was never worried about money and was even able to save a little bit from my stipend. Lancaster University of course provided a great facility; I remember the unique privilege of having a SS-NMR spectrometer at my entire disposal for over a whole year. Other instruments were managed by very helpful staff, among which I am particularly grateful to Sara Baldock for the 3D printer, Nathan Halcovitch for the XRD facility and Geoff Akien for the wider NMR facility. I am also grateful to the JMTC staff for the great range of very accessible and well-managed instruments and for the lovely weeks I got to spend there. Finally my thanks go to the members of the Examination Panel for their efforts in the assessment of my work.

Contents

1 Introduction.....	1
1.1 Synthesis of Activated Carbons.....	2
1.2 Microscopic Structure.....	4
1.3 Ion Adsorption Properties.....	7
1.4 Aim of the Project.....	10
2 Theoretical background	13
2.1 Nuclear Magnetic Resonance	13
2.1.1 Fundamentals of NMR.....	13
2.1.2 Basics of an NMR Experiment	14
2.1.3 NMR Interactions.....	16
2.1.4 Ring currents	25
2.1.5 Experimental Techniques.....	26
2.1.6 Relevant NMR-Active Isotopes	36
2.1.7 Exchange Averaging in 1D NMR Spectra.....	38
2.2 Gas Sorption	43
2.2.1 Sample Preparation and Measurement.....	43
2.2.2 Fitting of Isotherm	46
2.3 Raman Spectroscopy	52
2.3.1 Origin of Raman Scattering	52
2.3.2 Application to Carbonaceous Materials.....	53
2.4 Powder X-Ray Diffraction.....	55
2.4.1 Fundamentals of Diffraction	55
2.4.2 Diffraction Experiment	57
2.4.3 Practical Example: Graphite	57
3 Methodology and Interpretation Guidelines	61
3.1 Synthesis of PDCs	61
3.1.1 Standard Synthetic Procedure	61
3.1.2 Optimized Procedure.....	64
3.1.3 Sample Nomenclature	67
3.2 NMR	68
3.2.1 Sample Preparation	68
3.2.2 Fitting of Solvent Evaporation.....	69
3.2.3 Appearance of Optimized Samples.....	74
3.2.4 Particle Size Effects	79
3.2.5 The Effect of Burn-off	89
3.2.6 The Effect of Solvent Properties.....	92
3.2.7 Summary of perspectives	97
3.3 GS	101

3.3.1 Sample Preparation	101
3.3.2 Qualitative Isotherm Analysis	101
3.3.3 Data Treatment and Interpretation	103
3.4 Raman	109
3.4.1 Sample Preparation and Detection	109
3.4.2 Deconvolution of Spectra	110
3.5 Summary of Materials and Methods	112
4 Investigation of the Structure of PDCs	115
4.1 Structure After Steam-Activation at 900 °C	115
4.1.1 XRD and TEM	115
4.1.2 Raman	117
4.1.3 Gas Sorption and NMR	120
4.2 Exploration of Other Activation Conditions	124
4.2.1 Pore Structure After Steam-Activation at 700 °C	124
4.2.2 Evolution of the Pore Network After Steam-Activation at 700 °C	131
4.2.3 KOH Activation	139
4.3 Porosity Development in PDCs	143
4.3.1 Macroscopic Mechanism	144
4.3.2 Microscopic Porosity Development	146
4.4 Conclusion to Chapter 4	150
5 Alkali Ion Adsorption Properties	151
5.1 Comparison of Alkali Ions	151
5.1.1 Effect of BO	151
5.1.2 Concentration Dependence of ¹³³ Cs Chemical Shifts	152
5.1.3 Specific Ion Effects	154
5.2 Concentration Effects	157
5.3 Rationalising the Concentration-Dependent $\Delta\delta$	160
5.3.1 Pore Properties	160
5.3.2 Quantification	164
5.3.3 Testing the Hypothesis	165
5.4 Impact on Applications	169
5.5 Conclusion to Chapter 5	170
6 Charging Using a New Ex-situ Method	173
6.1 Introduction	173
6.2 Swagelok Cell	178
6.2.1 Description of the Design	178
6.2.2 Results	179
6.3 New Design	182

6.3.1 Description of the Design	182
6.3.2 Self-discharge characterization	186
6.3.3 Ex-situ NMR method	194
6.4 Conclusion and Future Work.....	201
Conclusions.....	203
Bibliography	207
Appendix.....	219

List of Abbreviations and Acronyms

BET	Brunauer-Emmett-Teller	NLDFT	Non-Local Density Functional Theory
BO	Burn-Off	NMR	Nuclear Magnetic Resonance
CA	ChronoAmperometry	NRMSD	Normalized Root Mean Square Deviation
CDC	Carbide-Derived Carbon	OD	Ordered Domain
CDI	Capacitive DeIonization	PAS	Principal Axis System
CSA	Chemical Shift Anisotropy	PDC	PEEK-Derived Carbons
CP	Cross-Polarization	PDF	Pair Distribution Function
CT	Central Transition, or Contact Time	PEEK	PolyEther Ether Ketone
CV	Cyclic Voltammetry	PFG	Pulsed Field Gradient
CW	Continuous Wave	Ppm	Parts per million
Cyl	Cylindrical	PSD	Pore Size Distribution
DD	Disordered Domain	PTFE	PolyTetraFluoroEthylene
DF	Density Functional Theory	PV	Pore Volume
DOR	DOuble Resonance	PXRD	Powder X-Ray Diffraction
EFG	Electric Field Gradient	QSDFT	Quenched Solid Density Functional Theory
EM	Electro-Magnetic	RDF	Radial Distribution Function
EXSY	EXchange Spectroscopy	RF	Radio-Frequency
FID	Free Induction Decay	RFR	Rotating Frame Reference
FT	Fourier Transform	RMSD	Root Mean Square Deviation
FWHM	Full Width at Half Maximum	RMSE	Root Mean Square Error
GS	Gas Adsorption	SEM	Scanning Electron Microscopy
HOMO	Highest Occupied Molecular Orbital	ST	Satellite Transition
IUPAC	International Union of Pure and Applied Chemistry	TEM	Transmission Electron Microscopy
LUMO	Lowest Unoccupied Molecular Orbital	TPPM	Two-Pulse Phase Modulation
MAS	Magic Angle Spinning	XRD	X-Ray Diffraction
MD	Molecular Dynamics		
MQMAS	Multiple Quantum Magic Angle Spinning		
NICS	Nucleus Independent Chemical Shift		

1 Introduction

Microporous activated carbons play a major role for the energy decarbonization of our society. Thus they are produced at a low cost in over a million tons annually for many applications including supercapacitors^[1], hydrogen storage^[2], water desalination^[3] and CO₂ capture^[4]. Many applications exploit the high surface area, micropore volume, conductivity, and chemical resistance that activated carbons offer. Essentially, activated carbons allow to multiply the efficiency of processes that depend on the area of a solid-liquid or a solid-gas interface. For example during the charging of supercapacitors and during water desalination, which are certainly the most relevant applications to this thesis, ionic species are pulled out of the solution towards a charged surface. This process requires input of energy, which is then returned as the ions are released in the solution in a fast and highly reversible charge-discharge cycle. In this narrower context, activated carbons compare well to an increasingly diverse and complex variety of supercapacitor carbon materials such as nanotube-based architectures^[5], conducting polymers^[6-8], as well as graphene-derived materials^[9,10] and of course all sorts of composites thereof^[11-13]. What activated carbons don't offer in control and performance, they make up in simplicity and durability, which is why they are privileged for commercial use. To improve the efficiency of activated carbons, all relevant aspects, *i.e.* the synthesis, the structure and the properties, must be studied together as they have a direct impact on each other.

1.1 Synthesis of Activated Carbons

There are various methods to produce these materials, for example through zeolite-templating, by converting carbides, or in composites with nanotubes or graphene oxide, but this thesis focuses on the two-step method of carbonization followed by activation because it is the most common approach for large-scale applications.^[14] The carbonization step produces an almost pure carbon material from a raw natural or synthetic precursor by removing all heteroatoms at high temperature under an inert atmosphere, while by-products such as tar, oil and gases are released. The activation step introduces porosity through gasification of carbon atoms using a variety of oxidizing agents. The percentage of material removed in either step defines the burn-off (BO), which is generally used to compare the extent of activation. Both these steps determine the structure and properties of the end-product, and so their mechanisms have been studied since many decades. This is a challenging task because the structure strongly depends on the synthetic conditions and is highly variable within and across samples. We can therefore as of now stress the importance of studying each system in depth through a combination of many techniques.

The mechanism of carbonization depends on the starting material. On one hand, some materials like anthracene, saccharose or cellulose convert into the thermodynamically stable non-porous highly oriented pyrolytic graphite at temperatures up to several thousand degrees Celsius.^[6,7] On the other hand, non-graphitizing materials such as coconut shell, wood or phenol-formaldehyde, do not fully graphitize even at high temperatures and are inherently porous, albeit with small pore volumes and poorly connected pores. The structural order in such carbons is only partial and does not extend on length scales above a few nanometres, yielding few-layers, distorted graphitic domains observable by Transmission Electron Microscopy

(TEM).^[17] Kercher *et al.* observed the growth of graphite-like features with X-Ray Diffraction (XRD) and proposed the so-called quasipercolation model.^[18] This concept stipulates that the low-density carbonaceous disordered phase present at the early stages of the carbonization process transforms into the more dense randomly-oriented graphite-like domains. The initial porosity created during carbonization is thus attributed to the densification of the matrix.

The chemical reaction of carbon gasification taking place during the activation step consists of the oxidation of carbon atoms into CO or CO₂. Common alternatives to oxygen as oxidizing agent include steam and CO₂. The steam-carbon and the CO₂-carbon reactions were extensively studied in the late 1940s to determine reaction kinetics and the competitions between H₂O, H₂, CO and CO₂ on the reactive sites.^[10,11] Those species react with carbon atoms of incomplete valence shells. The proposed mechanism of the reaction between water and carbon, Figure 1.1a, involves splitting of water into H and OH which undergo a 1,3-addition on a conjugated alkene chain, so two carbon atoms with unsatisfied valencies are involved (active site 1). H₂ is then released leaving only the oxygen atom, which produces CO after cleavage of the carbon chain. H₂ can also adsorb on site 1 by splitting into two hydrogen atoms. The CO₂ reaction however is formulated as adsorption of a single oxygen atom on one sp² carbon atom of incomplete valence shell (active site 2) with simultaneous release of CO, followed by the same cleavage of the chain to release another CO molecule, see Figure 1.1b. The CO molecules are also able to adsorb on individual carbon atoms of site 2 but do not undergo any further reaction. More recently the kinetics were found to generally increase quickly with temperature above 700 °C, with steam gasification being always faster than CO₂ gasification.^[21] The competition between gas molecules for the active sites was investigated more recently: steam and CO₂ tend to compete only in low surface

area samples^[13,14], while H₂ and CO have different inhibitory effects on the two reactions.^[24] This is summarised in Figure 1.1c. H₂ can occupy the sites reactive towards steam and CO₂, therefore inhibiting the steam and CO₂ activation, whereas CO inhibits only the CO₂ activation. Side reactions not observed under common conditions include slow regeneration of CO₂ from adsorbed CO and water molecules, and further gasification of carbon in excess of hydrogen.

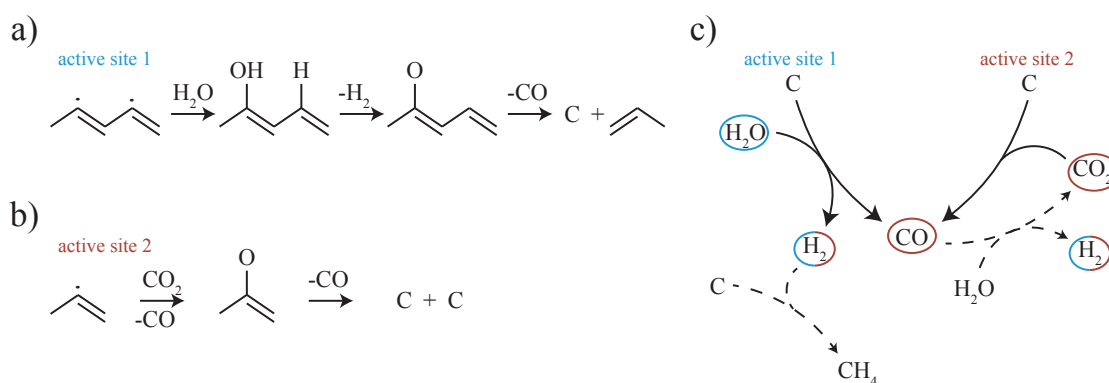


Figure 1.1: Reaction mechanism of the steam activation a) and CO₂ activation b), and c) scheme of the competition between the species. Species circled with the same colour compete for adsorption on the same active sites. The dashed arrows represent normally slow reactions.

1.2 Microscopic Structure

The main properties of interest of activated carbons pertain to their porosity, particularly the microporosity, as defined by the IUPAC, namely pores smaller than 2 nm. To understand where the microporosity stems from, insight into the structure of carbons is necessary. Over the years many different models of the structure were proposed and focused on the length scale of the pore sizes, *i.e.* a few nanometres.

XRD and TEM have historically been the two most prominent techniques for the investigation of nanostructures of carbon materials such as carbon black, soot,

glassy carbon and nanotubes.^[25] The work of Franklin is often cited as the first effort to characterize the structure of amorphous carbons, which were drawn as nearly ideal graphitic domains of small dimensions calculated using the Warren equations, with some proportion of disordered phase.^[26] A recent updated model was proposed with emphasis on the ordered graphite-like domain (OD) and somewhat more disordered domains (DD) as well as the truly amorphous domain, and stipulates that carbons possess mostly the first two phases after high temperature treatments above 600 °C.^[27] The work of Ban *et al.* among others showed that the layers in the OD should be depicted as distorted instead of planar, based on TEM observations, with XRD used in conjunction to have an average estimation of their dimensions.^[19,20] Evidence for a small amount of fullerene-like structures were found in non-graphitizing carbons and it was postulated that these were the stable defects preventing graphitization.^[30] The model that was proposed did however not take into account the long-standing evidence of short-range order. The concept of fullerene-like structures were then reconciled with the idea of graphite-like structures by the work of Hawelek *et al.* using a combination of molecular dynamics and radial distribution functions.^[31] Good agreement between experimental data and computational models were obtained with few-layer graphite-like ODs distorted by a range of different defects such as non-six-membered rings, dangling bonds and out-of-plane C-H groups.

In summary, although the molecular structure is not yet fully described for all carbon materials, there is consensus around the concept that nanometer-sized imperfect graphite-like ODs exist in non-graphitizing carbons, with some proportion of DD where the higher density of defects in the sheets prevents the formation of stacks during carbonization, as shown schematically in Figure 1.2. The number of parallel sheets varies, as well as their orientations and points of contact. Assuming no reorganization

of the structure, several possible pore development mechanisms can be imagined, and are outlined with the number 1 – 4: 1) expansion of pore initially created during carbonization, 2) new pore resulting from etching of DD only, 3) new pores resulting from etching of various numbers of sheets in OD only and 4) new pores resulting from a combination of mechanisms.

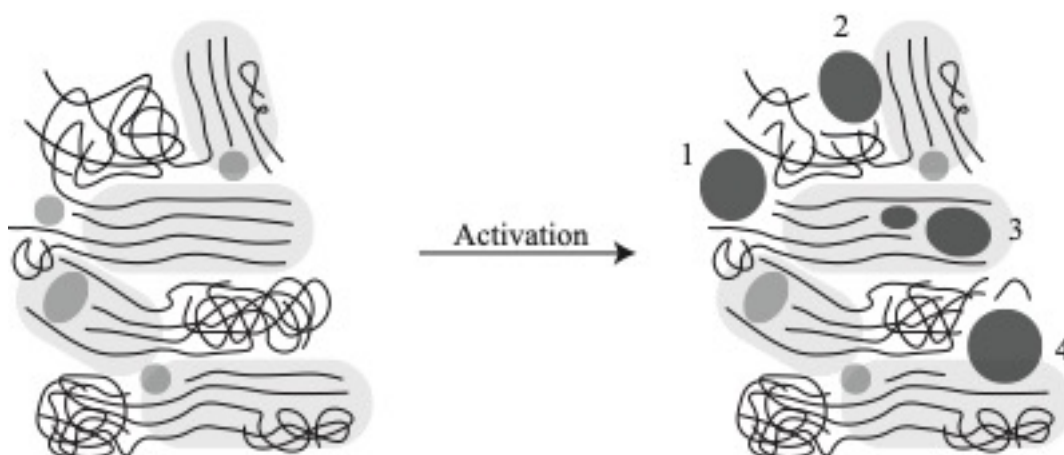


Figure 1.2: Schematic representation of the microscopic structure of activated carbons and possible mechanism of pore development during activation. The continuous black lines represent sp^2 domains, either in light grey areas (OD) or in bundles (DD), the light grey circles are micropores present before activation, the dark grey circles are the pores created during activation. The numbers 1 – 4 represent various activation mechanisms.

With this level of order in activated carbons, one might wonder why the exact pore etching mechanism within such structures has not yet been clearly and directly observed experimentally. This is partly due to the difficulty of obtaining nanometre-thin samples, which makes TEM images quite crowded even after significant activation^[32]. As for Gas Sorption (GS), despite being a choice technique tailored to the study of pores, the difficulty resides in the interpretation of the data, as will be discussed in Chapter 2. There is very little experimental work in the literature describing the

structure of the pores themselves, despite a breadth of computational simulations aimed at reproducing gas sorption patterns with various building blocks based on graphene-like fragments. Models that manage to reproduce Pair Distribution Functions (PDF)^[24–26], TEM images^[27,28] or GS isotherms^[38] are based on very similar structures consisting of few-layer ODs with pores located between the sheets.

Regarding experimentally-derived models, Gun'ko *et al.*^[39] proposed that pores are created within these ODs upon etching of individual sheets, and possess discrete albeit distributed sizes due to small residual clusters in the pores. Furthermore, little rearrangement of the structure during activation was seen with TEM, implying that the structure of activated carbons is rigid, often in contradiction with computational studies that allow extensive structural relaxation. However no mention was made of pores etched within the DD. Recently, a comprehensive study by Xing *et al.* backed up by a combination of several analytical tools and molecular dynamics showed that the CO₂ activation mechanism in various carbons consists in the removal of layers of graphene-like sheets, whereby the most defective regions are etched at a faster rate.^[40] Such work has many implications for the study and use of carbon-based devices because it gives the first description of the structure of pores and pore walls, from which all the properties of porous carbons result.

1.3 Ion Adsorption Properties

The study of activated carbons specifically in the field of supercapacitors has produced a lot of fundamental knowledge about the mechanism of adsorption of various species such as ions, but also solvents, ionic liquids, gases etc. Supercapacitors are high-power energy storage devices which function through the electrosorption of ions on microporous carbon electrodes. Most commercial supercapacitor devices employ

organic electrolytes due to their moderate voltage window and good ionic conductivity. However, there has been considerable recent interest in the development and study of aqueous electrolytes based on inorganic salts.^[32–35] Aqueous electrolytes have the combined advantages of being relatively cheap, environment-friendly and simple to prepare and handle.^[45] Furthermore, they are also relevant to the closely related technology of capacitive deionization (CDI) which employs the same capacitive mechanism for the energy-efficient production of fresh water.^[37,38] However, despite the growing interest in both supercapacitor and CDI devices, the precise details of the properties and behaviour of aqueous electrolyte ions within microporous electrodes is still not well understood and continues to be the subject of extensive research. Most of the progress in this area has come from theoretical modelling which has led the way in building up a microscopic picture of the behaviour of aqueous ions in confined environments. Over the last decade numerous studies have revealed that factors such as specific ion properties,^[48] relative pore/ion sizes,^[40–42] and ion solvation energies^[43,44] can have a strong influence on adsorption phenomena, with important implications for the charging mechanisms in electrochemical devices. One important factor recently discussed in the literature is the relative “ionophobicity” and “ionophilicity” of the system, or the propensity of the ions to enter the pores before charging, and has been shown to have significant effects on the charging dynamics and energy capacity.^[45,46] Therefore to fully understand the factors influencing the charging mechanism, it is also necessary to have a detailed picture of the ion-pore system in the absence of an applied potential.

A technique that has recently gained prominence for studying ion adsorption in porous carbons is NMR spectroscopy. NMR has the advantage of being element

selective and so can be used to observe a specific species in isolation, and is also fully quantitative such that adsorbed ions and solvent species can be independently “counted” in the uncharged or charged state.^[47,48] The key phenomenon that allows this is the so-called Nucleus-Independent Chemical Shift (NICS), which arises from the magnetic shielding due to circulation of electrons in the carbon surface, thereby enabling adsorbed species to be distinguished from those in bulk solution.^[49–54] The NICS is dependent on the distance of the adsorbed species from the carbon surface and has therefore been used as a probe of the pore structure of a range of porous carbons. It is important to note that the observed difference of chemical shift between adsorbed and free species depends on many other factors, therefore the term $\Delta\delta$ is preferred when referring to the “measured NICS”. Borchardt *et al.* showed that the $\Delta\delta$ of adsorbed organic electrolyte species varied in accordance with the pore size of titanium carbide-derived carbons (CDCs) which have very well-defined porosity.^[60] This was supported by Forse *et al.* who also showed that ion adsorption in CDCs is significantly reduced when the average pore size is smaller than the solvated ion size.^[63] In a subsequent study, density functional theory (DFT) was used to show that for model carbon slit pores, the NICS depends upon both the pore width and the size and curvature of carbon fragments making up the pore walls.^[64]

However, recent studies have started to reveal that additional factors such as the carbon domain size and exchange phenomena also contribute to the observed $\Delta\delta$, meaning that these need to be accounted for when interpreting experimental data.^[56–58] A model system that allows to control the exchange phenomena and therefore facilitates the study of adsorption phenomena with NMR is a microporous carbon derived from pyrolysis and activation of polyether ether ketone (PEEK) polymer. PEEK-derived carbons (PDCs) have a simple synthesis procedure which produces a high-surface area

microporous carbon where the pore structure can be easily influenced through the activation conditions.^[59–61] For this reason, PDCs have been used as a model system in a number of NMR studies of microporous carbon adsorption phenomena led by the Wu group.^[62–67] In particular, Xing *et al.* used DFT calculations to relate the magnitude of the observed $\Delta\delta$ to the pore size, and on this basis proposed a simple NMR methodology for characterising the pore size distribution in PDCs.^[72] This approach has been extended to gain insight into pore filling phenomena in similar materials.^[64,67] However, such “NMR porosimetry” approaches rely on the assumption that the $\Delta\delta$ is primarily influenced by the proximity of the adsorbed species to the carbon surface. While this may be valid when comparing the same species in different PDCs, it may be necessary to account for additional contributions to the $\Delta\delta$ when comparing different species in the same system (*e.g.* ions and solvent molecules).

1.4 Aim of the Project

The research presented in the following chapters overall aims at developing methods to investigate the structure-properties relationship of activated carbon using a combination of analytical techniques, with a focus on NMR, and propose or explore new approaches for the tailoring of activated carbons.

In Chapter 2, necessary theoretical bases of the employed techniques, namely NMR, GS, Raman and XRD, will be presented and some key phenomena discussed.

Chapter 3 will present the methodology of the experiments and data treatment, as well as explain prerequisites for the interpretation of spectra.

Chapter 4 will be about the characterization of the structure of PDCs, specifically the development of the pores from a microscopic point of view, *i.e.* pore

structure and PSD, as well as from a macroscopic point of view, *i.e.* the connectivity of pores and the spatial distribution of environments.

In Chapter 5 a very simple existing NMR methodology will be used to study the effect of various synthetic conditions on the adsorption of aqueous alkali ions under no applied potential. Properties of individual pores will be extracted and compared.

Last, Chapter 6 will be a proof-of-concept for a new design of electrochemical cell allowing to easily record subsequent NMR experiment under Magic-Angle Spinning (MAS) conditions. Model carbons will be used and the results benchmarked against literature data.

2 Theoretical background

2.1 Nuclear Magnetic Resonance

2.1.1 Fundamentals of NMR

Depending on their composition, nuclei may have a spin quantum number $I > 0$. In this case, they have a magnetic dipole moment. The nucleus is then said to be NMR-active. The value of I is an integer or a half-integer, for example $I = 1/2$ (such as ^1H , ^{13}C , ^{15}N , ^{31}P), $I = 1$ (such as ^2H , ^6Li , ^{14}N) or $I = 3/2$ (such as ^7Li , ^{11}B , ^{23}Na , ^{39}K). We define the magnetic quantum number m_I to describe the orientation of the spin, in its own set of spatial dimensions. There are $2I+1$ possible values of m , called spin states, which are degenerate. However, in a magnetic field, B_0 , the Zeeman energy (in joules) associated with each nuclear spin is no longer degenerate and is defined by:

$$E_m = -\gamma m \hbar B_0$$

where γ is the gyromagnetic ratio and is specific to each isotope and \hbar is the reduced Planck constant. To manipulate the spins, an Electro-Magnetic (EM) radiation can be applied to interact with the magnetic dipole moment of the nucleus. Transitions between spin states of $\Delta m = \pm 1$ are observed when the EM energy corresponds to ΔE_m . At the field strengths typically used in NMR (several tesla), the appropriate EM frequency is in the Radio-Frequency (RF) regime. The transition energy between the states, the temperature and B_0 define the population difference according to the Boltzmann

distribution. Hence there are slightly more spins aligned with B_0 than opposed to B_0 . To simplify and introduce new concepts with more ease, the frequency of the transition (rad.s^{-1}) is commonly used :

$$2.2 \quad \omega_0 = -\gamma B_0$$

where ω_0 is defined as the Larmor frequency of the spin. It corresponds to the frequency of precession of the nuclear magnetic moment around the axis of B_0 . This precession is the basis for the excitation and detection of NMR frequencies.

2.1.2 Basics of an NMR Experiment

The RF pulsing, used to trigger the transition between spin states, and the signal detection are done with a coil surrounding the sample. For magnetization to be able to induce an electric current in the coil, just like a moving magnet, it needs to have a rotating magnetic moment. Note that at equilibrium, the multitude of randomly oriented spins contained in the sample are precessing at the Larmor frequency. They precess, however, out of phase and their individually-induced currents arising from the transverse components of their magnetic dipoles cancel out. The total magnetization is therefore constant and oriented along B_0 , due to the small population difference. It is used to define the orientation of the z axis used in experimental formalism.

To excite nuclear spins, an appropriate RF is pulsed in the coil, and perturbs the magnetic field around the nuclei by adding its own contribution. The spins are now out of equilibrium and will therefore acquire a rotational motion, called nutation when induced by an RF, described by:

$$2.3 \quad \omega_1 = -\gamma B_1$$

where B_1 is now the effective magnetic field around the nucleus. The pulse power and duration can be chosen so that the magnetization is orthogonal to B_0 at the end of the pulse in the Rotating Frame Reference (RFR), to maximize the induced current in the coil. The pulse is then referred to as a 90° pulse. Figure 2.1 illustrates the process of spin manipulation and the measurable effect on the magnetization in the RFR. The RFR is a practical tool to visualize (and measure) the magnetization trajectories. The nutation during the 90° pulse takes place on the yz plane because the precession on the xy plane is cancelled by the rotation of the reference frame at the same frequency, hence RFR.

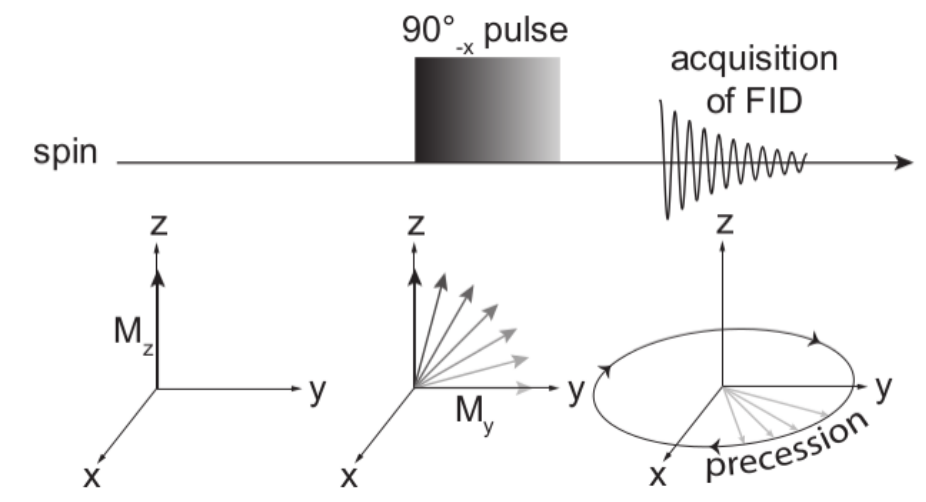


Figure 2.1: Schematic representation of the manipulation of the bulk magnetization M with a 90°_{-x} RF pulse and subsequent detection of the FID. The orientation of the magnetization at thermal equilibrium defines the z axis.

Due to relaxation processes, the xy -component of the magnetization will decohere over time. The induced current will therefore decrease, and is for this reason called Free Induction Decay (FID). This means that the signal can be detected for a limited duration only. The FID contains time-domain signal with the same periodicity as the precession of the spin. In the RFR however, the periodicity is in the $\mu\text{s} - \text{ms}$ time

scale, because it is the difference with the Larmor frequency that is measured, as opposed to the actual frequency with the ns periods. The frequencies contained within the signal are extracted by Fourier Transform (FT). Note that the signal intensity, corresponding to the integral of the peak in the frequency-domain obtained by FT, is proportional to the number of contributing spins, which makes NMR a quantitative method. Typically, ω_1 is much smaller than ω_0 , between 10 and 100 kHz. For example, if a spin needs 10 μs to achieve a full nutation period, then $\omega_1 = 1/10^{-6} \text{ s} = 100 \text{ kHz}$. NMR spectrometers are usually referred to with the Larmor frequency of the ^1H nucleus: a magnet operating at 16.4 T is called a 700 MHz.

2.1.3 NMR Interactions

The observed precession frequency of a spin, ω_{obs} , depends on its magnetic and electric environment. The magnetic environment of a nucleus can be influenced by magnetic fields generated by neighbouring spins and by local electronic environment. The frequency deviation with respect to a reference value ω_{ref} specific to each isotope is the chemical shift δ in ppm, and is plotted in an NMR spectrum. The perturbation on the Larmor frequency can range from a few Hz to 10^7 Hz and the strongest interaction is not the same in all systems.

Chemical Shielding Interaction

The local electron cloud generates its own magnetic field, which modifies the field experienced by the nucleus. The higher the electron density, the more attenuated the external magnetic field B_0 . This is the origin of the field-independent shielding constant σ , describing how the nucleus is shielded from B_0 by the electrons and is therefore in a slightly different effective magnetic field B_{eff} inducing a slightly different observed precession frequency of this individual spin ω_{obs} :

$$2.4 \quad \omega_{\text{obs}} = -\gamma B_{\text{eff}} = -\gamma B_0 (1 - \sigma)$$

We see from this definition that the chemical shift increases with decreasing electron density. The spectrum is plotted as a difference relative to a reference Larmor frequency, called chemical shift.

$$2.5 \quad \delta = 10^6 (\omega_{\text{obs}} - \omega_{\text{ref}}) / \omega_{\text{ref}}$$

With no other interaction visible, which was the case using the first spectrometers at the beginning of magnetic resonance spectroscopy, the ^1H NMR spectrum of ethanol, for example, contains three peaks (Figure 2.2). The oxygen atom being electro-attractive, the electron density, and thus the shielding, around the ^1H nuclei gradually decreases the closer they are. This allows to assign from right to left the $-\text{CH}_3$, $-\text{CH}_2$ and $-\text{OH}$ hydrogen nuclei. The integral of the peak is also a clue for the assignment in quantitative spectra. Note that this spectrum was recorded on a modern solid-state spectrometer, and the reason that no contribution to the spectrum other than the chemical shielding is visible is due to the insufficient homogeneity of the magnetic field.

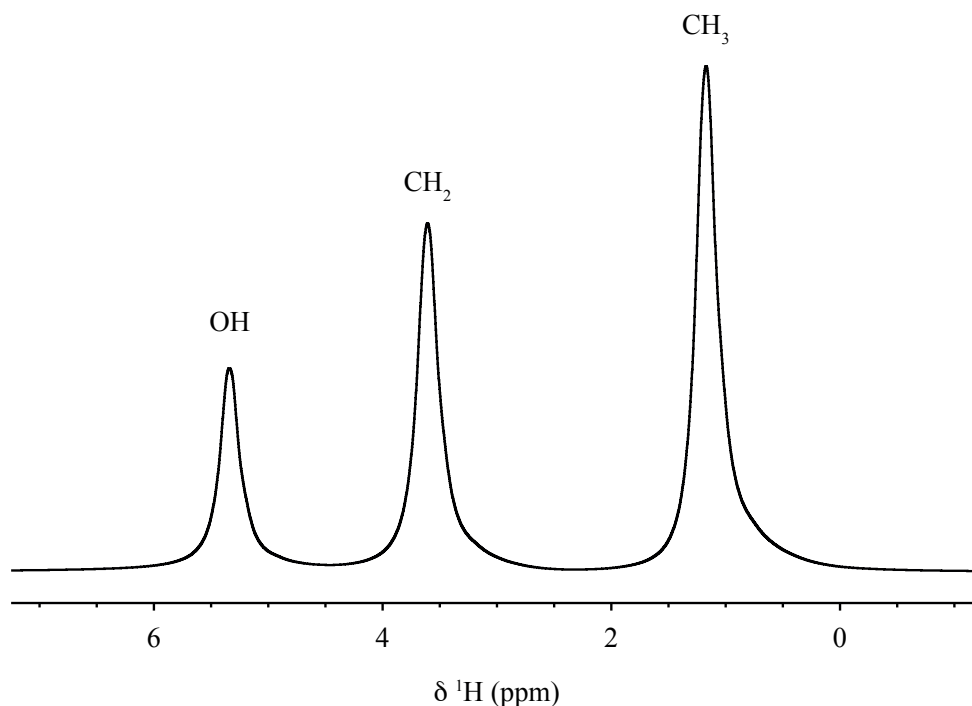


Figure 2.2: ^1H NMR spectrum of ethanol taken on a 400 MHz spectrometer, reminiscent of a low-resolution solution-state spectrum taken in 1951 by Arnold *et al.* at Stanford University^[77] showing only the electron shielding interaction.

In many cases, the chemical shielding is not isotropic. Instead, it must be described by a 2nd rank tensor, the Chemical Shift Anisotropy (CSA) tensor. Nuclei showing a CSA effect have non-spherical bonding environments and the shielding depends on the orientation of the tensor with respect to B_0 . The chemical shift is then expressed by the following equation:

$$2.6 \quad \delta = \delta_{11} \sin^2 \theta \cos^2 \phi + \delta_{22} \sin^2 \theta \sin^2 \phi + \delta_{33} \cos^2 \theta$$

where δ_{11} , δ_{22} and δ_{33} are the diagonal components of the chemical shift tensor. θ and ϕ describe the orientation of the tensor with respect to B_0 . Equation (6) can be factorized by $\cos^2 \theta$ to evidence the dependence on the angle θ in the Haeberlen convention:

$$2.7 \quad \delta = \delta_{\text{iso}}(\Delta/2)[(3 \cos^2 \theta - 1) + \eta(\sin^2 \theta \cos 2\phi)]$$

where $\delta_{\text{iso}} = (\delta_{11} + \delta_{22} + \delta_{33})/3$ is the isotropic chemical shift, $\Delta = \delta_{33} - \delta_{\text{iso}}$ relates to the magnitude of the CSA, and $\eta = (\delta_{22} - \delta_{11})/\Delta$ to the asymmetry. The consequence of the CSA is that NMR spectra of powders, where each crystal has its own orientation, show a distribution of chemical shifts. This effect is illustrated with Pb^{II} in $\text{Pb}(\text{NO}_3)_2$ in Figure 2.3.

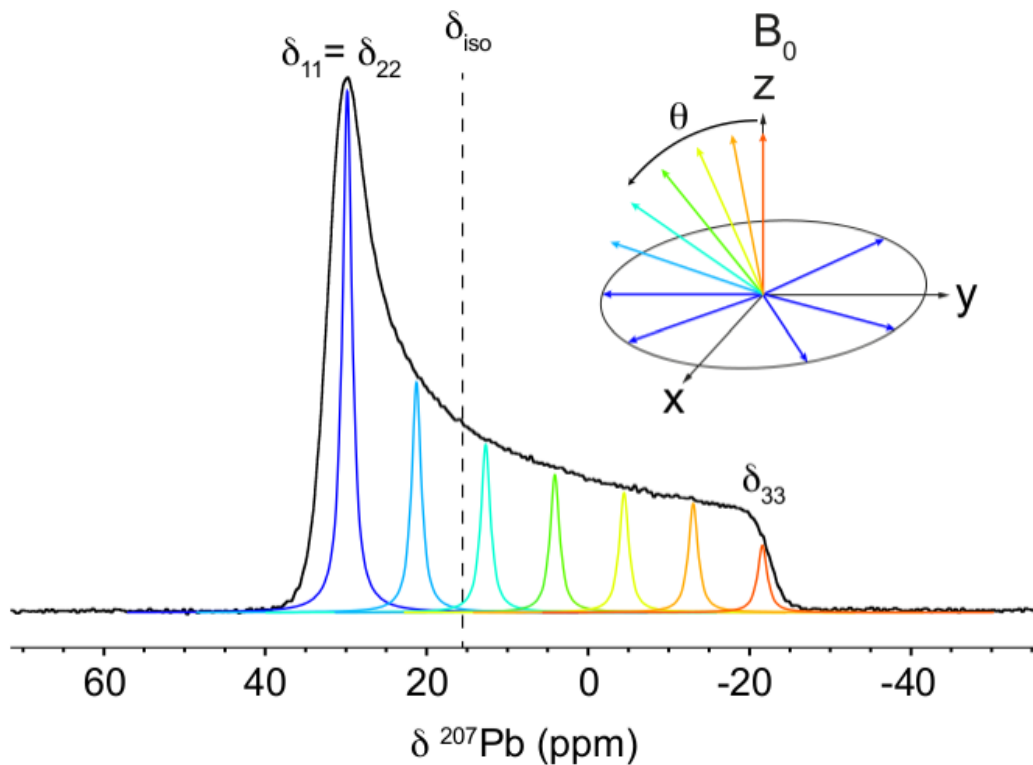


Figure 2.3: Static Solid-State NMR spectrum of $^{207}\text{Pb}(\text{NO}_3)_2$. The black line is the observed spectrum, the coloured lines represent contributions from different crystals with each their own orientation of the principal axis of the CSA tensor, relative to B_0 , shown as coloured arrows.

The shape of the CSA pattern is the sum of the contribution of all crystals in the powder, which are oriented according to a spherical distribution. In the example shown,

the CSA tensor of Pb^{II} is axially symmetric; the biggest component δ_{33} is orthogonal to the two smallest and identical components, δ_{22} and δ_{11} , so in this particular case, only the orientation of δ_{33} matters. For this reason, in Figure 2.3 the tensor is simply represented with the vector δ_{33} . Because of the dependence on $\cos^2 \theta$, all crystals with tensors oriented orthogonally to B_0 , no matter the orientation on the xy plane, will give the maximal chemical shift, depicted in blue. On the contrary, only one orientation parallel to B_0 gives the minimal chemical shift in red. This explains why there is a maximum in the pattern. The position of the maximum depends on the asymmetry of the tensor, that is related to the symmetry of the molecules. A CSA where $\delta_{11} = \delta_{22}$, like shown in this example, is characteristic of axially symmetric molecules, so some information can be obtained by examining the static powder pattern of a sample.

J Coupling

When two nuclei share a bond, the nucleus-electron interaction of one atom has an effect on the nucleus-electron interaction of the second atom. This is why this coupling is said to propagate through bonds. It is written nJ , in Hz, where n is the number of bonds separating the two nuclei. In solution-state NMR, J coupling is very useful for the assignment. In low-field spectrometers, the J coupling in molecules with several neighboring $-\text{CH}_n$ groups may be unresolved, see Figure 2.2, leading to simplified peak structures. At higher fields however, the fine structure becomes visible and it is possible to assign the peaks to particular groups. The ethanol spectrum is then more detailed (Figure 2.4), the coupling constant between $-\text{CH}_2$ and $-\text{CH}_3$ is found to be roughly 5 Hz. Note that the $-\text{OH}$ proton is acidic and is subject to exchange in pure ethanol or in protic solvents, but not in CDCl_3 , which explains the different chemical shift of this peak.

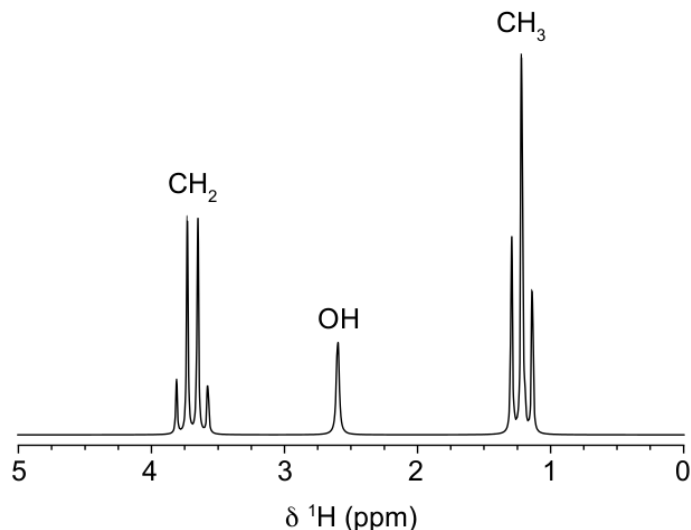


Figure 2.4: Calculated ^1H NMR spectrum of ethanol based on the experimental data of 40 μL EtOH in 0.5 mL CDCl_3 recorded at 89.56 MHz, taken from the National Institute of Advanced Industrial Science and Technology (AIST), SDBS No. 1300HSP-01-876. The chemical shifts are different from pure ethanol because proton exchange is limited in CDCl_3 .

Importantly, the J coupling is mainly isotropic, which means that it does not suffer from any powder-pattern line broadening. In solid-state NMR, it is not frequently resolved because of a less homogeneous field, as well as additional broadening of the peak coming from other interactions, although some 2D experiments allow to observe it.^[78]

Dipolar Coupling

This interaction operates by direct dipole-dipole coupling through space. The coupling constant ω_D between two spins I and S , in Hz, is given by:

$$2.8 \quad \omega_D = -\frac{\mu_0}{4\pi} \frac{\gamma_I \gamma_S \hbar}{r_{IS}^3} \frac{1}{2} (3\cos^2\theta - 1)$$

where μ_0 is the permeability of vacuum, r_{IS} is the distance between the two nuclei, and θ the angle between B_0 and the line passing by the two nuclei, as illustrated in Figure

2.5. There are two important parameters of the dipole-dipole coupling that are particularly relevant in NMR experiments. First is the dependence on the angle θ between B_0 and the internuclear vector, which indicates that the interaction is anisotropic. In solution-state NMR, this interaction is averaged by the fast isotropic tumbling of the molecules as well as the rotational freedom of the bonds. In powders however, the relative orientation of the atoms is maintained. The observed Gaussian broadening of the peaks is the result of dipolar couplings with many partners. In some powder samples, narrowing of peaks can indicate averaging of this interaction, therefore can be used to evidence some kind of motion.

The second parameter is the proportionality to $1/r_{IS}^3$. This means that only close spins interact, and it is possible to gain information about the 3D conformation of a molecule using the strength of the dipolar coupling.

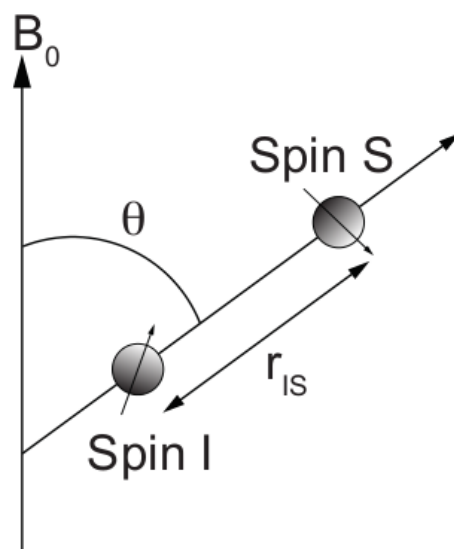


Figure 2.5: Schematic representation of two spins in the magnetic field B_0 , and amplitude of ω_D versus θ .

Quadrupolar Coupling

The quadrupolar coupling is the interaction of a quadrupolar nucleus, *i.e.* of spin $I \geq 1$, with the surrounding Electric Field Gradient (EFG). The magnitude of the quadrupolar coupling strongly depends on the symmetry of the bonding atoms and to a lesser extent the atoms further away. This interaction is approximated by a sum of decreasing contributions, of which only the first and second terms are usually visible. The first order quadrupolar interaction is given by:

$$2.9 \quad \omega_Q = (\omega_Q^{\text{PAS}}/2)[(3\cos^2\theta - 1) + \eta_Q (\sin^2\theta \cos 2\phi)]$$

where PAS stands for “Principal Axis System” used to orient the quadrupolar coupling tensor; $\omega_Q^{\text{PAS}} = 3\pi C_Q/(2I(2I - 1))$ with C_Q relating to the magnitude of the interaction, and $\eta_Q = (V_{yy} - V_{xx})/V_{zz}$ relating to the shape of the quadrupolar tensor with V_{zz} the biggest component out of these three orthogonal components in the PAS. The effect of the interaction is shown in Figure 2.6 for a spin $I = 3/2$, such as ^{23}Na , in a single crystal. The three transitions between spin states of $\Delta m_I = \pm 1$ (two Satellite Transitions, ST, and a Central Transition, CT) give only one peak of frequency ω_0 (Hz) in the absence of EFG (Figure 2.6a). In presence of an EFG, the energy of all spin states are shifted, resulting however in a shift of the STs alone, by a factor of $2\omega_Q$ (Figure 2.6b). The CT is not affected to the first order approximation. Now considering all crystallites in a powder, the transition frequencies become distributed because of the angle dependence of the quadrupolar tensor, in a similar way to the CSA. However, unlike the CSA, the first-order quadrupolar coupling gives a splitting rather than a shift, so a symmetrical powder pattern is observed.

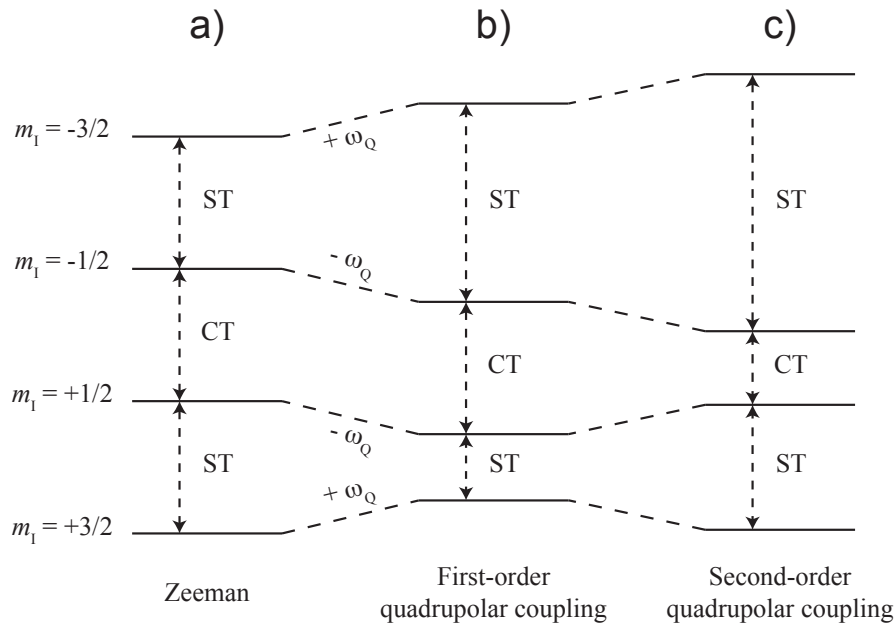


Figure 2.6: Energy diagram of the spin states of a quadrupolar nucleus of spin $I = 3/2$: a) only Zeeman interaction shapes the spectrum; b) 1st order quadrupolar interaction shifts the STs now visible in the spectrum of a single crystal; c) 2nd order interaction modifies the CT and STs.

When the EFG is especially large, the second order quadrupolar interaction becomes visible, and the eventual CT is also affected (Figure 2.6c). This interaction order is described by:

$$2.10 \quad \omega_Q \propto [(3\cos^2\theta - 1) + (35\cos^4\theta - 30\cos^2\theta + 3)]$$

The additional angle dependence broadens the CT into another powder pattern. Due to the large size of the quadrupole interaction, the 1st-order powder pattern is very broad, so only the lineshape of the CT is studied experimentally when investigating nuclei with a half-integer spin.

2.1.4 Ring currents

When carbon atoms are organized in rings with an alternation of single bonds and double bonds, we call it an aromatic ring, for example the six-membered phenyl ring. The key effect arising from aromaticity is that the π electrons constituting the carbon-carbon double bonds are delocalized, meaning that they are effectively able to move from bond to bond unlike in the σ bonds. When immersed in a magnetic field perpendicular to the plane of the aromatic ring, ring currents appear. In addition, the current produces a magnetic field, as shown in Figure 2.7. The induced magnetic field B_{induced} is antiparallel to B_0 above the ring, or inside the shielding cone in blue, but parallel outside of the cone. Because the chemical shift is proportional to the local magnetic field, it will increase or decrease depending on the location relative to the aromatic ring.

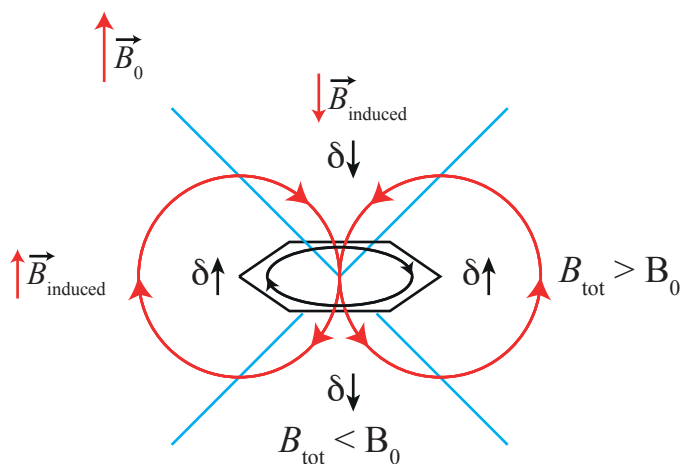


Figure 2.7: Scheme of the ring currents (black circle with arrows) and resulting magnetic field B_{induced} (red circles with arrows). The blue lines represent the shielding cone, inside which spins are shielded resulting in a smaller chemical shift.

Ring currents allow *e.g.* to identify aromatic protons in solution state NMR because they appear at ~ 7.2 ppm, *i.e.* shifted to higher chemical shifts where B_{induced} augments B_0 . In the study of activated carbons, adsorbed species are generally located above the rings and therefore experience a reduced total magnetic field resulting in a smaller chemical shift. The reduction of the chemical shift is only function of the magnitude of B_{induced} , which decreases with the distance to the ring, but not of the nature of the species. The Nucleus Independent Chemical Shift (NICS) is thus defined as the difference between the chemical shift in presence and in absence of ring currents, and allows to determine how far from the aromatic surface species are located.

2.1.5 Experimental Techniques

The difference between solid samples and solvated samples is the mobility of the atoms: in solution, fast isotropic tumbling allows any atom to experience all orientations with respect to B_0 on a timescale that is faster compared to the size of the interactions present. This means that in solution-state NMR, orientation-dependent interactions, namely CSA, dipolar and quadrupolar coupling are not generally visible. In SSNMR, significant broadening of the resonances can occur because of these orientation-dependent interactions. This reduces the resolution which is problematic when multiple sites are present in the same material. It is however possible to “manually” remove those interactions to narrow down the peaks, and thus increase the signal-to-noise ratio and improve the resolution.

Magic-Angle Spinning (MAS)

Thanks to their $3 \cos^2 \theta - 1$ orientation dependence, the CSA, dipolar and first-order quadrupolar couplings can be averaged. Figure 2.8 (left) shows the variation of the $3 \cos^2 \theta - 1$ term versus θ . At an angle of 54.7° , this term is null. To average the

orientation of the crystals or the spin-spin vectors, spinning can be applied on the sample at this angle with respect to B_0 . The spinning frequency must be approximately equal or higher than the size of the interaction to average it. Typically, MAS rates between 10 and 100 kHz are used.

What we observe in practice is not the isotropic resonance only, but a breakdown of the powder pattern into spinning side-bands instead, see Figure 2.8 (right). They are sidebands of the isotropic chemical shift δ_{iso} and arise from the Fourier Transformation of the signal, which explains why they are separated by the spinning rate, in Hz. Their intensities follow the pattern of the static spectrum; hence, the faster the sample is rotated, the less intense the spinning side-bands become and the higher the signal-to-noise ratio of the central peak gets.

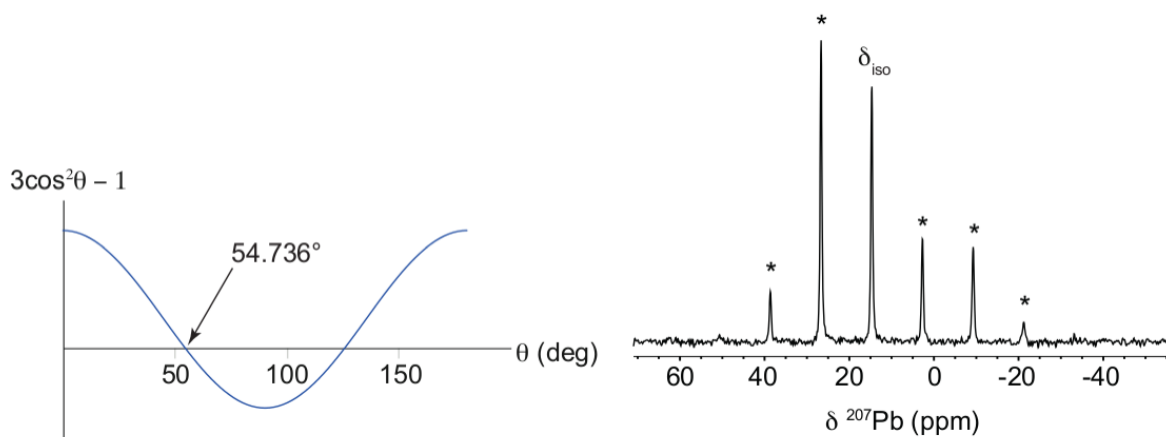


Figure 2.8: Variation of the $3 \cos^2 \theta - 1$ term with θ (left). Solid-State NMR spectrum of $^{207}\text{Pb}(\text{NO}_3)_2$ at MAS rate 8 kHz, asterisks denote spinning side-bands (right).

In the case of a quadrupolar nucleus, like ^2H or ^{27}Al , the same effect of MAS is observed but the side bands intensities follow the first-order the quadrupolar powder pattern. Figure 2.9 (left) shows the ^2H MAS spectrum of deuterated malonic acid. There

is no CT because of the spin 1 of deuterium, and the second-order quadrupolar coupling is small. The inset shows a magnification of a set of peaks. Due to the strong dependence on the MAS angle, this sample is commonly used to accurately set the angle to 54.7° by maximizing the intensity of these peaks to reduce their linewidths. The second-order quadrupolar coupling cannot be removed with MAS, as illustrated in Figure 2.9 (right), showing the affected CT of $\text{Al}(\text{acac})_3$, because of the additional angle dependence shown in Eq. 2.10. The second-order quadrupolar coupling can also be averaged by isotropic tumbling in solution.

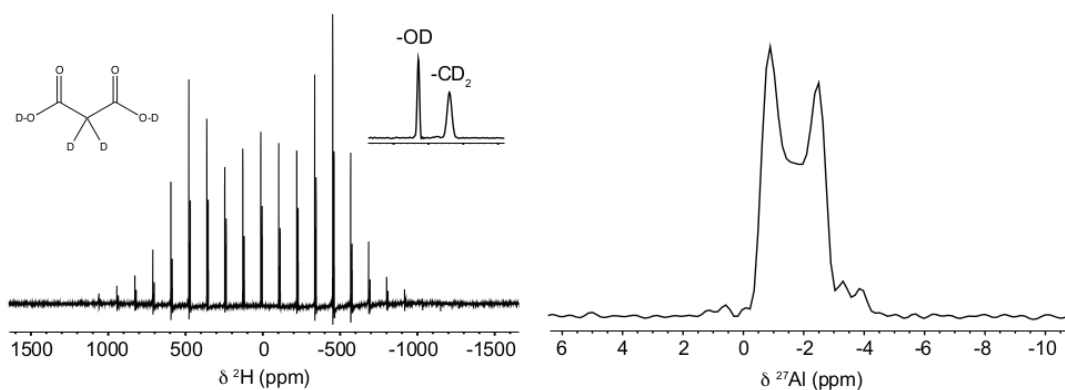


Figure 2.9: Left: ^2H spectrum of deuterated malonic acid with zoom on one spinning side band under MAS at 12.5 kHz showing the first-order quadrupole interaction in a powder. Right: ^{27}Al MAS NMR spectrum of $\text{Al}(\text{acac})_3$ showing the second-order quadrupolar broadening of the CT.

Decoupling

Despite the $3 \cos^2 \theta - 1$ dependence of the dipolar interaction, MAS is in many cases insufficient to fully average it, especially when the coupling is very strong, for example between ^1H in organic samples. Thus, in addition to averaging the orientation of the spins by physically rotating the sample, it is possible to rotate the spins themselves. Removing the dipolar coupling between two neighboring spins is done by

averaging the magnetic field perturbation generated by all neighboring spins S on its coupled partner I by continuously flipping the orientations of S . On the timescale of an acquisition, all spins S will therefore exert an averaged perturbation, being oriented along B_0 as much as opposed to B_0 . The effect on the spectrum is that all chemically identical spins will produce only one peak of higher integral and intensity. Note that the number of coupling partners of different elements one can neutralize is limited by the number of channels in the probe, usually up to four. Also, care has to be taken not to damage the probe by applying an intense decoupling pulse for too long. Different decoupling pulse sequences have been developed to neutralize heteronuclear dipolar couplings, *e.g.* between ^1H and ^{13}C , and homonuclear couplings, like ^1H - ^1H .

Considering heteronuclear decoupling, the first and easiest way to decouple is to pulse a continuous radio-frequency at the Larmor frequency of the nucleus which is not detected. This is the Continuous-Wave (CW) technique. So in the case of a typical ^{13}C experiment that requires ^1H decoupling, the decoupling pulse is at the ^1H frequency while the ^{13}C FID is detected. However, the Two-Pulse Phase Modulation (TPPM) sequence used in this work, as well as other phase-cycled decoupling sequences, were developed after it was found that at high MAS rates, the decoupling loses its efficiency.^[79] Figure 2.10 shows the building blocks for this sequence, a repetition of two phase-shifted pulses.

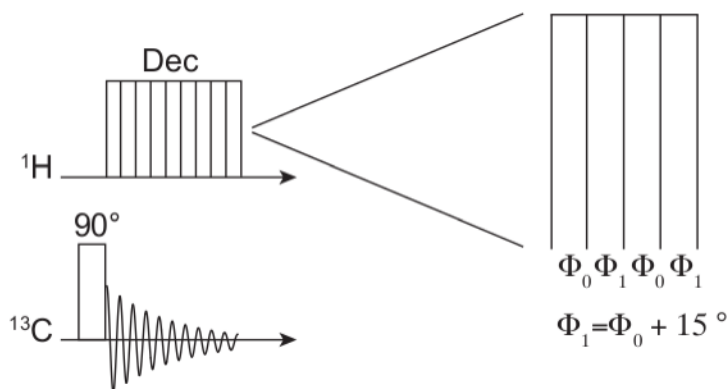


Figure 2.10: Simple pulse sequence to acquire a ${}^1\text{H}$ -decoupled ${}^{13}\text{C}$ spectrum with detail of the decoupling pulse in the TPPM sequence.

Cross-Polarization (CP)

To increase the sensitivity, another strategy can be applied in addition to MAS and decoupling, namely Cross-Polarization (CP).^[80] It is used to transfer a strong polarization from a high-sensitivity nucleus I , to a low-sensitivity nucleus S . The signal enhancement is proportional to γ_I/γ_S . This technique makes use of the dipolar coupling between two spins of different isotopes. A common example is to transfer the magnetization of ${}^1\text{H}$ to ${}^{13}\text{C}$ spins in organic samples, and achieve up to a four-fold signal enhancement. The first step of the CP technique, illustrated in Figure 2.11, is to create a detectable magnetization of ${}^1\text{H}$ using an RF, *i.e.* to bring the angle of average orientation of ${}^1\text{H}$ spins in the plane of the detection coil by applying a 90° pulse. Then, the magnetization vector of ${}^1\text{H}$ spins is maintained through time by applying a continuous “locking” RF for a chosen period of time called “contact time” (CT). In the same time, an RF pulse is applied at the frequency of ${}^{13}\text{C}$ spins, for the same length of time. The orientation of ${}^{13}\text{C}$ spins being at equilibrium at the beginning of this, *i.e.* the magnetization of the spins is aligned with B_0 , it has no component on the xy plane and

the oscillation takes place without precession. To transfer the detectable component of ^1H to ^{13}C spins, the nutation frequencies of both nuclei must be identical, which is when the so-called Hartmann-Hahn condition is met: $\gamma_I B_{1I} = \gamma_S B_{1S}$, where B_{1I} and B_{1S} are the locking and contact RF pulses respectively.^[81] The acquired magnetization of ^{13}C spins is recorded at the end of the contact time.

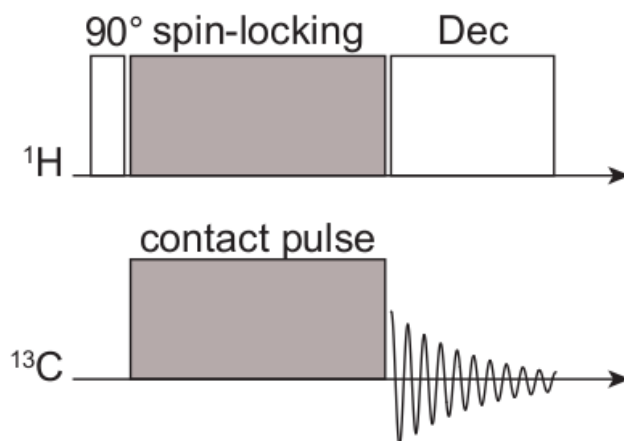


Figure 2.11: Pulse sequence for Cross-Polarization from nucleus I to nucleus S and subsequent detection of S signals. Usually used in conjunction with MAS as well as decoupling during acquisition, which however limits the acquisition time. In practice, the pulse power is increased linearly to make sure the matching conditions are found for all nuclei.

The length of the contact time is important when one spin I is coupled to several other spins S . Magnetization transfer is more efficient the stronger the coupling. By repeating the CP experiment with various contact times and looking at the evolution of the signal of S , it is therefore possible to get some information on the distance between the spins I and S . Figure 2.12 depicts the evolution of peak intensities in alanine with various contact times.

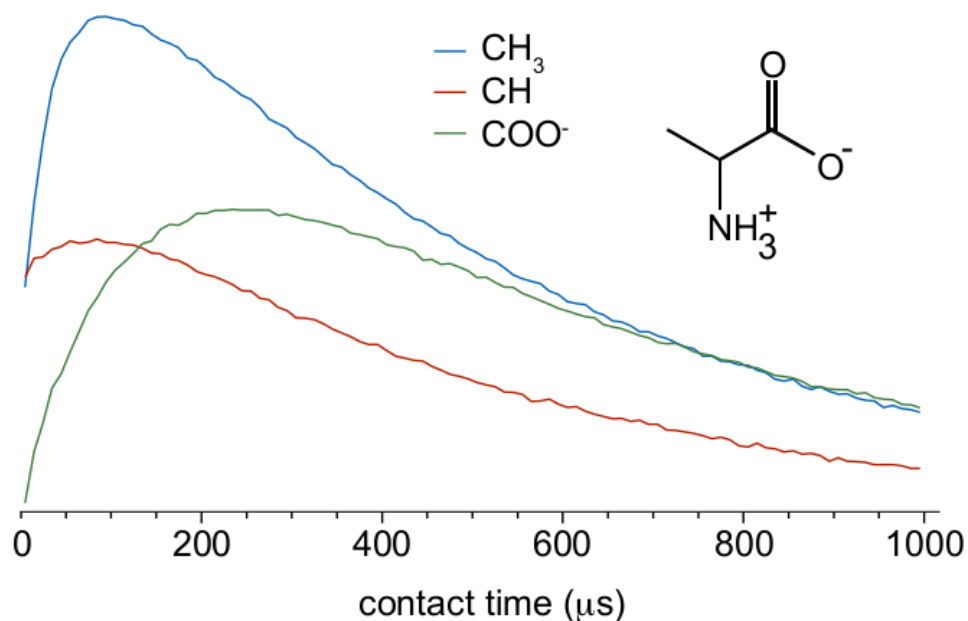


Figure 2.12: ^{13}C CPMAS NMR peak intensities of $-\text{CH}_3$, $-\text{CH}$ and $-\text{COO}^-$ of alanine recorded as a function of contact time.

It can be seen that the $-\text{CH}_3$ signal is strong even with short CT, which is normal considering that the ^{13}C nucleus receives magnetization from three ^1H . The $-\text{COO}^-$ carbon atom on the other hand, has no close ^1H nuclei, therefore smaller dipolar couplings. It can be seen that the signal slowly grows with increasing CTs. Note that for longer CTs, the signal will decrease at a rate depending on the relaxation of the particular spin under spin-locking conditions. The time constant for this process is referred to as $T_{1\rho}$.

Relaxometry

This procedure exploits the effect of the environment on the relaxation dynamics of a nucleus. There are two relaxation constants, T_1 and T_2 , related to two different phenomena, each able to provide information.

When a nuclear spin is shifted out of equilibrium by a radio-frequency pulse in a magnetic field, it will undergo exponential relaxation back to equilibrium according to a longitudinal relaxation constant T_1 . This phenomenon is due to fluctuations of the local magnetic field on the timescale of the Larmor frequency. When an NMR experiment requires the initial magnetization to be aligned with B_0 , the experimentalist has to wait a certain delay before doing another scan and improve the signal-to-noise ratio, to allow some spins to flip back to the ground state. This “recycle delay” is usually fixed to five times the value of T_1 to get a quantitative signal, but can be shortened to $1.2 \times T_1$ to get the best signal-to-noise ratio at a sacrifice of quantitation. T_1 relaxation times can vary between milliseconds, minutes and even hours.

Measuring T_1 can be done with the inversion-recovery experiment, described in Figure 2.13 (left). The downside of this pulse sequence is that recycle delays of at least $5 \times T_1$ must be used to ensure full relaxation of the spins. For nuclei with long T_1 , a faster variant, the saturation-recovery experiment (Figure 2.13, right), can be used. This does not require the magnetization to build up again, and instead starts from an isotropically distributed, or saturated, magnetization. The drawback of this method is that saturation is sometimes hard to achieve. Implementing random delays between each saturation pulse is a possible solution. Both methods work by measuring the intensity of the signal after each scan, and incrementing the delay to plot the recovery of the z component of the magnetization as a function of the delay. Note that the T_1 values for every spin of a system can be obtained, but if the peaks in the spectrum overlap, a multi-component exponential has to be fitted, which proves less reliable.

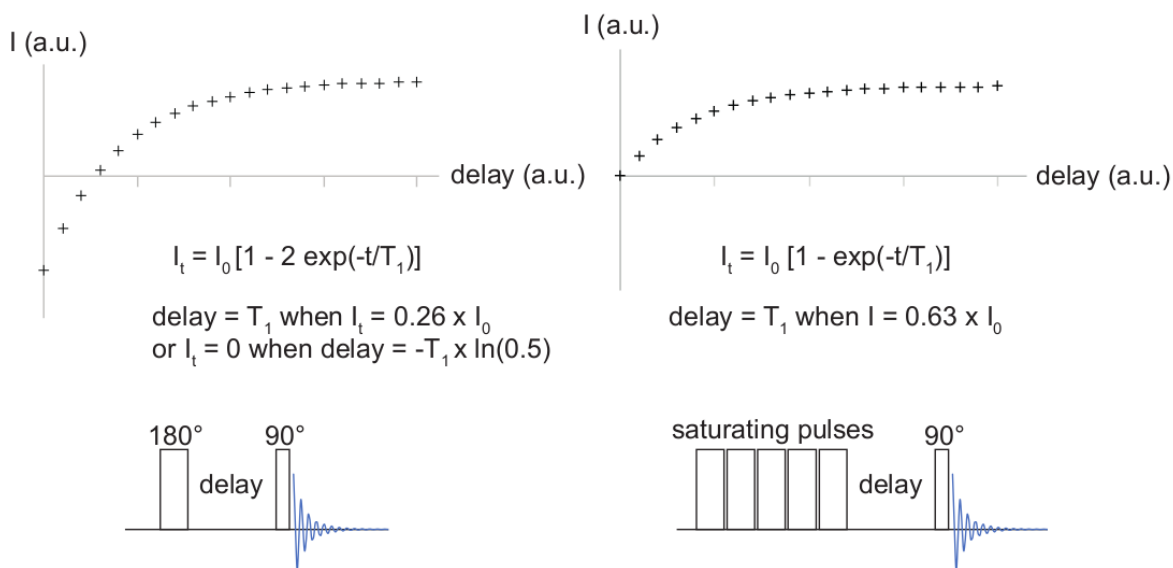


Figure 2.13: Pulse sequences and simulated data obtained with the inversion-recovery (left) and saturation-recovery (right) experiments.

The second time constant exploitable does not correspond directly to a relaxation but to a dephasing of individual spins after excitation: immediately following an RF pulse, all magnetically identical spins are aligned in the same direction, and their signal is identical and maximal, they are said to be coherent. However, as they precess, they inevitably lose coherence due to a number of processes. Two contributions – homogeneous and inhomogeneous – are distinguished, to which are attributed the T_2 and T_2^* time constants. There are several phenomena responsible for the dephasing. They include heteronuclear or homonuclear couplings, dynamics, as well as B_0 fluctuations and gradients.

To recover the coherence, it is possible to “refocus” the spins in an echo. The main use of this concept, in this thesis, is to cancel the broad probe background in ^1H spectra with the DEPTH pulse sequence, shown in Figure 2.14.

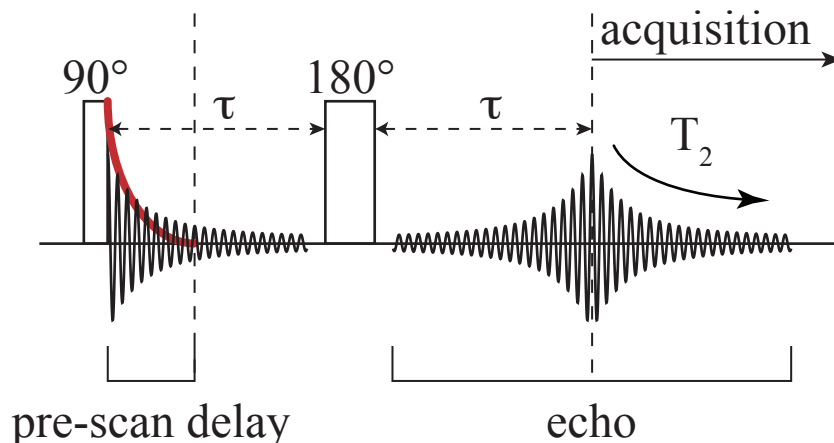


Figure 2.14: DEPTH pulse sequence showing the spin echo. The thick red decreasing line represents short-lived signals such as ring down and probe background that should not be recorded. The left vertical dotted lines represents the beginning of the acquisition in the case of a single pulse sequence, while the right vertical dotted line represents the acquisition in the DEPTH pulse sequence.

The background comes from a short-lived signal from protons in the MAS stator, represented as the thick red line, decreasing, through T_1 , faster than the FID after the initial 90° pulse. Other short-lived signals include the probe ring down, which is a residual of the relatively very intense RF pulse. When using a single-pulse excitation, the FID acquisition cannot start immediately after the 90° pulse because of these signals. A pre-scan delay of several μm must be intercalated, during which signals of interest with fast T_2 relaxations also decrease leading to a significantly smaller signal-to-noise ratio. The echo is produced with a 180° pulse after a delay τ (typically μs or ms) which has the effect of inverting the order of the spins; those with the highest precession frequency now lag behind those with lower precession frequencies. Once they catch up, after another delay τ , the coherence is again in its initial state and gives the maximum signal. As is schematically shown, the FID is acquired starting from the maximal intensity of the echo (right vertical dotted line), while in the case of a one-pulse

sequence (left vertical dotted line) from a lesser intensity. Of course more complex experiments further manipulate the magnetization after the coherence is recovered. Importantly, some contributions to the dephasing can or cannot be refocused depending on the pulse sequence, allowing the operator to manipulate the spins according to his needs. This way, it is possible to refocus selectively heteronuclear couplings over homonuclear couplings for example. It should be noted that in powders, the FID rarely outlasts a few dozen of ms, but when it does, it can indicate motion-averaging of some couplings. This results in a smaller linewidth of this particular species. Therefore some dynamics information can be retrieved from an analysis of T_2 values.

2.1.6 Relevant NMR-Active Isotopes

When comparing NMR-active nuclei, the parameters used to characterize the sensitivity of a nucleus are: relative natural abundance of NMR-active isotope versus inactive isotopes to know how many spins can be expected in a sample, and the gyromagnetic ratio because it determines the signal intensity per spin. Experimental considerations are given by the spin value to know what interactions might complicate the spectrum, and the T_1 relaxation constant which determines the recycle delay, that is how rapidly the scans can be repeated.

^1H

This nucleus has nearly 100 % natural abundance, a spin $I = 1/2$ therefore no quadrupole moment, and the highest gyromagnetic ratio γ so generates a strong FID. The high γ value requires a channel to be dedicated to it (and ^{19}F), so proton manipulation can be done routinely without giving up another nucleus. T_1 relaxation times are usually only a couple of seconds. Data acquisition is therefore fast. For all these reasons, ^1H nuclei are commonly used as magnetization source in CP experiments.

In many samples however, the strong dipolar coupling proves challenging. It can also be used to probe pores in materials via water content.

²H

This isotope of hydrogen has a spin $I = 1$ and a small quadrupole moment with typical values of quadrupolar splitting on the order of magnitude of 10^5 Hz. If there are microsecond-scale dynamics in the system, giving two different splittings, the shape of the peak depends on the equilibrium. For this reason, although deuterium NMR requires isotopic enrichment (natural abundance of 0.01 %), which can be costly and not always accessible by synthetic routes, it is widely used to probe dynamics, like aromatic ring rotation or guest diffusion.

⁷Li

This is the most abundant isotope of lithium (92.4 %) with a spin $I = 3/2$, high γ and small quadrupole coupling constants. It is employed here as a guest in porous materials to probe the pore size. The small chemical shift range of ⁷Li (± 2 ppm for most materials) is overcome by the $\Delta\delta$ of the porous carbon material (see following section), and the quadrupole interaction is absent in solution.

¹³C

This nucleus has a spin $I = 1/2$ and is often observed in organic matter. Because of its low abundance (1 %) and low sensitivity compared to protons, it is most of the time employed in conjunction with ¹H for CP, with high-power decoupling during acquisition. The signal is then enhanced up to a factor of 4, and the recycle delays are shortened to the proton's value. It can provide structural information on the activated carbon and behavioural information on organic adsorbates.

²³Na

This nucleus has a spin $I = 3/2$, 100 % abundance, high sensitivity and a very short T_1 relaxation constant. In this work, sodium ions are used to study the porosity of materials. When the ions are in solution, ²³Na signals do not present a quadrupolar broadening, and are therefore rapidly acquired.

¹³³Cs

This nucleus also has 100 % natural abundance. Its quadrupole moment originating from a spin $I = 7/2$ is relatively small. Caesium ions are also relatively easy to use in the study of porosity although the experiment require slightly longer recycle delays compared to ¹H, that is up to ten seconds. As observed in reference CsCl solutions of varying concentration and also in CsCl adsorbed in activated carbons, the chemical shift is concentration dependent.

2.1.7 Exchange Averaging in 1D NMR Spectra

Averaging of NMR signals is a common phenomenon observed when individual nuclei explore several magnetic environments. In the case of a solvent adsorbed in porous carbons, the diffusion of solvent molecules between regions giving rise to different NICS affects the NMR spectrum. The perturbation depends on the average time each molecule remains in each environment. Considering a nucleus able to explore two environments, several cases can be distinguished: the slow exchange regime where both peaks may be broadened but without being shifted, the intermediate regime where both peaks have merged into a single very broad peak, and the fast exchange regime where the single peak narrows.^[82] To understand these observations, we can turn to the underlying principles of the Fourier transform.

In the fast exchange regime, the resulting peak is located at the average of the chemical shifts weighted by the residence time in each environment. To illustrate this, various NMR signals were simulated using cosine waves and subsequently Fourier Transformed by fitting cosine functions of variable frequencies, whereby the NMR spectrum is obtained as the integral of the product between the original and the fitted functions (full details of the simulation are given in Appendix 1). This simulation is a simplified case of fast exchange where motional broadening is not accounted for. Its purpose is to show how the averaged chemical shift depends on the relative dwell times. Figure 2.15 (a) shows the simulated NMR signals; the blue component oscillates at a frequency of 30 Hz and the red components oscillates at 50 Hz. The ratio of the time spent oscillating at either frequency is given: an average of approximately 32 Hz is obtained when adopting 30 Hz for 0.1 ms and 50 Hz for 0.01 ms, and an average of 40 Hz is obtained when oscillating at both frequencies for the same time. For better visibility, the angle in radians travelled as a function of time is plotted in Figure 2.15 (b). The spectra obtained after Fourier Transformation, Figure 2.15 (c) show how the apparent frequency of the exchange-averaged peak depends on the residence time in each environment. When the residence times of the nucleus in both environments are identical, we call it a symmetric exchange. This is found for example in an acid-base mixture when $\text{pH} = \text{pKa}$, where by definition both acid and conjugated base are equimolar. However, asymmetric exchange is more relevant to the present study due to the large population difference between the in-pore and ex-pore environments, and also between the volume of the different connected pores.

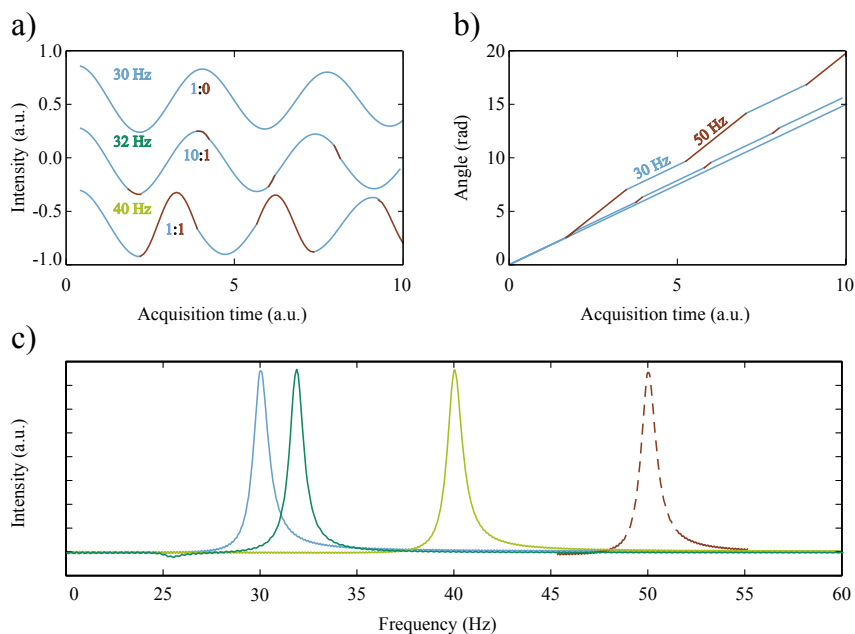


Figure 2.15: Portion of simulated cosine waves oscillating at 30 Hz (blue) or 50 Hz (red) for various period of times a), angle evolution in function of time b) and corresponding Fourier Transformed spectra c).

Experimental measurement of diffusion-related phenomena is a useful approach to learn more about characteristics such as pore connectivity, tortuosity... Diffusion coefficients of adsorbed species can be determined experimentally via NMR using Pulsed Field Gradient (PFG) techniques.^[83] A number of PFG NMR studies have shown that diffusion of species confined in carbon micropores is reduced significantly compared to bulk solution. Furtado *et al.* observed a broad distribution of local diffusivities for a carbon with a bimodal pore size distribution which was interpreted in terms of restricted internal diffusion between pores of different sizes.^[84] PFG NMR measurements on ethylene carbonate and dimethyl carbonate mixtures by Alam & Osborn Popp showed that diffusion coefficients for species adsorbed in carbon micropores were reduced by up to a factor of five compared to bulk solution.^[85] Forse

et al. used PFG NMR to study microporous carbon supercapacitor electrodes and observed significant reductions in the diffusion coefficients of adsorbed species, although acetonitrile solvent species were found to diffuse faster than the larger electrolyte ions.^[86]

While PFG NMR provides significant insight into the dynamics of species confined within the porous carbon network, further information regarding the dynamic exchange of species between pore environments and also between the in-pore and ex-pore environments can be obtained from exchange spectroscopy (EXSY) measurements.^[87] In this experiment, for which the pulse sequence is shown in Figure 2.16, the first pulse and subsequent delay allows the single-quantum magnetization to precess at a characteristic frequency. The second pulse converts this coherence into a population state, which is maintained for a duration called the mixing time, t_{mix} . For zero mixing time it is expected that there will be no diffusion and for long mixing times it is expected that the solvent molecules will reach an equilibrium between the different pore locations. After the mixing time a third pulse is applied, and the spins once again precess at their characteristic frequencies and a signal is detected. After a Fourier transformation of both time dimensions is performed, a 2D spectrum is obtained. Magnetization that has not been exchanged will have precessed at the same characteristic frequency during both times, giving rise to a peak on the diagonal of the spectrum. Magnetization that has been exchanged between in-pore and ex-pore locations will have precessed at one frequency initially and another during detection. A peak will appear off-diagonal in the spectrum and at the direct-dimension chemical shift of the spin where the molecule finally resided. These two cases give rise to diagonal peaks and cross-peaks, respectively. Further information can be extracted about by

performing the experiment with varying mixing times. Integrating the cross-peak area and plotting as a function of mixing time yields a build-up curve, from which exchange rate constants can be extracted.^[75,81]

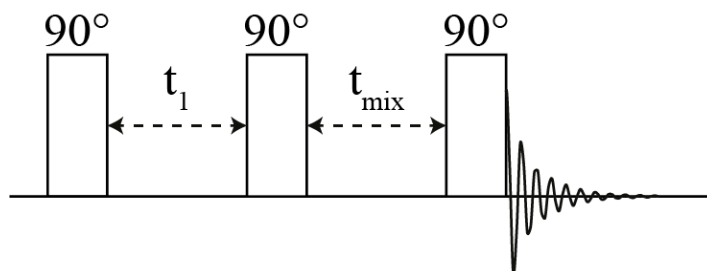


Figure 2.16: Pulse sequence of the EXSY experiment. For each t_{mix} chosen, the sequence is repeated with increasing t_1 values.

The EXSY approach was applied by Alam & Osborn Popp who showed that the in-pore environment is inhomogeneously broadened due to species occupying a range of pore environments, between which exchange takes place on the millisecond timescale.^[85] Griffin *et al.* showed for a commercial porous carbon saturated with an organic electrolyte that in-pore – ex-pore exchange of the anionic species also takes place on the millisecond timescale, although did not fit well to a single exchange process.^[56] Fulik *et al.* subsequently showed that build up curves in EXSY data for commercial activated carbon saturated with organic electrolyte can be interpreted in terms of two processes with different rates, *i.e.* a slow process attributed to diffusion from the centre of the particle to the surface, and a much faster process attributed to effective exchange between ex-pore and in-pore.^[67] In addition, it was shown that exchange dynamics can also affect the observed $\Delta\delta$ and lineshape in 1D spectra, whereby the onset of in-pore – ex-pore exchange upon saturation of the micrometre-sized particles leads to a reduction of the observed $\Delta\delta$.^[63] In these typical cases, the

diffusion path between the ex-pore and in-pore environment is much shorter, allowing faster exchange of species between ex-pore and in-pore which leads to partial or complete exchange averaging of the in-pore and ex-pore resonances.

2.2 Gas Sorption

For this technique, experimental aspects will be discussed to establish how the data is collected, which will allow to take a practical approach to the theory behind the data treatment.

2.2.1 Sample Preparation and Measurement

The gas adsorption experiment consists in the progressive introduction of a probe gas into the cell starting from a low pressure, while monitoring the pressure variations. The pressure is given as p/p_0 , *i.e.* relative to an internal atmospheric pressure reference p_0 at the same temperature as the sample. Figure 2.17 illustrate the procedure and the various phenomena taking place. During activation, various adsorbed species present in air are removed (blue circles). The initial pressure in the range $10^{-9} - 10^{-5}$ will determine the beginning of the isotherm and the smallest detected pore size, and depends on the performance of the vacuum components. A cell containing the sample is immersed in a cryogenic liquid bath, typically the same species as the probe gas, *e.g.* liquid nitrogen at 77 K for nitrogen adsorption, which means that the probe gas will condensate in the sample and diffuse in the liquid state through the pore network.

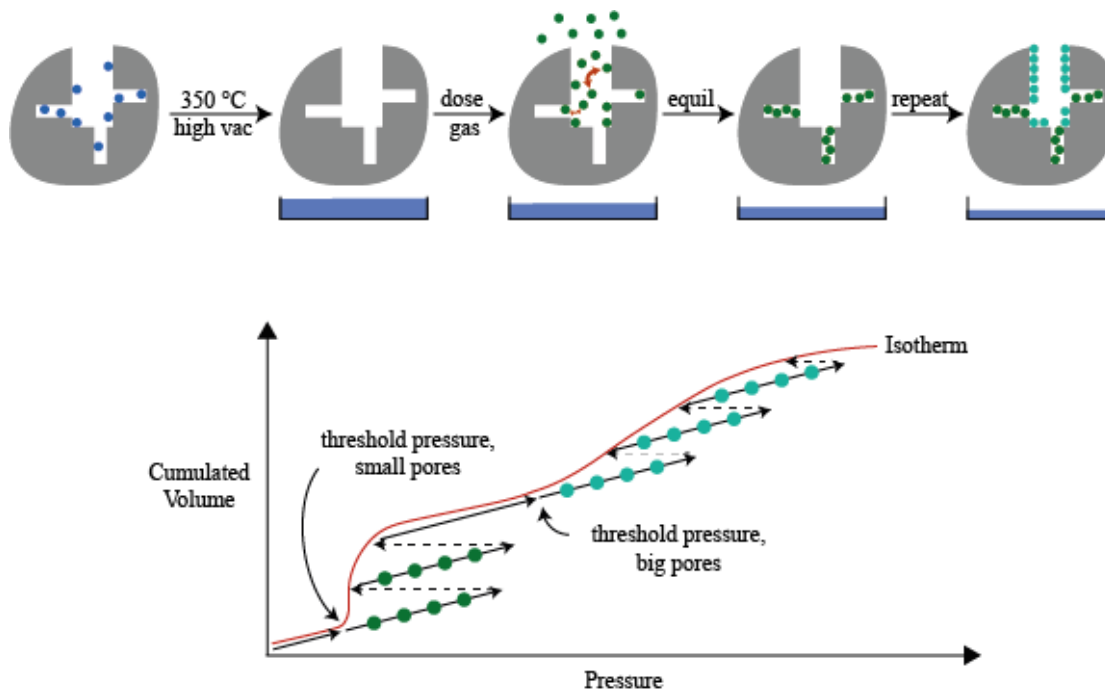


Figure 2.17: Scheme of the gas adsorption experiment: diffusion of gas molecules in the particles and real-time measured data. The grey bodies are the particles, the white rectangles are the pores (two sizes), the blue circles are initially adsorbed molecules, green and cyan circles are probe gas molecules adsorbing in the small and big pores, and the blue rectangle is the cryogenic bath. In the graph, the black arrows represent dosing of a known amount of gas, the dashed arrows represent the diffusion of gas during equilibration time, and the red line is the obtained isotherm.

Known amounts of probe gas are introduced step-wise (black arrows in the graph), which immediately causes the measured pressure to increase. The system is then isolated and allowed to reach equilibrium; as the gas molecules diffuse into the pore network, they experience variable attractive interactions with the pore walls. Because physical adsorption is a reversible process (red double arrows), on a first approximation the gas will diffuse into the smallest pores, in which the attractive interactions are the strongest. Therefore at equilibrium the first gas molecules introduced (green circles) will occupy the smallest available pores (small white rectangles). When the pressure

has decreased to a stable minimum (dashed arrows), the next dose is introduced. When all the small pores are saturated, the next smallest available pore (big white rectangles) are progressively filled with the gas molecules (cyan circles) once the pressure is high enough. In reality, several pores are filled simultaneously, but to various extents according to a Boltzmann distribution. The isotherm is obtained by plotting the cumulated volume of probe gas versus the corresponding equilibrium pressures.

The probe gas can virtually be any gas molecule. For example hydrogen is very often used to characterize the performance of hydrogen storage materials. The limitations of using just any species, besides the pressure and temperature required for the gas phase, is in the data treatment step, where only specific gases have been benchmarked to calculate *e.g.* pore size distributions from DFT methods, such as nitrogen, argon, CO₂ or krypton. These gases have advantages and disadvantages arising from specific properties such as quadrupole moment, size and boiling point.^[89] Notably, the quadrupole moment of nitrogen hinders its diffusion in small pores and requires a liquid nitrogen bath. Argon has the combined advantages to be monoatomic and therefore non-quadrupolar, and adsorb at higher pressures thus diffusing faster than nitrogen but also requires a liquid nitrogen or argon bath. CO₂ can be used at 0 °C in an electronically controlled cryostat thus eliminating the problems arising from cryogenic liquid evaporation, but can also suffers from slow diffusion.^[90] Typically however, a combination of gases is employed to obtain a reliable image of the porosity. Finally, sample characteristics such as tortuosity, surface functionalities or volume of subnanometre pores all determine the experimental time required, making GS a lengthy characterization method where few samples can be run per week.

The appearance of successfully acquired isotherms yields general information on the porosity. At a glance it is possible to determine whether the sample is microporous or mesoporous for example, depending on the pressure range at which the cumulated volume increases stepwise. Several steps in the isotherm indicate several pore populations. When recording the adsorption branch (as shown in Figure 2.17) as well as the desorption branch (starting from $p/p_0 \sim 1$ and removing adsorbed probe gas molecules instead) of mesoporous materials, hysteresis loops can give information on the rigidity of the pores as well as bottle-neck effects. Isotherms and hysteresis loops have been classified by the IUPAC into several types depending on the pore populations and shapes^[91], but activated carbons used in this project are microporous and therefore of type I without hysteresis. The total pore volume is directly obtained from the cumulated dosed volume of gas at $p/p_0 = 1$, and is perhaps the only true result one can obtain, within experimental error, because no further calculations, simplifications and assumptions are involved, as discussed hereafter.

2.2.2 Fitting of Isotherm

A variety of methods of analysis of the isotherm have been developed over the years, applicable to specific p/p_0 ranges. Briefly, early methods by Horvath-Kawazoe^[92], Dubinin-Astakhov and Dubinin-Radushkevich^[86-88] can be applied to microporous carbons but with shortcomings in terms of applicability to various sample textures or pore geometries, and overestimation of pore volumes.^[96] Another method that is widely applied despite known errors is the BET method, developed to obtain surface area of mesopores, not micropores. The most recent DFT-based methods are more versatile and more robust, and were used to analyse the samples in this work. The DFT-based methods consist in fitting the experimental isotherm using a library of calculated isotherms for a range of pores sizes of particular geometry (slits, cylinders,

spheres, or mixture thereof), called a kernel. This procedure yields pore size distribution and surface area.

Building of a Kernel

The most recent kernel available in Quantachrome software is the Quenched-Solid Density Functional Theory (QSDFT) kernel, consisting in a library of around one hundred calculated isotherms and developed by Neimark *et al.*^[90–92]. In more detail, the calculated isotherms represent the density profile of a gas in a certain pore at any pressure, which depends on fluid-fluid and solid-fluid interactions. Interactions between molecules are characterized by the resulting potential, positive in case of repulsion and negative in case of attraction, as a function of the intermolecular distance r , and are modelled using Lennard-Jones potentials^[100], of which a general equation is as follows:

$$2.11 \quad U = A[(B/r)^{12} - (B/r)^6]$$

where A and B give the energy and the intermolecular distance of the most stable state of the system. The shape of this function is illustrated in Figure 2.18. Fluid-fluid interactions are responsible for deviations from the equation of state of perfect gases, that is they determine the gas density, liquid-vapor equilibria... The parameters can be determined for example by measuring the viscosity of a gas at various temperatures and pressure. Solid-fluid interactions are determined using chemically similar but non-porous surfaces, *i.e.* graphite in the case of carbon materials. The solid-fluid potential is modelled with an additional distance-dependent term introduced by Steele^[101], yielding an equation of the shape:

$$2.12 \quad U_{sf} = C * B^2 * A \left[(B/r)^{10} - (B/r)^4 - \frac{B^4}{r^3} \right]$$

where C contains the structural parameters of graphite, *i.e.* interlayer distance and density. In this case it is found that B affects the gas-graphite distance as well as the energy of the most stable conformation.

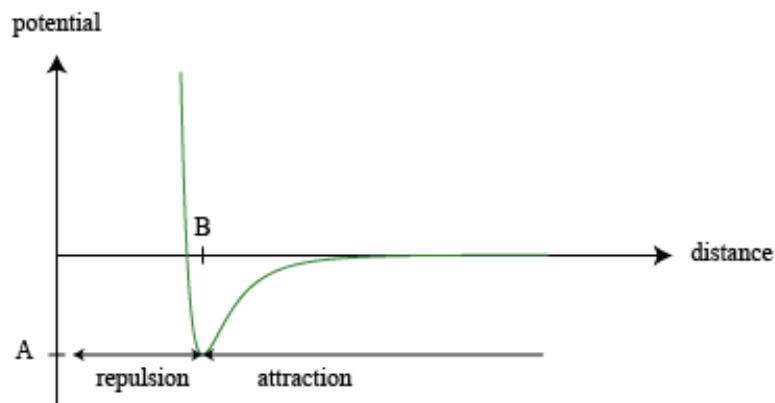


Figure 2.18: A 12-6 Lennard-Jones potential giving the forces between two molecules in function of the inter-molecular distance.

To give some examples to better understand the parameters, a smaller value of A is taken for nitrogen compared to argon (94.45 vs 118.05), which means that the fluid-fluid attractive interactions are weaker in nitrogen as reflected by its lower boiling point (77 K versus 87 K). The parameter B is bigger for nitrogen than for argon (3.575 and 3.305) consistent with the bigger size of the diatomic species. On the other hand, similar values of A are taken for nitrogen and argon in the solid-fluid potential so any difference in adsorption behaviour would result from differences of B . For comparison, the interaction of gas with zeolites depends much more on the nature of the gas, where for nitrogen B is 147.25 and for argon it is 171.24.

Another kernel is NLDFT, unfortunately this method suffers from the absence of 1 and 2 nm pores in the PSD due to the two steps in the isotherms, reflecting the capillary condensation phenomenon, *i.e.* layer-by-layer adsorption on flat graphene

sheets (second and third adsorbate layer), although it has been shown that this can be mitigated by implementing finite-sized slit pores.^[102] In real samples containing a range of defects such as non-six-membered rings or surface functional groups, the layer-by-layer adsorption is not clearly defined. One novelty introduced in QSDFT to improve the PSD is the surface roughness parameter. In practice, this is simply implemented by a transverse gradient of density of the pore walls, as illustrated in Figure 2.19. Other types of defects are however not directly expressed in the kernels and the gradient cannot be changed. Other kernels have introduced a similar concept of intermediate density of the pore wall but are not yet included in data treatment softwares.^[103]

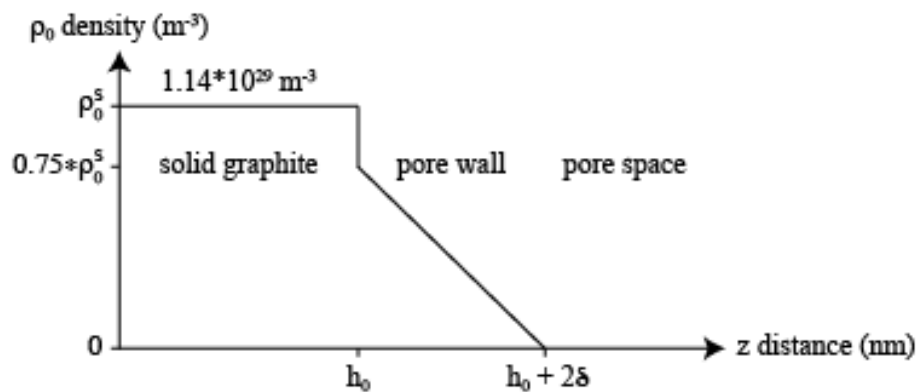


Figure 2.19: Gradient of density of the pore walls introduced in the QSDFT kernel to suppress the layer-by-layer condensation phenomenon and improving the fit around 1 and 2 nm pores. h_0 is the thickness of the solid wall set to 2×0.34 nm and δ is the roughness parameter set to 0.13 nm.

Fitting Procedure

Figure 2.20 shows an experimental isotherm (red line) obtained from a hierarchically porous sample with two distinct pore sizes: three small pores and one big pores connecting them (red area).

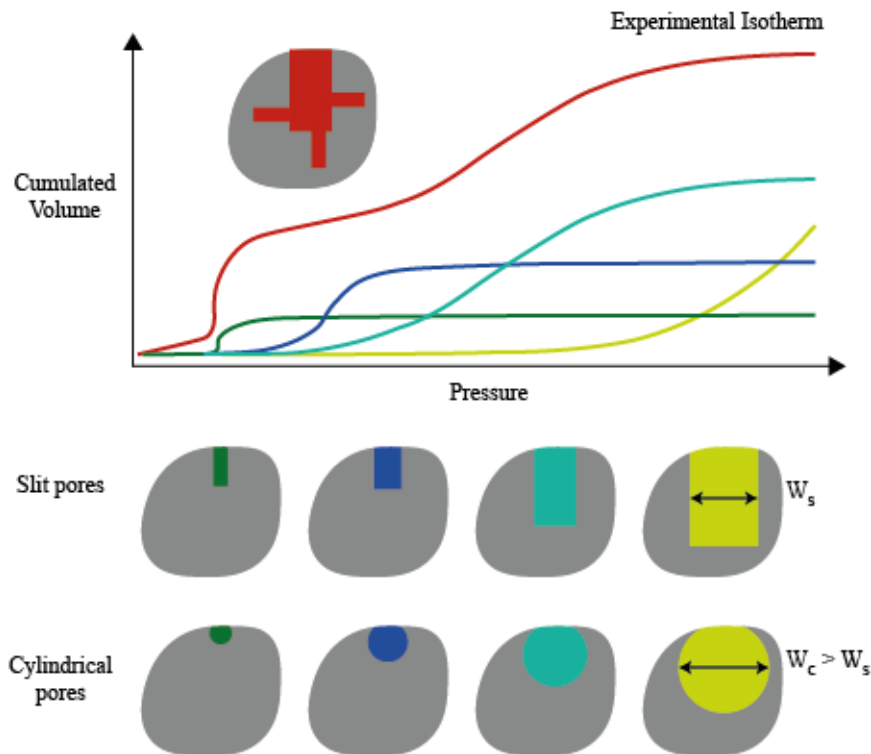


Figure 2.20: Fitting procedure of the experimental isotherm (red line) with kernels of calculated isotherms (green, blue, cyan and yellow lines). The grey bodies are the carbon particles, and the coloured areas within are pores of specific sizes, in which adsorption follows the corresponding calculated isotherm.

The green, blue, cyan and yellow lines are the calculated isotherms, showing a step at specific pressures. In practice, the ~ 100 experimental isotherms are made of ~ 100 points, but the resolution is then enhanced by the extrapolation of up to ~ 400 additional points per isotherm. These points are located at defined p/p_0 values that coincide with the points of the calculated isotherms. Note that the kernels do not necessarily have the same resolution. The cumulated adsorbed volume at each p/p_0 point, $N_{\text{exp}}(p/p_0)$, is then fitted by a linear combination of all isotherms, even if their adsorption step takes place at pressures that are orders of magnitude different, because

all pores are partially filled at any pressure. This corresponds to solving the following equation:

$$2.13 \quad N_{exp}(p/p_0) = \int_{D_{min}}^{D_{max}} N_{exp}(p/p_0, D) f(D) dD$$

where D_{min} (0.385 nm or bigger depending on experimental conditions) and D_{max} (33.24 nm) are the smallest and biggest pores of the kernel, and $f(D)$ is the PSD function. As can be seen in Figure 2.20, the step pressure in the green line matches the first step pressure of the isotherm. By taking three green pores, the step volume also matches. The cyan isotherm perfectly matches the second step of the experimental isotherm, indicating that the pore volume needs no scale-up. The steps of the blue and yellow lines do not match any step in the red line, therefore no (or very few) blue nor yellow pores will appear in the PSD. The fitting procedure allows to express the fitted isotherm as a function of pore size instead of p/p_0 . The PSD is then simply obtained as the slope of the isotherm, in this case a bimodal distribution of green and cyan pores. Multimodal PSD offer the possibility to gain insight into the connectivity of pores by comparing PSD from a series of probe gas molecules of different sizes^[104]. Note that because of non-linear dependence of adsorption pressure on pore size, small pores are better resolved. This appears in the isotherm as sharper steps for small pores compared to big pores.

Importantly, any kernel can be used to fit the isotherm through linear combination of each individual calculated isotherm, but some will give a better fit than other. The quality of the fit is an indication that the sample contains pores that are better approximated by this or that geometry, but this does not mean that the pores have that particular geometry, as the kernels are based on regular and infinite pores. The kernels have been tailored to samples of known structure, for example slit pores for

microporous carbons, cylindrical mesopores for alumina-silica templated carbons, spherical pores for zeolite templated carbons... The state-of-the-art GS analyses unfortunately still suffer from discrepancies, especially the PSD of less-well defined structures obtained through different data treatment methods on different instruments.^[82,98] The experimentalist must therefore make an informed choice regarding the kernel, interpret any resulting PSD features and discuss extensively the appropriateness of the chosen geometry with respect to the true, imperfect and variable pore shape of the sample.

2.3 Raman Spectroscopy

Herein are briefly described the concepts necessary to record and interpret Raman scattering spectra of activated carbons.

2.3.1 Origin of Raman Scattering

Raman scattering results from the inelastic scattering of incident photons, where the photons are emitted in all directions with a different energy from the photons absorbed. The energy differences involved are in the infra-red, corresponding to vibrational states. The conservation of energy and momentum of the system allows only certain vibration modes of the material. The energy diagram illustrating this process is shown in Figure 2.21. If the scattered photon has a lower energy than the incident photon, then the material transitions from a low-energy state to a higher energy state. This is the Stokes scattering. If on the contrary the scattered photon has a higher energy, it is the anti-Stokes Raman scattering, which is possible only if the material was in an excited state prior adsorption of photon.

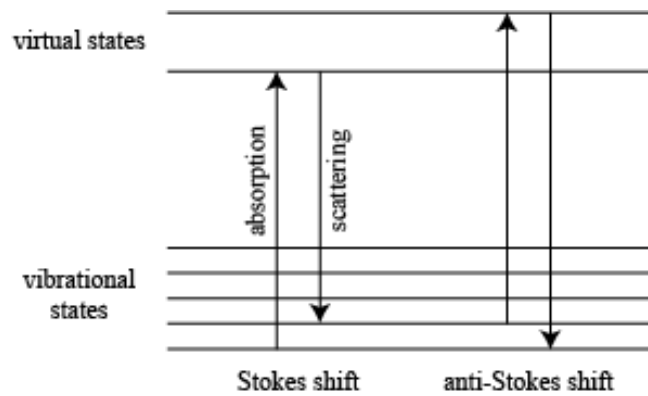


Figure 2.21: Stokes and anti-Stokes transitions between vibrational states at the origin of the Raman scattering phenomenon.

The advantage of Raman scattering over resonant spectroscopies is that the light source does not need to match any particular transition for its observation, which means that a variety of constant light sources, ranging from ultra-violet to near infra-red can be employed. A disadvantage is that the Raman scattering is an inefficient process, meaning only a small percentage of photons will be scattered inelastically, while most will be scattered elastically through the Rayleigh process and must be filtered out. For these two reasons high intensity monochromatic lasers are commonly employed.

2.3.2 Application to Carbonaceous Materials

Graphite-like materials show a variety of bands with different physical origins: the G band (1580 cm^{-1}), the D band (1350 cm^{-1}), and other bands arising from combinations of these such as D+G (2940 cm^{-1}) or the overtone 2D (2690 cm^{-1}).^[106] Much structural information on activated carbons can be extracted from the study of the G and D bands alone.

Origin of G and D Bands

The two corresponding vibrational modes are shown in Figure 2.22. The G band originates from E_{2g} vibration mode of graphitic clusters, and the D band from A_1' stretching mode of C=C bonds. The latter is invisible in pristine graphite and therefore requires the presence of defects such as C(sp²)-H or C(sp³).^[107]

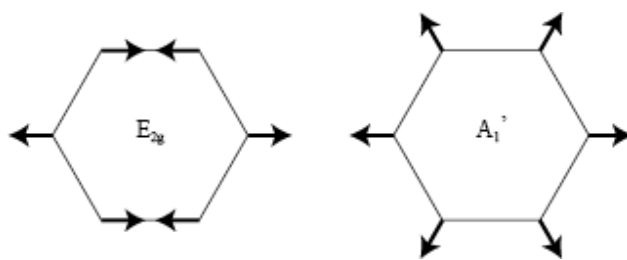


Figure 2.22: E_{2g} and A_1' vibrational mode at the origin of the G and D bands.

Use of G and D bands

Guidelines on how to interpret Raman spectra of activated carbons were taken from Ferrari *et al.*^[101,102]. To extract information on the activation mechanism with Raman, a typical method is to follow the position and width of the G and D bands as a function of BO.^[110] The variation of the size of the cluster of sp² carbon atoms impacts the peaks in several ways: with decreasing size, *i.e.* amorphization, the G and D band become concertedly broader and shift to lower frequencies relative to the bands in highly-oriented pyrolytic graphite. There are therefore four redundant trends at disposal, making the results all the more robust. The G and D bands are commonly best fitted with two sets of bands each, which has been suggesting there are two regions of different levels of order^[111]. G1 and D1 are significantly narrower than G2 and D2 so bands 1 are assigned to the OD and bands 2 to the DD. The ratio D/G reflects the size of the cluster of sp² carbon atoms in the respective domain. According to Ferrari and

Robertson, the variation of D/G as the domain size decreases depends on the width of the G band: D1/G1 with G1 narrower than 40-60 cm^{-1} decreases, while D2/G2 with larger G bands (typically 120 cm^{-1}) increases.

2.4 Powder X-Ray Diffraction

2.4.1 Fundamentals of Diffraction

Compared to local probes like NMR, Raman and GS, XRD is a global probe, characterising crystallographic planes on “bulk” scale (>2 nm). In XRD, it is the X-rays re-emitted through Rayleigh scattering by the inner-shell electrons that are detected. This is an isotropic phenomenon, however, when the material contains a sufficiently large number of regularly spaced atoms, interferences between the X-rays individually scattered by each atom come into play, and allow to relate the angle at which some interferences take place with the interatomic distance. Interferences arise from the phase difference of two parallel waves: when the phase difference is 180° , or anti-phase, the electromagnetic oscillations cancel out, *i.e.* destructive interference, and when the phase difference is 0° , or in phase, the oscillations add up to a maximum intensity, *i.e.* constructive interference. Figure 2.23 shows the mechanism of phase shifting giving rise to constructive and destructive interferences.

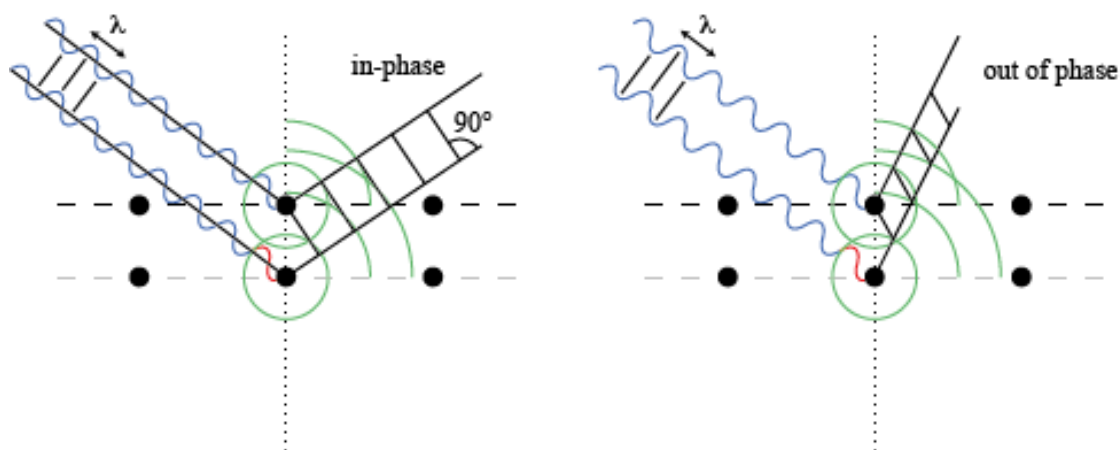


Figure 2.23: Scheme of diffraction of an incident electromagnetic wave, showing two angles at which happen a constructive interference (left) and a destructive interference (right). The coloured lines are the waves (blue for in-phase incident waves, red for additional oscillations causing de-phasing, green for scattered waves), the black lines are guides to the eyes to assess the phase, the dashed lines are crystallographic planes passing by atoms (black dots), and the dotted line is the normal to the incidence point.

Parallel and in-phase incident waves (blue) hit different atoms, the red portion of one wave is the additional distance it has to travel until reaching an atom. The isotropically Rayleigh-scattered waves are then emitted (green circles, only a portion is shown for clarity). Maximum constructive interference happens at angles where the emitted waves are in phase, *i.e.* when the short black lines passing by identical phase points of both waves are perpendicular to the propagation direction. In the left scheme, this is the case so a maximal signal will be detected, but in the right scheme this is not the case, so a weaker signal or none at all will be detected. This phenomenon causes the diffracted X-ray beam to be detectable only at specific incident angles. In addition, the wavelength of the beam must be comparable to the interatomic distance to probe interferences happening in the unit cell. Cu K α sourced X-rays of wavelength $\lambda = 1.5 \text{ \AA}$ therefore allow to probe distances ranging from few \AA to few nanometres.

2.4.2 Diffraction Experiment

The most common instrumental geometry, used in this work, is the Bragg-Brentano geometry, illustrated in Figure 2.24.

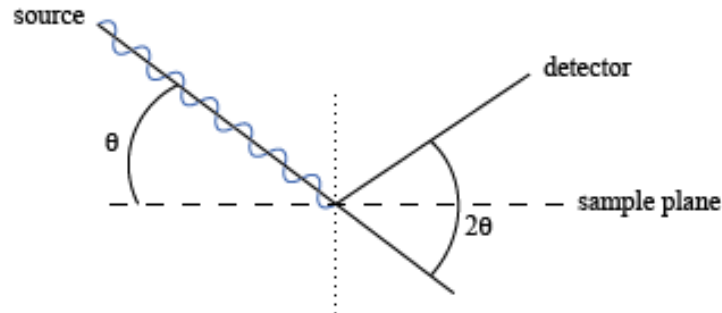


Figure 2.24: Bragg-Brentano geometry.

This geometry is meant to scan the incident angle typically from 0° to 60° while detecting only the constructively interfering waves if present. Other geometries allow to fix the incident angle and measure the intensity of the scattered waves over a range of angles. The empirical Bragg's law, reorganized as follows, is then used to calculate the interplane distance from the angle of constructive interference:

$$2.14 \quad d = n * \lambda / (2 \sin \theta)$$

where n is a positive integer, λ is the X-ray wavelength and θ the incident angle as shown in Figure 2.24. The number n means that for any interplane distance d , several peaks will be detected at different angles.

2.4.3 Practical Example: Graphite

Graphite is a good example to illustrate a practical phenomenon whereby only certain peaks are visible due to a preferential orientation of the crystals in a powder.

Indeed in the Bragg-Brentano geometry, only diffraction caused by atomic planes at an angle θ from the incident beam can be detected, as shown in Figure 2.25. For the angle θ_1 (left), the planes separated by the smallest distance can be detected, but only the blue crystal is suitably oriented, the red crystal will therefore not contribute to the signal. Similarly for another plane in the crystal, detected at angle θ_2 (right) bigger than θ_1 because of the larger interplane distance.

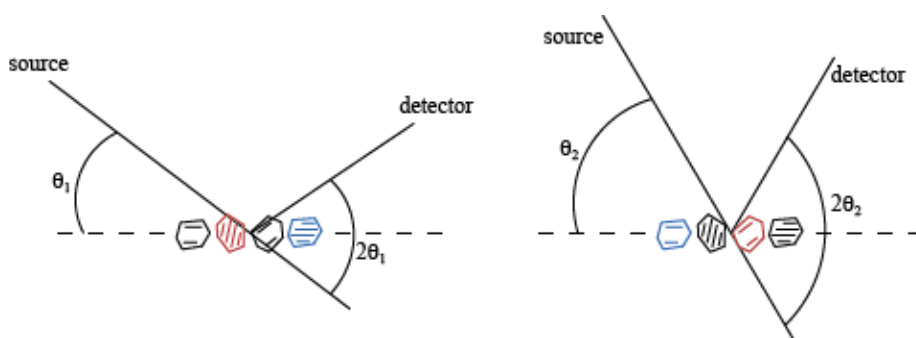


Figure 2.25: Illustration of the selective detection of crystallographic planes in adequately oriented crystals. The polygons represent single crystals in a powder, with the parallel lines inside being planes of interest, for simplicity only one plane is represented per crystal. Red and blue polygons are the crystals where the interplane distance corresponds to the θ angle, but only the blue planes contribute to the scattering of X-rays, because the red one is not adequately oriented. The black polygons do not contribute because the interplane distance is not adequate.

This means that the sample must contain a large number of isotropically oriented crystals, such as a finely ground powder. Graphite flakes being flat due to exfoliation along the graphene layers, stack horizontally face-to-face in the sample holder. Because of this, only the crystallographic planes parallel to the graphene sheets will produce diffraction, so only the family of peaks corresponding to the c axis of graphite can be detected. Randomly-oriented finely ground graphite powder or single-crystal XRD

allows us to observe all peaks. Figure 2.26 shows the PXRD pattern of standard graphite flakes (blue) and the single-flake pattern (red). The peaks are named with the Miller indices, which represent the orientation of the crystallographic plane responsible for the diffraction in the system of coordinates of the crystal, of which that of graphite is shown [112].

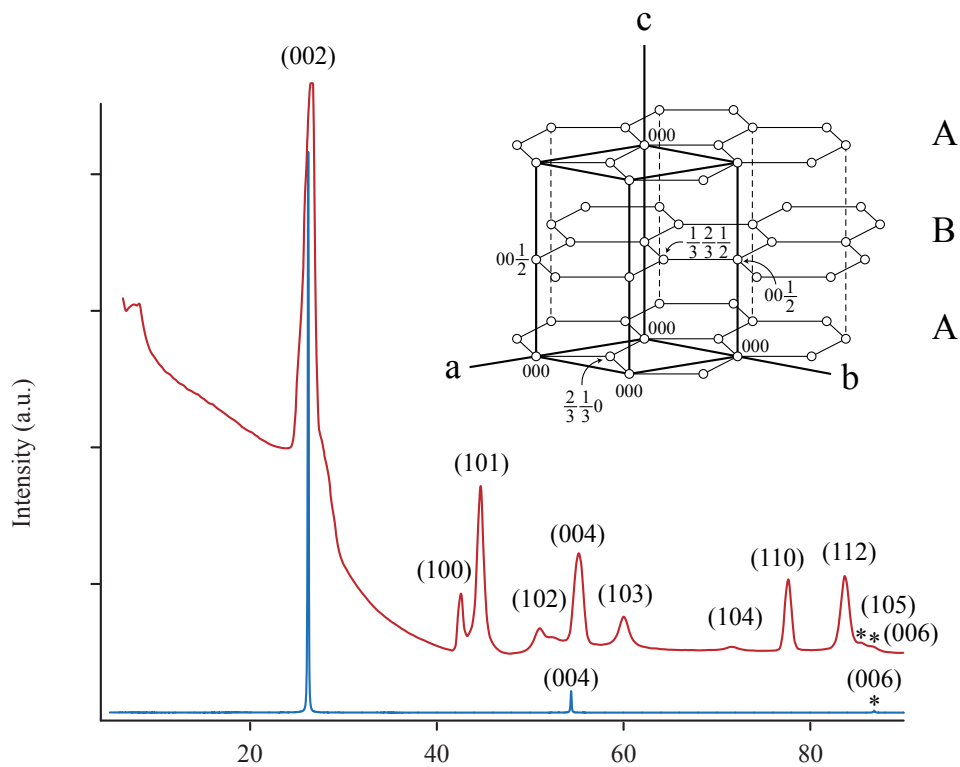


Figure 2.26: Powder pattern of graphite flakes (blue) and single-crystal pattern of one flake (red).

3 Methodology and Interpretation Guidelines

In this chapter the synthesis procedure of PDCs is described, starting from a literature procedure, subsequently improved after showing that the activation was not homogeneous. Some practical tips for the characterization are given and the data treatment protocol for each technique is discussed in detail to justify the approaches that do not always follow the literature.

3.1 Synthesis of PDCs

3.1.1 Standard Synthetic Procedure

PDCs were synthesised following a procedure similar to others in the literature.^[61,63] PEEK polymer was first carbonised in an alumina boat within a tube furnace at 900 °C under 0.5 L/min flowing N₂ gas for 2 hours before being cooled to room temperature. The resulting carbon slug was ground in a mortar into particles of approximately 0.5 mm diameter before being subjected to a steam activation step where the sample was heated in an alumina boat at 900 °C under flowing N₂ gas that was bubbled through deionised H₂O in a Dreschel bottle before entering the tube furnace.

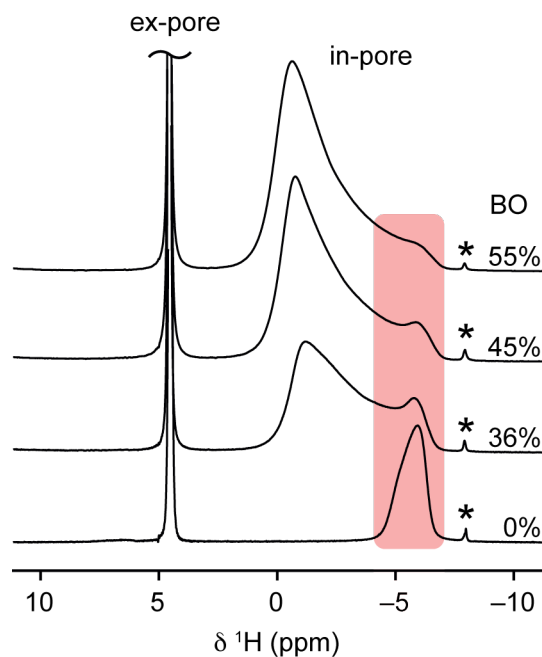


Figure 3.1: ^1H MAS NMR spectra of PDCs steamed at $900\text{ }^\circ\text{C}$ with burn-offs between $0 - 55\%$, saturated with deionised H_2O . The red area from -4 ppm to -7 ppm highlights the region of the in-pore feature corresponding to H_2O molecules in intrinsic micropores resulting from the carbonisation process. Asterisks denote spinning sidebands.

As a quick characterization tool, NMR was used first to assess the reproducibility of literature synthesis procedures. Figure 3.1 shows ^1H MAS NMR spectra of PDC samples with burn-offs between $0 - 55\%$ which were saturated with deionised H_2O . In each spectrum, the sharp ex-pore resonance at $\delta = 4.8\text{ ppm}$ corresponds to bulk water between the carbon particles, while in-pore resonances due to adsorbed H_2O molecules are shifted to between $\delta = -1$ and -6 ppm . For the $\text{BO} = 0\%$ sample (*i.e.* carbonised PEEK that was not subjected to steam activation), the observation of an in-pore resonance shows that the carbonisation process itself results in some degree of intrinsic porosity which is accessible to H_2O molecules. The large $\Delta\delta$ of 10.8 ppm suggests that these intrinsic pores are very small – approximately 0.8 nm in width. The spectra of PDCs with $\text{BO} = 36 - 55\%$ exhibit in-pore resonances with

smaller $\Delta\delta$, which is expected due to the larger pores that the steam activation introduces into the carbon structure. However, in all three steam-activated PDCs, the in-pore lineshape is broad and asymmetric, with significant intensity remaining at $\delta = -6$ ppm.

To investigate the origin of these features, two-dimensional exchange spectra were recorded on the BO = 45 % sample (Figure 3.2). For the shortest mixing time, τ_{mix} , of 0.5 ms (Figure 3.2a), the in-pore resonance is confined to the diagonal line, showing that the broadening of this resonance is inhomogeneous, *i.e.*, the water molecules occupy a range of pore environments leading to a distribution of NICS values. For a longer mixing time of 5 ms (Figure 3.2b), off-diagonal correlations between ex-pore resonance and the in-pore resonance with smallest $\Delta\delta$ signify exchange on this timescale between species adsorbed in the largest pores and those in the bulk solution. For $\tau_{\text{mix}} = 50 - 500$ ms, (Figure 3.2c,d) broadening of the diagonal in-pore resonance also signifies exchange between pores of different sizes. Overall these observations show that the steam activation process results in particles with different average pore sizes, including some particles or regions of particles that remain unactivated (as shown by the remaining in-pore resonance at $\delta = -6$ ppm). The adsorbed H₂O molecules undergo interparticle exchange whereby they first exchange with the bulk solution before exchanging with pores of different sizes in other particles. We note that even with a mixing time of 500 ms, no exchange was observed involving the unactivated pores at $\delta = -6$ ppm, indicating that diffusion within these subnanometre pores is severely restricted and H₂O molecules adsorbed within them remain effectively isolated from the rest of the porous network.

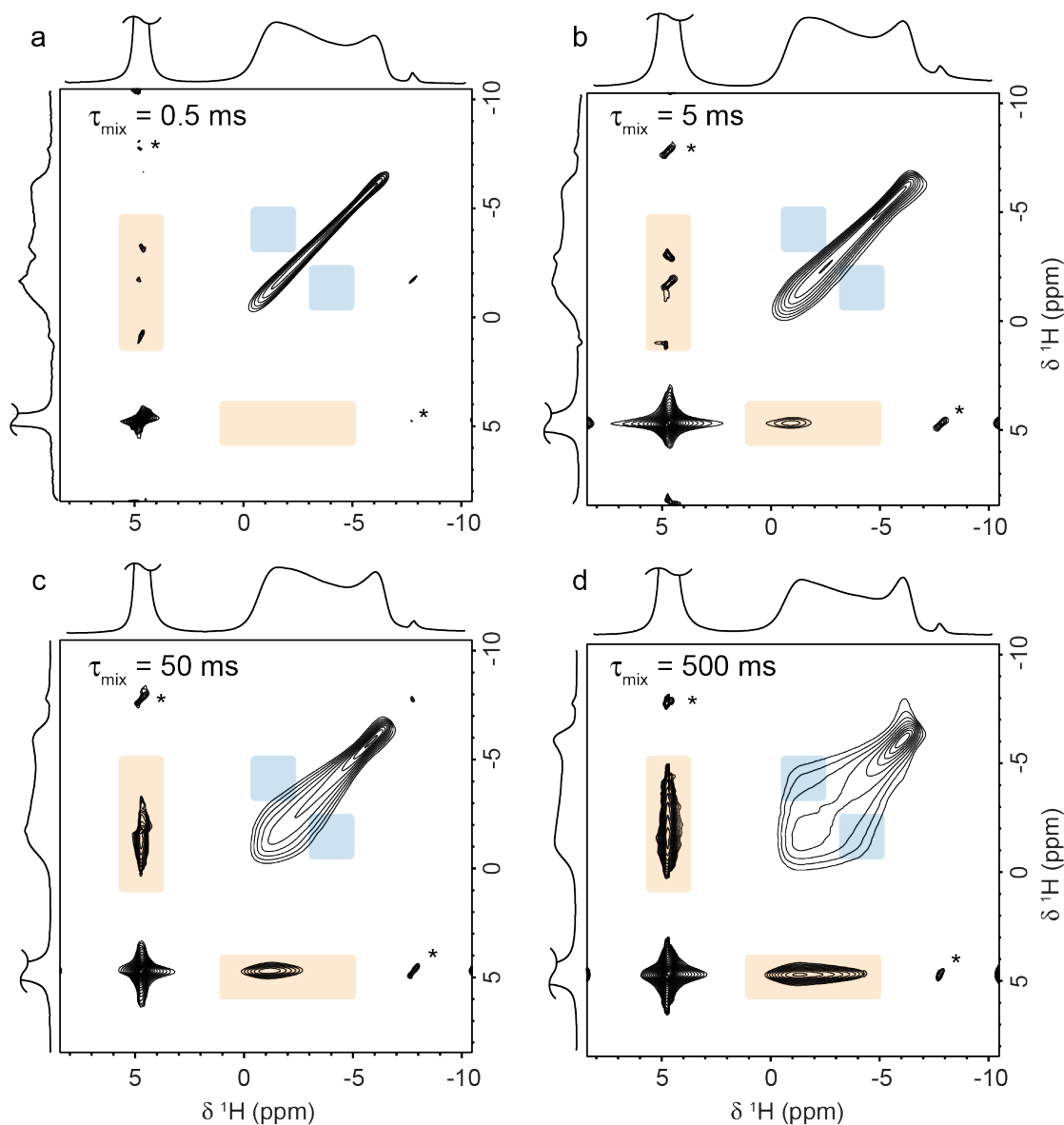


Figure 3.2: ^1H MAS exchange NMR spectra with mixing times of (a) 0.5 ms, (b) 5 ms, (c) 50 ms and (d) 500 ms using 15 mg of PDC with burn-off 45 % saturated with 15 μL of deionised H_2O . Highlighted areas indicate where cross-peaks are expected for in-pore – ex-pore exchange (orange) and in-pore – in-pore exchange (blue). Spinning sidebands are denoted by asterisks.

3.1.2 Optimized Procedure

A likely reason for the pore structure inhomogeneity is the large particle size distribution obtained when the carbonised PEEK is manually crushed prior to steam activation. In an effort to reduce the particle size distribution, the crushed carbonised

PEEK was passed through a sieve of mesh size 62 μm prior to steam activation. The sieving process selects particles smaller than the mesh size in at least two dimensions, meaning that elongated particles with one dimension larger than the mesh size can be selected if the short axes are small enough. The DLS analysis on the other hand yields a statistical distribution of particle sizes derived from their diffusion coefficients, which depends on their hydrodynamic size. Figure 3.3 shows the particle size distributions and Table 1 the values describing the distribution for several mesh sizes employed. It can be seen that the sieving qualitatively reduces the particle size down to the selected mesh size with tolerances varying from $\pm 20 \mu\text{m}$ to $\pm 100 \mu\text{m}$. Note that the sieving method is not very practical to obtain particles with sizes comparable to YP50, which is probably prepared by ball-milling. To isolate comparable particles, the sedimentation rate is a better method; small particles stay suspended longer and can be recovered after the big particles have sedimented. Possible parameters affecting the distribution of sizes could be, besides the quality and nominal size of the mesh, the amount of powder deposited on the sieves, the time spent crushing the carbon between the sieving, the duration of sieving, and the possibility of very fine particles coating the sieve which could alter the apparent mesh size. Following this procedure, the modal particle size after using the 62 μm mesh was found to be 92 μm , with 98 % of the carbon particles having a diameter of less than 200 μm .

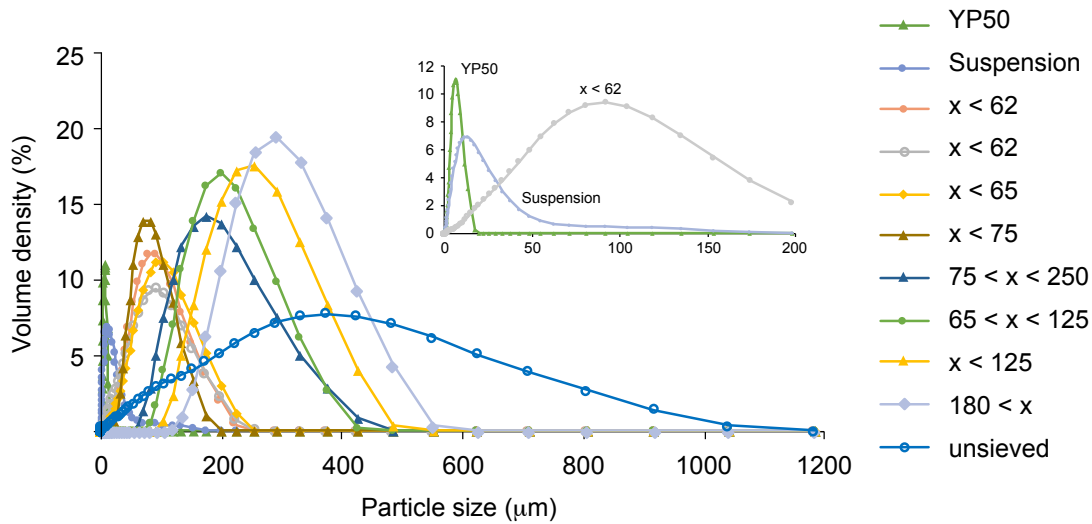


Figure 3.3: Particles size distributions obtained with different sieves. The suspension was obtained by manually grinding PDC particles and letting sedimentation proceed for 2 minutes after a short sonication period. YP50 was measured as received.

Table 1: Statistical values describing the particle size distributions. $D_x(n)$ is the size limit below which n % of the particles are smaller. The x parameter is the expected particle size (in μm) when sieved.

Name	$D_x(5)$	$D_x(10)$	$D_x(50)$	$D_x(90)$	$D_x(98)$
YP50	1.83	2.49	5.76	10.8	14.1
suspension	2.13	3.10	11.0	32.5	78.7
$x < 62$	28.2	37.3	79.4	144	186
$x < 62$	12.3	20.1	71.1	145	192
$x < 65$	23.3	33.5	85.2	156	200
$x < 75$	36.0	42.1	74.1	124	155
$75 < x < 250$	89.4	102	174	293	371
$65 < x < 125$	111	124	194	297	356
$x < 125$	137	153	238	354	421
$180 < x$	172	191	283	409	481
unsieved	19.6	42.4	242	519	691

Further modifications to the activation protocol were: the humidity was controlled by fixing the gas flow rate in the furnace tube to 0.5 L min^{-1} and the water temperature within the Dreschel bottle to $30 \text{ }^\circ\text{C}$. The sample was also spread with a uniform layer thickness of less than a mm on the surface of an inverted alumina boat to minimize turbulence and homogenise the contact with the atmosphere.

3.1.3 Sample Nomenclature

The samples are hereafter named according to the activation conditions; the carbonization conditions are not reflected in the name because they were always the same, namely 2 hours at $900 \text{ }^\circ\text{C}$ with a $10 \text{ }^\circ\text{C}/\text{min}$ ramp in nitrogen flowing at $0.5 \text{ L}/\text{min}$. The samples were named with the following building blocks: $Dx(50)$ “activating agent”_temperature_BO. Not all samples were analysed with DLS, so except specified, the sample was sieved through the $62 \text{ }\mu\text{m}$ mesh and the $Dx(50)$ should be around $80 \text{ }\mu\text{m}$. If not specified, the activating agent was steam. For example a PDC sieved through the $62 \text{ }\mu\text{m}$ mesh, without DLS analysis, and then steamed at $900 \text{ }^\circ\text{C}$ to a $\text{BO} = 56 \text{ } \%$ would be called 900_56 , while the same PDC activated by KOH at $800 \text{ }^\circ\text{C}$ to a $\text{BO} = 45 \text{ } \%$ would be KOH_800_45 . In case of a second activation step, the temperature and BO is added to the name; for example $900_29_700_7.5$ was steamed first at $900 \text{ }^\circ\text{C}$ to a $\text{BO} = 29 \text{ } \%$ and then again at $700 \text{ }^\circ\text{C}$ to a $\text{BO} = 7.5 \text{ } \%$. A few samples were recarbonized in nitrogen gas ($0.5 \text{ L}/\text{min}$) at $900 \text{ }^\circ\text{C}$ for 4 h, so the letter C followed by the BO is added; for example 700_24_C16 was steamed at $700 \text{ }^\circ\text{C}$ to a $\text{BO} = 24 \text{ } \%$ and then recarbonized which removed another $16 \text{ } \%$ of the mass.

3.2 NMR

To exploit NMR to its fullest, it is important to determine if and how the NMR spectra presented hereafter are affected by diffusion-related phenomena. Thus in this section, a comparative NMR study is presented using the optimized PDC samples and commercial samples with different solvents.

3.2.1 Sample Preparation

Although the sample preparation is quite straightforward, here are some important considerations that must be adopted in some cases to ensure reproducibility.

Sample Wetting

To ensure the activated carbon powder in the rotor be wetted thoroughly to obtain exact ex-pore and in-pore peak integrals, it is advised to introduce the solvent progressively and at various spots using a microsyringe. It is possible that the liquid surface tension between the particles is greater than the capillary forces and thus prevents the liquid from spreading and wetting all the particles. This would artificially make the ex-pore peak seem greater with a smaller in-pore peak. This phenomenon is of special concern with a very fine powder that was densely packed and using polar solvents.

Parameter Optimization

In general, the parameters of the pulse program are optimized with a reference, and applied to the sample. However it was found with activated carbons wetted with various solutions that parameters like the 90° pulse length varied with the concentration and the volume of solvent introduced. This is ascribed to the attenuation of the RF pulse power by the sample because the nutation frequency depends on the pulse power.

Therefore it is best to quickly optimize parameters affecting the quantification of the spins when such is the goal.

Solvent Evaporation

Because the temperature of the sample under typical MAS conditions increases slightly, it is possible that a portion of solvent evaporates. This will cause the ex-pore peak to appear smaller, while the in-pore peak remains constant due to the higher evaporation enthalpy arising from the confinement. Evaporation of solvent can cause pressure in the rotor to increase and even disturb the rotor cap and MAS stability. To prevent evaporation, a PTFE plug must be added in the rotor. However apolar solvents will diffuse through the plug so in addition, the PTFE plug must be replaced or wrapped in a hydrophilic material such as a hydrophilic Celgard™ membrane. This proved very efficient even when using low-boiling organic solvents such as cyclohexane for long EXSY experiments where MAS is maintained for several days, provided careful assembly. However if the solvent is evaporating, this contribution to the decrease of the ex-pore intensity must be taken into account to analyse the EXSY data. The method employed is explained hereafter.

3.2.2 Fitting of Solvent Evaporation

The build-up of the ratio cross-peaks/diagonal-peaks follows a single tanh function in the case of a single distinguishable exchange rate constant as in Eq. 3.1:

$$3.1 \quad I_{\text{cross}}/I_{\text{diag}} = A \tanh(k_1 * t_{\text{mix}})$$

In big particles, diffusion from the centre of the particle to the surface is a measurable process, and must therefore be taken into account by adding another tanh term, as shown in Eq. 3.2. Here, t_{mix} is the mixing time of a 2D experiment, k_1 and k_2

describe the exchange rate constants, which are expected to depend on the diffusion coefficient, the percolation path etc, and finally A and B could be related to the volumes of solvent undergoing the corresponding exchange process.

$$3.2 \quad I_{\text{cross}}/I_{\text{diag}} = A \tanh(k_1 * t_{\text{mix}}) + B \tanh(k_2 * t_{\text{mix}})$$

In absence of solvent evaporation, the integral of the ex-pore peak remains constant over the course of all 2D experiments, as shown in Figure 3.4a for sample 83_900_20 (where $D(50)$ is 83 μm and the BO is 20 %) saturated with water. In this case, Eq. 3.2 typically provides a much better description of the build-up curve than Eq. 3.1 (Figure 3.4c). Evaporation of water can easily be prevented by fitting a PTFE plug in the NMR rotor. When the hydrophobic solvents were used, a PTFE plug alone proved useless because the solvents can diffuse through it. In these cases, a piece of hydrophilic Celgard™ membrane was wrapped around the PTFE plug. This proved 100 % effective provided careful assembly. Due to noise levels or inaccuracies of the integration of the peaks, $I_{\text{cross}}/I_{\text{diag}}$ was not always zero at $t_{\text{mix}}=0$, therefore an additional time-independent term I_0 is added to yield Eq. 3.3, which provides a better fit. Eq. 3.5 provides no further improvement as expected because there was no evaporation.

$$3.3 \quad I_{\text{cross}}/I_{\text{diag}} = A \tanh(k_1 * t_{\text{mix}}) + B \tanh(k_2 * t_{\text{mix}}) + I_0$$

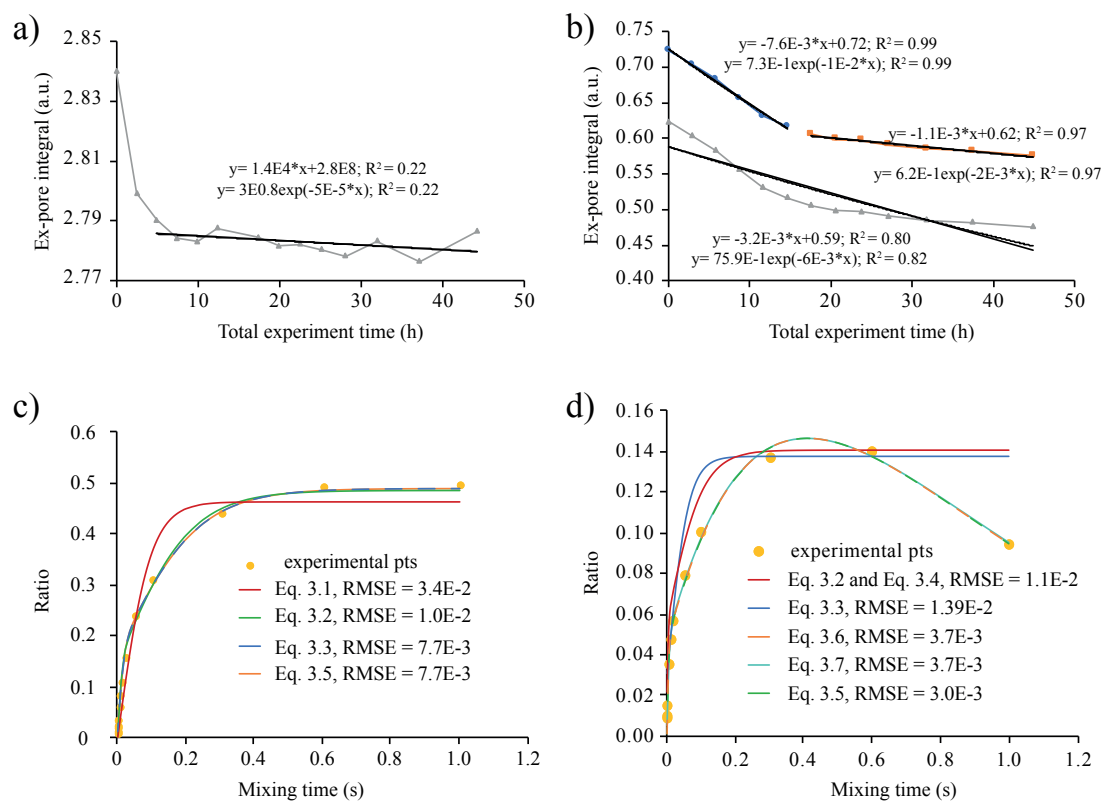


Figure 3.4: Integral of the ex-pore peak of sample 83_900_20 saturated with water a) and sample 15_900_20 saturated with cyclohexane b), taken from 1D NMR spectra recorded after each 2D experiment in function of total experiment time, and c) and d) corresponding build-up curves of I_{cross}/I_{diag} fitted with different equations.

In cases where evaporation still occurred but significant ex-pore peak remained after the experiments, the data was kept but had to be scaled with a time-dependent factor. The choice of the function to describe the evaporation kinetics was not straightforward, as the evaporation seemed linear with time but could also be fitted relatively well with an exponential decay (Figure 3.4b). For this sample, two distinct regions (blue and red points) may indicate that the seal was perturbed during the experiment, changing the evaporation rate. In case of strong or irregular evaporation, care must be taken when interpreting the exchange rate constants.

Fitting the data in Figure 3.4d with a linear or an exponential decay rate is done using Eq. 3.4 and Eq. 3.5 respectively. However, the in-pore peak is never affected by evaporation, presumably due to the higher enthalpy of evaporation of confined solvents, so I_{diag} cannot decrease below the in-pore peak integral. Therefore the build-up curve has an asymptotic behavior in case of evaporation, even though it may not appear in our figures, which can be modelled using Eq. 3.5. T_{evap} is the evaporation time constant, which is big when evaporation is slow, and D reflects the limit of I_{diag} after evaporation took place for infinite t_{mix} .

$$3.4 \quad I_{\text{cross}}/I_{\text{diag}} = (A \tanh(k_1 * t_{\text{mix}}) + B \tanh(k_2 * t_{\text{mix}})) * (a * t_{\text{mix}} + b) + I_0$$

$$3.5 \quad I_{\text{cross}}/I_{\text{diag}} = (A \tanh(k_1 * t_{\text{mix}}) + B \tanh(k_2 * t_{\text{mix}})) * (C * e^{-t_{\text{mix}}/T_{\text{evap}}} + D) + I_0$$

Visually, the fits are often identical with several equations, and some parameters are not always necessary. For example in Figure 3.4c, Eq. 3.3 and Eq. 3.5 give the same fit error and same k_1 and k_2 values, as do Eq. 3.6 and Eq. 3.7 in Figure 3.4d, which are defined as:

$$3.6 \quad I_{\text{cross}}/I_{\text{diag}} = (A \tanh(k_1 * t_{\text{mix}}) + B \tanh(k_2 * t_{\text{mix}})) * (C * e^{-t_{\text{mix}}/T_{\text{evap}}})$$

$$3.7 \quad I_{\text{cross}}/I_{\text{diag}} = (A \tanh(k_1 * t_{\text{mix}}) + B \tanh(k_2 * t_{\text{mix}})) * (C * e^{-t_{\text{mix}}/T_{\text{evap}}} + D)$$

However these parameters converge to 0 if unnecessary, therefore Eq. 3.5 provides the most general case and will be used to extract the exchange rate constants in all cases.

The error on the data points were propagated from the error on each peak. To get the signal-to-noise ratio, the rows passing through the maxima of the diagonal peaks were extracted for three 2D spectra of mixing times 3 ms (the first to show visible cross-peaks), 10 ms and 1 s. The error on the peak integral was defined as $1/(\text{signal-to-noise ratio})$. The error on I_{diag} and I_{cross} were calculated as $(E_{\text{ex}}^2 + E_{\text{in}}^2)^{1/2}$, and the error on the ratio $I_{\text{cross}}/I_{\text{diag}}$ as $I_{\text{cross}}/I_{\text{diag}} * ((E_{\text{cross}}/I_{\text{cross}})^2 + (E_{\text{diag}}/I_{\text{diag}})^2)^{1/2}$. It emerges that as soon as the cross-peaks are visible, the error on $I_{\text{cross}}/I_{\text{diag}}$ is less than 0.02 %. These error bars are therefore within the dots of Figure 3.4. Error on the fit is given as the root mean squared error, which is the value minimized by the Solver add-on of Excel to optimize the fit.

Table 2: Parameters used to fit the build-up curves of the exchange experiments. The solvents are abbreviated by H (hexane), C (cyclohexane) and W (water). The Root Mean Square Deviation (RMSD) value was used to converge the fits but the Normalized RMSD (with respect to the maximum $I_{\text{cross}}/I_{\text{diag}}$ value) is shown to compare samples.

		Exchange processes				evaporation			I_0	NR MSD
		k_1	A	k_2	B	C	T_{evap}	D		
YP50	H	784	1.1	104	1.4	2.4E-1	8.5E+0	9.9E-5	8.1E-2	1E-2
	C	257	3.8	23	5.3	1.1E-5	3.4E+2	7.8E-2	6.7E-2	2E-2
	W	1117	0.4	165	0.2	4.8E-1	2.3E+6	1.4E-1	1.3E-1	1E-2
80_	H	39	0.7	2	2.2	4.1E-2	3.9E+4	1.9E-1	2.3E-2	1E-2
900_	C	10	0.8	1	2.6	3.0E-1	2.2E-2	1.7E-1	1.6E-2	7E-3
54	W	57	2.2	4	2.9	0.0E+0	1.0E+1	1.6E-1	4.0E-2	2E-2
21_	H	289	2.4	9	2.7	1.3E-2	4.6E+5	3.8E-2	2.5E-2	3E-2
900_	C	69	1.2	3	2.0	6.1E-2	8.9E+3	1.2E-1	3.6E-2	2E-2
54	W	597	0.5	50	0.7	3.9E-1	1.9E+3	2.0E-1	5.3E-2	2E-2
83_	H	11	0.2	1	1.2	8.9E-2	9.8E-1	1.2E-1	0.0E+0	8E-2
900_	C	/	/	/	/	/	/	/	/	/
20	W	54	1.0	4	2.1	1.4E-1	4.8E+5	1.2E-2	1.3E-2	2E-2
15_	H	39	1.0	3	1.5	2.8E-5	2.5E+1	1.2E-1	4.1E-2	2E-2
900_	C	141	0.1	0	6.1	4.3E-1	4.7E-1	1.0E-4	4.4E-3	2E-2
20	W	162	1.4	6	2.3	1.8E-1	6.6E-1	1.3E-5	3.9E-2	5E-2

Table 2 gives all obtained parameters. Trends mentioned in the paper can easily be observed in this table: for any sample, the exchange rate constants increase in the order cyclohexane < hexane < water, and are bigger in small particles. Note that the process with higher rate has the smallest constant ($A < B$) but the difference is less pronounced in small particles. This may suggest that process 1 corresponds to exchange between in-pore and ex-pore, while process 2 corresponds to intra-particle diffusion, which involves the majority of the solvent.

3.2.3 Appearance of Optimized Samples

For the sieved PDCs, the increased resolution of the in-pore resonance allows the $\Delta\delta$ to be measured more accurately and interpreted in more detail. Figure 3.5 shows ^1H MAS NMR spectra of PDCs sieved prior activation and saturated with deionised H_2O . The BO = 0 % sample shows no change from the unsieved PDC showing that the intrinsic porosity following carbonisation is not altered by the sieving process. However, the spectra for the sieved steam-activated PDCs exhibit much narrower and more symmetric in-pore resonances with very little evidence of the $\delta = -6$ ppm resonance corresponding to the unactivated pores. This confirms that the steam activation process is particle-size dependent, and therefore careful control over the particle size is important in order to achieve a homogeneously activated sample. The NICS reduces with increasing burn-off, which is consistent with previous studies on PDCs and has been interpreted in terms of increasing pore size.^[72]

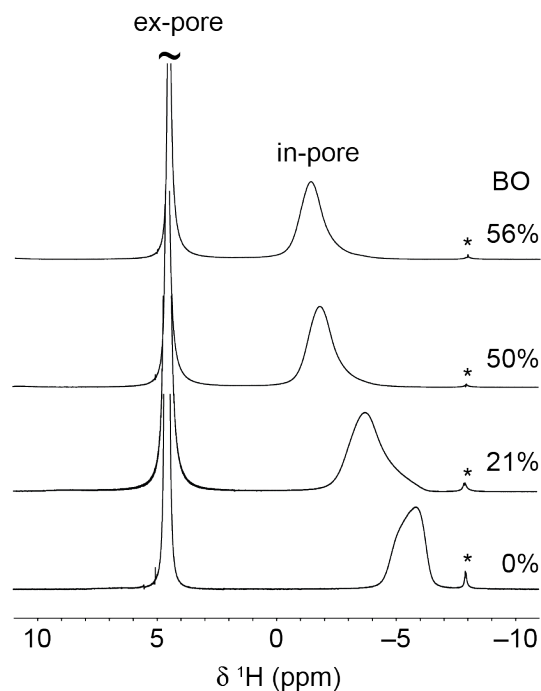


Figure 3.5: ^1H MAS NMR spectra of PDC samples which were sieved prior to steam activation and saturated with deionised H_2O . Asterisks denote spinning sidebands.

Exchange between in-pore species and species located near the particle surface or in the ex-pore environment could potentially influence the $\Delta\delta$, as demonstrated recently by Fulik and co-workers^[67]. As detailed in Chapter 2, in the limit of fast in-pore – ex-pore exchange, the in-pore resonance will be observed at the average between the true NICS and the ex-pore chemical shift, weighted by the size of the subpopulation of ex-pore species that are involved in the exchange process. In the case of intermediate exchange (when the exchange rate is comparable to the absolute frequency difference of the in-pore and ex-pore environments), smaller changes in the $\Delta\delta$ can also be observed, together with line broadening effects. Exchange effects are most evident when comparing NMR spectra of samples with and without excess free liquid, whereby a reduction in the $\Delta\delta$ is observed upon saturation of the sample due to the onset of the exchange process. To investigate the possibility of such effects, NMR spectra were

recorded for a sieved PDC sample with BO = 62 % which was soaked with increasing volumes of H₂O (Figure 3.6). At loadings significantly lower than the total pore volume V_{pore} (as determined by gas sorption measurement), the in-pore resonance is observed at -1.3 ppm. As the loading is increased, an ex-pore resonance appears at 4.6 ppm when the injected volume equals the total pore volume. At this point and also at higher loadings, very little change is observed in the shift of the in-pore resonance, and the shift of the ex-pore resonance is very close to that for bulk H₂O (4.8 ppm). This suggests that exchange between in-pore and ex-pore species is slower than the NMR timescale in this experiment and does not significantly affect the $\Delta\delta$ in this system.

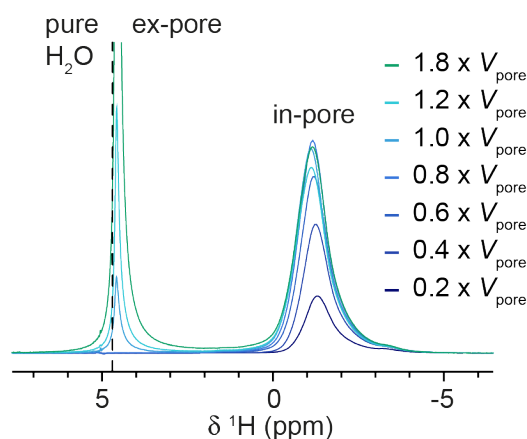


Figure 3.6: ¹H MAS NMR spectra of sieved PDC with BO = 62 % soaked with increasing amounts of deionised H₂O relative to the total pore volume as measured by gas sorption (V_{pore}).

To investigate this further, exchange experiments were performed on a sieved PDC sample with BO = 57 % (Figure 3.7). At a short τ_{mix} of 0.6 ms (Figure 3.7a), no significant in-pore – ex-pore exchange is observed and the in-pore resonance is confined to the diagonal line indicating that its width is again inhomogeneous in origin a distribution of pore environments. For a longer τ_{mix} of 50 ms (Figure 3.7b), in-pore – ex-pore cross peaks are observed, showing that exchange takes place on this timescale.

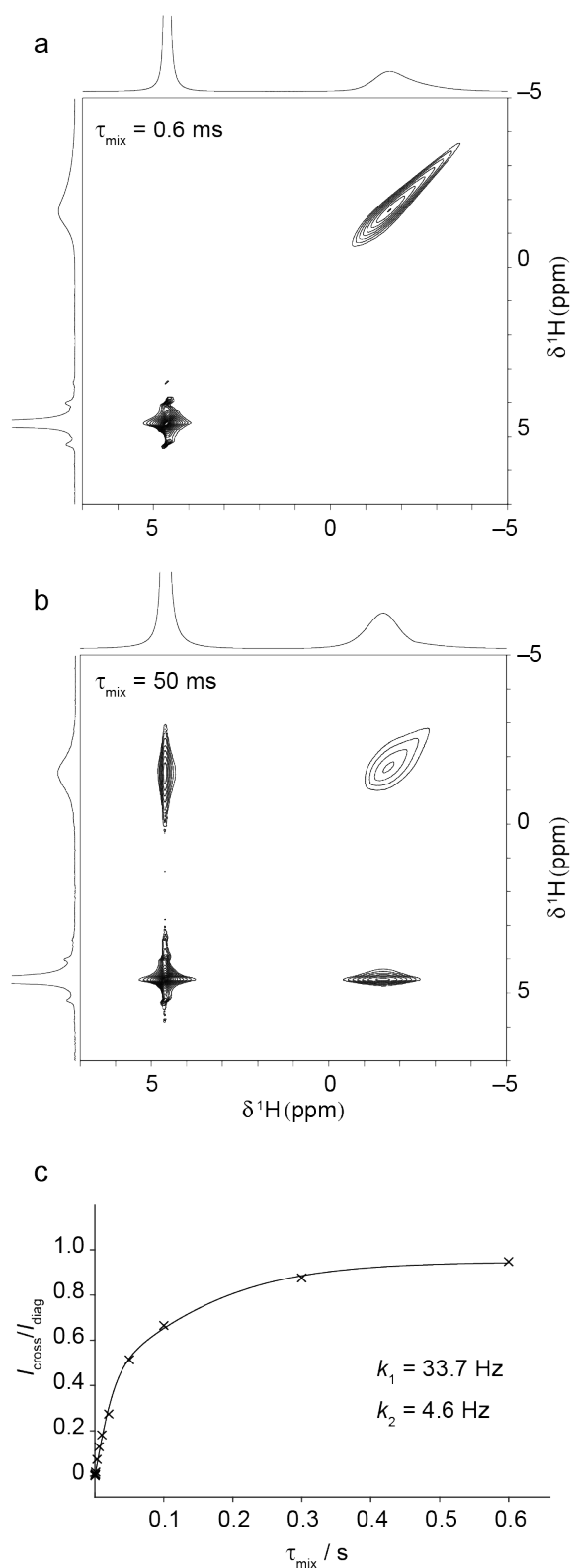


Figure 3.7: ^1H MAS exchange NMR spectra of sieved PDC with BO = 57 % with mixing times of (a) 0.6 and (b) 50 ms. (c) Plot of the ratio of cross-peak and diagonal peak intensities ($I_{\text{cross}}/I_{\text{diag}}$) as a function of mixing time in the exchange experiments.

To gain more quantitative insight into the exchange processes present, cross-peak integrals were extracted from exchange spectra recorded for τ_{mix} between 0 – 600 ms. In principle, the rate constant of a two site exchange process, k , can be determined from the build-up of the integrated intensity ratio of cross peaks and diagonal peaks ($I_{\text{cross}} / I_{\text{diag}}$) as a function of τ_{mix} . However, as found in previous work by Griffin *et al.* and Fulik *et al.*,^[47,58] a poor fit was obtained when the expected dependence on $\tanh(k\tau_{\text{mix}})$ was assumed. Indeed, Fulik *et al.* showed that a better fit could be obtained assuming the presence of two exchange processes characterised by different rate constants corresponding to in-pore – ex-pore exchange near the surfaces of the carbon particles (k_1), and the diffusion of in-pore species from the centre of the particles to the surface (k_2). In this case, $I_{\text{cross}} / I_{\text{diag}}$ is described by:

$$3.8 \quad I_{\text{cross}}/I_{\text{diag}} = A \tanh(k_1 \tau_{\text{mix}}) + B \tanh(k_2 \tau_{\text{mix}})$$

As shown in Figure 3.7c, Eq. 3.8 gives a good fit to the experimental data, yielding values of $A = 0.43$; $B = 0.51$; $k_1 = 33.7$ Hz and $k_2 = 4.6$ Hz, because water did not evaporate. However, we note that the rate constants obtained are significantly smaller than those previously determined by Fulik *et al.* for organic electrolytes in a commercial microporous carbon. This may be partly attributed to the different chemical properties of the H₂O molecules studied here, although we note that the diffusion coefficients of unconfined H₂O species (*vide infra*) are comparable with organic electrolyte species to within an order of magnitude.^[72] A more important factor is likely to be the relatively large carbon particle size used in our experiments. As mentioned above, the modal particle size of the sieved PDC particles is 92 μm which is nearly two orders of magnitude larger than the particle size of the commercial carbon used in the previous study. This means that the interfacial region where fast in-pore – ex-pore

exchange takes place across the surface of the particles is much smaller compared to the interior volume of the particles, and therefore diffusion processes within the particles (*i.e.* fast exchange between pores of different sizes) should be the dominant factor in controlling the overall in-pore – ex-pore exchange process. Because the interfacial region is so small, the slow timescale of the intraparticle diffusion process effectively masks the contribution from the faster in-pore – ex-pore exchange process at the particle surface. Indeed, in contrast to the previous study by Fulik *et al.* the results from the exchange experiments do not show a clear distinction between a fast timescale exchange process at sub-millisecond τ_{mix} and a much slower process at longer τ_{mix} . Therefore, rather than parameterising the interfacial in-pore – ex-pore exchange process, the k_1 value obtained from our fit most likely encompasses a more complex exchange process within a larger interior region near the particle surface which is not fully decoupled from the much slower intraparticle diffusion kinetics.

Overall, the saturation build-up and exchange experiments show that the overall in-pore – ex-pore exchange kinetics are significantly reduced in the sieved PDCs due to the large particle size. In the absence of significant exchange effects, it should therefore be possible to investigate the influence of the carbon pore structure on the NICS through comparison of PDCs with different burn-offs.

3.2.4 Particle Size Effects

Further investigation of the dependence of exchange processes on the particle size was done to directly observe the impact of particle size on 1D NMR spectra, or at least to better estimate the range where exchange may or may not affect the spectra. Thus two activated PDC samples were reduced from approximately 100 μm particle size to approximately 15-20 μm by sieving. The samples were in the first instance

wetted using a microsyringe with a defined volume of deionized water less than the pore volume (PV), then with a volume greater than PV, to observe the ^1H NMR spectrum before and after saturation. We have previously shown that this method allows us to compare the $\Delta\delta$ averaged over the whole pore network without, and then including, perturbations related to in-pore – ex-pore exchange. This is because the in-pore peak before sample saturation corresponds to water located in completely filled particles that are not yet surrounded by water. Figure 3.8(a) and (b) show the spectra of samples 80_900_54 and 21_900_54, respectively. The in-pore peak shifts by approximately 0.2 ppm upon saturation, regardless of the particle size. This means that in this range of particle size, diffusion of water out of the pores has a negligible impact on the NICS for most of the adsorbed water, and the width of the in-pore peak is solely due to the distribution of average NICS. However, exchange averaging has a measurable impact on the ex-pore peaks. In both samples they were fitted with a narrow and a broad component, the intensity and full width at half maximum (FWHM) of which vary. The broad component is assigned to ex-pore water having experienced the pores for a period of time, and is therefore also partially homogeneously broadened by exchange-averaging; the longer the residence time in the pores, the broader and the more shifted the broad component is, *i.e.* the bigger the ratio $V_{\text{in}}^{\text{exch}} / V_{\text{ex}}^{\text{exch}}$ as per Figure 3.18. In big particles, the broad component amounts to 30 % of the ex-pore peak with a FWHM = 0.30 ppm and is located within 0.10 ppm of bulk water chemical shift. On the other hand, with small particles the broad component represents 82 % of the total ex-pore water with a much bigger FWHM = 0.70 ppm and is shifted by 0.20 ppm relative to bulk water. This indicates a slight increase of $V_{\text{in}}^{\text{exch}} / V_{\text{ex}}^{\text{exch}}$ when the particles are reduced, in other words, a bigger proportion of ex-pore water is able to experience the in-pore environment for a longer time.

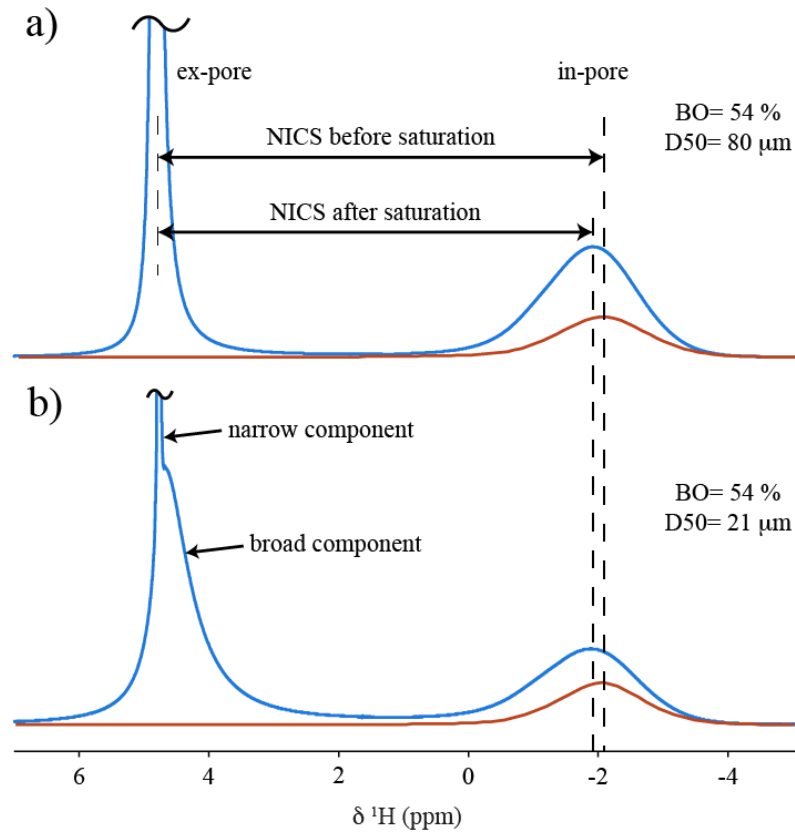


Figure 3.8: ^1H NMR spectra of a) 80_900_54 injected with 0.2*PV (red) and 2.3*PV (blue) of water and b) 21_900_54 injected with 0.3*PV (red) and 2.3*PV (blue) of water. The dashed lines show the maxima of the in-pore peaks.

To explain the broadening of the ex-pore peak, we must adopt the point of view of water molecules that spend the majority of their time in the ex-pore environment, where I believe the packing of the particles plays an important role. A simple model consisting of spherical particles (Figure 3.9) allows us to calculate exchange rates as a function of the particle diameter (Figure 3.10). Briefly, the volume V_P of 8 spherical particles of diameter d is calculated, and subtracted to the volume of the enclosing cube, V_C , to get the ex-pore volume. V_C is then divided by 6 to get the ex-pore volume at the centre of the cube. The radius of a sphere of such volume is used to calculate the dwell

time of water in this sphere assuming a diffusion coefficient of $2.3 \times 10^{-5} \text{ cm}^2/\text{s}$. The exchange frequency is finally the invert of this dwell time.

With $80 \text{ }\mu\text{m}$ particles (similar to 80_900_54) we find exchange rates of 2.5 Hz, and 36.7 Hz with 21_900_54 particles. The $\Delta\delta$ being around 3000 Hz, the exchange regime would be slow in both cases, which is consistent with our observations, and increases by a factor of 15 when reducing the particle size from $80 \text{ }\mu\text{m}$ to $21 \text{ }\mu\text{m}$.

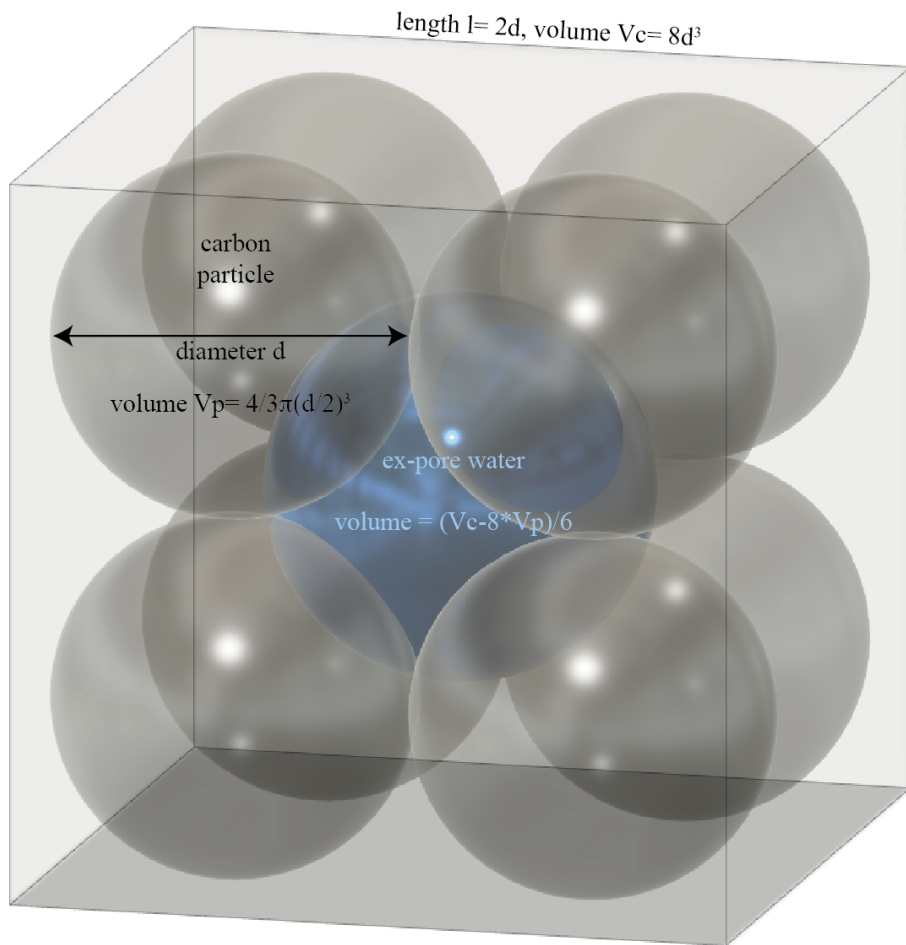


Figure 3.9: Model of spherical carbon particles (grey spheres) used to calculate diffusion times required for ex-pore water (blue sphere) to reach the in-pore environment of the closest particle.

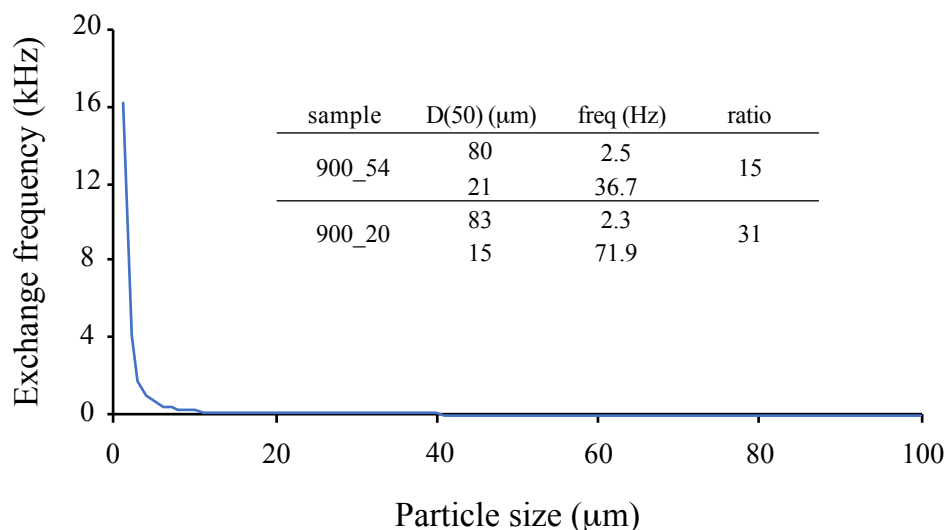


Figure 3.10: Exchange frequency calculated assuming that the carbon particles are spherical.

Examples of 2D EXSY NMR spectra are shown in Figure 3.11(a) and (b) corresponding to sample 80_900_54 and 21_900_54 saturated with water. The mixing time (t_{mix}) was 20 ms for both spectra, and the cross-peaks are more pronounced with small particles, giving a first indication that the exchange is faster. Figure 3.11(c) and (d) show the build-up curves of the intensity ratio of cross-peaks over diagonal peaks. Visually, we can see that the curve for big particles reaches the maximum after long t_{mix} intervals, whereas for small particles the build-up is complete within 0.1 s.

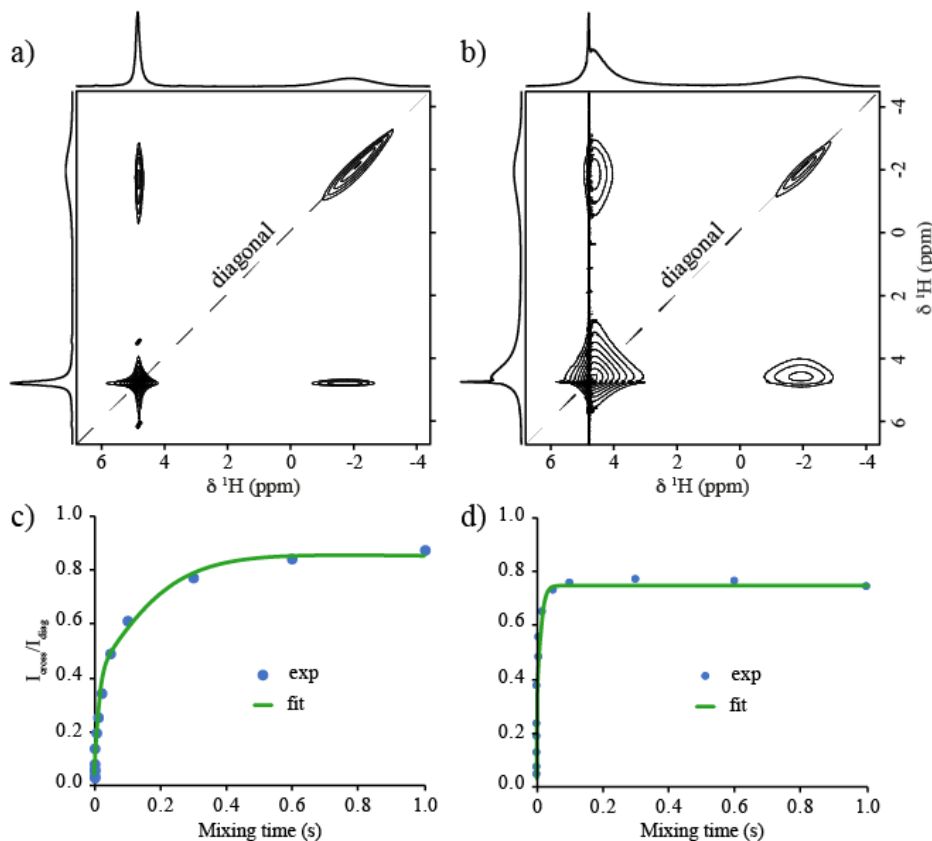


Figure 3.11: 2D exchange spectra for (a) 80_900_54 and (b) 21_900_54 taken with $t_{\text{mix}}=20$ ms, and (c, d) build-up curves of the ratio of cross- and diagonal peak intensities ($I_{\text{cross}}/I_{\text{diag}}$) as a function of mixing time.

Over the course of our experiments, it was observed that the ex-pore resonance reduced in intensity due to evaporation from the NMR rotor leading to a global reduction in $I_{\text{cross}}/I_{\text{diag}}$ for EXSY spectra recorded at the end of the series with long mixing times. Although the exact kinetics of the solvent evaporation are complex and were not studied in detail, we found that this could be accounted for with sufficient accuracy through the incorporation of an exponential term with a characteristic decay constant T_{evap} (see 3.2.2). Rate constants were therefore extracted from the EXSY data using Eq. 3.5 as explained. The fits were optimized by minimizing the Root Mean Squared Deviation (RMSD) between calculated and experimental points, to converged

values around 10^{-2} . The error on the data points were calculated from the signal-to-noise ratio of each peak for a selection of 2D spectra and propagated to $I_{\text{cross}}/I_{\text{diag}}$, and were found to be smaller than 0.02 %. The best fit for 80_900_54 was obtained with $k_1 = 57$ Hz and $k_2 = 4$ Hz, and for 21_900_54 with $k_1 = 597$ Hz and $k_2 = 50$ Hz. The carbon particles with $D_{50} = 21$ μm showed around 10 times faster in-pore/ex-pore diffusion versus the $D_{50} = 80$ μm particles. This is close to the factor of 15 which we obtained from our simple calculations based on spherical particles (Figure 3.10) and shows the impact of the particle size on the rate of the exchange processes, with larger particles significantly reducing the exchange kinetics between the in-pore and ex-pore environments. Therefore, particle size is an important factor to take into account when comparing in-pore – ex-pore exchange phenomena in porous carbon samples.

Regarding the in-pore resonances, the shape and position in the NMR spectrum is largely unaffected by in-pore – ex-pore exchange despite the difference in particle size. We can therefore assume that the diffusion path out of the particle from any point of the pore network, apart from the very surface, is simply too long and exchange-averaging of the in-pore environment is in the slow regime. This would mean that if the particle size is decreased further, at some point the in-pore peak should also become affected by faster diffusion of in-pore water into the ex-pore environment. To test this hypothesis, 6 μm -sized YP50 particles were wetted with deionised water. YP50 is a commercial activated carbon, and similar to our PDCs with respect to composition, pore size distribution and average pore size.^[113] The ^1H NMR spectra before and after saturation are shown in Figure 3.12.

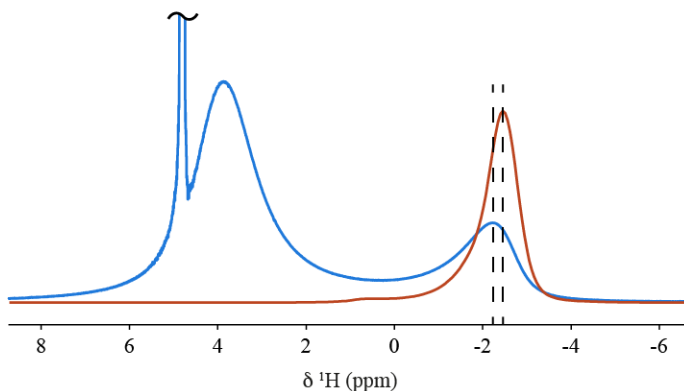


Figure 3.12: ^1H NMR spectra of YP50 wetted with 0.5*PV (red) and 5.3*PV (blue) of water. The dashed lines show the maxima of the in-pore peaks.

As expected due to the small particle size, an ex-pore peak with sharp and broad components is observed. Relative to 21_900_54, the broad component is shifted significantly more, consistent with smaller inter-particle voids that facilitate adsorption of ex-pore water in close proximity. The in-pore peak shifts from a $\Delta\delta$ of 7.3 ppm to 7.0 ppm upon saturation, which is similar to 21_900_54, however the intensity decreases significantly, and we notice that the peak exhibits a tail towards the ex-pore peak. This means that after saturation, a significant proportion of adsorbed water is able to quickly diffuse into the ex-pore environment and therefore does not appear at the purely in-pore chemical shift, but rather intermediate between the ex-pore and the in-pore chemical shifts. The exchange rate constants were estimated to be $k_1 = 1117$ Hz and $k_2 = 165$ Hz. Assuming that k_1 relates to the ex-pore – in-pore exchange process that we calculate as a function of the particle size (Figure 3.10), we find that 4 μm particles give a similar exchange rate. This is good agreement considering that 10 % of YP50 particles are smaller than 2.5 μm (Table 1), especially because for particles smaller than 10 μm the exchange rate increases sharply. This explains why YP50 presents a relatively flat valley between the two broad peaks: even a narrow particle size

distribution in the few-micrometre range gives a very broad distribution of exchange rates, therefore generating exchange-averaged peaks at a continuum of shifts.

One point worth addressing is whether the inhomogeneous broadening of the in-pore peak is responsible for the broadening of the exchange-averaged ex-pore peak, which can give an idea of the reliability of the exchange rate constants obtained. The Express software^[114] was used to simulate the ¹H NMR spectrum of water-saturated YP50 shown in Figure 3.12, to assess the origin of the broadening of the averaged ex-pore peak: inhomogeneous like the in-pore peak (case A), or homogeneous due to exchange only (case B). The in-pore peak was divided into three components to represent the distribution of NICS. In case A (Figure 3.13a), all the different homogeneous components making the in-pore peak are partially exchange-averaged with part of the sharp ex-pore environment, and in case B (Figure 3.13c), only one of the in-pore components partially undergoes exchange-averaging. In case A, the resulting broad averaged peak is itself inhomogeneously broadened in addition to the broadening that depends on the exchange rates (Figure 3.13b). This case corresponds to a particle where the various in-pore NICS are homogeneously distributed radially, and therefore solvent molecules adsorbed therein exchange with ex-pore at similar rates. Case B depicts a particle where there is a radial distribution of NICS, which implies that the NICS located closer to the surface will exchange at a faster rate than those located closer to the centre. The broad averaged ex-pore peak is in this case homogeneously broadened only (Figure 3.13b). As can be seen, the experimental spectrum can be reproduced with both cases. This simulation does therefore unfortunately not allow to make conclusions regarding the origin of the broadening of the ex-pore peak.

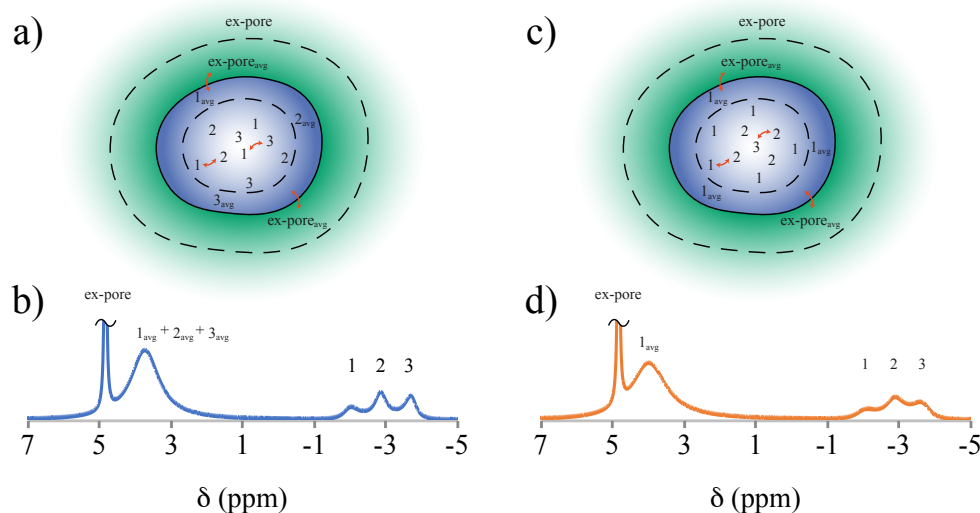


Figure 3.13: Scheme of exchange-averaging modalities in a carbon particle for case A (a) and B (c). Simulated ¹H NMR spectra corresponding to case A and B (b and c). The numbers 1, 2 and 3 represent the homogeneous components of the in-pore peak, which undergo exchange-averaging with the ex-pore peak when the subscript “avg” is added. The amplitudes of the various peaks were chosen to match the experimental integrals: the sharp ex-pore is 20 % of the total integral, the broad ex-pore is 60 % and the non-exchanging in-pore is 20 %.

However in 2D EXSY spectra, for any t_{mix} , the ex-pore peak shows symmetrical off-diagonal broadening (diamond-shaped peak), meaning the broadening is homogeneous. This suggests that one component of the in-pore peak is much more exposed to the ex-pore environment than the other components. In consequence the values of exchange rate constants may be more reliable than if the broadening were inhomogeneous. This result is consistent with a radial distribution of NICS in the particle, in agreement with our previous observations where the centre of particles of diameter greater than 100 μm is poorly affected by steam activation. The particles employed here were smaller than 100 μm but it seems that a small gradient of activation

still remains. It is possible that the valley between ex-pore and in-pore is the result of in-pore – ex-pore exchange broadening, in the fast or slow regime, of the other components of the in-pore peak, which are located further and further away from the surface, and therefore have access to smaller and smaller volumes $V_{\text{ex}}^{\text{exch}}$.

In summary, from these observations it could be deduced that particles smaller than 10 μm offer a diffusion path short enough for water to diffuse out of the pores at a rate that affects the in-pore peak as well. However, given that the diffusion coefficient of adsorbed water depends on the pore size, we cannot compare 21_900_54 and YP50 because they have different average pore sizes. These can be estimated using the $\Delta\delta$ before saturation.^[72] We obtain for 21_900_54 and YP50, 1.17 nm and 1.10 nm respectively. Therefore, it is necessary to investigate the effect of average pore size, which can be tuned by controlling the burn-off, on the diffusion of water and the appearance of the spectra.

3.2.5 The Effect of Burn-off

The effect of burn-off, and thus average pore size, on the dynamics of water in PDCs can be described by comparing 900_54 samples (high burn-off) with 900_20 samples (low burn-off). Figure 3.14 shows samples 83_900_20 (a) and 15_900_20 (b) injected with water. The $\Delta\delta$ of samples 900_20 are 8.4 – 9.0 ppm, giving an average pore size less than 1.0 nm, which is smaller than sample 900_54, in agreement with the linear dependence of the average pore size on the burn-off^[60,62]. The in-pore peaks appear to contain two components as is sometimes observed for samples with low burn-off. Possibly, the degree of activation was not homogeneous from the surface to the centre of the particles. In sample 83_900_20, the in-pore peak is constant regardless of the injected volume (shift <0.10 ppm). Half the ex-pore peak was fitted with a sharp

component of FWHM < 0.1 ppm, and half with a broad component of FWHM = 0.16 ppm with a difference in chemical shift < 0.10 ppm. This suggests in the first instance that the in-pore – ex-pore exchange process is in a slower regime than in 80_900_54, where the broad component was broader and the in-pore peaks were shifted slightly, in agreement with the study mentioned earlier^[115]. With small particles 15_900_20, 90 % of the ex-pore peak is broad, FWHM= 0.35 ppm but within 0.10 ppm of the bulk water, suggesting again limited exchange with negligible V_{in}^{exch} .

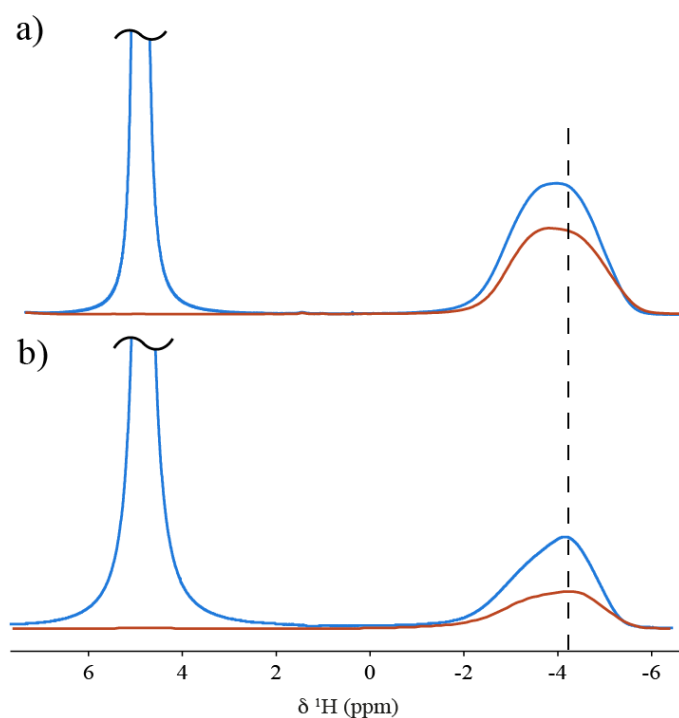


Figure 3.14: ^1H NMR spectra of a) 83_900_20 injected with 0.7*PV (red) and 3.6*PV (blue) of water and b) 15_900_20 injected with 0.2*PV (red) and 3.6*PV (blue) of water. The dashed lines show the maxima of one component of the in-pore peaks.

The exchange rate constants provide a more quantitative description of the impact of average pore size. For the big particles 83_900_20, $k_1 = 54$ Hz and $k_2 = 4$ Hz, which are comparable to the values for 80_900_54 (57 Hz and 4 Hz). This was perhaps not expected from the 1D spectra, where 83_900_20 appeared much less affected by

diffusion. However, one must keep in mind that the exchange regime depends not only on the actual rates, but also on the chemical shift difference of the two environments involved. The $\Delta\delta$ of samples 900_20 is higher than in samples 900_54, so even identical exchange rates still situate 900_20 in a slower regime than 900_54.

For the small particles 15_900_20, $k_1 = 162$ Hz and $k_2 = 6$ Hz, which are three times as fast when compared to 83_900_20. However, the calculated factor was 31, which is a clear discrepancy. Given that sample 15_900_20 contains particles smaller than sample 21_900_54, we can attribute the discrepancy to a burn-off effect and not to a particle size effect. Besides the average pore sizes, other structural parameters that could perhaps vary with burn-off are oxygen content, and tortuosity due to the smaller amount of mesopores. These observations also raise the question of homogeneity of the diffusion coefficients within the particle: it is likely that at low burn-offs a bigger gradient of activation within the particle is present.

Overall, these results show that a smaller average pore size hinders exchange as opposed to a smaller particle size, which promotes it. Since YP50 has a smaller average pore size than 21_900_54 but higher exchange rate constants, we can safely deduce that in YP50, the particles are truly small enough to allow for in-pore – ex-pore exchange to affect the in-pore peak. These conclusions are in agreement with simulations,^[116] and also an experimental study focusing on diffusion measurements in hydrophobic slit pores by neutron-scattering.^[117] The material contained approximately 95 % carbon with 5 % oxygen on the surface of the pores, and average pore sizes of 1.2 and 1.8 nm, which is similar to our PEEK-derived carbons. It was found that the diffusion coefficients of water in the 1.2 and 1.8 nm pores are 40 % and 30 % smaller than that of bulk water, respectively. Furthermore, on the very surface of pore, water diffuses at

$0.035 \times 10^{-5} \text{ cm}^2 \text{ s}^{-1}$ and $0.014 \times 10^{-5} \text{ cm}^2 \text{ s}^{-1}$ respectively, which is two orders of magnitude slower than in the bulk. Counter-intuitively, the value on the surface of the bigger pores was found to be nearly half that in the smaller pores, which was attributed to the promotion of slightly faster concerted motion in extreme confinement, although the centre of the pore followed an overall slower regime.

3.2.6 The Effect of Solvent Properties

Many applications of porous carbons (such as electric double-layer capacitors) commonly employ electrolytes in organic solvents as an alternative to aqueous electrolytes. To extend the knowledge presented here to such systems, it is desirable to be able to predict how the $\Delta\delta$ may be affected. The viscosity and the polarity are the two parameters that will be considered here as tools to predict the diffusion regime adopted by any solvent.

The effect of polarity can be estimated by comparing water and cyclohexane which have the same viscosity, but different dipole moments. YP50 is chosen for this comparison because the exchange rates are high enough to significantly impact the NMR spectra. The exchange rate constants were measured to be 1117 Hz and 165 Hz for water, and 257 Hz and 23 Hz for cyclohexane, which means that cyclohexane diffuses roughly four times slower. On one hand, this could be related to increased van der Waals interactions with the hydrophobic surface of the pores, as was also found to be the case in a xerogel using the same solvents^[115]. On the other hand, the bulk self-diffusion coefficient of cyclohexane is smaller than for water ($1.42 \times 10^{-5} \text{ cm}^2 \text{ s}^{-1}$ vs $2.3 \times 10^{-5} \text{ cm}^2 \text{ s}^{-1}$)^[118], which could also contribute. At this stage it is unclear whether other parameters such as the different molecular sizes of water and cyclohexane play a role. Figure 3.15 shows the ^1H NMR spectrum of YP50 wetted with cyclohexane.

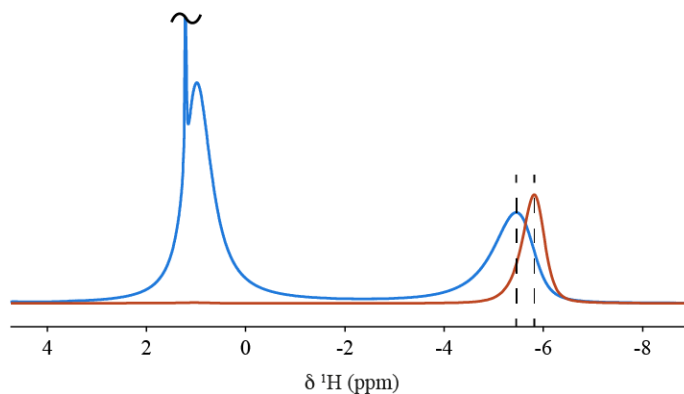


Figure 3.15: ^1H NMR spectra of YP50 injected with 0.3*PV (red) and 2.9*PV (blue) of cyclohexane. The dashed lines show the maxima of the in-pore peaks.

As expected with such high exchange rate constants, we see a narrow and a broad ex-pore peak, and an in-pore peak that decreases and shifts upon saturation, much like in Figure 3.12 with water in YP50. With water and cyclohexane, the in-pore peaks are similar; they shift by 0.30 ppm and are broadened by a factor two upon saturation. Interestingly, we note that the $\Delta\delta$ of cyclohexane (and hexane) is smaller than water by 0.2 – 0.3 ppm, which means that the apolar solvents are on average located in slightly bigger pores than water. The diffusion being faster in big pores, this is in contrast with the slower exchange kinetics measured, showing that solvent parameters are prevalent over pore size effects. The broad ex-pore peak is narrower and less shifted in cyclohexane (FWHM= 0.64 ppm and shift = 0.27 ppm) than in water (FWHM = 1.69 ppm and shift = 0.98 ppm), consistent with smaller exchange rate constants.

The effect of viscosity can be observed by comparing cyclohexane (0.89 cP) and hexane (0.30 cP) which have the same very low polarity. Figure 3.16 shows the ^1H NMR spectrum of YP50 wetted with hexane. Unlike water and cyclohexane, hexane shows two ex-pore peaks, which are simply due to the two visible proton environments

on the molecule; 1.28 ppm are the CH₂ and 0.88 ppm are the terminal CH₃ protons. The in-pore peak before saturation can be fitted with two broad peaks 0.30 ppm apart, which is similar to the difference between the CH₂ and CH₃ chemical shifts. This suggests that all protons of adsorbed hexane molecules roughly experience the same NICS, therefore the molecule is either tumbling isotropically or aligned with the pore wall. The exchange rate constants are $k_1 = 784$ Hz and $k_2 = 104$ Hz for hexane in YP50, which is approximately three times the rates seen for cyclohexane. Therefore in this case, the exchange rate was roughly proportional to the viscosity, as hexane is three times less viscous than cyclohexane.

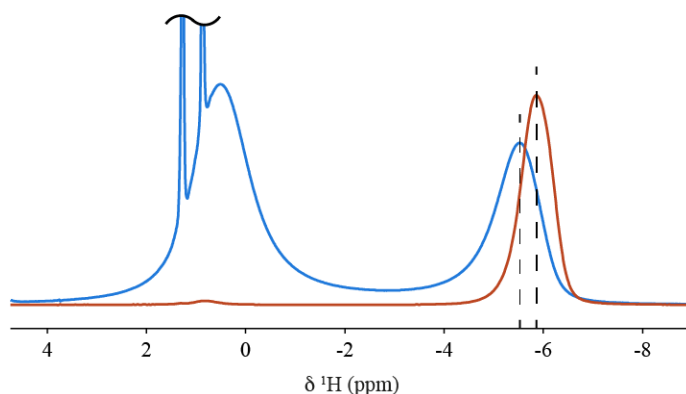


Figure 3.16: ¹H NMR spectra of YP50 injected with 0.3*PV (red) and 3.0*PV (blue) of hexane. The dashed lines show the maxima of the in-pore peaks.

More interestingly, the broad ex-pore peak is shifted by 0.61 ppm relative to the average between the two narrow peaks, and the FWHM = 1.30 ppm. These values are between the values for cyclohexane and water. This is consistent with the shift and width being proportional to the exchange rate constants as they are even higher for water in YP50. Overall, pronounced solvent exchange affects the ex-pore and in-pore peaks

and the valley between the two peaks, but the ex-pore peak seems to be the most reliable indicator to estimate perturbations due to exchange effects.

Further discussion is required about parameters that could not be assessed with this set of experiments, for example the kinetic diameter of the solvent molecules. This factor was not considered separately because it was first assumed to be reflected in the viscosity parameter, although in pores of similar size, viscosity and diameter may have independent contributions to the exchange kinetics. In addition, to identify the impact of this factor alone, two solvents with similar viscosity and polarity but different molecular sizes should be compared. The kinetic diameter of water and cyclohexane perhaps contributes to the exchange rate difference.

These experiments suggest that cyclohexane can form organized structures in slit-like micropores, which affects its diffusion coefficient. In the 83 μm particles, exchange was too slow to be observed, and by decreasing the particle size to 15 μm , the exchange became visible but the rate was higher than that of hexane and also of cyclohexane in the other PDC samples, which goes against the trends. Another interesting observation is that there are two in-pore peaks in 900_20 before saturation, as shown in Figure 3.17. A simple explanation could be that in addition to cyclohexane, there is some moisture in the biggest pores not fully saturated, given that the secondary in-pore peak, at -2 ppm, is close to the -4 ppm of the water in-pore peak. However after saturation both peaks shift to the right, but any initial moisture would be completely replaced by the organic solvent, or displaced towards even bigger pores, so the second peak should have disappeared, or shifted to the left. Instead, the small in-pore peak is therefore likely to come from a few isolated mesopores while the other

peak is from micropores and mesopores that are in contact. The 3.3 ppm $\Delta\delta$ of the small peak gives a pore size of 2.2 nm and the 7.7 ppm $\Delta\delta$ of the main peak 1.0 nm. In 80_900_54 there was only one in-pore peak, meaning that there are no isolated environments.

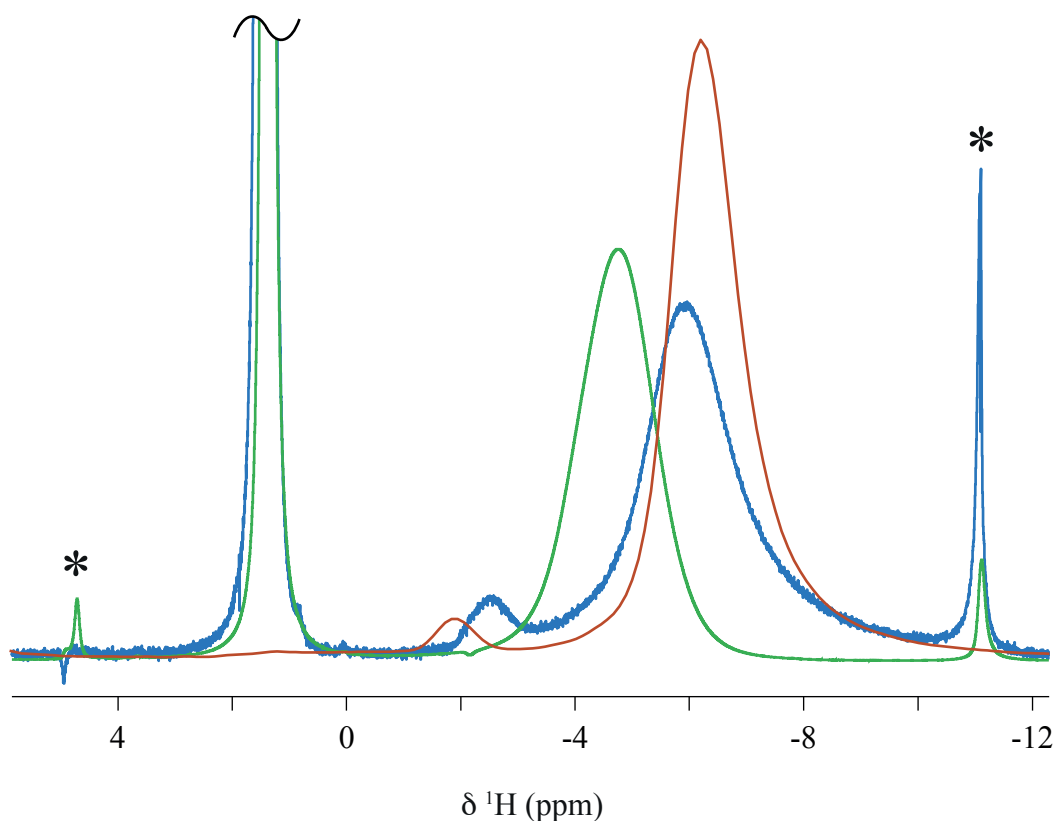


Figure 3.17: ^1H NMR of 80_900_54 saturated with cyclohexane (green) and 83_900_20 before (red) and after (blue) saturation.

Thus, it is believed these observations are all related and hint towards the ability of cyclohexane to form organized structures in slit-like micropores, which affects its diffusion coefficient. The diffusion coefficient of confined cyclohexane was shown by Fomin *et al.* to drop to zero in slit pores smaller than 2.1 nm, and its density to increase two fold from 2.6 nm to 1.2 nm pores.^[119] Another study showed that cyclohexane

forms a monolayer in 0.8 nm pores and a bilayer in 1.0 nm pores with a denser hexagonal packing structure resembling the solid phase.^[120] Similar behavior has also been observed for propylene carbonate which was observed to form an ordered structure upon nanoconfinement.^[121] In a disordered structure the packing is expected to be less efficient, nonetheless the diffusion coefficient may still be significantly lower. The exchange rate constants determined take into account the diffusion of species in all types of pores located in V_{in}^{exch} . When cyclohexane forms an immobile structure in the smallest pores, only the diffusion coefficient in the biggest pores where it is still liquid contributes to the exchange rate constant, explaining why in 15_900_20 the exchange rates are much higher than in the other PDC samples. The amount of mesopore is smaller than in 900_54 and YP50, so the long-range diffusion within the particles is probably significantly slower. In that regard, the gradient of NICS will be less well averaged, and even more so with slow diffusing solvents like cyclohexane.

In conclusion to this study of diffusion-related perturbation of NMR spectra of solvent-saturated activated carbons, it emerges that for PDCs steam-activated at 900 °C of median diameter superior to $\sim 70 \mu\text{m}$, regardless of the solvent, the spectra are not affected. When using particles of median diameter inferior to $10 \mu\text{m}$, solvent diffusion effect can come into play, but this depends now on the solvent diffusion coefficient and on the BO. The $\Delta\delta$ can be related with confidence to the average pore size of the sample.

3.2.7 Summary of perspectives

On a macroscopic length scale, different chemical shifts can be attributed to different regions inside and around a porous carbon particle. Figure 3.18 illustrates a carbon particle (black continuous line) saturated with a solvent.

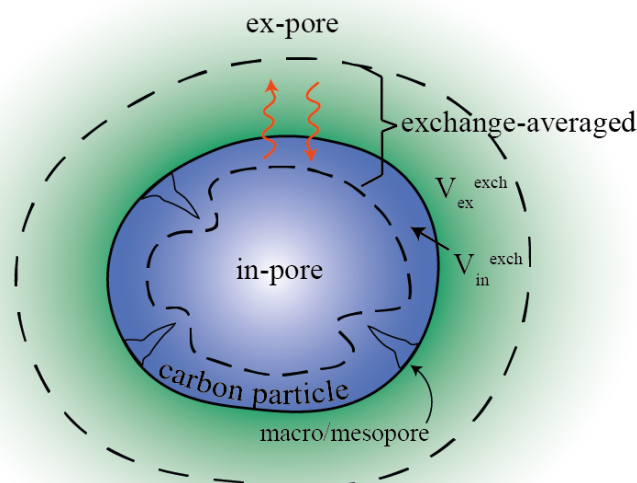


Figure 3.18: Scheme of an activated carbon particle (black continuous line, delimiting the ex-pore/in-pore boundary) saturated with solvent, blue for adsorbed and green for bulk. The orange arrows represent fast exchange of molecules between the two environments. The colour gradient represents the probability that a solvent molecule exchange during data acquisition. Molecules between the two dashed lines may exchange fast enough to appear at the exchange-averaged chemical shift, with V_{in}^{exch} and V_{ex}^{exch} standing for the volume of such exchanging solvent initially in-pore or ex-pore respectively.

Molecules in the green region adopt the ex-pore chemical shift, and molecules in the blue region an in-pore chemical shift. The deeper the colour, the more likely the molecule is to change environment within a certain time. The dashed lines represent the boundaries between molecules undergoing fast and slow exchange: within the dashed lines, the in-pore/ex-pore exchange (orange arrows) is frequent enough for the chemical shift to be averaged. Note that the ex-pore dashed line is at a constant distance from the particle surface because the ex-pore diffusion coefficient is constant. The in-pore dashed line however is distorted due to inhomogeneities of in-pore diffusion

coefficients and wraps around big mesopores penetrating deep into the particles. In summary we expect two non-exchanging peaks corresponding to ex-pore solvent far from the particle and in-pore solvent in the core of the particle, and a broadened peak, corresponding to solvent molecules undergoing fast exchange.

The position of the exchange-averaged peak depends on the time the molecules spend in each environment. However in practice, when adsorption and desorption are at equilibrium, the solvent molecules exchange by pairs because the volumes of exchanging adsorbed solvent $V_{\text{in}}^{\text{exch}}$ and exchanging free solvent $V_{\text{ex}}^{\text{exch}}$ are constant. The diffusion coefficient in the pores is smaller than in the bulk, so for the in-pore molecules to exchange in the fast regime they must reside closer to the interface. Therefore, $V_{\text{in}}^{\text{exch}}$ is smaller than $V_{\text{ex}}^{\text{exch}}$. The residence time of the exchanging solvent molecules can now be correlated to $V_{\text{in}}^{\text{exch}}$ and $V_{\text{ex}}^{\text{exch}}$ and the in-pore/ex-pore ratio of diffusion coefficients. Experimentally it is possible to calculate $V_{\text{in}}^{\text{exch}}$ and $V_{\text{ex}}^{\text{exch}}$ from the position and volume of the broad ex-pore peak.

On a microscopic length scale, a lot of information can be retrieved even from the simplest 1D spectra depicted in Figure 3.19. Considering a simple system containing only two pores of different sizes (Figure 3.19a) arbitrarily set as 0.8 nm and 1.1 nm, the NMR spectrum of adsorbed species will depend on the exchange kinetics between the two pores, which depends on the distance between the pores. Merlet *et al.* simulated the broadening of exchange-averaged in-pore lineshapes with respect to the distance between different pores.^[66] The maximum distance between pores that still allows for an averaged NICS was found in the 0.1 – 1 μm range, assuming that the in-pore diffusion coefficient is the same as ex-pore. Figure 3.19b shows the spectrum of species in this system when the distance between the pores is smaller than 0.1 μm and therefore

allows for coalescence of the individual in-pore peaks shown in dashed coloured lines. Using the equation by Xing *et al.*, the 0.8 nm pore gives a NICS of 11 ppm and the 1.1 nm pores 7 ppm. If the big pores have a volume twice as big as the small pores, the averaged peak therefore appears at 8.3 ppm. The lineshapes have been simulated arbitrarily but reflect the broadening of the distribution of environments with increasing activation.^[122]

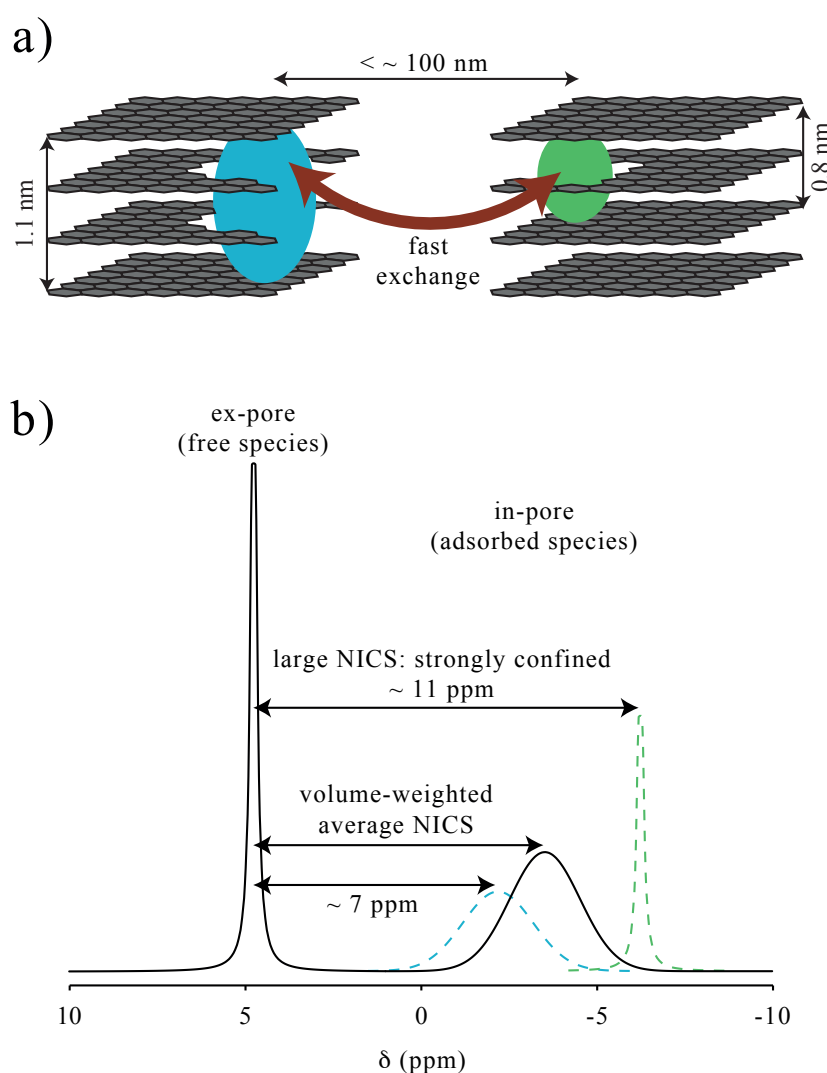


Figure 3.19: a) Scheme of a simple two-pore system allowing exchange of adsorbed species, and b) the corresponding NMR spectrum assuming fast exchange (black line) or with resolved in-pore peaks (dashed coloured lines) in the case of slow exchange.

3.3 GS

3.3.1 Sample Preparation

Here is described the standard procedure taken from the autosorb iQ/AsiQwin Operating Manual P/N 05098-4.0 Rev B (Quantachrome Instruments). Prior knowledge of sample properties are required to make informed choices on sample preparation, that is approximate surface area (m^2/g) and most importantly stable temperature range. A sample surface area of 15 – 20 m^2 is the minimum for precise measurements. Activated carbons typically have surface areas in the range 1000 m^2/g . Therefore a mass of 20 mg is necessary, but masses up to 50 mg can be used. The sample is introduced in a dry measurement cell, consisting of a cylindrical stem and a spherical bulb. The diameter of the stem and bulb can vary to facilitate introduction of various samples, but for non-aggregating carbon powders, the smallest size is suitable, and has the advantage of minimizing the volume of probe gas required. Degassing of the sample, or activation, is done at the maximum temperature allowed by the sample, under high vacuum. For carbons, the maximum nominal temperature of 350 °C is typically used without concerns for decomposition. Pressure controlled heating allows to minimize the amount of steam present in the cell.

3.3.2 Qualitative Isotherm Analysis

All the information on the sample is obtained from analyses of the isotherm. The first step is therefore to assess the success of the experiment. Indeed several problems can arise if some parameters were not set properly, or hardware malfunctions.

Equilibration Time

Because the diffusion is much slower the smaller the pores, equilibration times depend on the pore size and therefore the pressure range. The experiment is limited in time due to evaporation of cryogenic liquid, so the equilibration times must not be too long either. For unknown samples, it is often the case that a standard equilibration time for a particular dose point is insufficient, for example if there is a large volume of gas adsorbing at the corresponding pressure. The isotherm will therefore contain a pressure value that was not minimal, *i.e.* located somewhere on the corresponding dashed arrow in Figure 2.17 rather than at the tip. Subsequent points are likely to be wrong as well because of the now higher than expected volume that has to diffuse to equilibrium. This problem appears in the isotherm as irregularities in the normally monotonically increasing curve, which usually renders the isotherm totally unusable.

Void Space Measurement

Before the adsorption experiment, the sample is typically saturated in one step with helium at room temperature and at cryogenic temperature, to determine the volume of the cell excluding the sample but including the pore volume. This is necessary to calculate the actual amount of adsorbed probe gas at any point of the isotherm because of the equilibrium between molecules in the gas phase and adsorbed phase. Helium is used because it quantitatively fills the pores. However it diffuses too slowly to be used as the actual probe gas, and so must be removed before recording the isotherm. This removal, albeit done at room temperature under high vacuum is still slow, typically allowed to proceed over 2 hours. Residual helium may cause the apparent cumulated volume to decrease at high p/p_0 , while it theoretically should increase monotonically. A solution to this issue is to measure the void space after recording the isotherm, which however does not allow to interrupt the measurement of the isotherm at any point at the cost of not being able to analyse it altogether.

Gas Leak

The pressures in the system are below 10^{-5} (p/p_0) when characterizing micropores with nitrogen, therefore even a slow leak can introduce errors, whereby data points are shifted to the right. The instrument controls can recognize leaks when the pressure of the system is superior to the pressure of the introduced amount of gas and interrupt the experiment. The isotherm will also look irregular.

Cryogenic Bath

If the total experiment time exceeds the tolerance of the Dewar, the sample temperature is not maintained at cryogenic level. This problem is common when equilibration times are overestimated, or when a too large surface area is to be covered. The pressure in the system increases drastically with the temperature of the cell, which causes the instrument to release the pressure thereby interrupting the measurement.

In summary it is important to properly acquire the entire isotherm up to $p/p_0 \sim 1$ to make sure that the appearance does not reveal any problem. In addition, any truncation of the isotherm can introduce artefacts in the PSD.

3.3.3 Data Treatment and Interpretation

A discussion on the choice of kernel and interpretation of the PSD is given based on results from an activated carbon sample analysed with a number of available approaches. As can be seen in Figure 3.20, the choice of kernel has a significant impact of the appearance of the PSD. When using NLDFIT with slit pores (NLDFIT_slit), one broad irregular population from 1 to 3 nm is obtained with a minor subnanometre feature. With QSDFT_slit, the smoother distribution appears bimodal with a subnanometre pore population roughly equal to the broader 1 – 2 nm population.

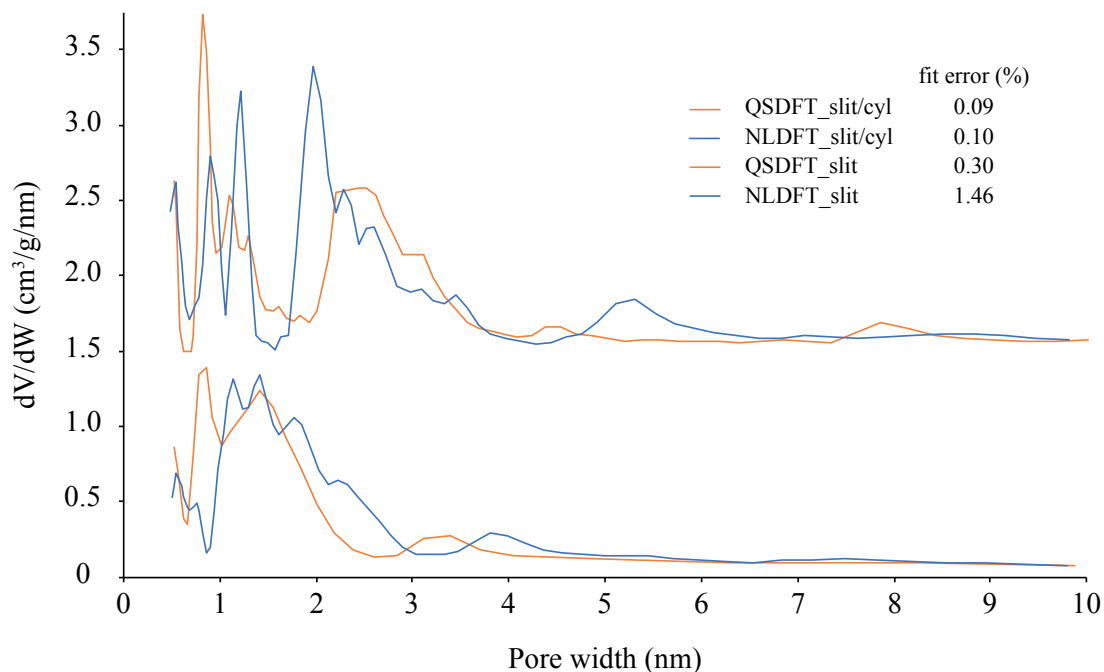


Figure 3.20: Quantachrome PSD of 900_79 determined by NLDFT and QSDFT calculations on a nitrogen adsorption isotherm assuming slit pores only (NLDFT_slit and QSDFT_slit), or with slit (0 – 2 nm) and cylindrical (2 – 33 nm) pores (NLDFT_slit/cyl and QSDFT_slit/cyl, respectively, shifted by 1.5 cm³/g/nm for clarity). Errors on the fit of the isotherm calculated by the software for each model are given.

Regarding the NLDFT_slit PSD, one must keep in mind that the loss of 1 nm pores, and in consequence overestimation of the 1 – 1.5 nm pore volume relative to QSDFT_slit, is due to the poor fit in the corresponding region of the isotherm (see Figure 3.21). The errors on the fits calculated by the software are 1.46 % and 0.30 % for NLDFT_slit and QSDFT_slit, which correspond to a quite significant visible improvement of the fit. So far the results of QSDFT and NLDFT agree well.

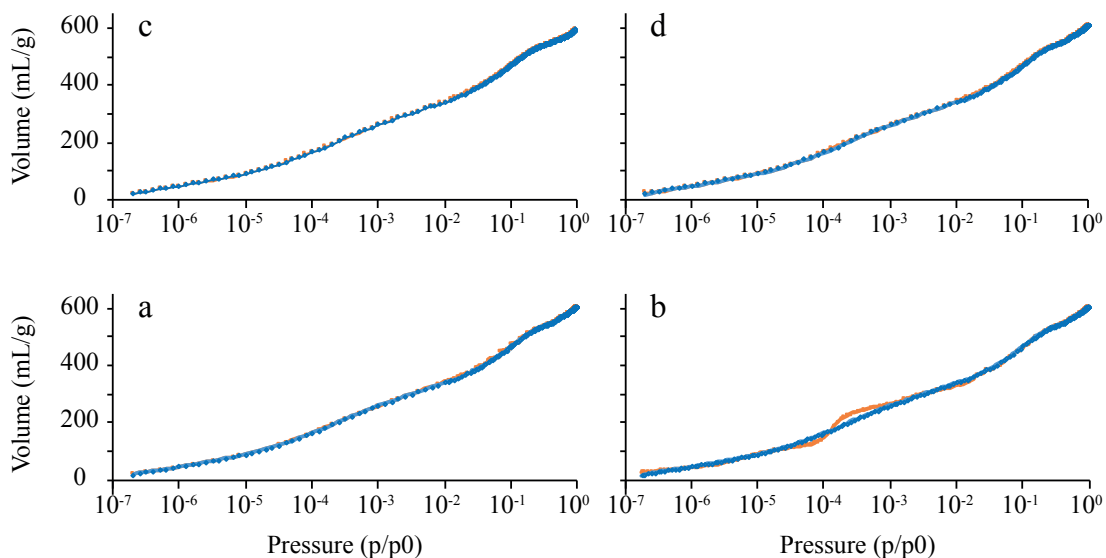


Figure 3.21: GS isotherms (blue) of the reference activated carbon sample fitted using several kernels (red): QSDFT_slit (a), NLDFIT_slit (b), QSDFT_slit/cyl (c), and NLDFIT_slit/cyl (d). The p/p_0 axis is in logarithmic scale.

The addition of cylindrical pores in the model (NLDFIT_slit/cyl and QSDFT_slit/cyl) has several effects on the fit and the PSD. First, although to the naked eye the fits seem identical, the errors on the fit decrease further to $\sim 0.1\%$. Note that other kernels, such as the spherical pore kernel, give a noticeably worse fit; it would seem that slit pores are required. The slit and slit/cyl kernels give almost identical errors but the PSD present some significant differences, so a deeper understanding is required. The decrease of the errors is in agreement with the authors of the QSDFT kernels who suggested that the slit/cylindrical pore model is “more suitable for samples with a substantial degree of activation that leads to the formation of slit-shaped micropores”.^[98] On this topic, a combined neutron and X-ray study aiming at characterizing the pore shape was conducted by Jafta *et al.* who came to the conclusion that in Kynol, an activated carbon cloth with very similar PSD, subnanometre pores are strongly asymmetric, consistent with a well-defined slit shape, while on a length scale

larger than 1 nm, the structure is less well defined, as expected in materials without long-range order.^[123] Therefore it is reasonable that the shape of big micropores may be fitted better by a combination of slit and cylindrical pores, which could be regarded as more isotropic slits, rather than slit pores alone. This was probably the intentions of the authors who set the transition from slits to cylinders at 2 nm.

However the reason for a better fit is because the region of the isotherm from $\sim 10^{-3}$ to $\sim 10^{-1} p/p_0$ is simultaneously fitted with two kernels. This is because the condensation of nitrogen in cylindrical pores of 2 – 3 nm in diameter takes place at the same pressure than in slit pores of 1 – 2 nm in diameter due to increased confinement.^[90,91] This effect explains why some populations are shifted to bigger pores, such as the portion of the broad 1 – 2 nm population shifted beyond 2 nm, or lesser features at 4 and 3.5 nm (slit) shifted to 5.5 and 4.5 nm (slit/cyl). While the slit/cyl kernels may be useful when subnanometre slit pores are clearly resolved from less-well defined mesopores, in the case of PDC unfortunately the use of slit/cyl results in an artificial gap around 1.5 nm.

When taking this effect into account, one can say that the appearance of the slit/cyl PSD is similar to the slit PSDs, *i.e.* bimodal with a well-defined subnanometre slit pore population, and a less-well defined population that may be approximated as 1 – 2 nm slit pores or a combination of 1 – 1.5 slits and 2 – 3 nm cylindrical pores.

The Micromeritics results are processed with a different approach: for activated carbon a variety of kernels are available, all with slit pores, but different aspect ratios, *i.e.* ratio of pore length over width, can be chosen, as shown in Figure 3.22a.

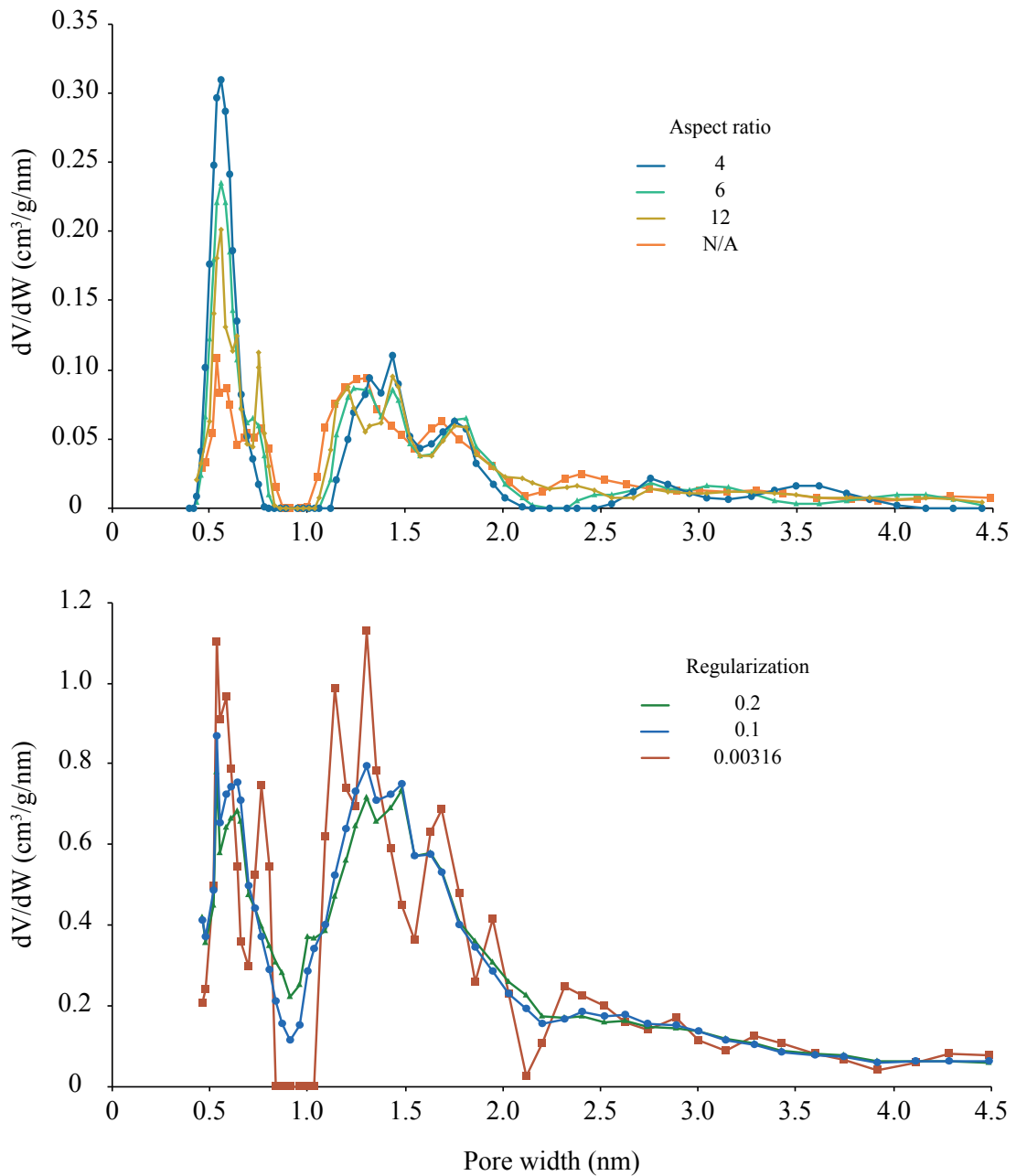


Figure 3.22: Micromeritics PSD of 900_79 determined by NLDFT assuming slit pores of different aspect ratios (top), and PSD with different regularization parameters using the default kernel (bottom). The aspect ratio of the default kernel is N/A.

As the aspect ratio increases, *i.e.* as the pores become more elongated, the volume of the small pores decreases while the volume of the pores around 1.1 nm and 2.2 nm increases, but overall the main pore populations are conserved. The aspect ratio

is not given for the “default” kernel. Another parameter that can be changed is the regularization, Figure 3.22b. This is a somewhat arbitrary procedure and it is recommended to find a good compromise between the error on the fit and the roughness of the PSD. It is generally used as an artificial way of compensating the poor fit around 1 nm and 2 nm as well as to smoothen features that are thought to be artifacts. This should however be avoided when the objective is to interpret the features of the PSD.

Finally, argon was also used as a probe molecule with Quantachrome and shows a similar bimodal PSD (see Figure 3.23). The confidence in the PSD is higher for small pores because the gas condensation happens at a more specific pressure, as can be seen from the spacing of the calculated isotherms in the kernels.^[97]

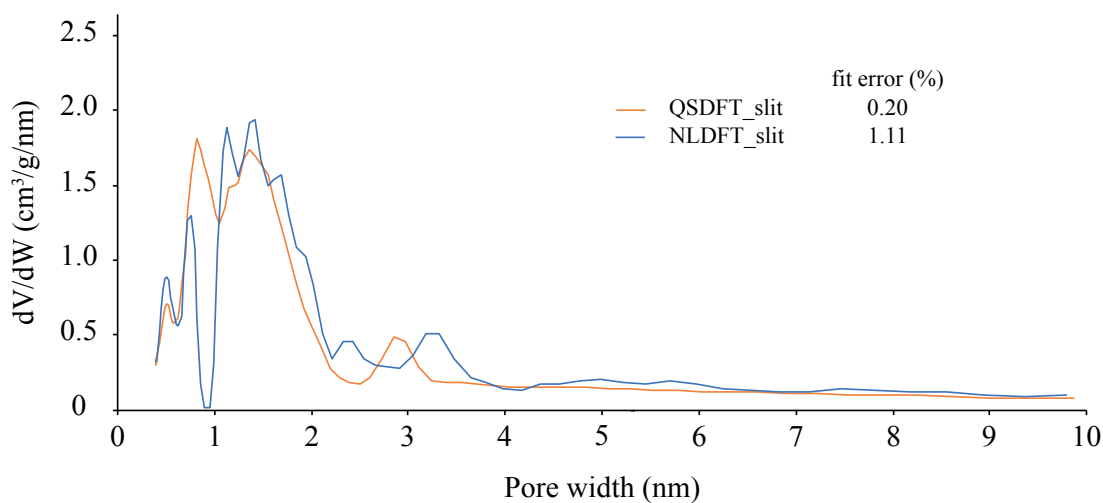


Figure 3.23: Quantachrome PSD of 900_79 determined by NLDFT and QSDFT calculations on an argon adsorption isotherm assuming slit pores only (NLDFT_slit and QSDFT_slit).

In conclusion to this discussion, the PSD of our reference sample appears to contain two populations of slit-shaped pores: 0 – 0.9 nm and a broad 1 – 2 nm. These features are found in a variety of activated carbon samples,^[90,114,116,117] so we believe

the above remarks to be relevant to a broad community. It is important to understand the structure of the kernels and what methods were used to obtain the calculated isotherms. The QSDFT_slit kernel was able to significantly improve the fit of the NLDFIT_slit kernel mainly by blurring out the capillary condensation phenomenon. This was achieved by introducing a density gradient of the pore walls, decreasing linearly from graphite density to 0. However, no specific defects or structures were modelled. Furthermore, the use of the hybrid slit/cyl kernel seems to bring QSDFT and NLDFIT back on an equal footing, which makes the choice of kernel all the more arbitrary. With a deepened understanding of the kernels, the results can now be interpreted more carefully.

3.4 Raman

3.4.1 Sample Preparation and Detection

Between 4 and 6 spectra are recorded per sample, at different spots, to get an average picture and avoid sample degradation. It was noted that the spectra are more reproducible in terms of signal-to-noise ratio when the sample was previously dried. This can perhaps be explained by interferences of water with the photons, either directly from the incident laser or from the much lower-intensity scattered Raman light. Another major concern is the damaging of the sample under high laser exposure. Indeed if the standard power of 100 mW is chosen, holes can be burned with the laser spot during acquisition, which ultimately yields poor reproducibility. Longer exposure times can compensate for lower powers to achieve the same signal-to-noise ratio, which depends on the number of photons scattered. Typically 5 s at 30 mW with a laser wavelength of 532 nm were suitable to obtain D and G bands with similar signal-to-noise ratios.

3.4.2 Deconvolution of Spectra

The Raman community is not unanimous as to what method to deconvolute Raman spectra is the best, with equally often used simple lineshapes such as Gaussian and Lorentzian^[126], or more complicated functions such as pseudo-Voigt and Breit-Wigner-Fano^[110], and more. This is due to the wide variety of samples and defects that influence the Raman scattering processes.

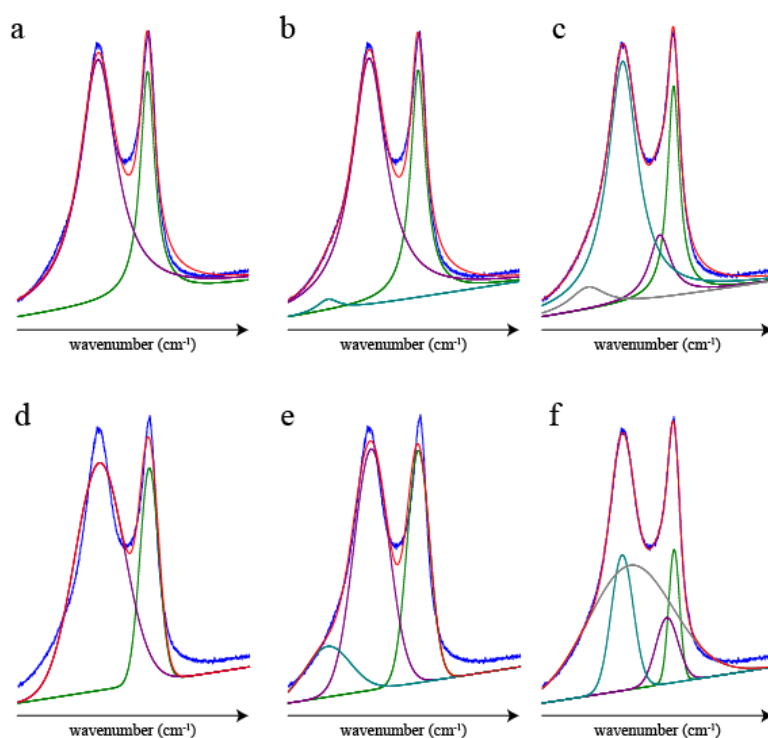


Figure 3.24: Deconvoluted Raman spectrum of a non-activated sample using 2, 3 and 4 Lorentzian bands (a, b, c) and using 2, 3 and 4 Gaussian bands (d, e, f).

In this work, an informed choice between Gaussian and Lorentzian was made based on the reproducibility of the results across the measurements done on any one sample. For example, Figure 3.24a, b and c show the deconvolutions of a Raman spectrum of a carbon sample not submitted to any activation using two, three and four bands. It appears that two and three Lorentzian bands are insufficient to properly fit the

region between the peaks and the low-wavenumber region. The high wavenumber side is not quite ideal but a fifth band, of Gaussian or Lorentzian shape, if added converges to zero. The same procedure was repeated with Gaussian bands, Figure 3.24d, e and f, which at first sight gave an equally good fit using four bands, except for the high wavenumber region, which was worse. Critically, the D2 band did not seem to always converge to self-consistent widths and intensities across and within samples. In the trends described earlier, if G2 is broader, less intense and left-shifted compared to G1, so should D2 relative to D1.

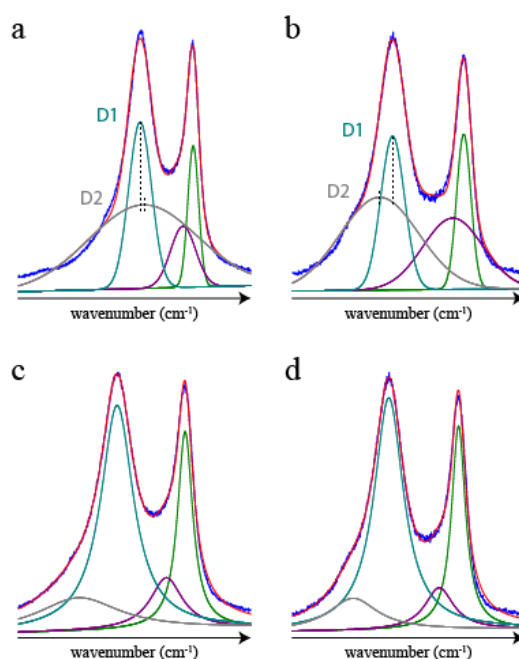


Figure 3.25: Two different Raman spectra of the same sample (spectrum 1: a and c, spectrum 2: b and d) deconvoluted with four Gaussians (a and b) or four Lorentzians (c and d). The dashed lines in a and b are the maxima of the D1 and D2 bands.

This was not always the case in certain samples, as exemplified in Figure 3.25a and b, where the D2 band is either left- or right-shifted relative to D1. The four Lorentzian bands gave homogeneous results over all samples and were also constantly

able to fit the shoulder at low-wavenumbers (were D2 should be) such as in Figure 3.25c and d, and were therefore used in the analyses.

3.5 Summary of Materials and Methods

To synthesize PDCs, PEEK pellets (Sigma Aldrich) were deposited on an alumina boat and introduced in an alumina tube furnace (Carbolite), heated to 900 °C for 4 h under N₂ flowing at 0.5 L/min. The resulting slug (BO = 49 %) was progressively crushed in a mortar and sieved through meshes of sizes 500 µm, 250 µm, 125 µm and 62 µm. The fraction of particles smaller than 62 µm, referred to as “non-steamed” sample, was further activated with steam, CO₂ or KOH. The sample was deposited on an alumina boat and introduced in an alumina tube furnace, heated to a chosen temperature for a given time under a gas flow rate of 0.5 L/min. For steam-activation, N₂ was bubbled in a water bath maintained at 30 °C, the temperature was set to 900 °C or 700 °C with dwell times up to 72 h. For CO₂ activation, pure CO₂ was flushed at 900 °C during 3 h. For KOH activation, the carbon was previously ground with KOH in a mass ratio KOH/C = 2.5, and pure N₂ was flushed at 0.5 L/min for 1 h at 800 °C. Subsequently the mixture was washed repeatedly with water until a neutral pH was obtained. All samples were dried in an oven at 80 °C before further use.

Solid-state NMR experiments were performed using 3.2 mm outer-diameter zirconia rotors and a 400MHz Bruker Avance III HD WB spectrometer operating at a magnetic field strength of 9.4 T. The magic-angle spinning (MAS) rate was 5 kHz. ¹H spectra were recorded using the DEPTH pulse sequence, with 16 scans, recycle intervals of 5 s and 90° pulses of 5.2 µs. Two-dimensional exchange spectroscopy (2D EXSY) experiments were acquired with 16 scans for each of the 600 t₁ increments with recycle interval of 0.4 s. The spectral widths were set to 6 kHz, the States-TPPI protocol was

used to achieve sign discrimination. ^1H spectra were referenced relative to the CH_3 resonance of alanine (1.2 ppm). The deconvolutions were made using the DMfit program to yield resonance intensity and width with a Gaussian-to-Lorentzian ratio between 0 and 1.

Nitrogen gas sorption measurements were carried out at 77 K using a Quantachrome Autosorb instrument or a Micromeritics 3Flex instrument. Prior to each experiment, the samples were outgassed at 300 °C for at least 10 h at 10^5 Pa. Quantachrome data was treated in ASiQwin using NLDFT or QSDFT methods on the adsorption branch assuming slit pores or slit/cylindrical pores, and Micromeritics data was treated in MicroActive using a variety of NLDFT kernels assuming slit pores. The regularization parameter is set at the intercept between the roughness curve and the error curve as widely recommended. Errors on the fits are calculated by the softwares based on the non-negative least-square method.

XRD patterns were acquired in the Bragg-Brentano geometry on a Rigaku SmartLab instrument using the $\text{Cu K}\alpha$ radiation generated at 10 kV and 200 A equipped with a D/teX-ULTRA 250 detector. The patterns were then deconvoluted in PDXL into a background and peaks of the Split Pearson VII geometry.

Raman spectra were collected using a confocal Raman system (InVia, Renishaw plc, Wotton-Under edge, UK), coupled to a 532 nm wavelength laser. Spectra were collected using a 50x long distance objective with a laser power at the sample of ~30 mW, exposure time of 5 s.

CHNS elemental analysis was performed on a Vario El Cube using sulfanilic acid as a control. A mass of 1 – 2 mg of sample was loaded in a tin boat. The combustion tube temperature was 1200 °C.

4 Investigation of the Structure of PDCs

All properties of PDCs relevant to applications such as adsorption and diffusion of solvents and ions depend on the structure of the pores and the pore network. Therefore before looking at the properties of PDCs, their structure will be investigated in this chapter. The first step is to reproduce literature samples, which commonly consist in carbonizing PEEK at 900 °C under a dry nitrogen atmosphere and subsequently activating the PDC at the same temperature in a steam-loaded nitrogen atmosphere. Other activation conditions such as steaming at lower temperatures or using other activating agents may develop other porosities, so the second step will be to explore other synthetic conditions to compare the samples and shed light on the meaning of tunable pore properties through rationalization of the activation mechanism.

4.1 Structure After Steam-Activation at 900 °C

4.1.1 XRD and TEM

XRD and TEM are often used together to yield respectively bulk and local estimates of the dimensions of OD of activated carbons in good mutual agreement.^[127] Figure 4.1a shows XRD patterns of the carbon as pyrolyzed, and after activation to BO = 34 % and 57 %. The peak around 22° is traditionally assigned to the (002) plane and

gives an interlayer distance of approximately 0.4 nm. Applying the Scherrer equation gives an apparent crystallite sizes approximately 0.7 nm thick, corresponding to three sheets in a stack, which is not uncommon^[24,26]. While XRD has been efficiently used to follow the structure evolution during carbonization, whereby the narrowing of the (002) peak with increasing carbonization temperature shows that the order in the OD increases, no trend was obtained when comparing the width of this peak for different activation conditions. The same observation that, once carbonization is complete, the values of OD size extracted by the Scherrer equation change little with activation time has been made^[120,121], so it seems that the Scherrer approach, although efficient to study the carbonization process where major changes in order and domain size occur, is less efficient for the activation mechanism. What does emerge from these samples is that the intensity of the (002) peak decreases with increasing BO. This suggests that the amount of ordered material decreases during activation, consistent with the literature, but this result alone does not allow to say whether it is transformed into a more disordered phase or whether it is altogether etched.

In the TEM image of sample 900_57, Figure 4.1b, sheets can be seen to stack in relatively ordered domains albeit not perfectly graphitic but distorted, much like most TEM images of activated carbons. The electron intensity profiles 1, 2 and 3 along the red lines show the interlayer spacing is on average 0.4 nm. Regions with more than three parallel sheets are often seen, but the interlayer distance is not strictly identical across the whole stack.

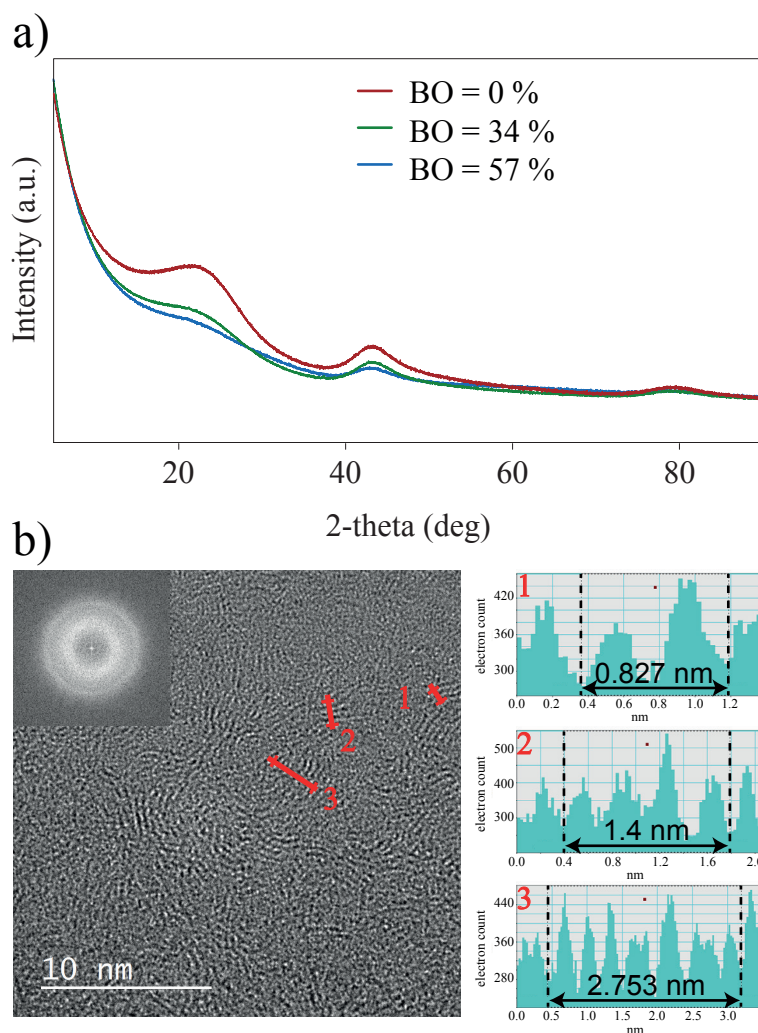


Figure 4.1: XRD patterns of samples 900_0, 900_34 and 900_57 a) and TEM image of samples 900_57 with intensity profiles along the red lines.

4.1.2 Raman

Figure 4.2 shows a typical Raman spectrum with the four fitted bands. The peak parameters were determined as an average of four to six measurements for each sample steamed at 900 °C to BO values from 0 % to 57 %. Despite significant error bars, the trends described in Chapter 1 may be identified, *i.e.* D1/G1 decreases and D2/G2 increases with increasing BO, see Figure 4.3, which indicates that steam activation at

900 °C reduces the size of both the OD and DD domains. In addition, G2/G1 decreases from 0.30 to 0.15, indicating that the relative amount of DD decreases.

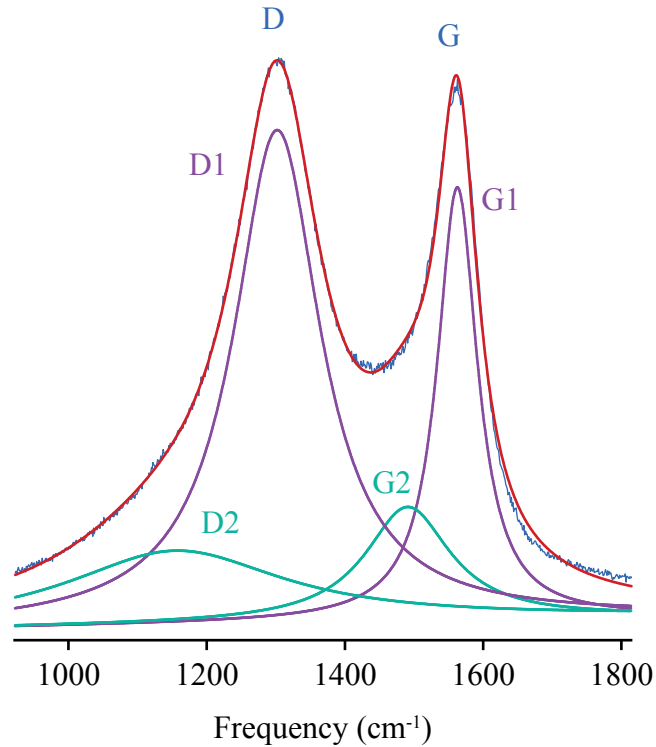


Figure 4.2: Typical Raman spectrum of a PDC sample with BO = 34 %. The experimental curve is in blue, with the fit in red and the individual components in purple and green.

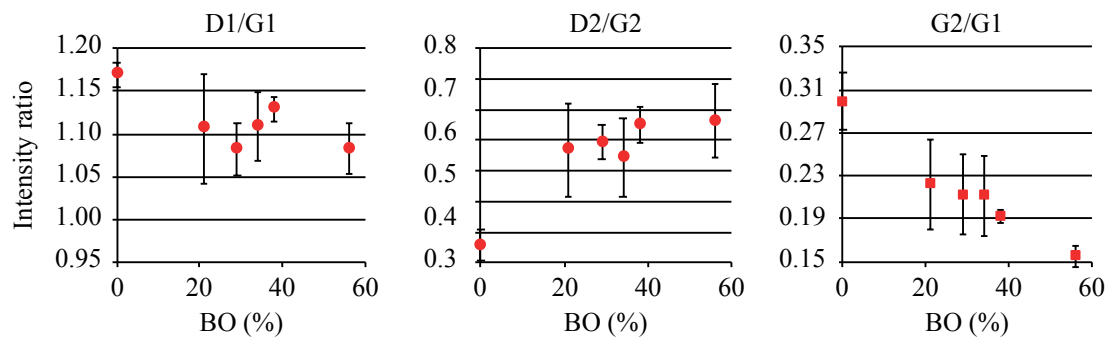


Figure 4.3: Variation of D and G band ratios of samples activated at 900 °C.

Further information on the activation mechanism can be extracted from the following trends as a function of increasing BO, see Figure 4.4. The FWHM of D1 decreases from 170 cm^{-1} to 117 cm^{-1} , the FWHM of G1 decreases from 68 cm^{-1} to 52 cm^{-1} , and the frequency of G1 increases from 1559 cm^{-1} to 1573 cm^{-1} . These three trends all indicate that the order increases in the OD during the steaming process. The frequency of D2 increases from 1146 cm^{-1} to 1181 cm^{-1} , indicating that the order in the DD also increases. In summary, both domains are reduced in size during steaming with little reorganization taking place, and the etching of the DD is slightly faster than the etching of the OD, which is consistent with the preferred etching of carbon atoms at defect positions.

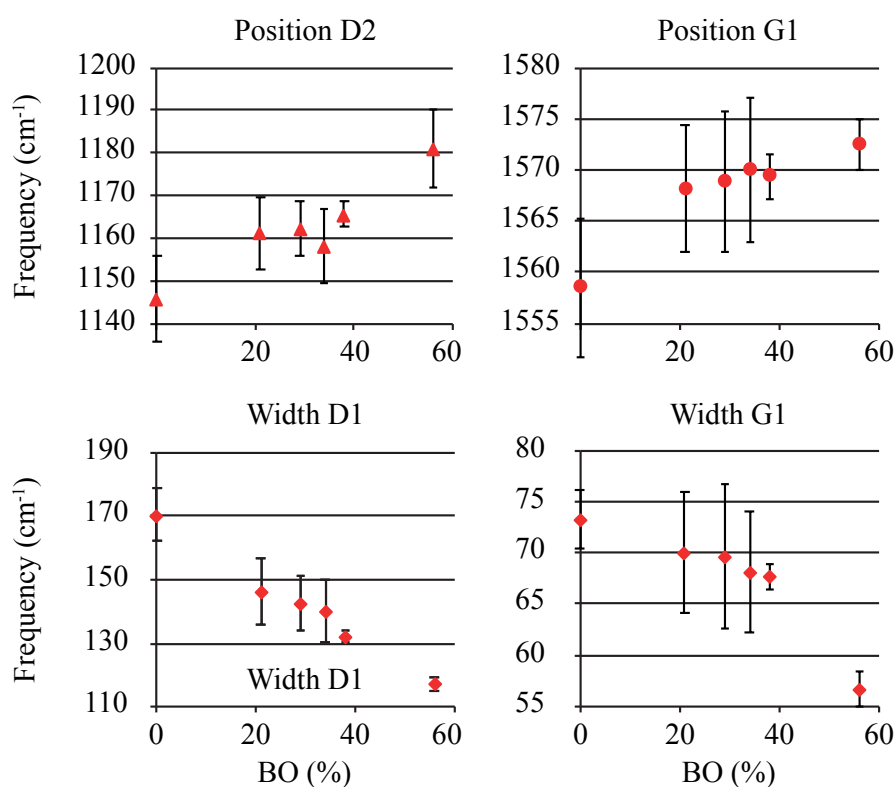


Figure 4.4: Variation of Raman peak parameters of samples activated at 900 °C.

4.1.3 Gas Sorption and NMR

As an independent probe of the evolution of the pore structure with burn-off, gas sorption measurements were carried out on PDCs with BO values in the range 0 – 62 %. As can be seen from Figure 4.5, the pore volume of pores bigger than 3 nm (0.5 on the logarithmic axis) is negligible and random compared to the three systematic pore sizes below 3 nm, confirming that the PDCs are predominantly microporous. In addition, species adsorbed in such big pores experience a ring-current shifts too small to be fully deconvoluted from ex-pore species. Higher diffusion coefficients in big pores are also thought to facilitate exchange-averaging with the ex-pore environment, which potentially makes species adsorbed in big pores completely indistinguishable from ex-pore species. For these reasons, only the three main pores were taken into account for the NMR interpretation.

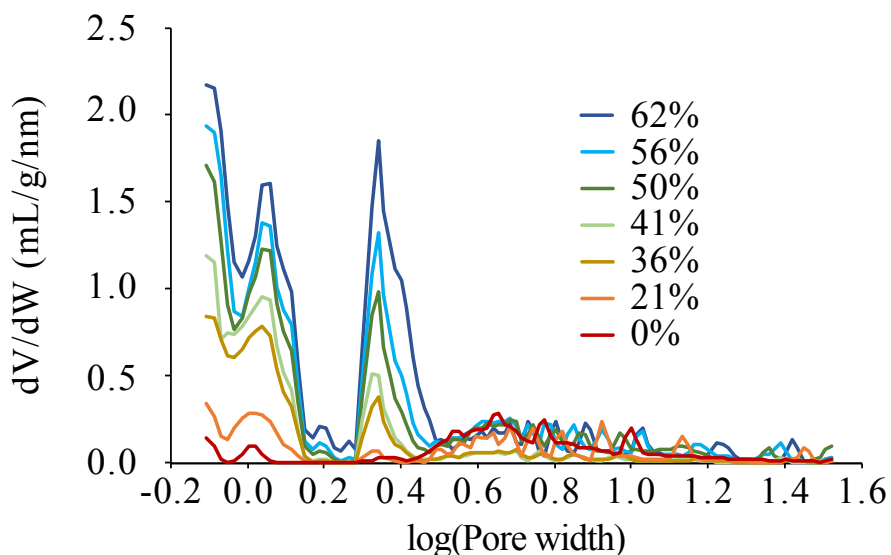


Figure 4.5: Logarithmic plot of differential pore volume between 0.8 and 33.0 nm for PDC samples with burn-offs between 0 – 62 %. All samples were sieved prior to steam activation as described in the main text.

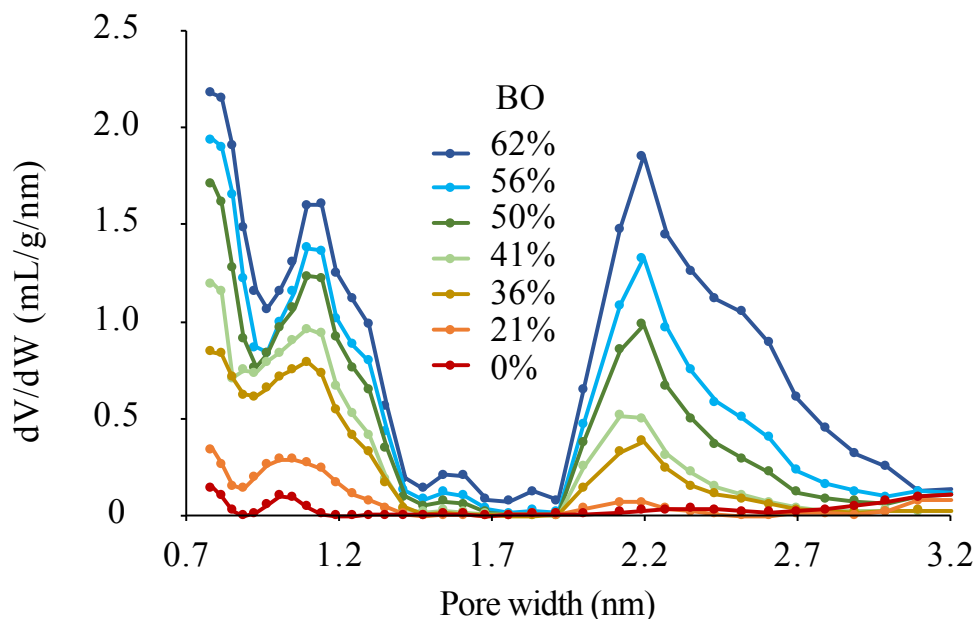


Figure 4.6: Plot of differential pore volume between 0.8 and 3.0 nm for PDC samples with burn-offs between 0 – 62 %. All samples were sieved prior to steam activation as described in the main text.

Pore size distributions between 0.8 – 3.2 nm are shown in Figure 4.6. The gas sorption results show that the pore sizes within each sub-population do not change significantly with increasing burn-off; instead, the relative proportions of pore sizes within each sub-population vary, with increasing porosity in the 2 – 3 nm range for higher burn-offs. This agrees with previous gas sorption measurements on PDCs^[51,61] and highlights an important distinction when using the $\Delta\delta$ as a probe of the carbon pore structure. In principle, H₂O molecules adsorbed in different sized pores should exhibit different NICSs, resulting in multiple in-pore resonances in the NMR spectrum. However, as seen in Figure 3.5, only a single in-pore resonance is observed for each BO value. This is explained by the fact that at ambient temperature the water molecules within the pore structure undergo intraparticle exchange between the different pore environments on a timescale that is faster than the NICS frequency differences.^[67] As a

result, a single resonance is observed with a $\Delta\delta$ corresponding to the average pore size. Therefore although the individual pore sizes do not change significantly with burn-off, the increase in the relative proportion of mesopores causes the average pore size to increase, resulting in a reduction in the $\Delta\delta$.

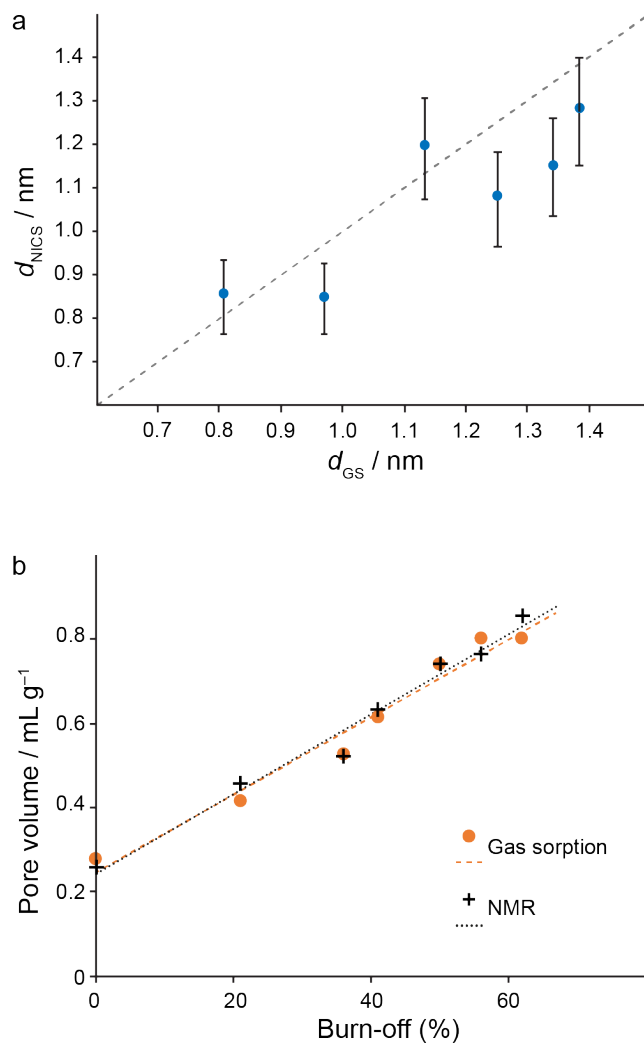


Figure 4.7: (a) Comparison of the average pore size derived from the NICS of in-pore H₂O species, d_{NICS} , and from gas sorption measurements, d_{GS} , for different PDC samples. The dotted line represents perfect agreement. Error bars are derived from the full width at half maximum of the in-pore resonance. (b) Comparison of total pore volume determined by NMR (crosses) and gas sorption (circles). Dotted and dashed lines represent best linear fits to the two datasets.

The pore sizes are again calculated using the semi-empirical formula by Xing *et al.*^[72]. Figure 4.7a compares the NICS-derived average pore size, d_{NICS} , with the average pore size from the gas sorption measurements, d_{GS} , for PDCs with BO between 0 – 62 %. Over the range of samples studied, there is reasonable agreement between d_{NICS} and d_{GS} , confirming that the NICS provides a useful probe of the pore size in PDCs. However, we note that there is a tendency for d_{NICS} to be underestimated compared to d_{GS} . This could arise from differences in the adsorption behaviour within the smallest pores of H₂O used in the NICS experiments and N₂ used in the gas sorption experiments. It is also possible that the equation relating the NICS to the pore size is not very precise for the smallest pores. Indeed, at this scale the magnitude of the ring-current effect is highly dependent on both the graphene domain size^[65] and the pore surface topology, and in particular whether an adsorbed species is located near a concave or convex face^[130]. The model proposed by Xing *et al.* is based upon a slit pore formed by two parallel circumcoronene molecules. If the local domain size or curvature within the PDCs differs significantly from this, it would lead to be a systematic discrepancy between d_{NICS} and d_{GS} . As a further probe of the pore structure, we also compared the total pore volume for PDCs determined from gas sorption with that determined from the integrated intensity of the in-pore resonance as a fraction of the total amount of liquid added to the sample. To directly correlate the intensity of the in-pore and ex-pore peaks with the volumes of liquid, in this case water, we need to assume that the density of the in-pore water is constant, and that the sensitivity is the same in both environments as well. As shown in Figure 4.7b, a strong linear relationship between burn-off and total pore volume is observed, and very good agreement is obtained from the two measurements. This confirms that NMR serves as a very useful probe of the pore volume in microporous carbon materials. Also we note that the good agreement with

the gas sorption pore volume is also evidence that in-pore – ex-pore exchange effects are not significant in these systems. In the fast exchange limit, the intensities of the in-pore and ex-pore resonances should be modified to account for the proportion of each population that is undergoing exchange. If this was the case, the integrated intensity of the in-pore resonance would not reflect the true proportion of species in the in-pore environment and poor agreement with the gas sorption data would be expected.

4.2 Exploration of Other Activation Conditions

To learn more about the steam activation mechanism on a bigger length scale, several other activation conditions were tested and compared to identify general and specific trends. Thus, information was obtained from steam-activation at 700 °C, CO₂ activation at 900 °C and KOH activation at 800 °C.

4.2.1 Pore Structure After Steam-Activation at 700 °C

Firstly, the activation kinetics were found to be approximately fifty times slower than at 900 °C; the same BO required a longer steaming time, in agreement with the studies mentioned in the Introduction. Precise reaction rates are however difficult to calculate because they depend on the steam to carbon ratio, and different masses of carbon were introduced. Figure 4.8 shows the gas sorption results of this series of samples obtained using the QSDFT slit/cyl kernel, but differences with the slit kernel will be discussed. Compared to our samples steamed at 900 °C (Figure 4.6), where the exact same pore populations were found in all samples while the respective volumes increased monotonically, the evolution of the PSD presents some differences. Sample 700_10 resembles any low-BO sample activated at 900 °C with well-resolved micropores and few pores in the range 1.5 – 3 nm. Samples 700_24 and 700_32 show

an unusual single, smooth and wide population between 0.7 nm and 2 nm, in addition to some pores smaller than 0.7 nm, but no 2 nm mesopores, as opposed to samples steamed at 900 °C to similar BO. Samples 700_55 and 700_68 again resemble 900 °C samples with a distinct bimodal microporous distribution and the cylindrical mesopores. Interestingly, while different PSD are obtained whether only slit pores are assumed or slit and cylindrical pores in the case of the usual samples, for the unusual samples 700_32, no difference is obtained, indicating that the absence of two populations is not simply due to the choice between these two kernels. In addition, it appears from the figure that the maximum of this single population is between the two populations of the bimodal distributions as if they were averaged. This is an interesting observation which deserves more investigation and could possibly bring some insight into the activation mechanism.

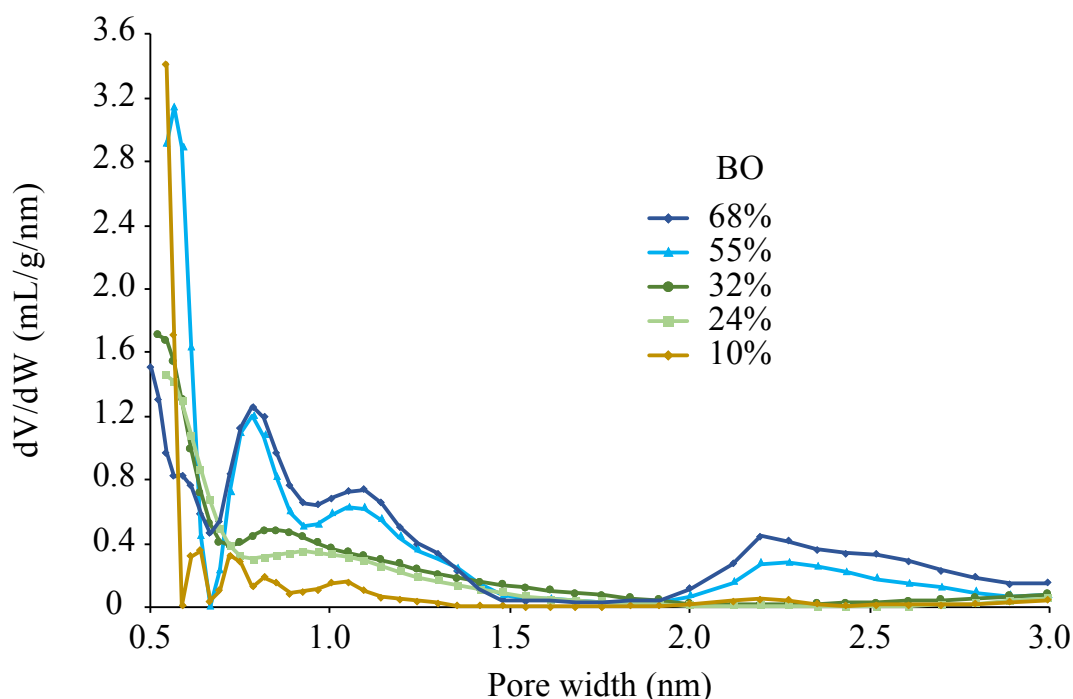


Figure 4.8: PSD of samples 700_10, 700_24, 700_32, 700_55, 700_68.

Several hypotheses can be envisaged at this point to explain the PSD of 700_24 and 700_32: a) the molecular structure of the pores created in the 24 – 32 % range of BO is different because different oxidising species are involved, b) the same pores develop but at different relative rates because the relative gasification kinetics of the reactive sites are different than at high temperature, c) the pores develop exactly in the same way as at 900 °C (except for slower kinetics) but the apparent gallery height within any one pore is irregular due to residual particles as proposed by Gun'ko *et al.*^[39].

Hypothesis 1

The first hypothesis is whether the gasification reaction itself is identical at low and high temperature. In fact, one product of the steaming is CO which may further react with H₂O to form CO₂, see reaction scheme in Figure 1.1. CO₂ is known to target different reactive sites on the carbon surface. In addition, even though the reaction rate of CO₂ is slower than steam and negligible at low temperatures, the two species may be in competition at low pressures^[131], which we suppose could be the case at high temperatures where steam is consumed rapidly. To see whether the porosity is developed differently by CO₂ and steam, a CO₂-activated sample was made using pure CO₂ at 900 °C, according to standard procedures^[130], and characterized by GS. The result is not significantly different than for steam-activated samples, see Figure 4.9, we can therefore conclude that a) the active sites for CO₂ and H₂O are homogeneously distributed within the structure, and b) the differences between high- and low-temperature steam-activation pore size distributions are not due to the different contributions of steam and CO₂, but are intrinsic to the reaction of the material with steam.

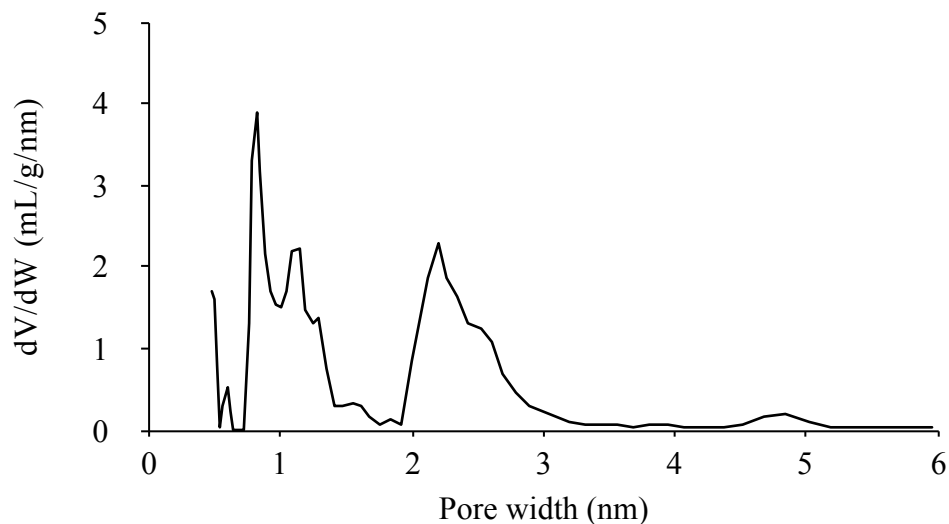


Figure 4.9: PSD of CO₂_900_66 calculated with the QSDFT_slit/cyl kernel.

Hypothesis 2

The next simplest hypothesis is that the fraction of material composing the DD, giving rise to the broad 1 – 2 nm slit pore population or the 2 – 3 nm cylindrical pores when etched, is left intact at 700 °C until higher BO. Such a hypothesis was in fact already proposed in the case of carbons derived from sawdust.^[132] A series of samples was characterized once again with Raman spectroscopy to follow the structural evolution on a molecular level. Figure 4.10 shows the various identifiable trends. The Full Width at Half Maximum (FWHM) of D1 decreases suggesting that defects in the OD are removed, although perhaps slightly slower than at 900 °C. The position of D2 does not increase significantly, suggesting that defects in the DD are not removed, unlike at 900 °C. And the ratio D2/G2 increases, meaning that the DD are still reduced in size. The other trends mentioned for the 900 °C series of samples were not visible due to uncertainty on the values. It seems that even at 700 °C the less ordered material is etched at comparable rate than the most ordered material, with however a slightly

higher level of disorder left in this latter domain. In summary there is no significant difference in reactivity of the carbon structure between 700 °C and 900 °C.

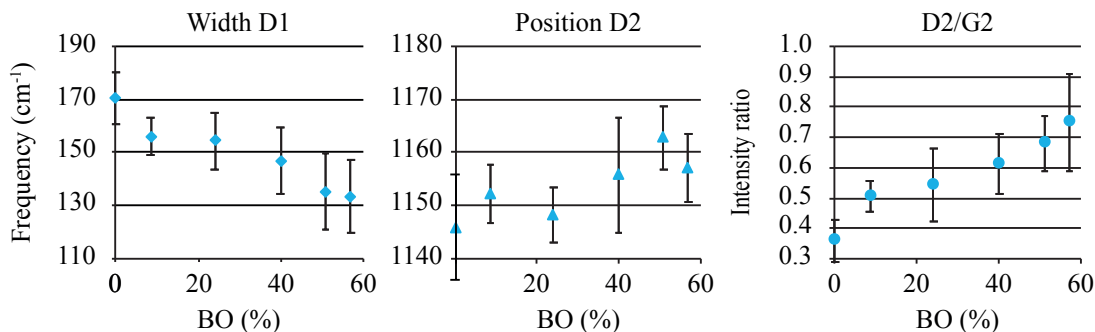


Figure 4.10: Variation of Raman peak parameters of samples activated at 700 °C.

Hypothesis 3

According to the third hypothesis, the pores are exactly the same in terms of structure, but they contain additional small particles, which have an effect on the apparent pore size. In a first instance we postulate that oxygen groups deposited during steam-activation may be the reason for a rougher texture. Indeed CO groups desorb at slower rates at 700 °C compared to 900 °C^[125,126], so there might be some leftovers. ¹³C NMR is normally able to detect several oxygen-containing functional groups such as carbonyl and epoxy groups^[135], however such features were not seen in the spectrum of 700_32 (Figure 4.11). In addition, elemental analysis yielded a typical composition of ~97 % carbon. Therefore if there are particles in the pores, they must be composed only of carbon with chemical shift around 130 ppm. For example, such particles could be made of low-molecular weight alkene groups weakly bonded to the pore walls. Such debris are normally not stable at high temperatures, so a second high-temperature treatment under inert atmosphere should clean the pores.

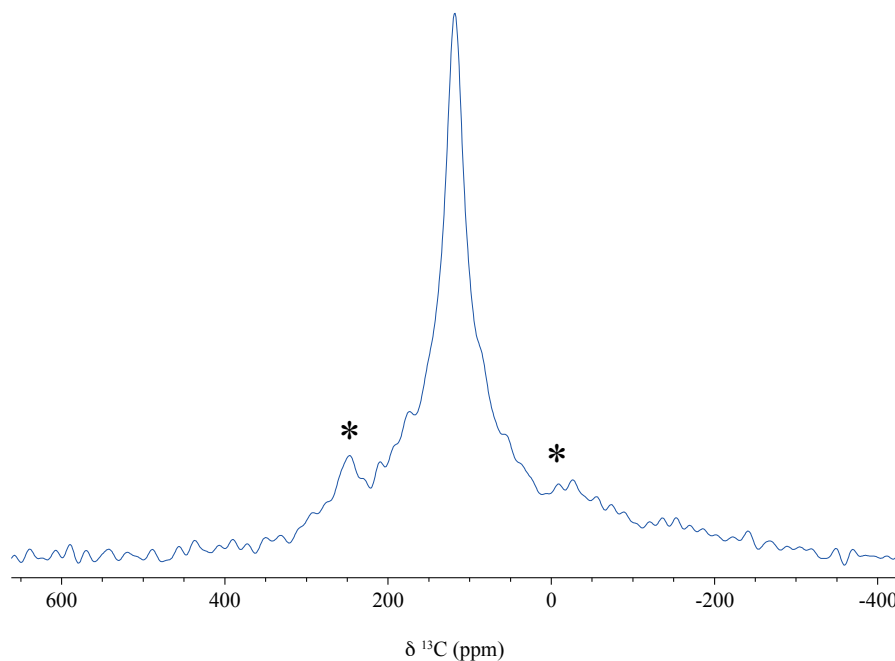


Figure 4.11: Direct excitation ^{13}C NMR spectrum of 700_32.

Thus sample 700_32 was heated at 900 °C under nitrogen for 4 h with an additional BO = 24 % giving sample 700_32_C24,. Elemental analysis again yielded a typical composition of ~ 97 % carbon, however a small decrease of the hydrogen content from 0.6 ± 0.04 % to 0.4 ± 0.01 % was found (obtained as the average of two measurements). Note that other samples such as 700_55_C36 also showed a reduction of hydrogen mass. We then compared the ^1H NMR spectra of water-saturated 700_32 and 700_32_C24, see Figure 4.12. There are several observations to be made but the main effect of recarbonization appears to be the shift of the most intense in-pore resonance from -4.3 ppm to -5.0 ppm. This increase of NICS is consistent with defects being removed causing the aromaticity of the pore walls to increase.

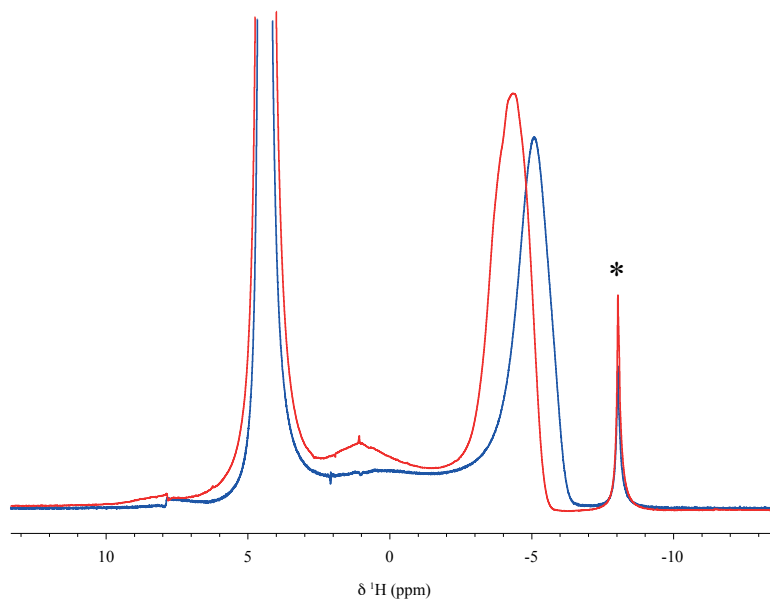


Figure 4.12: ^1H NMR of water-saturated PDC sample 700_32 (red) and 700_32_C24 (blue). The asterisk denotes a spinning side band.

In summary, before discussing the NMR spectra in more details, we conclude that at 700 °C, the slow etching of the sheets generates metastable structures that may partially occupy the pore space. The nature of the defects is however not clear. According to Zhu *et al.* during the gasification reaction, H_2 desorbs before CO and without being ever physisorbed as monoatomic hydrogen on the carbon surface^[136], which makes it unlikely that the defects are simply C-H groups directly on the carbon surface, also because there is a negligible and almost constant amount of hydrogen. However it is unknown whether hydrogen could react with carbon atoms of unsatisfied valency, so-called dangling bonds, left behind after CO desorption. The mechanism by which the defects affect the PSD could be, in addition to changing the effective local pore size, to catalyse the nitrogen adsorption by providing nucleation sites, thus reducing the adsorption pressure and the apparent pore size. Finally, in GS, the bimodal micropore distribution is recovered after recarbonization, see Figure 4.13, in agreement

with defects being the only cause for the merging of the pore populations. Future work could aim to vary the roughness parameter δ of the pore wall in the QSDFT calculations, set to 0.13 nm (see Chapter 2), for samples with carbonaceous debris where the pore wall might be better represented by a density gradient spreading over a longer distance.

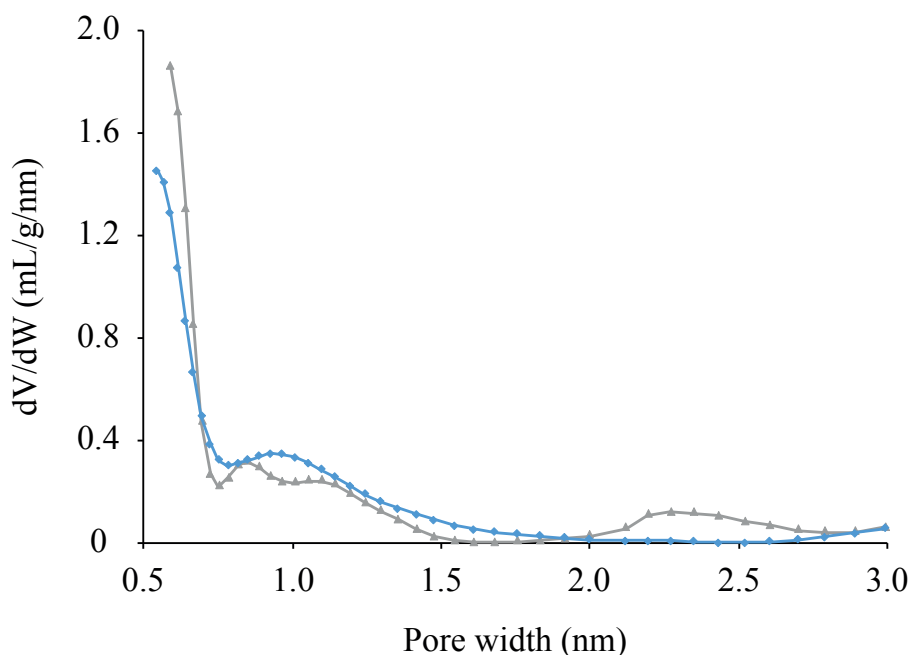


Figure 4.13: PSD of 700_24 (grey) and 700_24_C16 (blue) calculated with the QSDFT_slit/cyl kernel.

4.2.2 Evolution of the Pore Network After Steam-Activation at 700 °C

The surprising particularity of these two samples is the presence of a second smaller resonance at 1 ppm in NMR spectra (Figure 4.12), which also shifts to the same extent during recarbonization, to ~ 0 ppm. To determine whether these two environments are located in each particles, or whether some particles have been activated more than others, EXSY was performed on sample 700_55 saturated with water but after freezing the ex-pore water by cooling to -30.0 °C, such that in-pore/ex-

pore exchange is interrupted, as well as exchange between pores located in different particles. The 2D spectra, Figure 4.14, clearly show that there is a cross-peak between the two environments with increasing mixing time.

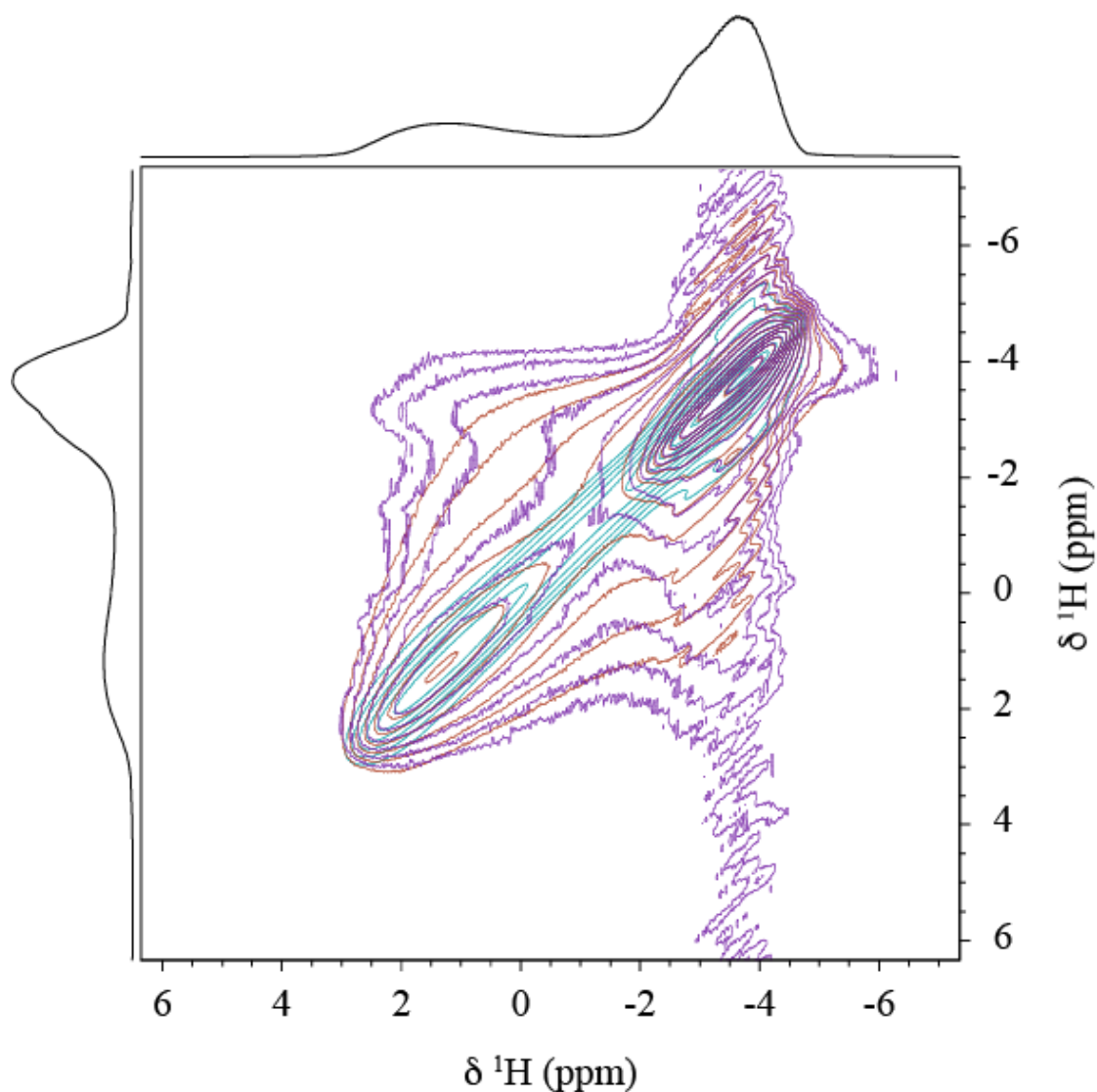


Figure 4.14: 2D EXSY ^1H NMR spectra of 700_55 saturated with water recorded at -30.0 °C, with t_{mix} of 0 ms (green), 100 ms (red) and 250 ms (purple).

In other words, we can deduce with confidence that the pore network is inhomogeneous within each and every particles and that diffusion of water is not fast enough for the whole pore network to be exchange-averaged.

To better characterize this series of samples with two in-pore peaks, we propose the following experiment: the sample is saturated with 1,4-dioxane and cooled beyond its melting point. The freezing point of dioxane has the interesting property to decrease upon confinement in pores smaller than 2 nm.^[120] Water on the other hand is very difficult to freeze in micropores even at temperatures as low as -50 °C. Therefore, if dioxane freezes above its normal freezing point of 12 °C, easily achievable in-situ, that would mean dioxane is located in micropores. Figure 4.15 shows the series of ^1H spectra recorded at various temperatures down to -30 °C. The ex-pore peak (~ 3 ppm) is taken as internal reference for temperature. As can be seen, this peak disappears between 16.0 and 5.0 °C. This is the sign that ex-pore dioxane has frozen, and the peak is now broadened beyond visibility due to enhanced ^1H - ^1H dipolar couplings typical of solids. The in-pore peak at ~ -4 ppm has started to disappear above 16 °C already, and continues to do so progressively until it is gone at -30 °C. The second in-pore peak at ~ 0 ppm increases until 0 °C, and then decreases to roughly the initial intensity until -30 °C but it never disappears. Therefore this experiment shows that the two in-pore peaks correspond to regions of the pore network with different average pore sizes. It is not straightforward to determine why the right peak increases at first, but there can be two reasons why the valley between the two in-pore peaks visible at room temperature can be affected. The valley either corresponds to a) solvent located in pores of intermediate sizes, or b) solvent that is able to exchange between the two environments, for example at the boundary between them. In the first case, the pores of intermediate size would allow for solidification at slightly lower temperatures, explaining why the right peak decreases progressively and why part the valley is also affected. In the second case, when solvent in the small pores freezes, the exchange is stopped and so the solvent that was exchanging would appear as solvent in big pores, explaining why the left peak

temporarily increases. However the fact that the left peak decreases at lower temperatures can be explained only by the presence of intermediate pore sizes, whether there is exchange or not.

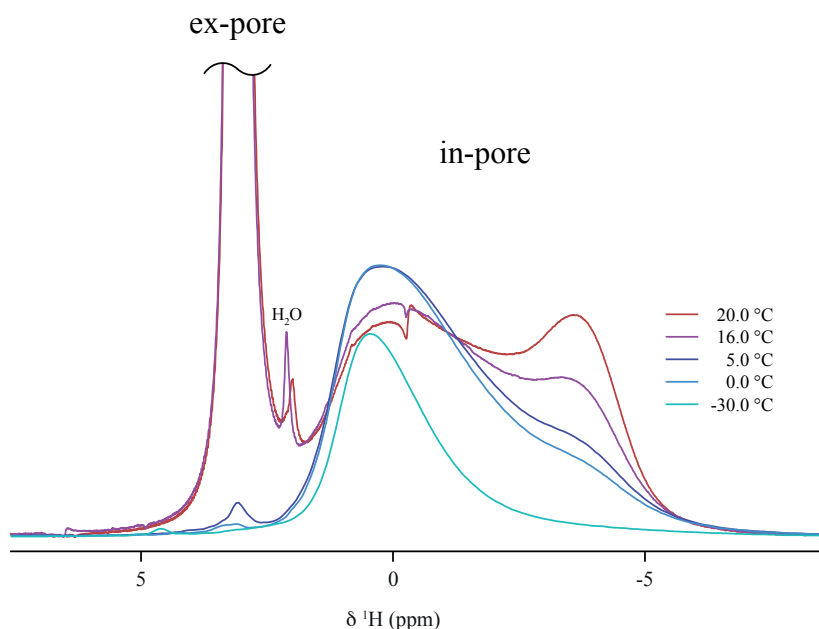


Figure 4.15: ^1H NMR spectra of 700_68 soaked with dioxane at variable temperatures.

Additional comments about the NMR spectra can be made to describe the structure of the pore network. An improved picture of the pore network is obtained after activating bigger particles of diameter between 250 μm and 125 μm (mesh sizes, no DLS measurement available) of a sample called big_700_0 to produce sample big_700_27. ^1H NMR of such large water-saturated particles, Figure 4.16, shows that more of the initial pores of $\Delta\delta \sim 10$ ppm are created. This means that with this particle size, during activation at 700 $^\circ\text{C}$, the steam does indeed wet the entire pore network homogeneously. In addition to these pores, pores of $\Delta\delta \sim 3$ ppm have appeared. This means that in sample 700_68 (Figure 4.15) and 700_32 (Figure 4.12), both in-pore peaks are in fact the average between various pores: the right peak corresponds to

regions of the pore network predominantly, but not completely, microporous, and the left peak to regions where micropores are in close proximity to much bigger volumes of mesopores, in agreement with the dioxane experiment. Therefore we could not extract any true pore size from the $\Delta\delta$ in the previous samples, as the big pores would have been underestimated and the small pores overestimated, because of solvent diffusion effects. The big particles of sample big_700_27 however, despite having been activated to BO similar than 700_32 show no valley between the two peaks, suggesting that the two corresponding regions of the pore network are separated by a slower or longer diffusion path that is hindering exchange-averaging.

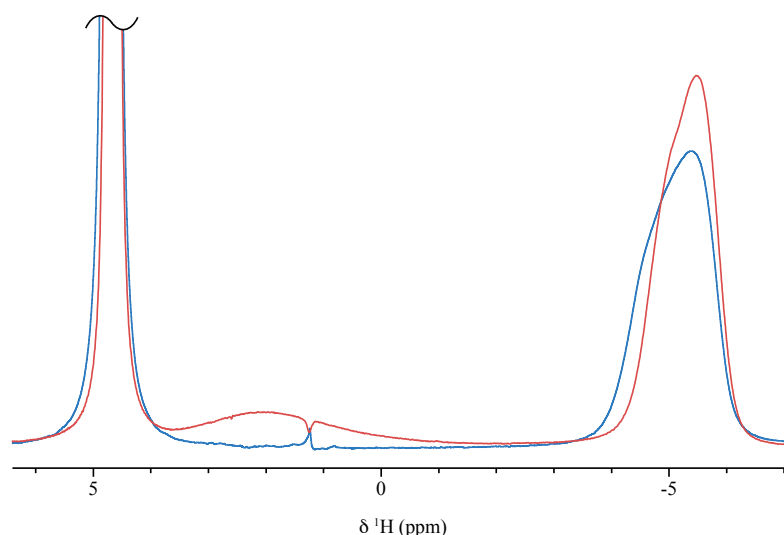


Figure 4.16: ^1H NMR of water-saturated PDC particles of size 250 – 125 μm , before activation, big_700_0, (blue) and big_700_27 (red).

The 2D EXSY spectrum of 700_55 (Figure 4.14) shows in-pore peaks elongated on the diagonal, unlike typically cross-shaped ex-pore peaks, which means that the in-pore peaks are the sum of a multitude of slightly different environments that are not exchange-averaged.^[85] Furthermore the peak at -5 ppm (Figure 4.16) does not shift

upon steaming even though it increases, while the peak at ~ -3 ppm is quite broader. This means that some types of pores that are created during steaming are the same as present before steaming with a quantized albeit slightly distributed size, while bigger and more variable pores are created. For the first time it is possible to make a connection between NMR spectra and GS PSD. In GS we observed a bimodal distribution: a well-defined 0.8 nm pore population originating from etching of one sheet in the OD, and another broader population ranging from 1 to 2 nm. Using the same equation as before, we obtain 0.8 and 2.3 nm pores. At first glance the small pores match the GS data, but the big pores are overestimated. On one hand, the extraction of pore sizes from the $\Delta\delta$ relies on a simplistic model where the pore walls are approximated as a planar polyaromatic cluster of finite size, which could mean the model deviates for pore walls that are not perfect slits and generate stronger or weaker ring currents. Diffusion averaging is taken into account within the pore to yield a single NICS per size, but in a real sample diffusion always occurs between neighboring pores. The values from NMR are therefore not too trustworthy but give an appreciable idea: there are small pores and decisively bigger pores.

On the other hand, both NMR and GS are quantitative techniques for the pore volume, therefore we compared the ratio of volumes of the small pores relative to the big pores. Sample 700_32_C24 and 700_68 were used for this purpose because the bimodal distribution in the PSD pattern is required. The ^1H NMR spectra were deconvoluted into an arbitrary number of peaks as to fit the ex-pore peak and the two in-pore environments including the valley as well as possible. Interestingly, matching NMR and GS ratios are obtained for sample 700_32_C24 (big pores/small pores = 2.6 for both techniques) and for sample 700_68 (1.6 for NMR and 1.5 for GS) under the following conditions. First, the PSD obtained on Quantachrome with the QSDFT slit

pores kernel was separated into populations smaller than 0.852 nm included, and superior to 0.926 nm included, which is the local minimum between the two populations. Second, only the in-pore component with the smallest $\Delta\delta$ was assumed to correspond to the 1 – 2 nm pore population, while all other in-pore components, including those located in the valley at $\Delta\delta \sim 6$ ppm, are considered as part of the small pores. However a NICS of 6 ppm gives a pore size greater than 1 nm according to Wu *et al.*, which would situate this pore in the second population. Therefore the pore network is likely to be more complex than how it appears. This result coincides with the deductions from the dioxane experiment that showed, besides the possibility of exchange-averaging effects, the presence of intermediate pore sizes unresolved by GS.

In that regard, many samples show other subnanometre populations at 0.6, 0.7, 0.8 and 1.0 nm (see Figure 4.8). The broad 1 – 2 nm population of pores could thus include a well-defined subpopulation around 1 nm corresponding to two adjacent sheets etched in the OD, in addition to a broad subpopulation corresponding to the inter-domain pores.

This hypothesis is worth considering because of the mentioned error in pore size calculations based on the $\Delta\delta$. In an OD, the pore walls can be made of several layers, which would produce stronger ring-currents, so it is possible that pores as large as 1 nm appear at a $\Delta\delta$ as big as 10 ppm (normally only 8 ppm). In addition, the 0.8 nm pores and the 1 nm pores may be located in the same OD, which would be close enough for the NMR resonances to be exchange-averaged and appear as the right peak.

Further to the steam-activation at 700 °C which showed that big pores are not very densely distributed in the particles, we propose the following experiment to learn more about the reactivity of the pore network vis-à-vis steam at 700 °C. Sample 900_29

was submitted to a second activation step at 700 °C for various times. The samples are denoted, 900_29_700_7.5, 900_29_700_23 and 900_29_700_56, where the last number is the BO achieved during the second activation step. The ^1H NMR spectra of this series of water-saturated samples are shown in Figure 4.17.

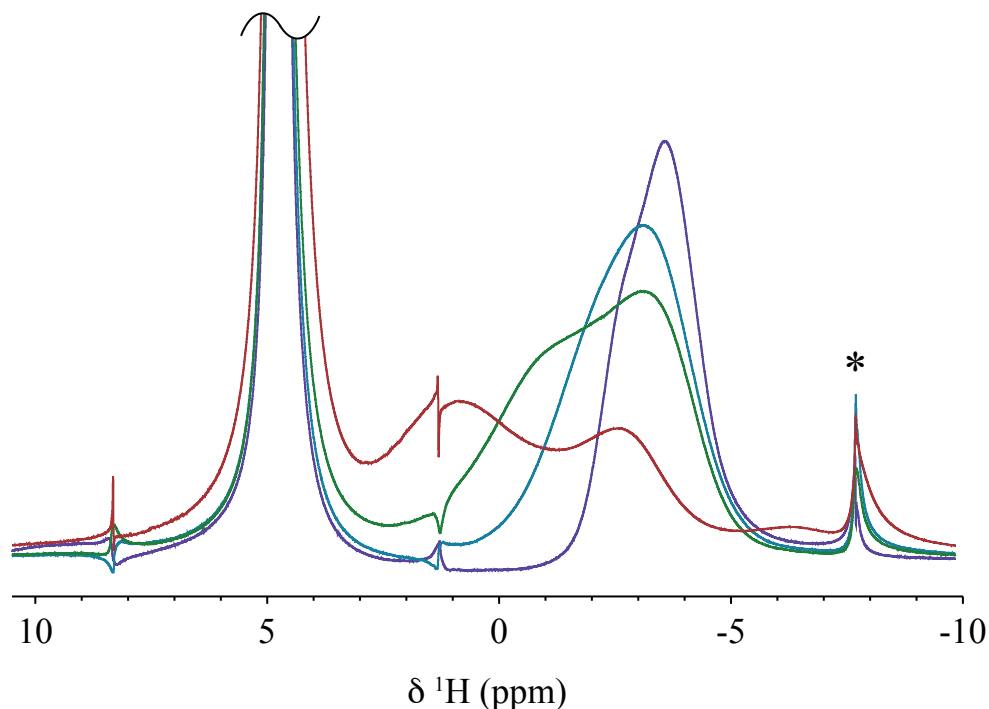


Figure 4.17: ^1H NMR of water-saturated 900_29 (purple), 900_29_700_7.5 (blue), 900_29_700_23 (green), and 900_29_700_56 (red). The two dephased signals on each sides of the ex-pore peak are artifacts.

We know that the in-pore peak of 900_29 at $\Delta\delta \sim 8$ ppm corresponds to regions containing all sorts of pores that are homogeneously dispersed in the particle and all very close to each other. The second activation step, at 700 °C, progressively gives rise to the expected environment at $\Delta\delta \sim 4$ ppm, while the peak at ~ 8 ppm progressively decreases. This means that the new, isolated, big pores emerge from regions initially contributing to that environment. The new environment becomes clearly visible only

when its volume is large enough to impede the exchange-averaging with the initial environment. That is why in 900_29_700_7.5 the new environment appears as a small shoulder, indicating a very slightly increased average pore size, even though the newly created pores are the same size as in 900_29_700_56. Furthermore, 900_29_700_56 and 700_32 were both obtained after 32 h of steaming at 700 °C but it appears that the gasification occurs about twice as fast in 900_29 than in the non-steamed sample. This suggests that the gasification is promoted in the 900 °C activated structure and then even more so in the newly activated structure.

4.2.3 KOH Activation

This last set of synthetic conditions is an additional demonstration that the pore sizes are quantized in PDCs and cannot take just any value, even though some variation is found due to permanent or metastable defects.

The pores are represented as slits within a layered structure reminiscent of graphite. This implies that if the layers are expanded, so are the pores. When KOH is used as oxidising agent, metallic potassium is generated in situ, which can intercalate in the graphitic structures.^[137] Therefore if the maxima of any one pore population is shifted to bigger values, it means that this pore is found within a layered structure. Activation of the starting carbon material with KOH was done following a procedure by Romanos *et al.*, who showed that 1.5 nm pores (calculated using the QSDFT kernel with slit pores) resulting from intercalation are created significantly at 800 °C or above, with KOH/C ratios of 2.5 at least.^[138] To minimize the contribution of steam that is produced during KOH treatment, we set the temperature to 800 °C where steam-activation was roughly ten times slower than at 900 °C (estimated on two steam-activated samples).

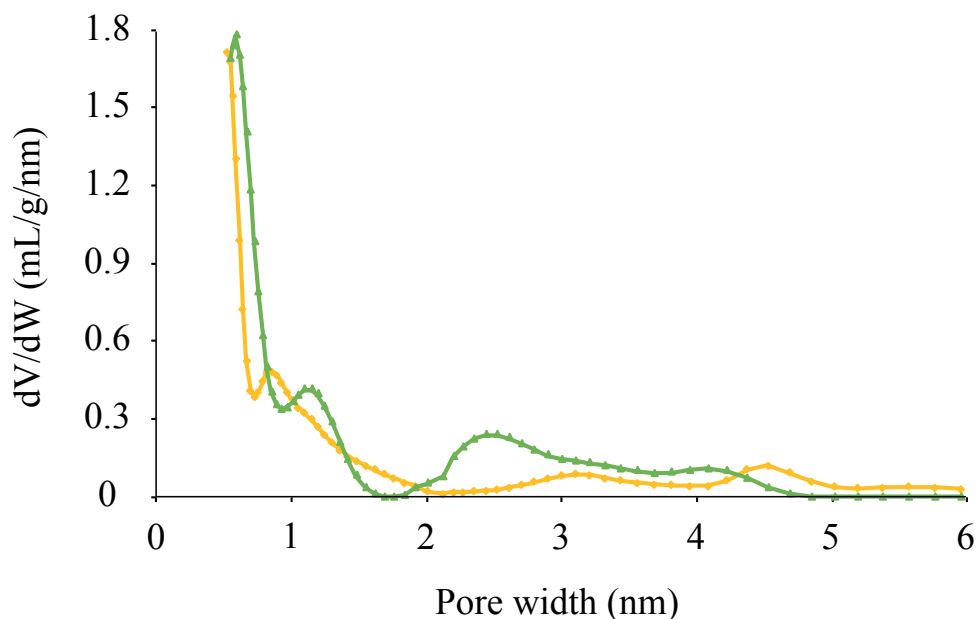


Figure 4.18: PSD of KOH_800_28 (green) and 700_32 (yellow) calculated assuming slit and cylindrical pores.

Figure 4.18 shows the PSD of sample KOH_800_28, *i.e.* activated to BO = 28 %, calculated using the QSDFT kernels with slit and cylindrical pores to better compare with sample 700_32. We find again a rather smooth microporosity, indicating that the pores are distorted, perhaps due to some carbonaceous debris if stable enough at 800 °C, or other defects. Compared to the similarly smooth PSD of 700_32, the maximum of the micropores is shifted by 0.3 nm from 0.8 nm to 1.1 nm, which is roughly what is expected for potassium intercalation. However another interpretation is that this peak is simply the usual broad population of pores between 1 and 2 nm, here split into 1 – 1.5 nm pores and 2 – 3 nm pores by the inclusion of cylindrical pores in the kernel as demonstrated with the reference sample. In this case the 0.8 nm pores would be the very high feature at the left edge of the PSD. This kind of huge feature is often, if not always, observed in PSD and more often than not appears to be a kind of fitting artefact due to a poor fit of the very first points of the isotherm. The cylindrical mesopores, although

their pore size is known to be unreliable, have also shifted from the usual 2.2 nm to 2.5 nm, *i.e.* by 0.3 nm again. This indicates that the slope of the adsorption isotherm increases at bigger p/p_0 relative to other samples. This can be visualised by treating the isotherm with slit pores only, in which case the 1 – 2 nm population actually tails off to ~ 3 nm when it normally reaches 0 by 2 nm with this kernel. Although little structural information can be deduced from this observation, it may originate from an inhomogeneous lattice expansion due to a variety of local KOH/C ratios.

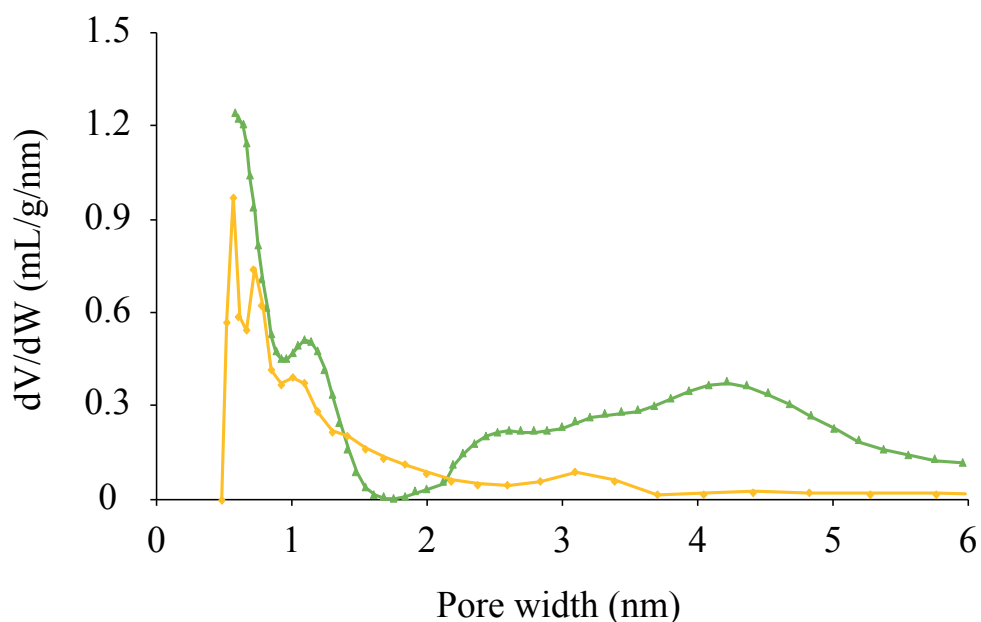


Figure 4.19: PSD of KOH_800_28_C33 (green) and 700_32_C24 (yellow) calculated assuming slit and cylindrical pores.

While the PSD of KOH_28 is inconclusive, useful information can definitely be retrieved from KOH_28_C33, see Figure 4.19. After the second high-temperature treatment, with additional BO = 33 %, *i.e.* slightly more than for 700_32_C24, sample KOH_28_C33 has not recovered the micropore features unlike samples steamed at 700 °C. The 2 – 3 nm pores still show a maximum at 2.5 nm in agreement with claims that

potassium deintercalation is not accompanied by collapse of the layers.^[137] In fact the only difference is the increase of the 3 – 6 nm population with a maximum at 4.2 nm. If the slit pore kernel is used, these pores appear smaller by ~ 1 nm in agreement with the artificial variation of size that depends on the kernel. Such pores have never been observed in this range of BO with steam-activated samples.

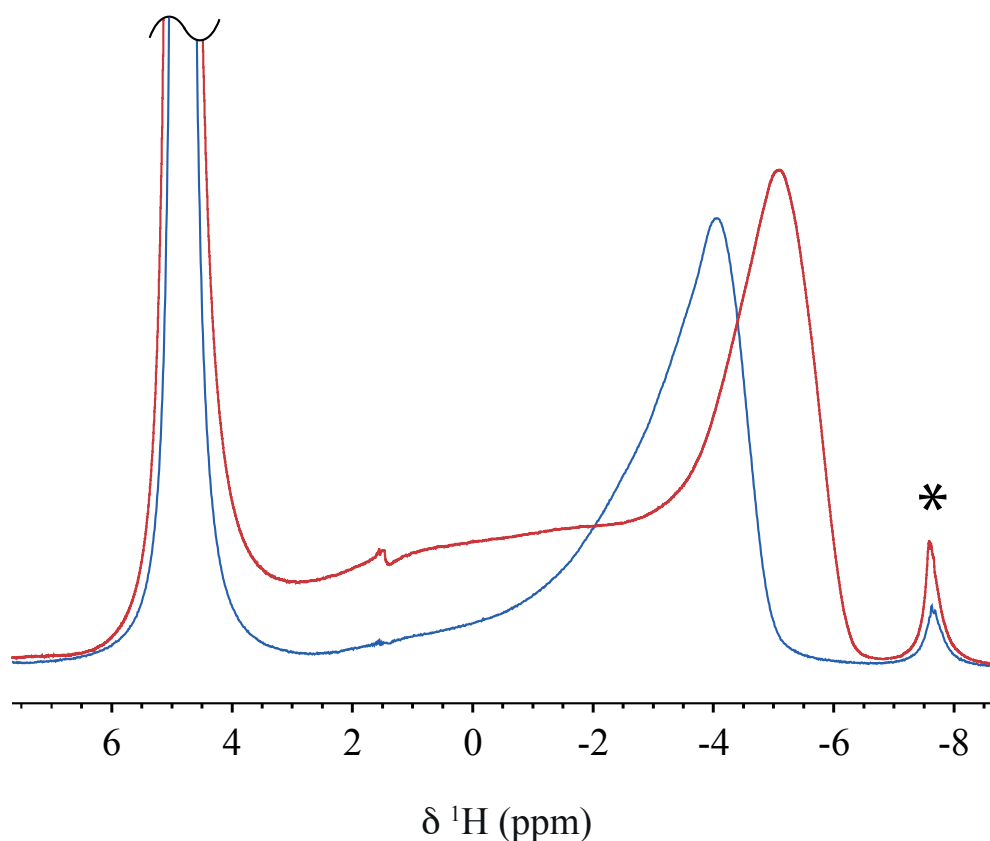


Figure 4.20: ^1H NMR of water-saturated KOH_28 (blue) and KOH_28_C33 (red).

The NMR spectra of KOH_28 and KOH_28_C33, Figure 4.20, differ more than the previous recarbonized samples. KOH_28 shows one major relatively symmetric in-pore peak and a second very small in-pore peak as discussed with samples steamed at 700 °C. This peak is very small so only a very small proportion of big pores are effectively isolated, as opposed to the steam-activation where most of the big pores

created were found isolated from the small pores. The KOH-activation at 800 °C is somewhat less homogeneous than steam-activation at 900 °C, but more homogeneous than steam-activation at 700 °C. Similar to previous recarbonization experiments, the right in-pore peak is right-shifted, consistent with an increase of aromaticity in the smallest pores. This suggests that KOH activation also introduces metastable carbonaceous debris. The volume of big pores can be seen to increase significantly upon recarbonization. Similar to 700_32_C24 there is no clear peak but rather a flat plateau suggesting a wide distribution of local average pore sizes. Nevertheless, this is consistent with the GS data: big pores ranging between 3 and 6 nm were created during the recarbonization.

In summary to section 4.2, the porosity was manipulated in two ways. First by low-temperature steaming, which caused a loss of resolution ascribed to metastable low-molecular weight carbonaceous debris. The pore network was found to be developed inhomogeneously despite steam spreading in the whole material, which made it possible for the first time to assign intervals of the PSD to NMR peaks. Second, potassium intercalation despite not allowing to unequivocally observe lattice expansion, showed that bigger pores are created in close proximity to the small pores apart from a small proportion. KOH activated samples allowed to confirm the assignment of mesopores to peaks with small $\Delta\delta$, after another high temperature treatment in dry nitrogen.

4.3 Porosity Development in PDCs

In section 4.1 and 4.2 we have investigated the evolution of the structure of PDCs during steam activation at 900 °C and 700 °C, and, to a lesser extent, during KOH

and CO₂ activation. We have shown with TEM and XRD that these carbons are made of randomly oriented, distorted OD. In conjunction with Raman spectroscopy, we have seen that there is a less ordered fraction of material, and that upon steaming at high and low temperature alike, both domains are etched. GS results were discussed in depth to identify features that come from the sample and those that depend on the data treatment. We found that PDCs inherently possess a bimodal pore size distribution with a narrow population around 0.8 nm and a broad one between 1 and 2 nm. By comparing GS and NMR results of samples activated under different conditions, we gained insight into the macroscopic activation mechanism related to the structure of the pore network as a whole, and the microscopic activation mechanism related to the structure of individual pores.

4.3.1 Macroscopic Mechanism

We propose in Figure 4.21 a macroscopic picture of the activation mechanism. Starting from carbonized particles with a few micropores (grey circles), KOH activation creates more 0.8 nm pores (green circles) and 1 – 2 nm pores (blue), but also a third population of bigger pores around 3 nm (purple). NMR showed only one significant peak, meaning that most of the pore sizes are found within any one region of the particle, allowing adsorbed water to experience all environments on the ms NMR timescale, albeit a small volume of big pores are isolated from the bulk of the pore network. Therefore KOH activation is quite homogeneous throughout the particle. I attributed this to the fact that the salt melts at temperature much lower than the onset of reaction, allowing it to spread before being consumed.

Steam at 900 °C produces a similar result to CO₂ at a first glance, although differences can be expected on the length scale of the particle due to different diffusion coefficients of steam and CO₂. Both populations of pores are also etched in close

proximity. The gasification competes with the diffusion of steam, causing the surface of particles to be more activated than the centre, which is why small particles are necessary for a thorough activation.

Steam-activation at 700 °C is much slower and no region of the particles, however big, are left unaffected, meaning that the diffusion of steam is now faster relatively and no activation front exists. However we found that the pore network is still inhomogeneous because of the two in-pore peaks of NMR spectra: significant volumes of small pores are left with no quick access to big pores, suggesting that the big pores develop more sporadically at 700 °C. By activating ~ 200 µm big particles, we saw that the right in-pore peak did not shift even though it increased, which meant that exchange kinetics between the two pore populations were very slow. This allowed quantification of the volume of the big and small pores, which roughly matched the two populations observed by GS. In the range 24 % to 32 % BO, GS yielded one unique pore population, but recarbonization at 900 °C allowed to recover the two populations. We attributed these observations to temporarily distorted pores due to metastable defects such as small carbonaceous debris.

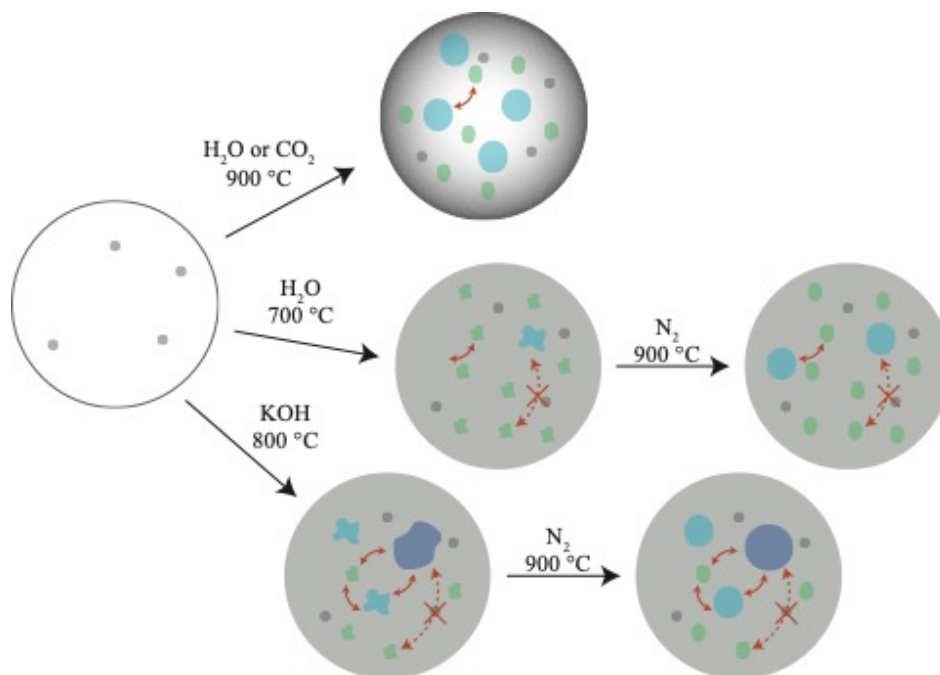


Figure 4.21: Macroscopic steam-activation mechanism of PDCs at 900 °C and 700 °C, and KOH-activation at 800 °C. The small grey circles are the micropores found before any activation, the coloured circles are the pores created during activation (green for ~ 0.8 nm, blue for 1 – 2 nm and purple for more than 3 nm pores, respectively), the red arrows represent exchange-averaging (continuous or dashed if taking place or not), the black colour gradient represents a gradient of activation along the particle radius.

4.3.2 Microscopic Porosity Development

On a microscopic length scale of a few nanometres, the activation mechanism is best visualized by the means of a structure model. We propose the following model, partly adapted from existing models such as proposed by Jenkins *et al.*^[28] with additional details derived from the experimental evidence presented above. It is reasonable to consider that PDCs consist of few-layers distorted OD, schematically depicted as parallel lines within grey areas in Figure 4.22. Before activation, the absence of the broad 1 – 2 nm pore population means that the inter-OD gaps are filled. We propose that the filler is the less graphitic material seen by Raman, depicted here as

bundles of entangled lines. However a few well-defined pores of size 0.6 nm, 0.7 nm, 0.8 nm and 1 nm (grey circles) are systematically seen, of which some are still resolved after activation. This gives an overall picture that agrees very well for example with the model of Kercher and Nagle but for the defects in the sheets.^[18]

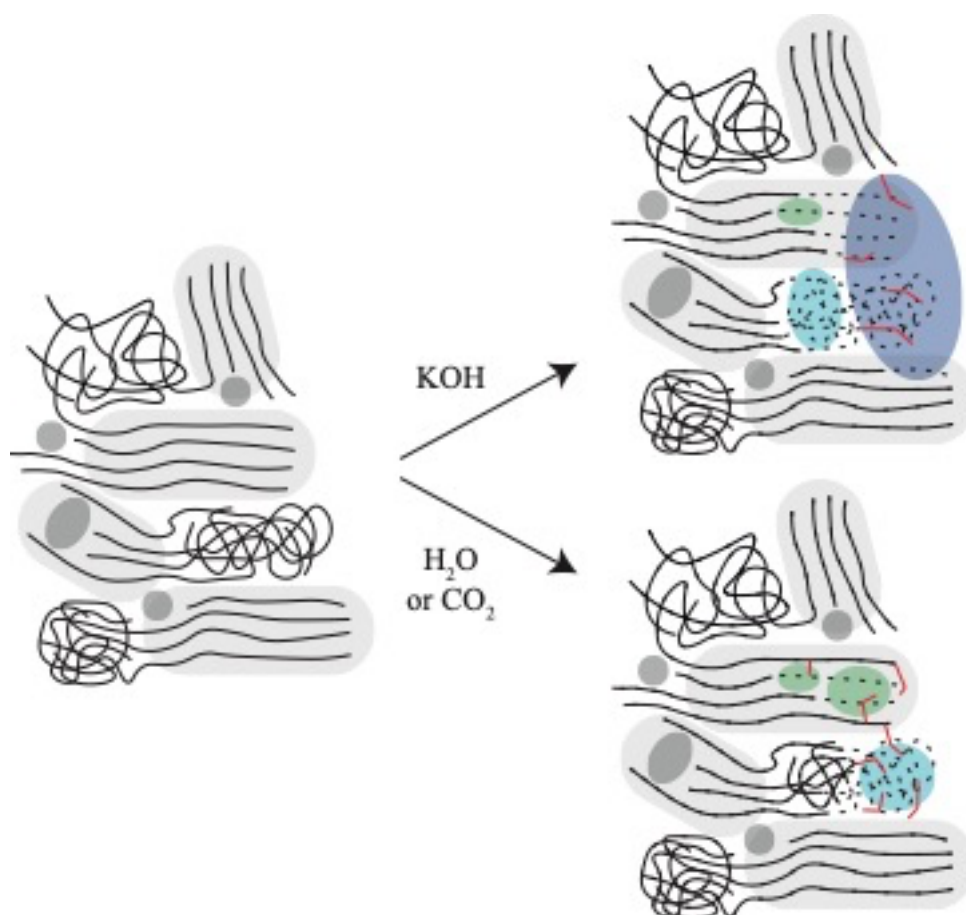


Figure 4.22: Microscopic steam-activation mechanism of PDCs at 900 °C and at 700 °C and KOH-activation mechanism. The continuous and dashed black lines represent sp² domains before and after being etched, the light grey areas are the OD, the dark grey circles are micropores present before activation, the coloured circles are the pores created during activation (green for subnanometre pores, blue and purple for 2 – 3 nm and more than 3 nm pores, respectively). The red lines are small metastable activation debris.

We showed with NMR that the steam activation step creates two populations of pores: small pores similar to those found initially (green), and more variable bigger pores (blue). This means that the small pores have quantized sizes, suggesting that they are located in OD and result from the etching of individual sheets. Because 1 nm pores are seen before activation, we propose that these pores be also located in OD and originate from etching of two adjacent sheets. This implies that the broad 1 – 2 nm pore population seen in PSD is the sum of two subpopulations, the 1 nm intra-OD pores (green) and the more variable inter-OD pores (blue). The gasification debris (red lines) that cause the pore populations to merge are quickly removed during 900 °C steaming, but less so at 700 °C allowing them to accumulate. Although not incorporated into gas adsorption data treatment softwares yet, perhaps the second generation of etched pores kernels developed by Lucena *et al.* could directly show the presence and removal of debris.^[139]

Steam and CO₂ molecules give very few big mesopores. We attribute this difference to the competition between the kinetics of diffusion and reaction with carbon. The presence of an activation front at 900 °C tells us that the gaseous oxidising agents diffuse in limiting stoichiometry into the pore network by being consumed after diffusing through the pore network. Therefore the next gas molecule to enter the pores can access the most reactive site. Indeed the work of Xing *et al.*^[40] suggests that the etching of sheets is self-catalysed due to the introduction of a defect upon etching of one carbon atom. This means that steam and carbon dioxide tend to create narrower but deeper pores. Although at 700 °C it would seem that the steam/carbon stoichiometry is different, no major difference was seen in that regard. Perhaps the same active sites are preferentially etched up to temperatures much higher than 900 °C.

On the other hand, the oxidizing agents derived from KOH can create pores bigger than 2 nm (purple), which could happen for example when an OD and neighboring DD are etched across the whole width. This could be due to a) larger volumes etched simultaneously, suggesting that the oxidising species are well spread throughout the whole particle before the onset of the reaction and that the reaction is faster than the diffusion, or b) that the reaction is less selective of the active site and proceeds more randomly than steam activation. Note that the lattice expansion due to intercalation alone cannot explain the appearance of such big pores, because the interlayer distance increases only by a few Å, so a higher number of adjacent sheets must be etched. In the case of KOH activation, debris were drawn in the purple pores because recarbonization affected this population, but not in the small pores because the two distinct pore populations were not restored, indicating that there are likely other sorts of defects.

As mentioned before, the small pores have been attributed to missing portions of sheets within OD. In addition, the big pores may be located between OD, *i.e.* in the DD, therefore acting as the channels in this pore network, in agreement with Scanning Tunnelling Microscopy studies that concluded that the microdomains are too small to accommodate pores bigger than 1 nm^[140]. Less well defined inter-OD pores are consistent with a random packing of the OD. Furthermore, the absence of broad 1 – 2 nm pores in the non-activated sample (see Figure 4.6) would mean the inter-OD space must be initially filled with matter, such as for example the more disordered material observed by Raman. However the overall absence of pores bigger than a few nm means that the packing is rather dense with no large DD, with the OD acting as barriers to the propagation of such pores.

4.4 Conclusion to Chapter 4

The structure and activation mechanism from the point of view of the pores and the whole pore network were investigated in the case of PDC using a combination of XRD, TEM, Raman, GS and NMR. GS results were discussed in depth to differentiate data treatment artefacts from true pore properties. We were able to identify several distinct pore populations within the apparent bimodal distribution thanks to samples prepared under various conditions. The low-temperature steam activation procedure was found to produce metastable structures that modify the apparent porosity, while creating inhomogeneous pore networks within particles.

5 Alkali Ion Adsorption Properties

The previous chapter showed that several pore sizes can be etched with steam. It is known in the literature that the adsorption of ions depends on the pore size. While NMR is the only technique as used herein that is able to probe the behavior of adsorbed species, the contribution of each individual pore size cannot be identified easily. For this reason, samples with homogeneous pore networks are used to compare the average behavior of alkali ions and extract general trends that can be related to ionic properties.

5.1 Comparison of Alkali Ions

5.1.1 Effect of BO

One of the advantages of using alkali metal chloride electrolytes as a model system is that all the stable cationic nuclei in this group except potassium are readily observable by NMR spectroscopy, allowing a systematic comparison. Figure 5.1 shows ^7Li , ^{23}Na , ^{87}Rb and ^{133}Cs MAS NMR spectra of PDCs with burn-offs in the range 0 – 58 % saturated with the corresponding aqueous alkali metal chloride solution at 1 M concentration. For all cations, no in-pore resonances are observed for PDCs with 0 % burn-off. This suggests that although the inherent porosity in the carbonised material is accessible to H_2O molecules (Figure 5.1a), the cations are too large to enter in a hydrated or partially hydrated state.

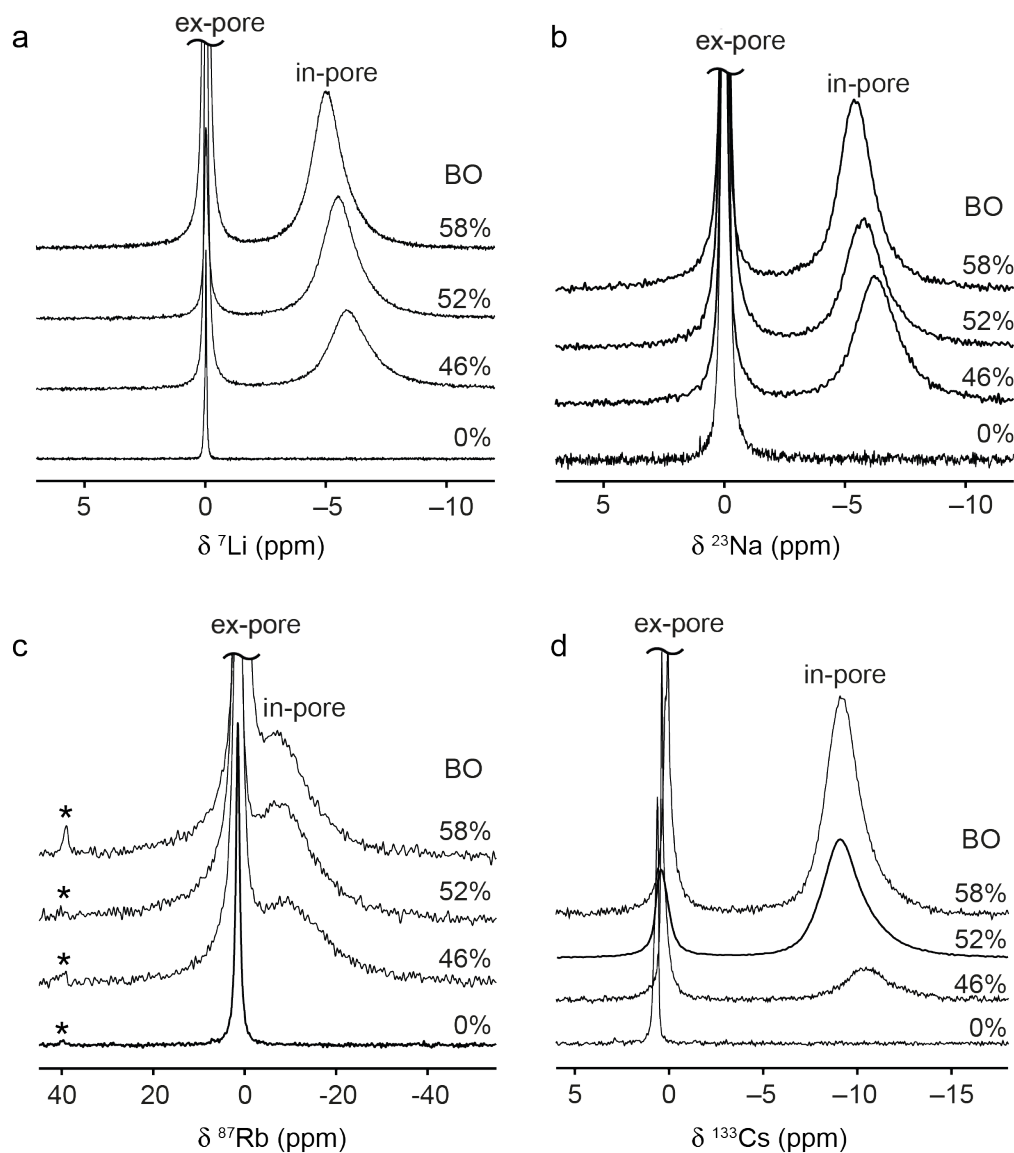


Figure 5.1: MAS NMR spectra of PDC samples steamed at 900 °C and saturated with 1 M aqueous solutions of (a) LiCl, (b) NaCl, (c) RbCl and (d) CsCl.

5.1.2 Concentration Dependence of ^{133}Cs Chemical Shifts

We note that for ^{133}Cs , the chemical shift of the ex-pore resonance for the PDC with 0 % burn-off differs by approximately 0.8 ppm compared to the other salt solutions. This is attributed to the strong concentration dependence of the ^{133}Cs chemical shift which is well known.^[133,134] For this sample, the selective adsorption of H_2O molecules increases the ex-pore concentration and shifts the ^{133}Cs resonance to

higher chemical shift. To extract the average perceived pore size from the ring-current shift, it is necessary to correct ^{133}Cs chemical shifts. This also allows to determine the concentration of the ex-pore species. The origin of the concentration dependence is complex, therefore, the calibration was performed empirically by recording the chemical shifts of neat CsCl solutions as a function of the concentration, ranging from 2 M to 0.01 M, which was expected to cover the effective concentration in the porous carbons. A very good fit was obtained with a polynomial equation, even though the obtained parameters cannot be related to physical parameters, see Figure 5.2.

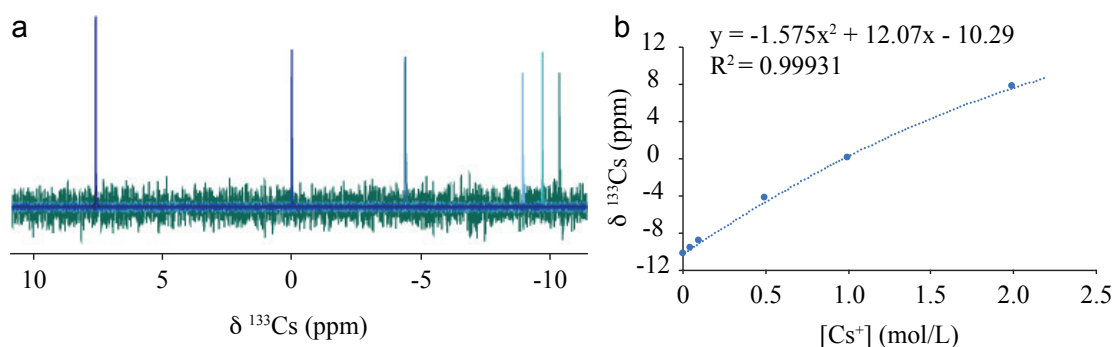


Figure 5.2: (a) ^{133}Cs NMR spectra of neat $\text{CsCl}_{(\text{aq})}$ solutions of concentrations 2 M, 1 M, 0.5 M, 0.1 M, 0.05 M and 0.01 M and (b) ^{133}Cs chemical shift as a function of concentration with fitted second degree polynomial curve.

To account for the concentration shift in the calculation of the NICS in PDCs, the average in-pore concentration (or more precisely molality) of caesium was determined from the ratio of the in-pore resonance integrals in the ^1H and ^{133}Cs NMR spectra. Using the calibration curve, the additional shift due to the in-pore concentration was then subtracted from the in-pore chemical shift to give the concentration-corrected ring-current shift. As a check, the ex-pore concentration was also determined in the same way from the ratio of ^1H and ^{133}Cs resonance integrals, and the total concentration

of the sample was found to be close to the concentration of the injected electrolyte. Based on the calibration curve, the 0.8 ppm shift corresponds to the ex-pore solution having a concentration of 1.1 M. This compares to 1.3 M as determined from the ratio of in-pore and ex-pore ^1H resonance integrals for the same sample. It is possible that the small discrepancy between these values is due to a small proportion of the Cs^+ ions becoming immobilised upon entry to the pores (due the very small pore width in this sample), in which case these would not be observed due to considerable quadrupolar and chemical shift anisotropy broadening. In this case the ex-pore concentration would be overestimated by the integral method. Another possible cause for the small discrepancy could be an additional minor contribution to the $\Delta\delta$, namely polarizability-dependent pore-ion interactions. This is worth considering because it could also explain the differences between the ions: the bigger the ion the more polarisable the electronic cloud. Unfortunately no data is available to quantify this effect on Cs^+ . It would be interesting to compare this contribution with Rb^+ but for that the concentration-dependence of its chemical shift should first be probed as well: if it does not depend on the concentration, then there is definitely an argument supporting an additional cause for the bigger $\Delta\delta$ of Rb^+ , otherwise it comes down to comparing poorly quantified values.

5.1.3 Specific Ion Effects

For the steam-activated PDCs, in-pore resonances are observed for each salt solution, with $\Delta\delta$ that decrease with increasing burn-off. Since only a single in-pore resonance is observed for each system, this shows that (like the H_2O molecules) the in-pore cations also undergo fast exchange between the different micropore environments, and the $\Delta\delta$ is a reflection of the exchange-averaged pore size. We note that in the ^{87}Rb

MAS NMR spectra much larger in-pore linewidths are observed, which extend far outside the typical NICS range. In this case, rather than relating to the structure of the carbon or cation behaviour, the large linewidth is attributed to fast quadrupolar relaxation due to the large quadrupole moment of this nucleus.^[143]

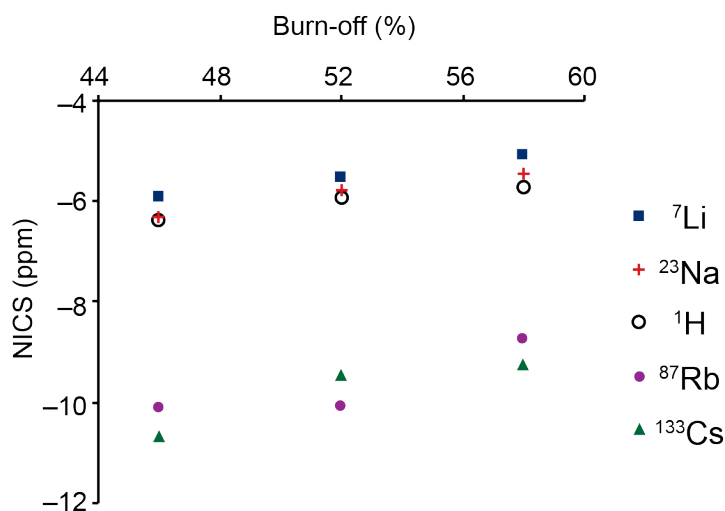


Figure 5.3: Plot of NICS as a function of burn-off for saturated PDC samples steamed at 900 °C. NICSs for cationic species were obtained from MAS NMR measurements on PDCs saturated with the corresponding 1 M aqueous chloride solution while the ¹H NICS values were obtained from PDC samples soaked with deionised H₂O.

In previous work on the adsorption of aqueous NaBF₄ in PDCs, similar $\Delta\delta$ were observed for all adsorbed species within a particular type of PDC.^[136,137] However, for the aqueous alkali metal chlorides, the $\Delta\delta$ differ significantly for the different cationic species. This is illustrated in Figure 5.3 which compares the $\Delta\delta$ observed for each nucleus with that of pure H₂O in each of the steam-activated PDCs. Compared to ¹H, the ²³Na and ⁷Li $\Delta\delta$ are slightly smaller for each burn-off value whereas the ⁸⁷Rb and ¹³³Cs $\Delta\delta$ are markedly larger by 4 – 5 ppm. Since all experiments were performed using PDCs with similar ~100 μm particle sizes, it is unlikely that the larger $\Delta\delta$ of ⁸⁷Rb and

^{133}Cs is related to in-pore – ex-pore exchange phenomena. Furthermore, the build-up experiment and exchange spectra in the previous section confirm that the ^1H $\Delta\delta$ is not significantly affected by exchange. If for some reason Rb^+ and Cs^+ had dramatically different exchange properties, the $\Delta\delta$ for these nuclei should be reduced rather than increased.

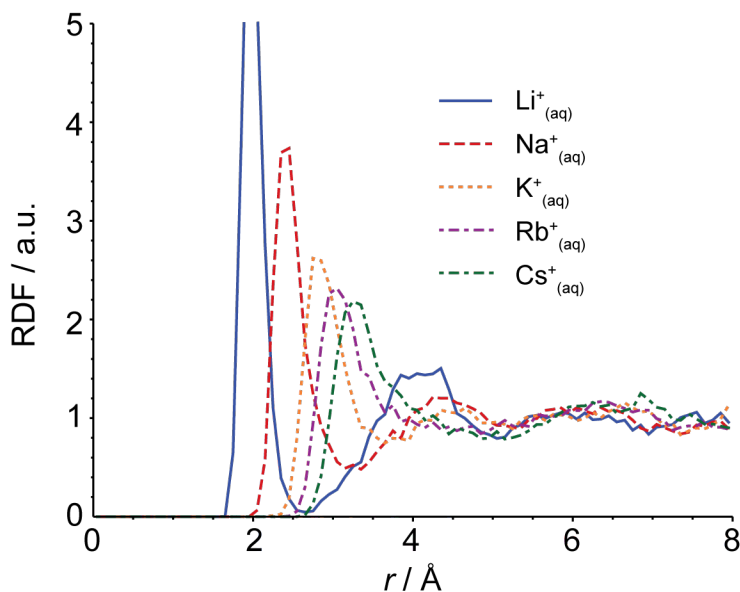


Figure 5.4: Radial distribution functions averaged over 17.5 ps *ab initio* molecular dynamics simulations for alkali metal ions in aqueous solution.

Therefore, to help rationalise the $\Delta\delta$ differences, a collaborator performed molecular dynamics simulations to estimate effective hydrated diameters for the alkali metal cations in aqueous solution. K^+ was included in the simulations for completeness although the low sensitivity of this nucleus precluded its observation in the NMR experiments. Figure 5.4 shows radial distribution functions (RDFs) averaged over 17.5 ps for each simulation. For each cation there is clear evidence of a structured hydration shell as indicated by the maxima in the RDFs corresponding to cation - oxygen distances, with a trend in increasing radius from 2.0 Å for Li^+ to 3.2 Å for Cs^+ . However,

Li^+ and Na^+ also show strong evidence of a second hydration shell with additional maxima at approximately 4.0 and 4.5 Å, respectively. Therefore, while Rb^+ and Cs^+ have larger ionic radii, in terms of the effective hydrated ion size, Li^+ and Na^+ are the largest species. In contrast to the H_2O molecules which are free to exchange between all positions within the pore, the large and strongly bound hydration shells of Li^+ and Na^+ prevent direct contact with the pore walls meaning that on average these ions reside further from the carbon surface and therefore exhibit a reduced NICS. Conversely, the smaller hydration shells of Rb^+ and Cs^+ means they can more closely approach the carbon surface and experience enhanced NICS. In addition, the fact that Rb^+ and Cs^+ are much less strongly hydrated means they are more prone to distortion and partial dehydration as they approach pore walls. DFT calculations have shown that the removal of water molecules from the coordination shells of hydrated ions leads directly to a significant increase in chemical shielding by several ppm.^[66,138] Although the physical origin of this shift is different to the ring current-induced NICS, both effects result in a shift to high field in the NMR spectrum, and therefore combine to increase the $\Delta\delta$.

5.2 Concentration Effects

The comparison of NMR spectra for the different aqueous solutions reveals how specific ion effects can influence the shift of the in-pore species. However, NMR spectra recorded for PDCs saturated with solutions of different concentrations, shown in Figure 5.5, reveal an additional concentration dependence. As the concentration of the injected electrolyte is reduced from 1 M to 0.05 M, the $\Delta\delta$ reduces significantly by up to 4.9 ppm (for Cs there is an additional shift due to the concentration dependence of the chemical shift). Fulik *et al.* have reported similar effects for BF_4^- species in organic electrolytes adsorbed on microporous carbons.^[67] Although the origin of the

concentration effect was not conclusively determined, in the systems studied, exchange effects on the $\Delta\delta$ were shown to be significant. To test if the concentration dependence observed in the current work is related to exchange effects, ^{23}Na and ^1H MAS NMR spectra were recorded for a PDC sample before and after saturation with 1 M and 0.1 M NaCl. For 1 M NaCl (Figure 5.6a), the pre-saturation $\Delta\delta$ is -6.0 ppm and this reduces by 0.4 ppm upon saturation of the sample.

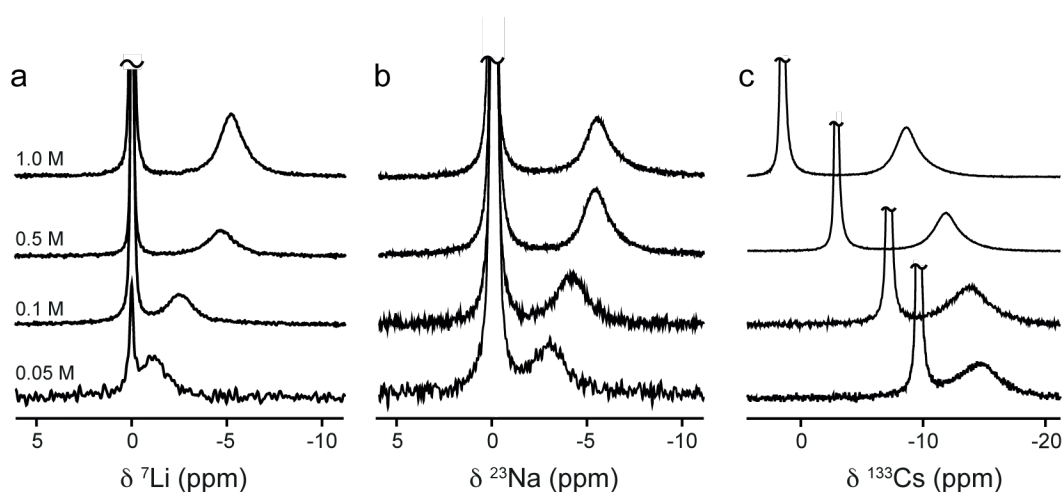


Figure 5.5: (a) ^7Li , (b) ^{23}Na and (c) ^{133}Cs MAS NMR spectra of 900_53 (a) and 900_56 (b and c) soaked with the corresponding chloride salt solution at concentrations between 0.05 – 1 M.

For 0.1 M NaCl, (Figure 5.6b) the $\Delta\delta$ reduces by a larger value of 1.65 ppm upon saturation. At first sight, this is consistent with exchange averaging of the NICS in the 0.1 M sample. However, it is important to note that ^1H MAS NMR spectra of the same samples (Figure 5.6c,d) show almost no change in the $\Delta\delta$ for both concentrations. Based on the exchange-averaging hypothesis, this would imply that the H_2O molecules are significantly less mobile than the Na^+ ions in the 0.1 M electrolyte. To quantify the relative mobilities of the Na^+ and H_2O species, NMR diffusion measurements were carried out on neat solutions. The diffusion coefficients, summarised in Table 3, show

that the average mobility of the H₂O molecules is approximately a factor of 4 higher than the cations in the same solution, so assuming exchange averaging alone, similar $\Delta\delta$ reductions should be observed for both species. Moreover, no difference in the Na⁺ diffusion coefficient is measured within experimental error between the 1 M and 0.1 M solutions. Although the ion mobility inside the micropores is expected to be lower than in the neat solution, similar exchange effects should be expected for both concentrations. These results suggest the concentration difference does not significantly affect the ion mobility, and therefore in-pore – ex-pore exchange averaging does not fully explain the observed reduction of the $\Delta\delta$ at low concentration.

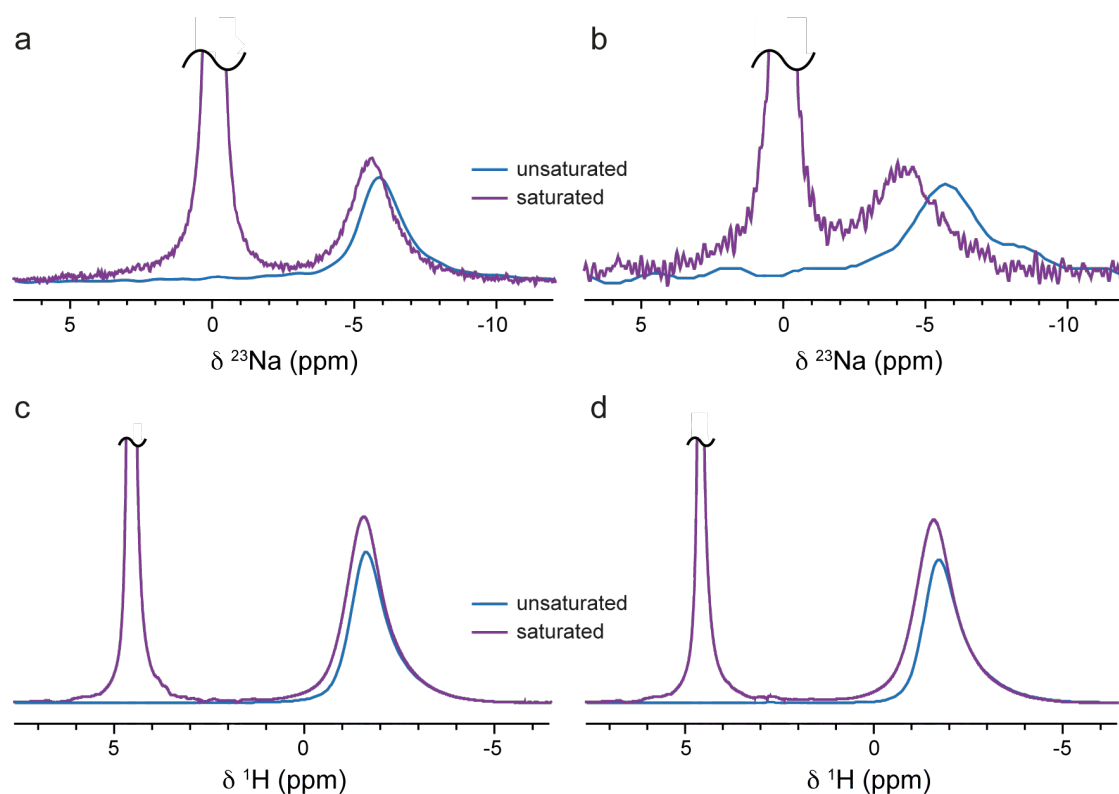


Figure 5.6: (a, b) ²³Na and (c, d) ¹H MAS NMR spectra of 900_53 loaded with (a, c) 1 M and (b, d) 0.1 M NaCl_(aq). Spectra are shown before saturation (blue line) and after saturation (purple line).

Table 3. Diffusion coefficients ($\text{m}^2 \text{s}^{-1}$) for H_2O and cationic species in aqueous salt solutions at 0.1 M and 1 M concentration.

[Na ⁺]	LiCl		NaCl		CsCl	
mol/L	$D(\text{H}_2\text{O})$	$D(\text{Li}^+)$	$D(\text{H}_2\text{O})$	$D(\text{Na}^+)$	$D(\text{H}_2\text{O})$	$D(\text{Cs}^+)$
0.1	2.28×10^{-9}	1.02×10^{-9}	2.30×10^{-9}	0.58×10^{-9}	2.30×10^{-9}	0.23×10^{-9}
1.0	2.06×10^{-9}	0.93×10^{-9}	2.17×10^{-9}	0.57×10^{-9}	2.40×10^{-9}	0.23×10^{-9}

5.3 Rationalising the Concentration-Dependent $\Delta\delta$

5.3.1 Pore Properties

An alternative explanation is that the NICS reduction arises from a redistribution of the in-pore ions within the porous network, with favoured occupancy of larger pores at low concentrations. This would cause the ions to reside further from the surface on average, resulting in a reduction in the NICS due to the distance dependence. Indeed, favoured occupancy of larger pores should be expected based on a number of theoretical studies that predict significant energy barriers (or positive adsorption energies) for the entry of hydrated ions to micropores.^[39,41–44,139] In these studies, the positive adsorption energy has been found to depend mainly upon the relative sizes of the pore and the hydrated ion. Therefore, in PDCs which contain a distribution of pore sizes there will be a distribution of adsorption energies, and at thermal equilibrium pores of different widths will be occupied according to Boltzmann statistics. The precise distribution of ions across different pore widths will depend upon the balance between the adsorption

energies for each pore and the chemical potential of the electrolyte ions. However, reducing the electrolyte concentration reduces the chemical potential of the ions, which should result in a redistribution of the ions between different pore sizes, with occupancy of larger pores becoming more favoured in order to minimise the total energy of the system. Since the $\Delta\delta$ corresponds to the average pore size that the ions explore, reduced occupation of smaller micropores and increased occupation of larger micropores should lead to a reduction in the $\Delta\delta$.

It is difficult to test this hypothesis directly as it is not possible to determine the local ion concentrations in pores of different widths due to fast exchange averaging between the different pore environments. However, insight can be gained from the average in-pore and ex-pore ion concentrations which are determined from the relative resonance intensities of cation and H₂O species in the NMR spectra. Based on the assumption of a positive adsorption energy, the average in-pore concentration is expected to be lower than the ex-pore concentration at thermal equilibrium. This is exactly what is observed in Figure 5.7 which shows the ratio of in-pore and ex-pore concentrations, C_{in}/C_{ex} , as a function of the neat electrolyte concentration in PDCs with low, intermediate and high burn-off. For all electrolytes, C_{in}/C_{ex} is lower than 1, showing that the average in-pore concentration is suppressed compared to the ex-pore electrolyte. Similar results were observed in previous work by Luo *et al.*, where in-pore Na⁺ concentrations in PDCs were reduced for a range of aqueous Na-based electrolytes.^[56] In that work, the in-pore cation concentration was found to be strongly affected by the nature of the anion. In the current work, the same chloride anion is used in all cases, and therefore differences in the in-pore cation concentration should reflect specific ion properties of the cations themselves. In general C_{in}/C_{ex} is highest for Cs⁺

(Figure 5.7a) which is the smallest ion with the greatest propensity for desolvation, intermediate for Li^+ (Figure 5.7b), and lowest for Na^+ (Figure 5.7c) which has the largest hydrated ion size and a strongly-held hydration shell. This is consistent with strongly solvated ions being energetically disfavoured from entering the porous network (or regions of it), while weakly solvated ions are able to fill the network to a higher level.

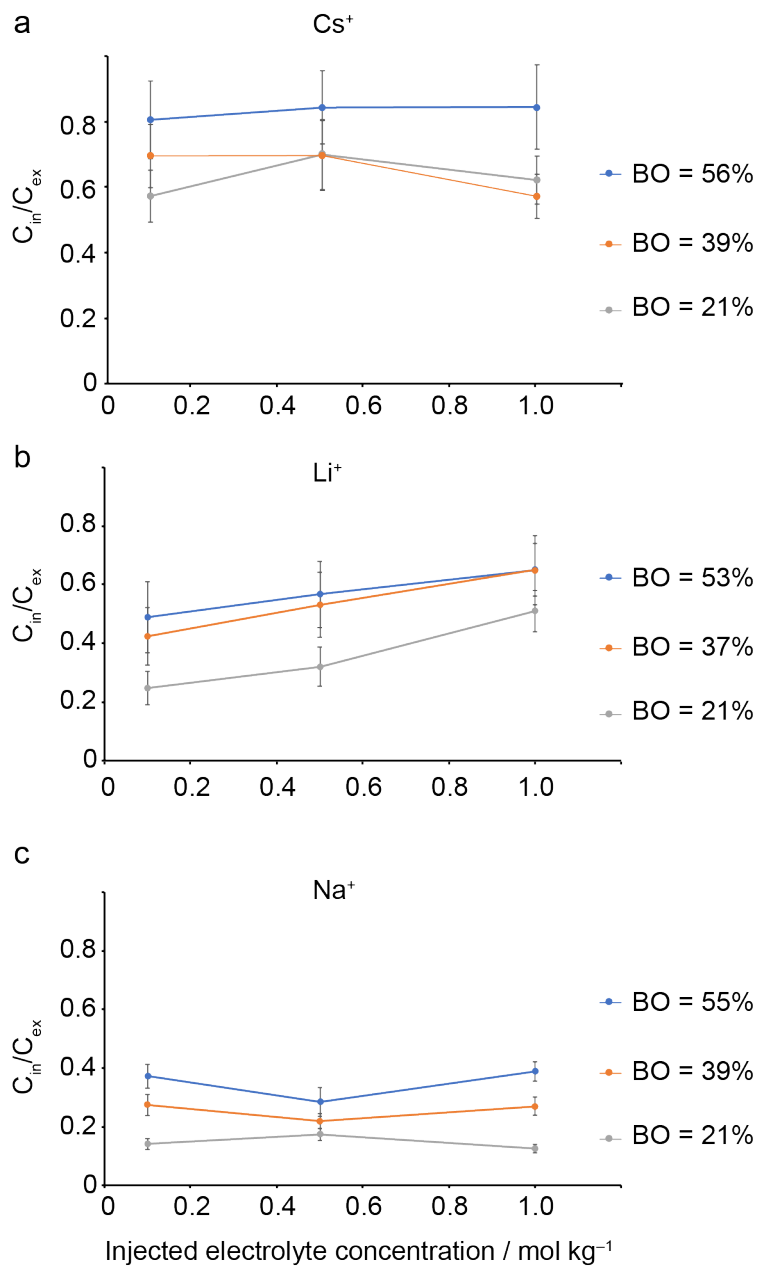


Figure 5.7: C_{in}/C_{ex} for (a) CsCl, (b) LiCl and (c) NaCl salt solutions as a function of injected electrolyte concentration and for PDCs with different BO values. Straight lines joining points are shown as a guide to the eye.

Additional insight can be obtained by comparing the C_{in}/C_{ex} values for each ion as a function of concentration. In Figure 5.7 C_{in}/C_{ex} remains approximately constant for Na^+ and Cs^+ and reduces slightly for Li^+ across the concentration range studied. This means that as the injected electrolyte concentration is reduced, the equilibrium in-pore concentration also reduces by a similar amount. The concomitant reduction in the in-pore ion population with the neat electrolyte concentration suggests that the in-pore population is largely dependent on the balance between the chemical potential of the ex-pore electrolyte ions and the positive adsorption energies of the pores in the PDC structure. As the concentration is reduced, the difference between the positive adsorption energy and the chemical potential of the electrolyte ions increases, forcing the ions out of the smallest pores and into the bulk electrolyte solution until a new balance is achieved.

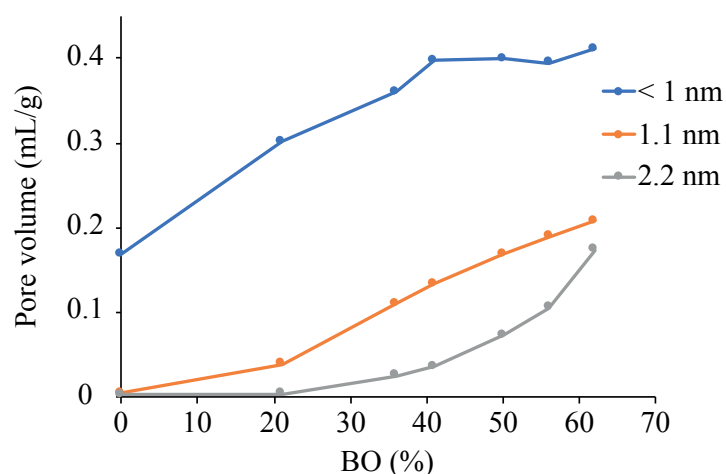


Figure 5.8: Pore volume of pores smaller than 1 nm (blue), around 1.1 nm (orange) and around 2.2 nm (grey) in samples of burn-offs in the range 0 % – 62 %.

It is possible to gain qualitative insight into the local adsorption energies associated with different pore sizes by comparing C_{in}/C_{ex} values for PDCs with different burn-offs. Figure 5.5 shows that in general for each of the cations studied, $C_{in/ex}$ increases with increasing burn-off. Based on the gas sorption data in Figure 4.6, a plot of the volume of each pore population versus the burn-off allows to assess how fast each pore is created, see Figure 5.8. PDCs with higher burn-off contain higher relative proportions of mesopores in the 2 – 3 nm range. The increase in $C_{in/ex}$ with burn-off therefore suggests that the introduction of a higher proportion of mesopores enables the porous network to accommodate higher concentrations of ions. This supports the expectation from theoretical studies that mesopores should provide lower energy adsorption sites than micropores, thereby allowing greater equalisation of the in-pore and ex-pore concentrations. This also further implies that reducing the total electrolyte concentration should result in a redistribution of the in-pore ions between the micropore and mesopore environments to minimise the total energy of the system.

5.3.2 Quantification

While it is not possible to obtain quantitative insight into the relative energetics of different pore sizes due to the high mobility of the ions inside the pores, it is possible to determine the energy difference associated with the average in-pore and ex-pore environments assuming occupancy of the two states according to the Boltzmann distribution using

$$5.1 \quad C_{in}/C_{ex} = e^{-\frac{\Delta G_{in-ex}}{k_B T}}$$

where $\Delta G_{\text{in-ex}}$ is the average free energy difference between the in-pore and ex-pore environments, k_B is the Boltzmann constant and T is the temperature. Using this simplified model, $\Delta G_{\text{in-ex}}$ at 298 K for 1M NaCl is found to be 5.1 kJ mol⁻¹ for PDC with 21 % burn-off, reducing to 2.2 kJ mol⁻¹ for 55 % burn-off. On the basis of MD simulations, Beckstein *et al.* have calculated significantly higher values of $\Delta G = 9 - 18$ kJ mol⁻¹ for the entry of hydrated Na⁺ ions to micropores between 1.1 – 2.0 nm in width.^[143] However, we note that the MD simulations were effectively carried out at infinite dilution, while $\Delta G_{\text{in-ex}}$ determined from the NMR measurements takes into account the chemical potentials of both in-pore and ex-pore environments. The non-zero concentration of the ex-pore electrolyte in the experimental system should significantly lower the energy difference between the in-pore and ex-pore environments. In addition, we note that the chemical potential of aqueous NaCl solution reduces by more than 10 kJ mol⁻¹ in the range 1 – 0.1 M.^[136,137] Since the predicted ΔG values for entry of hydrated Na⁺ to micropores are of comparable magnitude, it is highly feasible that changing the concentration over this range will lead to significant emptying of the smaller micropores in favour of lower energy adsorption sites in the larger micropores and mesopores.

5.3.3 Testing the Hypothesis

With samples steamed at 900 °C

The redistribution of ions within the porous network also explains the significant 1.65 ppm change in the ²³Na $\Delta\delta$ observed for the 0.1 M electrolyte upon saturation of the sample (Figure 5.6). Before saturation, the average in-pore concentration is forced to equal that of the neat electrolyte, and this will dictate the distribution of ions between large and small pores. However, after saturation, the system becomes free to redistribute

ions between the ex-pore and in-pore environments as well as within the porous network. Since the in-pore environment is energetically less favourable than the ex-pore environment, ions are expected to move from the in-pore to the ex-pore environment until the point where the energetic penalty of the increased ex-pore chemical potential balances the energetic gain from the redistribution of in-pore ions to favour occupancy of the mesopores. Based on the hypothesis that the redistribution of ions is driven by the higher adsorption energy in small pores, PDCs with a higher proportion of small pores should be expected to produce a more pronounced redistribution upon saturation and therefore larger $\Delta\delta$ reduction. To test this experimentally, the same saturation experiments, shown in Figure 5.9, were conducted in a sample with a smaller burn-off of 36 %, and hence a higher proportion of small pores relative to big pores.

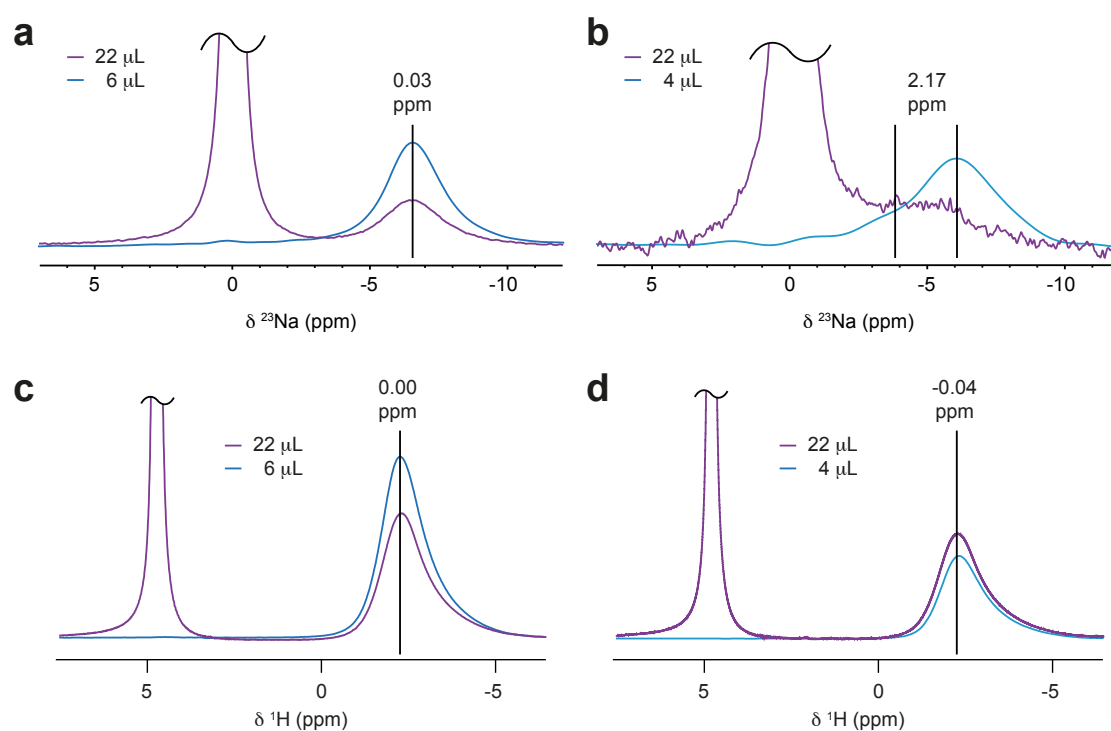


Figure 5.9: (a, b) ^{23}Na and (c, d) ^1H MAS NMR spectra of 900_36 loaded with (a, c) 1 M and (b, d) 0.1 M $\text{NaCl}_{(\text{aq})}$. Spectra are shown before saturation (blue line) and after saturation (purple line). The back vertical lines show the maxima of the peaks as determined by deconvolution.

The expected feature is observed: at 0.1 M (Figure 5.9b), the ^{23}Na $\Delta\delta$ reduction of 2.17 ppm is more pronounced than with the 53 % BO sample (which was 1.65 ppm), indicating that the average ion environment has changed to favour occupancy of larger pores. The ^1H NMR spectrum (Figure 5.9d) confirms with the constant $\Delta\delta$ that the diffusion of water has not increased in this sample, and suggests that the diffusion of Na^+ is also constant. Furthermore, the amount of adsorbed ions has decreased by 70 %, as calculated after deconvolution, while the amount of adsorbed water has slightly increased. This suggests that in addition to the redistribution towards bigger pores, a proportion of the sodium ions have desorbed and were replaced by water molecules. Interestingly, Figure 5.9a shows that at 1 M the $\Delta\delta$ of ions is constant but the adsorbed amount has decreased. This suggests that the average location of ions is unchanged, and therefore they must have desorbed equally from all pores. Figure 5.9c raises the question why the pores were not back-filled with water; one possible explanation is that the difference in chemical potential between ex-pore and in-pore environments for the ions is bigger than the adsorption energy of water. However, further experiments are required to validate this hypothesis.

With samples steamed at 700 °C

These samples have the particularity to show two distinct in-pore environments, corresponding to regions of a particle with different average pore sizes. As explained in Chapter 4, this unique feature originates from a slow steam-etching that is homogeneous over the whole particle. The pore network as obtained after carbonization of PEEK is thoroughly but mildly activated such that the volume of the smallest pores increases in

every point of space simultaneously, but the bigger 1 – 2 nm pores are created only sparsely. This results in scarce regions giving rise to a peak with $\Delta\delta \sim 3$ ppm surrounded by regions giving rise to a peak with $\Delta\delta \sim 8$ ppm. As a reminder, these yield average pore sizes of 2.3 nm and 1.0 nm respectively.

When such a sample is injected with a 1 M NaCl solution, two peaks are observed in the ^1H and ^{23}Na NMR spectra, and can therefore be integrated separately to extract the concentration in each environment. This is most visible before saturation is reached, as shown in Figure 5.10. Qualitatively it appears at one glance that the peaks have different relative intensities; the right peak is the most intense for water but it is the left one for sodium, suggesting that the concentration is higher in the big pores. Integration yields a concentrations ratio $[\text{Na}^+_{\text{small pores}}]/[\text{Na}^+_{\text{big pores}}] = 0.3$, which confirms that there are a lot more ions in the left environment. In other words this single experiment confirms the hypothesis that in a pore network made of distinct pore sizes there is a concentration gradient where the ions are more concentrated in big pores.

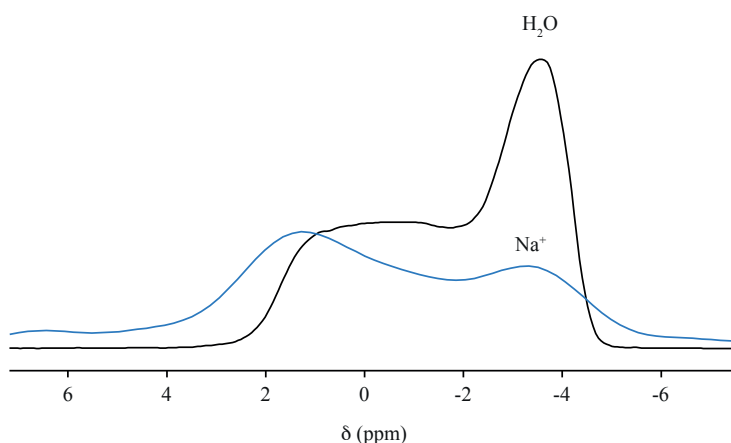


Figure 5.10: ^1H and ^{23}Na MAS NMR spectra of 700_68 loaded with 1 M NaCl.

5.4 Impact on Applications

One important consequence of the specific ion and concentration effects observed in this work is the potential influence on the charging mechanism in electrochemical double layer devices. Despite traditionally being assumed to function through ion adsorption, recent studies have shown that charge can be stored in microporous electrodes through at least three different mechanisms: counter-ion adsorption, ion exchange, and co-ion expulsion.^[38,47,135,136] The precise mechanism for a particular system is expected to be strongly influenced by the occupancy of the micropores in the absence of an applied potential. For pores that contain ions prior to charging, either of the three mechanisms is possible in principle, whereas pores that are initially empty can only charge through adsorption of counter-ions from the ex-pore electrolyte. Therefore, for large and strongly hydrated ions such as Na^+ which have a suppressed in-pore concentration prior to charging, counter-ion adsorption may be favoured over other charging mechanisms. Kondrat and Kornyshev have shown using mean-field theory that the existence of a superionic state during counter-ion adsorption in co-ion deficient nanopores can increase the differential capacitance up to the point where the pores reach saturation.^[61] This may help explain why Li- and Na-based aqueous electrolytes (which have a suppressed in-pore cation concentration at zero potential) show superior capacitance in aqueous supercapacitor devices.^[143] Furthermore, mean-field theory calculations and Monte Carlo have also shown that energy storage and charging dynamics can be increased if ions are thermodynamically disfavoured from entering the pores in the absence of an applied potential.^[45,46,140] Indeed, it has been shown that the use of so-called ionophobic pores (which are initially unfilled with ions prior to charging) can store energy more efficiently at high electrode polarisations and charge significantly faster. It may therefore be possible to tailor the

charging dynamics of supercapacitors by carefully controlling both the relative pore / ion size and concentration to maximise the suppression of the in-pore ion population in the absence of an applied potential, whilst still allowing electrosorption to occur when charging commences.

In addition to affecting the charge storage properties of supercapacitors, the zero-potential in-pore ion population may have important implications for the desalination efficiency of Capacitive DeIonization (CDI) devices. For Li^+ and Na^+ , the favoured counter-ion adsorption mechanism should be beneficial since the aim in CDI is to remove ions from the electrolyte solution. However, for Cs^+ , which is one of the main contaminants in nuclear waste effluents, the increased propensity for micropore filling prior to charging may favour ion exchange or co-ion expulsion. In principle, these charging mechanisms should result in no decrease or even an increase in the concentration of the bulk electrolyte since co-ions are ejected from the micropores during charging. Therefore in order to employ CDI for the treatment of water contaminated with nuclear waste may require careful design and optimisation of the micropore structure to minimise entry of the ions prior to charging.

5.5 Conclusion to Chapter 5

In this work we have performed a systematic study of aqueous electrolytes adsorbed on PDCs in the absence of an applied potential. Our experiments have provided fundamental insights into the factors affecting the NICS in these systems and highlight important effects that must be taken into account when studying these systems by NMR spectroscopy. We have found that careful control of the carbonisation and activation procedure is necessary to obtain homogenous PDC samples with evenly

activated particles. For homogeneously activated PDCs, the $\Delta\delta$ of H_2O , Li^+ or Na^+ follows the expected pore size dependence; however, comparison with different cationic and solvent species is less straightforward because the apparent NICS is also affected by differences in relative ion size and desolvation. We have also found that the $\Delta\delta$ for cationic species shows a dependence on the electrolyte concentration. This can be rationalised in terms of the thermodynamic redistribution of ions between pores of different sizes arising from the pore-size dependent energy barrier for pore entry in the absence of an applied potential, and links to the recently developed concept of pore ionophobicity^[55]. My results indicate that the PDC micropores are effectively ionophobic with respect to hydrated Li^+ and Na^+ ions, leading to expulsion from the smallest micropores at low electrolyte concentrations.

Overall this work highlights that a variety of factors can influence the apparent NICS of in-pore species and these effects must be carefully accounted for when using the $\Delta\delta$ to gain information about the carbon structure or ion behaviour. Furthermore, the information provided by $\Delta\delta$ measurements has potentially important implications for understanding ion behaviour and charging mechanisms in electrochemical devices.

6 Charging Using a New Ex-situ Method

6.1 Introduction

In this chapter I will demonstrate that a new setup for ex-situ NMR experiments of electrodes charged in a custom-made cell can offer reproducible electrochemistry and NMR measurements. In the previous chapter, the spontaneous ion adsorption in porous carbons was studied. It was shown that the pores spontaneously take up ions to significant concentrations, and that the equilibrium concentration depends on the pore size and on the species itself. The concentration of adsorbed ions decreases with pore size, and in general the alkali ion concentration decreases in the order $\text{Cs}^+ > \text{Li}^+ > \text{Na}^+$. In the context of supercapacitors, the initial distribution of ions in the pore network naturally has an impact on the charging mechanism. Before charging, ions are only weakly physisorbed in the pores with no particular structure, and diffuse fast within, between and out of the pores. During charging, the behavior of the electrolyte is not known in detail and depends on the electrolyte and on the carbon. To counterbalance the electric charges, the counter-ions should ultimately pack in a more ordered fashion onto the surface due to electrostatic adsorption, and the co-ions, *i.e.* ions with the same charge as the electrode, should yield the adsorption sites. However the ions are not necessarily able to diffusion freely to the most thermodynamically stable position in the

pore network. Steric hindrance and electrostatic effects can slow down the charging. The initial ordered packing of physisorbed ions onto the electrode surface is very fast because of the very short diffusion paths within the pores, however this process rapidly slows down as the physisorbed ions come from further and further away from the pore walls. If negatively charged pores contain an equal number of cations and anions, several mechanisms can lead to an excess of cations within the pores: anion expulsion, cation adsorption, or both simultaneously^[56]. If the pores were completely empty before deposition of negative electric charges, an excess of cations would be captured from the ex-pore solution. We can expect different charging kinetics for each mechanism due to, for example, the different diffusion coefficients of the species, or the ionic charge. The performance of supercapacitors and also capacitive water desalination processes depend on the charging mechanism: supercapacitors require quick charge and discharge cycles to achieve high output powers, but water desalination additionally aims at decreasing the ex-pore ionic strength^[47]. For this reason, the charging mechanism has been extensively studied with a variety of techniques in addition to NMR.^[143] For example infra-red spectroscopy can quantify each species during charging, but only in the ex-pore environment, while electrochemical quartz microbalance detects the resulting variation of the electrode mass due to ion and solvent adsorption/desorption alike.

Over the last decade, NMR was additionally employed to study the charging mechanism of activated carbon electrodes. In-situ charging NMR setups consist of a full electrochemical cell including carbon electrodes, separator and current collectors located in the probe. When studying only one electrode at a time, a key aspect of this approach is that one electrode should be shielded from the RF coil, *e.g.* with a copper foil^[75], or displaced outside of its magnetic field^[86], which introduces some biases with respect to true in-situ observations, for example regarding the charging kinetics of the

cell. A set potential, typically between a few hundred mV to a few V depending on the stability of the electrolyte solution, is then applied to the electrodes. The current measured typically decreases exponentially from the mA range to the μA range over a few seconds or minutes. The NMR spectra are recorded when the current has reached a stable and small value, while the potential is still maintained. A notable effect of charging carbon electrodes on the electrolyte's NMR spectra is a reduction of the NICS, because of the additional deshielding arising from the addition or removal of electrons from the carbon surface.^[137,141] Changes in the intensity of the in-pore resonances are also seen. The charging mechanism can be inferred from the variation of the in-pore resonance intensity, since this gives a quantitative measure of the ion populations under various applied potentials. For example in the case of $\text{NEt}_4^+ \text{BF}_4^-$ electrolyte solution in acetonitrile of concentration 0.5 M or 1.5 M, adsorbed in YP50F electrodes under potentials of ± 1.5 V, it was found that BF_4^- anions are not expelled under negative potentials, and that more are adsorbed under positive potentials, regardless of the concentration.^[56] However for other electrolytes such as $\text{NBu}_4^+ \text{BF}_4^-$ or lithium bis(trifluoromethane)sulfonimide, desorption of the anions was observed under negative potentials.

In many cases, the in-pore and ex-pore peaks overlap extensively in the absence of MAS, requiring a deconvolution of the spectra to extract the population of species in each environment. As we saw in previous chapters, this is the case in particles smaller than a few micrometres, giving rise to fast exchange kinetics between ex-pore and in-pore environments. Measurable diffusion kinetics, *i.e.* involving two environments that are not completely exchange-averaged, are another approach to gain insight into the charging mechanism. Forse *et al.* showed that the pore sizes of the material and the

electrolyte concentration have a direct impact of the diffusion coefficients of the species.^[86] For this reason it is all-the-more desirable to have resolved environments.

Ex-situ NMR of charged supercapacitors has been achieved to benefit from the increased resolution brought by MAS. Deschamps *et al.* charged carbon electrodes with $\text{NEt}_4^+ \text{BF}_4^-$ in acetonitrile and dried them before introducing them in MAS rotors.^[61] Note that they observed excellent stability of the charge state despite extensive manipulation, presumably because the ions are trapped in the pores in absence of ex-pore solvent. Using these carbon samples, both anions and cations were seen to be affected by positive and negative potentials, showing that the charging mechanism depends not only on the electrolyte composition but also on the carbon properties. Solvent molecules were also expelled out of the pores alongside the anions in the negative electrodes as more and more cations were adsorbed. On a similar note, YP50 electrodes charged with ionic liquids yielded again different charging mechanisms.^[150] Stable charge states were also observed without drying the electrodes. Other experimental tricks have been proposed by Forse *et al.*^[151] such as rotating the electrode by 90° inside the coil, which causes the peaks to shift due to susceptibility effects, resulting in an apparent increase in the $\Delta\delta$. $^{13}\text{C} \rightarrow ^1\text{H}$ CP MAS NMR of solvent adsorbed in a ^{13}C -enriched activated carbon sample has been used to filter out the ex-pore signal.

The main uncertainty associated with an ex-situ method is related to the possibility for the system to evolve between the opening of the circuit and the start of the NMR measurement. More specifically, the potential between the electrodes can vary. Various mechanisms for self-discharge have been extensively studied^[144-147] and will be investigated with the new setup to estimate the real state of the electrodes during NMR. This could be due to charges being consumed, also called a faradaic process such

as oxidation of the carbon surface or other components of the cell, but also to charge redistribution. In the charge redistribution mechanism, the ions diffuse from the quickly accessible pores where they piled up during charging, to less accessible pores. In this process, the potential drops because the electric charges in the carbon and the ions end up in closer vicinity. This process depends on the charging time because ions start filling the less accessible pores during the charging period, but not on the charging potential. Black and Andreas found in a similar carbon sample that to minimize the charge redistribution self-discharge, a many-hours hold time was necessary,^[156] even as long as 50 h.^[157]

The objective of this chapter is to show the applicability of a new design of cell for NMR measurements of carbon electrodes charged ex-situ. The design aims at facilitating the packing of the electrodes in MAS rotors by avoiding direct contact with the electrodes, as well as offering the possibility to use binder-free carbon electrodes. The self-discharge process was characterized as it is the main problem encountered with ex-situ experiments, while studying charging mechanisms themselves is left as a future project. A few standard electrochemistry experiments with aqueous NaCl were performed to compare the performance with the commercial Swagelok cell. Charging times between 20 s and 7200 s will be used, and the corresponding charge redistribution self-discharge rate constant determined. The faradaic self-discharge depends on the initial potential, so the electrodes will be charged at 0.4 V, 0.6 V, 0.8 V and 1.0 V, to identify the corresponding rate constant. Limitations and suggestions for improvement are also discussed at the end.

6.2 Swagelok Cell

6.2.1 Description of the Design

A standard device used to charge activated carbon electrodes is the Swagelok cell, named after the company which developed this leak-tight locking system to connect tubes. The tubes were simply replaced with solid metal cylinders to offer an electrically conducting support for the electrodes. Figure 6.1 shows the components of the Swagelok cell before and after assembly. The nut, body and ferrules are made of plastic and the current collectors are made of stainless steel. To prepare the cell for charging experiments, electrodes consisting of binder-free PDC particles are deposited on the current collectors, which are then inserted into the body through the ferrules. Electrolyte is added using a pipette and a filter paper separator is inserted between the electrodes to prevent direct contact. The nuts are then positioned and tightened, which allows to exert pressure on various components: the ferrules are pressed against the body and the current collectors to obtain a leak-tight junction, and the electrodes are pressed against the current collector which allows to have a constant contact. The leak-tightness and constant pressure on the electrodes are the two important features that contribute to the stability and reproducibility of the experiments. In addition, the relatively large ratio of contact area with current collector over thickness of the electrodes decreases the resistance of the electrode. Electrode masses up to several dozen of mg are typically used.

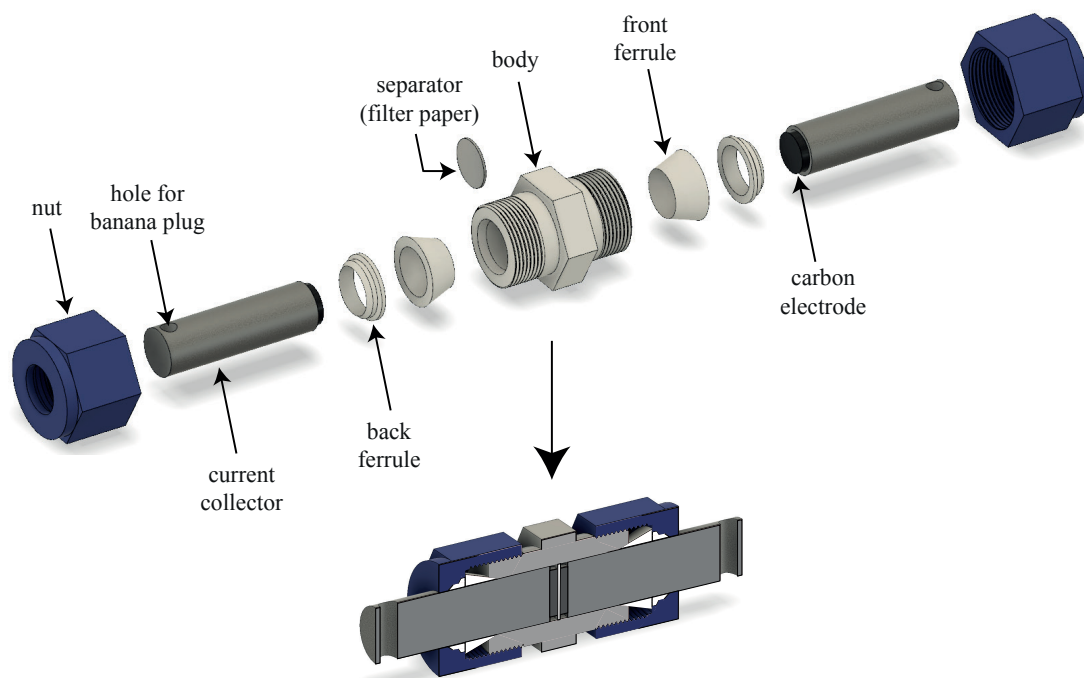


Figure 6.1: Components of the Swagelok cell before and after assembly for charging of carbon electrodes.

6.2.2 Results

In a first instance, simple Circular Voltammetry (CV) and Chrono-Amperometry (CA) measurements were done to verify that the binder-free electrode is indeed contacting the current collector and can be cycled normally. The results are shown in Figure 6.2. The CV experiment (top) is a measurement of the current under varying potential, typically swept linearly between two vertices, here 0 and 1 V, at a rate of 100 mV/s. In an ideal supercapacitor where charging is not limited by the diffusion of the ions, the curve is a rectangle. At very slow sweep rates, *e.g.* 0.1 mV/s, similar shapes can be obtained in real devices. To simply verify that the particles are being charged however, it was not necessary to sweep this slowly. The difference between the top and bottom halves of the CV curve indicates that the electrode is being charged.

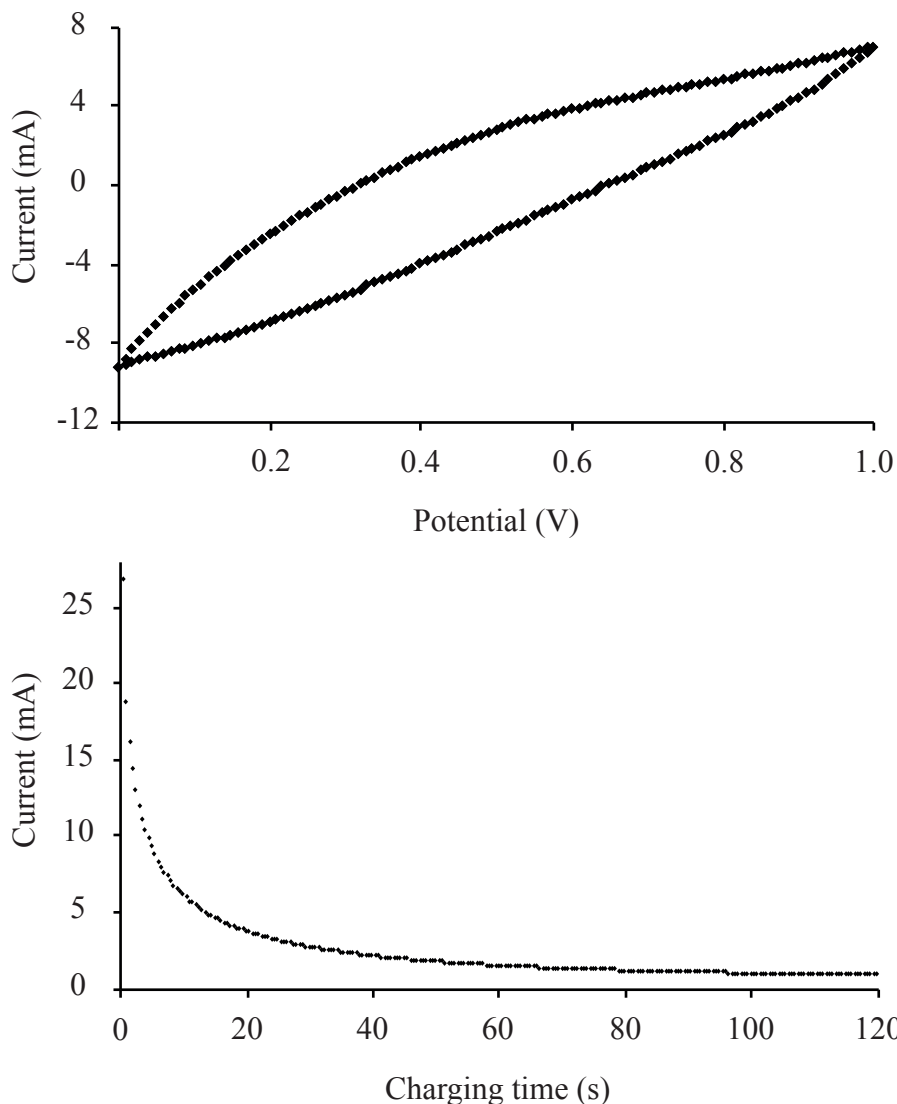


Figure 6.2: a) CV and b) CA experiments using PDC particles in a Swagelok cell.

The CA curve confirms it: starting from a neutral electrode, a potential of 1 V is applied for 120 s, while the flowing current is measured. The current flows only if the charges deposited on the carbon electrode are being screened by counter-ions coating the electrode surface. A strong initial current that is quickly decreasing is typical of carbon materials with tortuous pores where the charging is limited by the diffusion

of ions. The feature of interest in the CA is the asymptotic current, here 0.86 mA after 120 s. The current should tend towards zero, but the rate at which it decreases depends on the diffusion processes. An increasing current in any case indicates a faradaic consumption of electrons.

A comparison of the capacitance of these binder-free electrodes with binder-containing electrodes made with the same material is useful to further describe the charging efficiency. Indeed one problem than can occur when using big particles is that some particles are poorly connected to the circuit and may not be charged as fast. This can occur for example when a thin layer of water coats the particle. The specific capacitance in F/g can be calculated from the CA curve by integrating the area under the curve to yield the total number of charges and then dividing by the charging potential and by the mass. From the curve of Figure 6.2, *i.e.* for the Swagelok cell, this yields 30.8 F/g. When using electrodes made of YP50 with 5% w/w PTFE, the results is 40.9 F/g and 63.4 F/g with masses of 14 mg and 10 mg, which is significantly lower than the reported value of 93 F/g (same device, electrolyte and concentration)^[158]. This value was however obtained from an almost rectangular CV curve at a slow scan rate of 1 mV/s with 300 μm thick electrodes weighing about 14 mg, whereas in the present case the electrode was close to 1 mm thick for a similar mass. For the electrode in the new cell design shown below, the capacitance was 43.6 F/g, which is again lower than the reported value but comparable to the value in the Swagelok cell without binder. Therefore, the capacitances of PDC binder-free electrodes, in Swagelok cells and in the present cell design, compare quite well with optimized YP50 electrodes.

To briefly benchmark the self-discharge process (a more detailed discussion is provided later), the open-circuit potential decay after a charging period was measured during an interval of time and fitted with the rate constants shown in Table 4. These results are discussed later on in comparison with the values found using the new 3D printed cell.

Table 4: Self-discharge rate constants k_1 and k_2 (mV/s) with RMSE of the exponential fit of the last cycle.

Potential (V)	Time (s)	k_1 ($\times 10^{-1}$ mV/s)	k_2 ($\times 10^{-3}$ mV/s)	RMSE ($\times 10^{-3}$)
0.4	20	3.0	9.9	0.13
	120	0.7	0.9	0.21
1.0	20	3.3	3.9	0.88
	120	0.8	1.3	1.02

Subsequent NMR measurements of such binder-free electrodes is not very practical because the transfer of the sample into the NMR rotor involves extensive manipulation during which the particles come into contact with surfaces, or are eventually spilled. With free-standing electrodes the task is even more arduous as it is necessary to bend and push the electrode into the rotor. It is nearly impossible to reconstitute the electrode after NMR for further cycling.

6.3 New Design

6.3.1 Description of the Design

A new device was designed and 3D printed to facilitate the recording of NMR spectra under MAS condition. To keep the face-to-face geometry of the Swagelok cell,

it was necessary to charge the electrodes out of the NMR rotors and subsequently introduce them therein. Another important aspect coming with the use of carbon particles of 100 μm in diameter is that it is not possible to make free-standing electrodes, as the total surface area of the particles is too small for the PTFE binder to work. It was important to use such big particles to minimize exchange. The following prerequisites were identified: electrode mass > 5 mg for suitable NMR signal-to-noise ratio, high area/thickness ratio of electrode to minimize the resistance of the electrode, stable system during charging, *i.e.* pressure and wetting of electrodes, and last but not least, non-disturbing transfer of individual binder-free electrodes to the NMR spectrometer. Figure 6.3 shows the most recent generation of the device. The main innovation of the design is the packing of electrodes in a cylinder that can be inserted directly into the 7 mm MAS rotors, thereby allowing to transfer the electrodes without contact with the electrodes or current collectors. In the early stage of development, several aspects of the 3D printing process were investigated. Notably, the rigidity of the inserts depending on the wall thickness, the deviation of dimensions of printed components from the input dimensions, as well as the difference between the dimensions of male and female components that allow smooth assembly while minimizing the gaps. For example it was found that the outer diameter of the insert, set to 5.4 mm, matches well with the 6 mm inner diameter of the MAS rotors, whereas 5.3 mm would leave too much void space. In practice, the tolerance margins depend on the absolute dimensions of the parts so trial-and-error was found to be the best approach. To achieve a ratio area/thickness of the electrode comparable to the Swagelok setup, while maximizing the mass of carbon, a wide MAS rotor needed to be used, namely 7 mm. The 4 mm and 3.2 mm rotors were also used but no significantly-enhanced trade-off between electrode mass and dimensions, MAS rate and probe sensitivity was observed. Note, however, that the

corresponding MAS NMR probes do not necessarily cover the required range of Larmor frequencies. The 7 mm rotors are also easier to handle and the device components more durable. Despite threads being achievable in the 3D printer, high pressures on the electrodes easily damaged the components. Suitable results were finally simply obtained using rubber bands to immobilize and compress the current collectors. Because a leak-tight environment was not easily achieved without a high pressure, constant electrode wetting was maintained by the use of a “reservoir” of electrolyte solution contained in a relatively large piece of filter paper employed as additional separator, which can be flushed with fresh solution with no negative impact on the charging experiment.

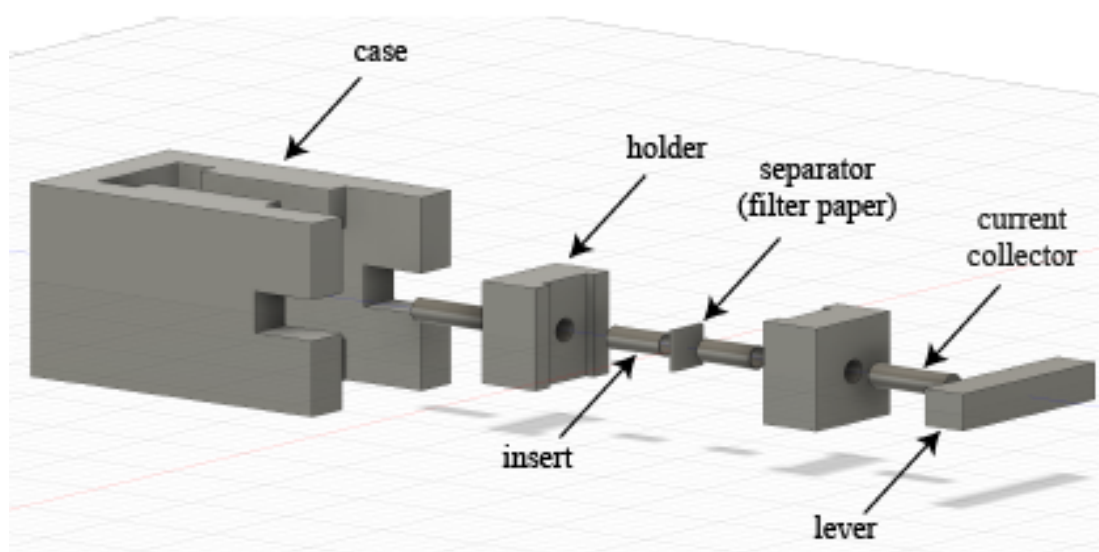


Figure 6.3: 3D printed components of the new design based on the Swagelok cell.

The setup is assembled as shown in Figure 6.4. After positioning the inserts in the holders, a pouch made of a 1 cm x 1 cm square piece of Celgard™ hydrophilic membrane is placed, ready to receive the electrode. The current collectors made of silver steel as defined by the British Standard BS-1407 are then introduced in the pouch

as to make contact with the electrode, and used to push the whole at the other extremity of the insert. A tight contact is obtained between the Celgard™ pouch and the current collector which prevents fine carbon particles to be dispersed. This allows to use binder-free carbon particles. The device is positioned in the case and pressure is applied on the current collectors by wrapping a rubber band around the case and the lever.

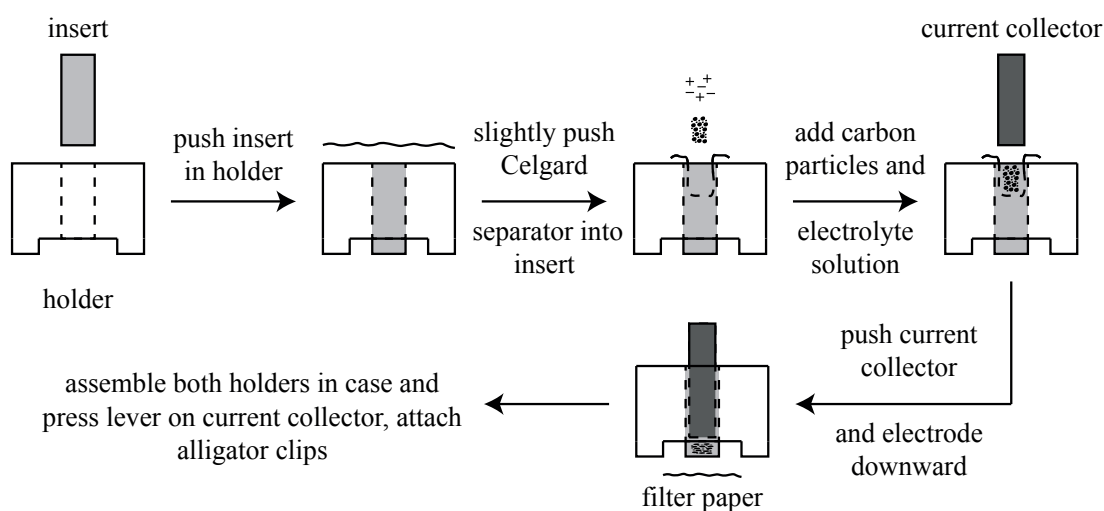


Figure 6.4: Steps for the assembly of the new device. The Celgard™ pouch is omitted in the last step for clarity.

The procedure to transfer the inserts into the 7 mm MAS rotors is shown in Figure 6.5. It is useful to record an NMR spectrum before charging, for reference, once the sample is packed in the insert, which also allows the MAS to pack more densely the particles and further increase the rigidity of the electrode. To do so, the current collector is removed with plastic tweezers, and the insert simply pushed further, out of the holder and directly into the rotor. In the 7 mm probe, it is necessary to put spacers to ensure the sample be located in the middle of the rotor otherwise no signal is detected. The Celgard™ pouch must be folded to avoid contact between the top spacer and the

electrode. After the measurement it can be unfolded and the current collector repositioned for the next charging experiment.

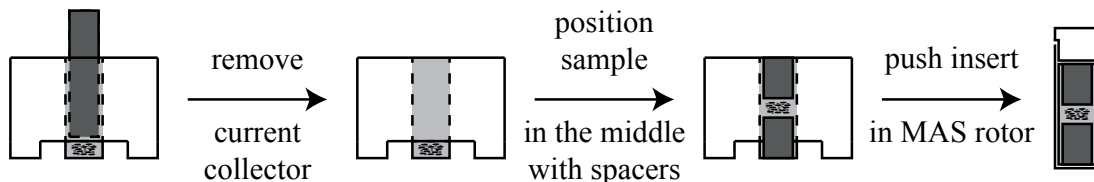


Figure 6.5: Procedure for the transfer of electrodes to MAS rotors. The Celgard™ pouch is omitted for clarity.

6.3.2 Self-discharge characterization

Charging time

To see how the charging time affects the self-discharge dynamics, the open-circuit potential decay was measured for 60 s after a charging step at 0.8 V of 20 s, 60 s, 120 s, 600 s, 1800 s or 7200 s. This is done by using the Mixed Mode of the Iviumstat program consisting of a chronoamperometry step followed by a chronopotentiometry step, as illustrated in Figure 6.6. It appeared that the main potential drop took place upon opening of the circuit, as low as 0.55 V for the shortest charging period. This effect is caused by the internal resistance of the cell, which depends on the ion concentration gradient as well as interfacial resistances between the various components of the cell. This could be easily reduced by repeating several charging/self-discharge cycles or allowing more time for the ions to diffuse, as shown in Figure 6.7.

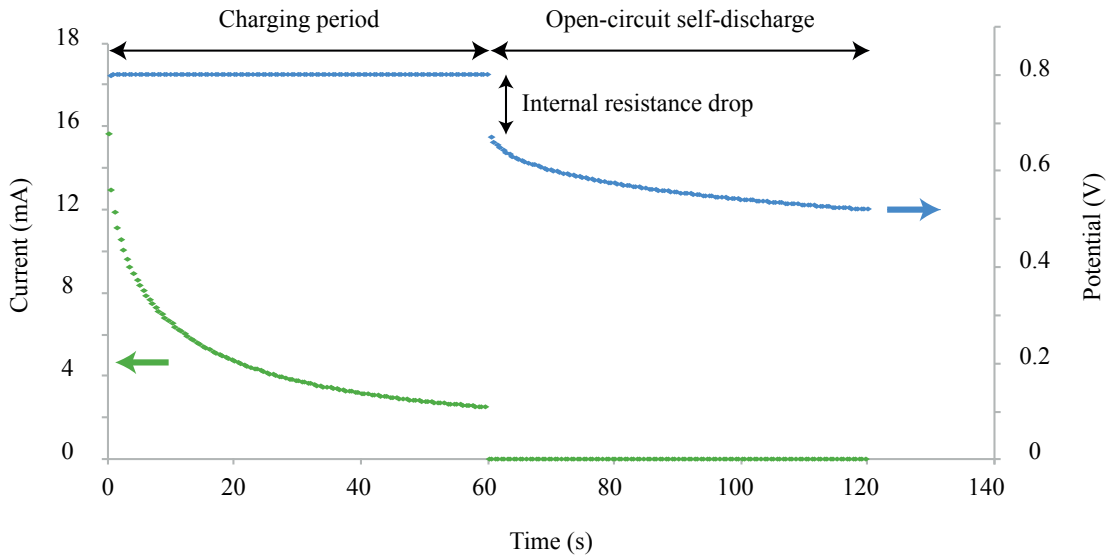


Figure 6.6: Example of charging/self-discharge measurement recorded in Mixed Mode.

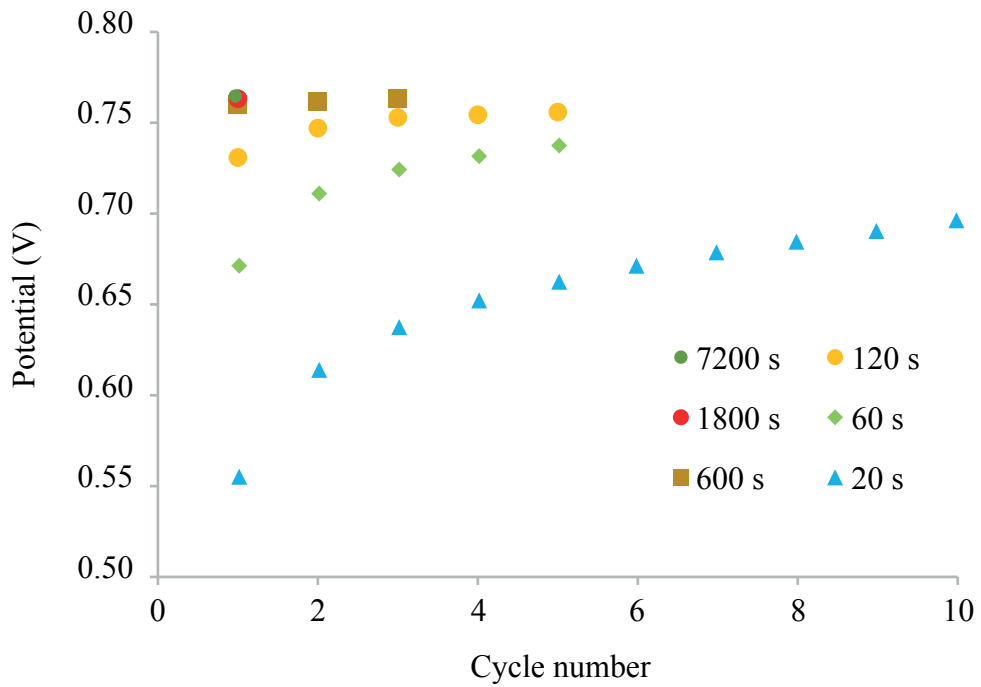


Figure 6.7: Initial open-circuit potential measurement for each charging time and cycle number.

The potential drop stabilizes around 0.04 V for charging times of 600 s and longer. The potential decay kinetics were then fitted using an exponential lineshape, with one or two rate constants (Eq. 6.1 and 6.2).

$$6.1 \quad V = A * e^{-k_1 t}$$

$$6.2 \quad V = A * e^{-k_1 t} + B * e^{-k_2 t}$$

Figure 6.8 shows the difference between the fit using Eq. 6.1 and Eq. 6.2. As can be seen, Eq. 6.1 fails at fitting the potential decay, but two rate constants provide a visibly good fit. The RMSE is also systematically reduced about ten-fold. The rate constants are compared in Figure 6.9. As can be seen, the general trend is decreasing, *i.e.* the self-discharge gets slower with longer charging times.

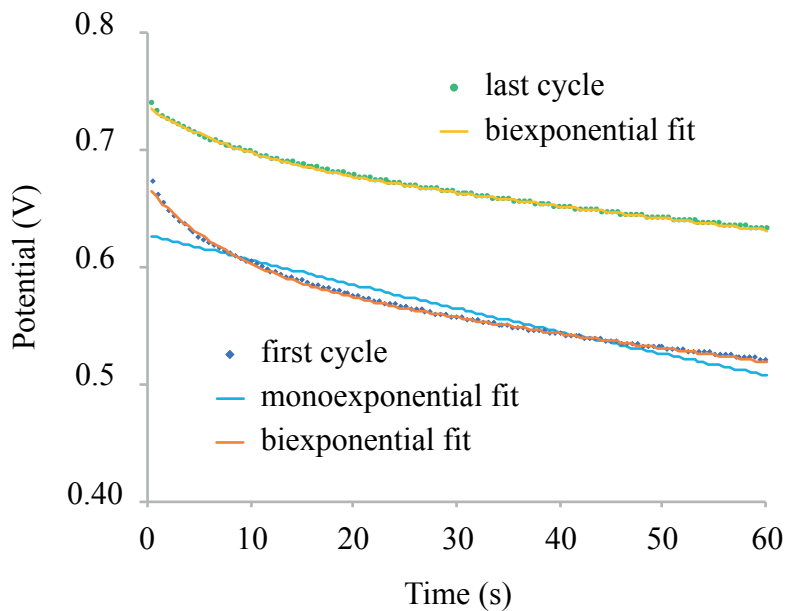


Figure 6.8: Fit of the potential decay using an exponential lineshape containing one or two rate constants.

The self-discharge was recorded for 60 s except for the two longest charging periods of 1800 and 7200 s, where it was recorded for 1800 s. In these two cases, it was noted that the RMSE was about ten-fold bigger than for the shorter charging periods. Additionally, the smallest rate constant did not follow the general decreasing trend across the charging times. For these reasons a third rate constant was added which provided a visibly better fit of the decay for short discharge times, RMSE comparable to the other fits, and a smooth trend. This observation suggests that the potential decay in fact follows a complex law and can be approximated by a biexponential only for short discharge times. At long discharge times slower phenomena taking place could also be comparable and more difficult to identify. For example, it is possible that the pore network comprises several bottlenecks and various geometries with their own charge redistribution rate constants.^[159]

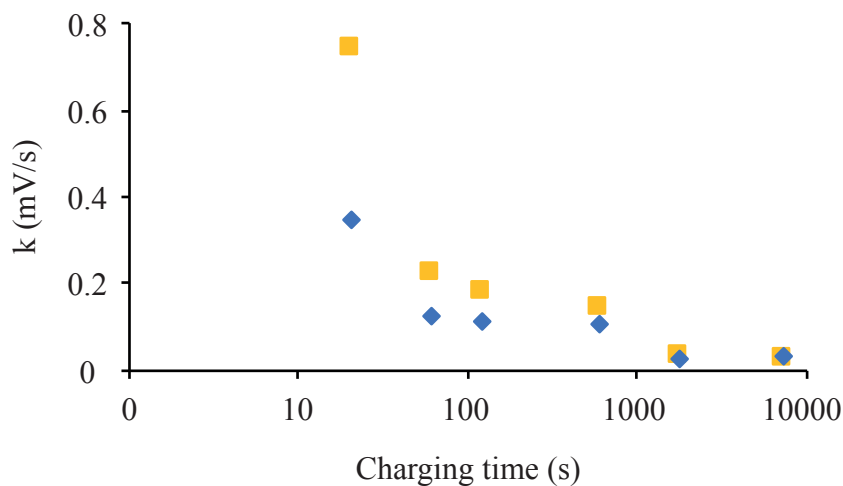


Figure 6.9: Self-discharge rate constants k_1 (blue diamonds) and k_2 (yellow squares) for charging times from 20 s to 7200 s at 0.8 V, in logarithmic scale. The k_2 constants are multiplied by 100 for clarity.

To discriminate faradaic from non-faradaic processes, the dependence of the decay with the charging potential is examined. Non-faradaic processes such as charge redistribution should not depend on the initial potential, unlike faradaic processes. Given the fitting difficulty for long charging times, only values up to 600 s were employed at other voltages.

Charging potential

To identify the mechanism behind the two major components of the decay, the self-discharge measurements were repeated after 20 s, 60 s, 120 s and 600 s of charging at 0.4 V, 0.6 V and 1.0 V. All rate constants and fit errors are given in Table 5, k_1 and k_2 are plotted in Figure 6.10 versus the charging potential. Overall, the k_1 rate constants (Figure 6.10top) are similar across the charging potentials, indicating that it corresponds to the charge redistribution mechanism. In addition, they are systematically about three times bigger after the 20 s charging period than for the longer periods. A possible interpretation is that a 20 s charging period is too short for ions to populate the least accessible pores, towards which a major proportion of all adsorbed ions diffuse towards. The fact that all cycles show a similar decay constant would indicate that 10 cycles is also insufficient to populate a significant portion of those pores.

For k_2 , Figure 6.10bottom, the values follow a clearly increasing trend with the potential, indicating that it reflects a faradaic process. It is not clear which exactly, but quite possibly corrosion of the current collector as some orange stains are often found on the separator after extensive cycling. In any case the values of k_2 are two orders of magnitude smaller than k_1 .

Table 5: Self-discharge rate constants k_1 and k_2 with RMSE of the exponential fit for all charging times at all potentials.

Potential (V)	Time (s)	first cycle			last cycle		
		k_1 ($\times 10^{-1}$ mV/s)	k_2 ($\times 10^{-3}$ mV/s)	RMSE ($\times 10^{-3}$)	k_1 ($\times 10^{-1}$ mV/s)	k_2 ($\times 10^{-3}$ mV/s)	RMSE ($\times 10^{-3}$)
0.4	20	3.0	7.7	0.63	3.1	1.8	0.14
	60	1.2	2.1	0.60	1.0	1.3	0.24
	120	1.1	1.4	0.29	1.2	1.0	0.15
	600	1.2	0.9	0.13	1.0	1.0	0.12
0.6	20	3.2	9.7	1.13	2.9	2.7	0.31
	60	1.3	2.0	1.17	1.3	1.3	0.45
	120	1.2	1.7	0.60	1.3	1.2	0.34
	600	1.3	1.2	0.29	1.0	1.1	0.27
0.8	20	3.4	7.4	0.98	3.3	3.7	0.52
	60	1.2	2.2	1.28	1.1	1.6	0.77
	120	1.1	1.8	0.81	1.1	1.4	0.53
	600	1.1	1.4	0.48	1.0	1.4	0.54
	1800	0.2	0.3	0.60	/	/	/
	7200	0.3	0.3	1.01	/	/	/
1.0	20	3.4	16.4	1.96	3.5	7.2	1.45
	60	1.4	3.4	2.74	1.5	2.4	2.34
	120	1.5	2.6	2.38	1.4	1.9	1.52
	600	1.4	1.9	1.48	0.8	1.9	1.11

In conclusion, effective charging of electrodes using this ex-situ setup can be done by repeating several cycles or by maintaining the charging potential for longer than 600 s. There are however other methods worth exploring involving a varying potential.

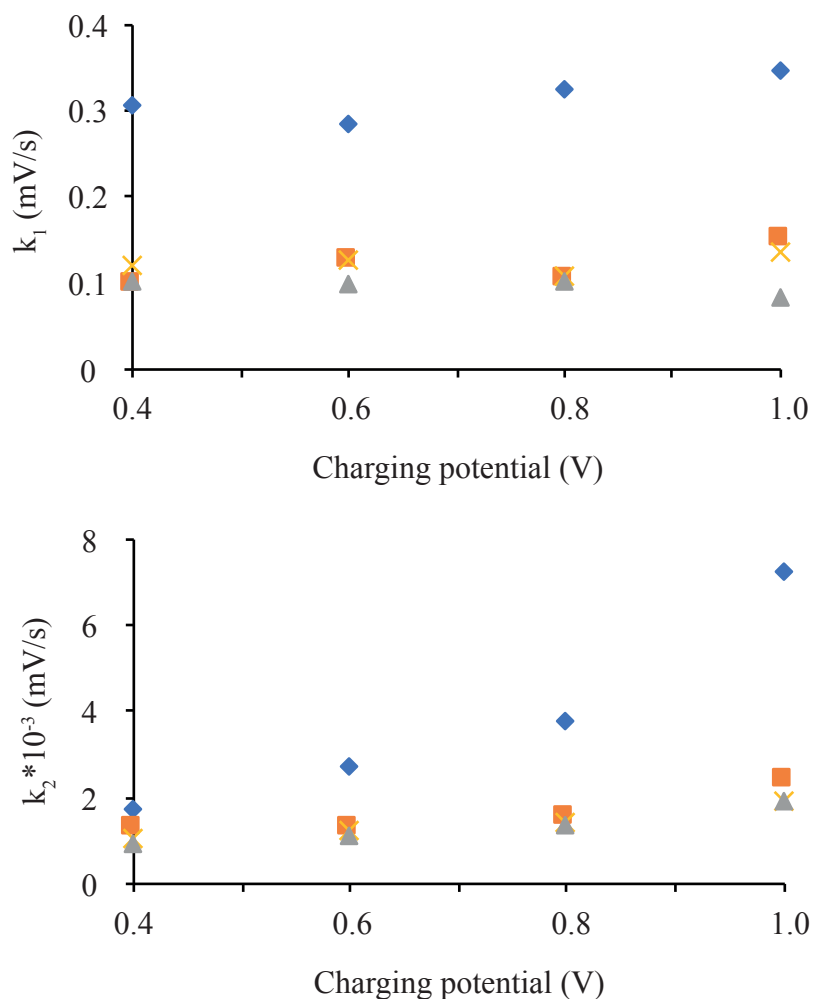


Figure 6.10: Rate constants k_1 (top) and k_2 (bottom) from the last cycle versus the charging potential for each charging time (blue for 20 s, red for 60 s, yellow for 120 s and grey for 600 s).

Comparing the self-discharge kinetics in the Swagelok cell (Table 4), it appears that the ion-diffusion self-discharge rate constants k_1 are very similar, decreasing from 0.3 to approximately 0.1 mV/s. The faradaic process self-discharge rate constants k_2 are also relatively similar, with values in the $\mu\text{V/s}$ range, except for the electrode charged at 0.4 V for 20 s, where it is 9.9 $\mu\text{V/s}$ compared to 1.8 $\mu\text{V/s}$. This significantly higher value is due to the HCl treatment done on the sample before the measurement in the Swagelok cell. In fact, after extensive cycling in the 3D printed cell, the sample turned

slightly orange due to the corrosion of the current collector, and its behavior during a preliminary cycling in the Swagelok cell was unusual in that the current did not reach a minimum during charging, but increased, indicating an extensive faradaic process. The sample was therefore washed in concentrated HCl, and then with water. The HCl solution turned slightly yellow, confirming the dissolution of traces of iron. It is not surprising that the very first subsequent charging shows a somewhat different behavior, because the chemistry of the carbon is altered. In conclusion, this comparison shows that the overall performance of the new cell is comparable to the Swagelok cell.

Dynamic charging

The term *dynamic charging* refers here to methods where the potential increases from 0 up to a maximum value over time. Such method has also been reported^[155] and a few options were therefore briefly compared with the static potential method. In method A, the potential is swept at 1 mV/s until 0.8 V are reached, which is the equivalent of half a CV cycle, and then the circuit is opened. A variation includes holding the potential at 0.8 V for 600 s before opening the circuit, method B. Finally in method C the cell is charged at a current of 1 mA/s, which is identical to the chronopotentiometry method used to record self-discharge but for the set current. The decays are fitted in the same way as earlier, the rate constants are given in Table 6. It emerges that method A, which took 600 s to reach 0.8 V, gives similar k_1 and k_2 values, as well as the potential value upon circuit opening, to the static potential method with a charging times of a mere 60 s. Therefore this method does not seem to come with any advantage despite the duration. Method B with an additional holding time of another 600 s provides no further improvement. Method C involved a similar charging time of 519 s and was remarkably similar in all three values. Therefore the static potential charging method is retained for the following ex-situ experiments.

Table 6: Rate constants for the open-circuit potential decay of methods A, B and C.

Method	k_1 (mV/s)	k_2 (mV/s)	initial potential
A	1.3E-01	2.0E-03	0.7405
B	9.7E-02	1.6E-03	0.7701
C	1.3E-01	2.0E-03	0.7460

6.3.3 Ex-situ NMR method

Electrochemistry

To assess the reproducibility of this method, three cells were assembled as described using a mass of 10 mg of neat PDC particles of average diameter roughly 0.1 mm, without binder, and soaked with 1 M NaCl (aq). The electrodes were preconditioned with a few shorter charge/self-discharge cycles to reach a constant voltage drop, then charged for 2 h at 0.8 V, after which ^1H and ^{23}Na NMR spectra were recorded at an MAS rate of 5 kHz. The delay between the disassembly and the recording of the NMR spectra of the positive electrode is less than 5 min, while the spectra of the negative electrode are recorded after approximately 20 min.

Nuclear-Magnetic Resonance

A background ^1H spectrum is first recorded of the 7 mm rotor containing the insert, Figure 6.11. Two peaks are assigned to the 3D printer resin, at 1.6 ppm and 3.4 ppm. Due to the fast spin relaxation in this solid, the peaks are substantially reduced using the DEPTH pulse sequence, which allows for better deconvolution of the in-pore peak.

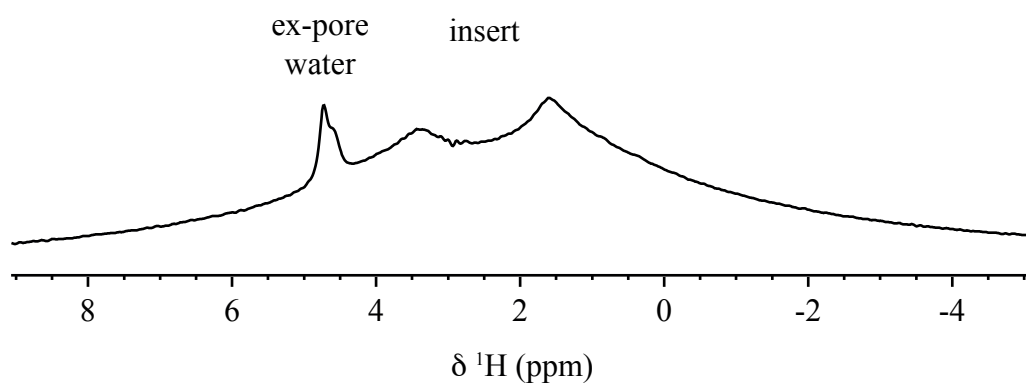


Figure 6.11: Background ^1H NMR spectrum of a wet insert.

The ^1H spectra of the reference electrodes, before charging, are shown in Figure 6.12(top). Despite multiple small artefacts around the strong ex-pore peak, the in-pore peak is well resolved and easily fitted. It can be seen that the two spectra are not exactly identical despite the best efforts to weigh and transfer the same mass of carbon to the cell. This can be explained by the rather delicate procedure where spillage of powder is difficult to minimize. In addition, it was noted that if the carbon was introduced at the bottom of the rotor, it would be totally invisible, hence the use of spacers to ensure that the carbon is always at the same position. However this means that quantitative detection in the 7 mm probe is more difficult than in 3.2 mm probes for example.

The ^1H spectra of the negatively charged electrodes in Figure 6.12(middle) show a clear shift of the in-pore peak by ~ 2.7 ppm. This is a common observation with in-situ NMR studies. The in-pore peak of the second cell (blue spectrum in the middle) shows a shoulder at ~ -3 ppm, close to the reference in-pore peak, assigned to a fraction of particles that were not in contact with the current collector. It is likely that the particles were trapped in the folds of the CelgardTM membrane when pushed into the insert. Likewise, the difference in intensities can be assigned to motion of particles towards less sensitive regions of the rotor.

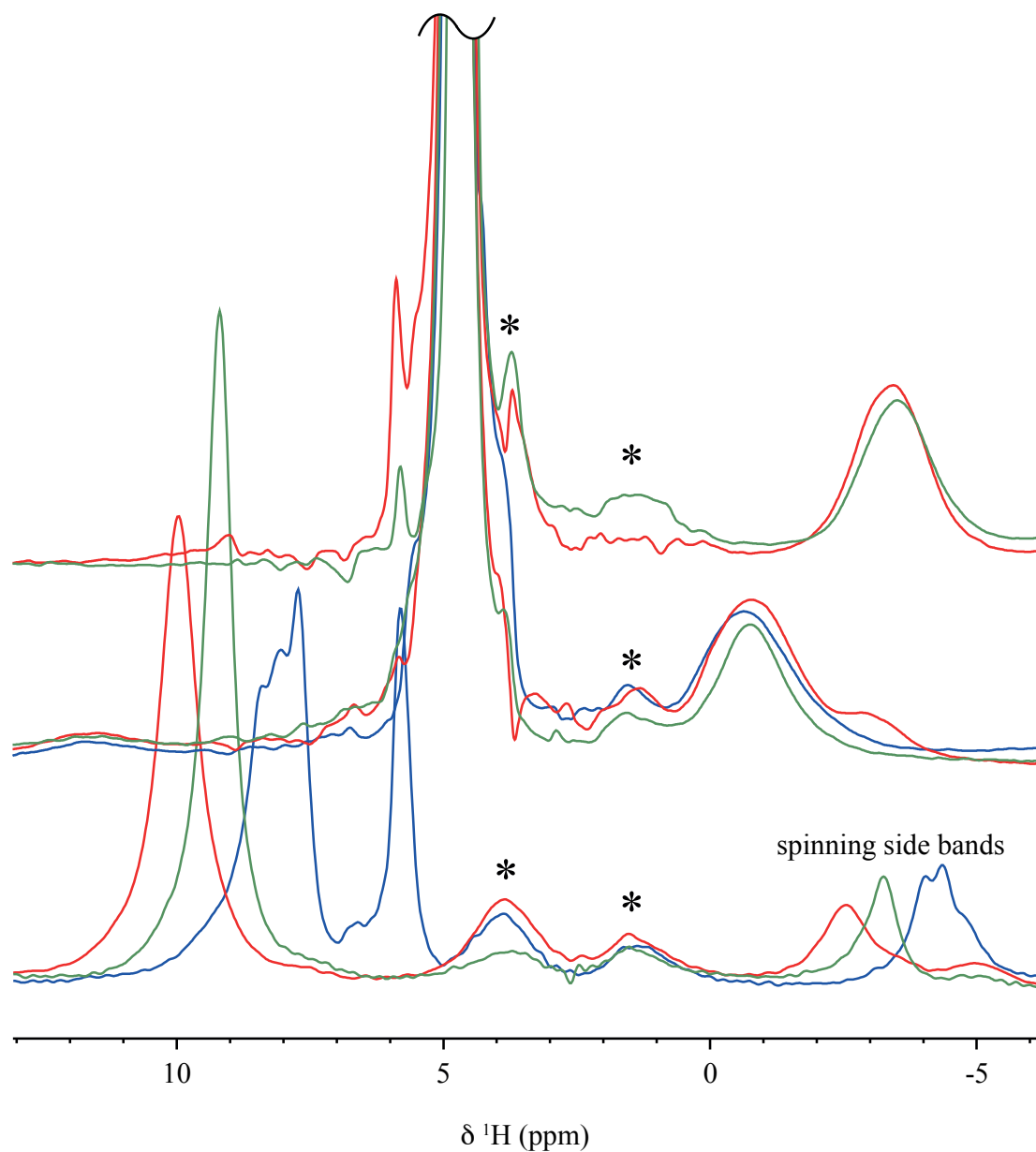


Figure 6.12: ^1H NMR spectra of the reference (top), negatively charged (middle) and positively charged (bottom) electrodes. The blue, red and green spectra correspond to the first, second and third cell. Some line-broadening (exponential multiplication with line-broadening factor of 50 Hz) was used for the top and middle spectra for clarity due to the extremely narrow line width of the ex-pore electrolyte, but analysis was done without it. The asterisks denote peaks due to the insert.

Finally, the ^1H spectra of the positively charged electrodes in Figure 6.12(bottom) are very different in several aspects. The most striking is the poor reproducibility of the spectra for this electrode. A strong peak is located between 7 and 10 ppm and one peak is missing. The reason for this has not been determined but one hypothesis is that some paramagnetic species are etched from the current collector and deposited on some component of the half-cell such as the membrane, on which orange stains do appear over time, and possibly adsorbed on the electrode. The ex-pore peak could be shifted by a few ppm this way, while the in-pore peak, where the concentration is the highest, displaced out of the spectral window. Moreover the concentration of paramagnetic species is unlikely to be the same for each electrode as the corrosion depends on many parameters including the polishing of the current collector, explaining why poor reproducibility was found for these NMR spectra.

The ^{23}Na MAS NMR spectra of the same electrodes are shown in Figure 6.13. At first sight the reproducibility seems better, as all three charged electrodes are almost indistinguishable. The reference electrodes (top) appear to contain two in-pore components, one at -5 ppm and one at -9 ppm. The in-pore peak coming from the spontaneous adsorption of cations is the latter one (assigned with the spectrum of the same sample recorded on a 3.2 mm probe). It is not clear what the second component could be but it is quite possibly related to the subtle orange stains visible on the CelgardTM pouches that were previously used for other electrodes. The charged electrodes were assembled with fresh pieces of CelgardTM. From the in-pore peak, the charging mechanism can be qualitatively described: the negative electrode takes up more cations, while the cation population does not seem to vary much in the positive electrode.

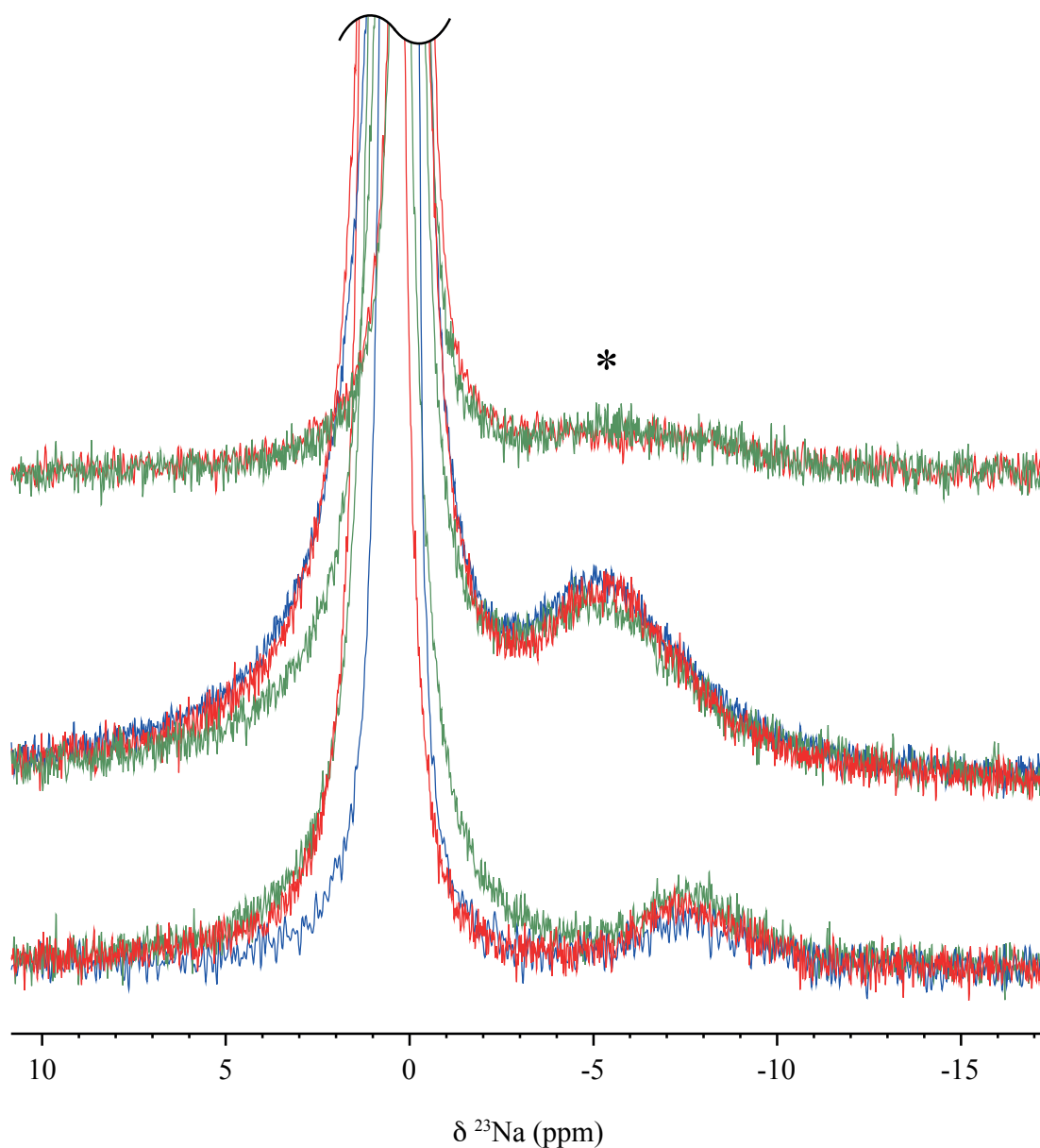


Figure 6.13: ^{23}Na NMR spectra of the reference (top), negatively charged (middle) and positively charged (bottom) electrodes. The blue, red and green spectra correspond to the first, second and third cell. The asterisk denotes the residual in-pore component of previously cycled separators.

Quantification of the Na^+ in-pore concentration was achieved following the same method as in the previous chapter. The ratio $C_{\text{in}}/C_{\text{ex}}$ for the reference electrodes was equal to 0.23, which compares well to the value of 0.20 found for the same sample

in the more quantitative 3.2 mm rotors and without insert or Celgard™ membrane. For the first negatively-charged electrode a ratio of 0.75 was found, which is an increase by a factor 3.3. For the positive electrode, this quantification could not be done due to the absence of ^1H in-pore peak.

Electrode stability

One recurrent problem throughout this thesis is the evaporation of water, which causes the electrolyte concentration to increase. In addition, the state of charge can vary during the NMR experiments. NMR spectra of the positive and negative electrodes were recorded 12 hours after transfer into the 7 mm rotors and compared with the fresh electrode spectra in Figure 6.14. A simultaneous decrease of the ex-pore peak of water (top left) and sodium (top right) would indicate a leak of the electrolyte solution. This is fortunately not seen for the negatively charged electrode. The in-pore peak of water shifts and increases a little, perhaps due to some minimal reabsorption of water from the ex-pore environment. Furthermore, no signs of self-discharge are observed. The charge redistribution takes place quite quickly after disconnection, as can be seen in the potential decay curves above: the fast component of the decay is visible for a mere minute or two, after which the decay is dominated by the slowest component assigned to faradaic processes. The ions are therefore already at equilibrium in the first NMR spectrum recorded, explaining why the evolution of the $\Delta\delta$ is observed after a delay. After 12 h, even the slow faradaic self-discharge could cause a significant difference in the charge state, however the ^{23}Na spectra show that no significant portion of ions diffuses elsewhere.

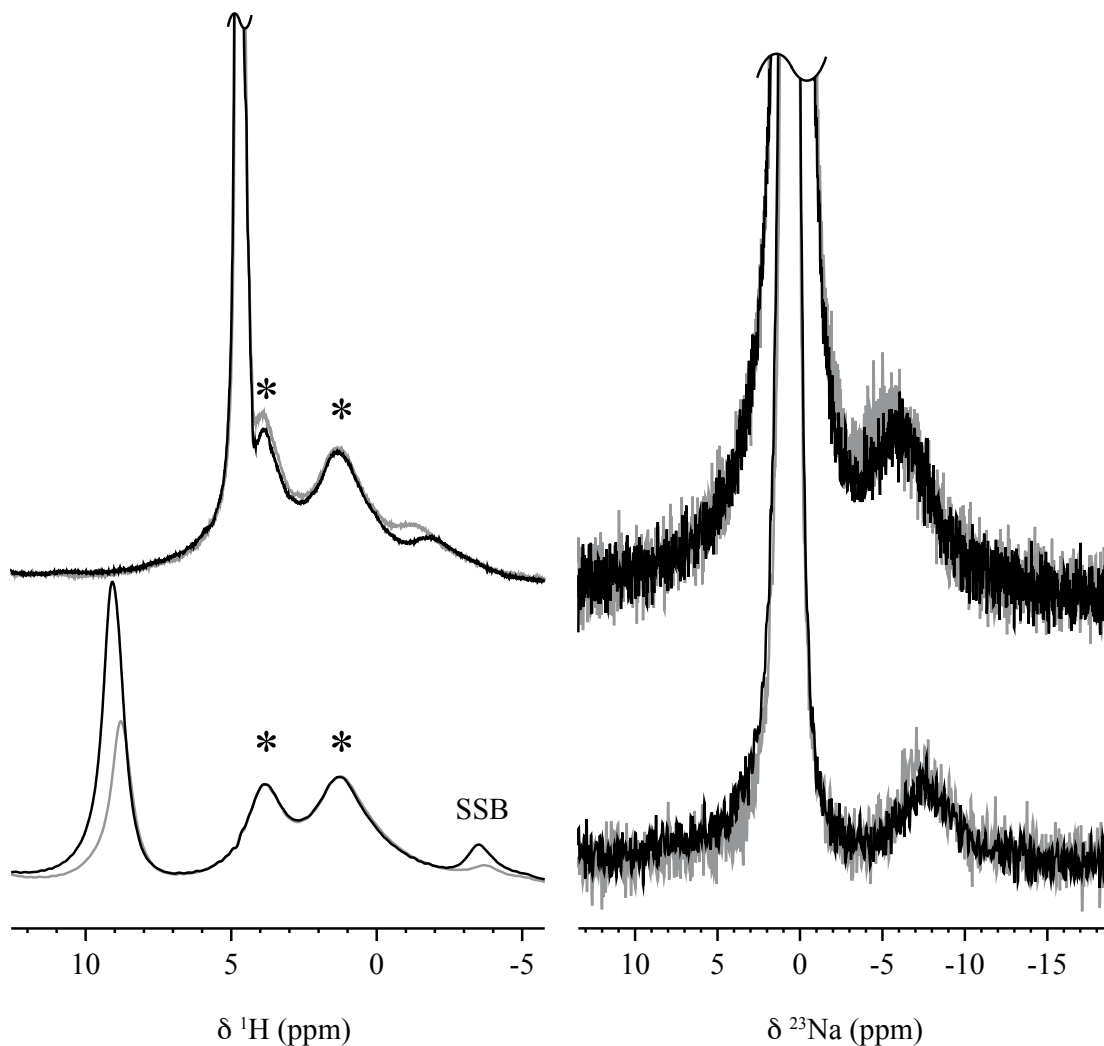


Figure 6.14: ^1H (left) and ^{23}Na (right) NMR spectra of negatively (top) and positively (bottom) charged electrodes, freshly disconnected (black) and after 12 h inside the 7 mm rotor (grey). The asterisks denote peaks due to the insert.

On the other hand, the positive electrode undergoes more significant changes. The sodium ex-pore peak of that electrode (bottom right) decreases almost by half, while the in-pore peak does not change as much. In the ^1H spectrum of this electrode (bottom left), the unassigned peak at 10 ppm is also seen to decrease by approximately half, which suggests it is most likely the ex-pore peak, indicating that the rotor may have leaked a little bit. This raises the question: where is the in-pore peak? Getting to

the bottom of this question would require extensive characterization of this electrode, or replacing the current collector with a better metal, which is however not the objective of this chapter.

6.4 Conclusion and Future Work

In conclusion, a new setup for ex-situ NMR experiments of charged electrodes was proposed in this chapter and shown to offer reproducible electrochemistry as well as NMR measurements. The negatively charged electrode particularly provided good results and showed the benefit of MAS to quantify populations of water and ions in the ex-pore and in-pore environments. A preliminary charging mechanism could be proposed for the negative electrode, namely adsorption of cations, but more work is necessary to confirm it. The positive electrode showed peculiar features possibly due to paramagnetic effects, therefore further electrochemical measurements and other characterisation methods are required to understand the complex behavior of the current collector in this electrode. It is possible that NaCl is responsible for the corrosion of the current collector, or that the metal used is simply not stable under this applied potential, which releases paramagnetic species in the electrolyte. Indeed no orange stains were observed even after extensive cycling of Swagelok cells. Both electrodes are overall relatively stable once disconnected, over the duration of the analyses which last only a few minutes. Self-discharge processes are not seen to affect the NMR spectra, contrary to what might have been expected from a diffusion of ions towards smaller pores, which should be accompanied by an increase in $\Delta\delta$. Deeper investigation of self-discharge phenomena is however beyond the scope of this chapter, however comparing carbons with various pore sizes could yield some information on the motion of ions during self-discharge.

This prototype generation of cell can obviously be improved in many ways. For example, the electrodes could be enclosed in a tighter compartment to avoid drying during long cycling, possibly reducing the corrosion of the current collectors, although this was mitigated by the use of a relatively large piece of filter paper as separator that could be wetted regularly with fresh electrolyte solution. Regarding the insert itself, the CelgardTM pouch which allows to contain carbon particles without the use of binder, was found to possibly trap some of the finest particles between the folds, thereby introducing errors in the effective electrode mass. A new design of the insert allowing a better introduction of binder-free particles into the insert and containment without a pouch would be a useful improvement. Moreover, the use of a reference electrode would provide a more precise application of the charging potential. However this would come with the inconvenience of having to run two cells if both electrodes are to be analysed. From the results shown here, the positive electrode deserves some deeper understanding, but the negative electrode seems a good candidate for ex-situ experiments, and could well be studied alone with a reference electrode. Finally, despite offering easy manipulation of the components of the cell thanks to their size, the 7 mm probe could be replaced by a 4 mm or even a 3.2 mm probe after scaling down the inserts and current collectors. This would bring the advantage of more reliable NMR experiments without the need to properly position the sample in the middle of the rotor with spacers.

Conclusions

Throughout this thesis, activated carbons have proven difficult to characterize as per their reputation. To bring the field one small step further, a deeper understanding of the main analytical tools needed first be developed. NMR has been used in the literature to determine average pore sizes, however the averaging process was poorly described. Home-made samples made the parameters influencing exchange-averaging more obvious. The ex-pore in-pore diffusion was promoted by small particle diameters and small hydrophobic species. When the pore network was inhomogeneously activated, it was found that diffusion between pores was too slow to average pores further than a only few dozen or hundreds of nanometres. GS was also an important technique subject to extensive debate. It was necessary to compare several data treatment methods to be able to extract the most reliable information. Three pore populations were thus distinguished: narrowly distributed subnanometre pores, more variable micropores and a minor population of slightly bigger pores. They were hypothetically attributed to pores within ordered and disordered domains found in activated carbons with some supporting evidence from other techniques. The reliability of the Raman spectroscopy approach was also assessed. There is no standard procedure at all in the literature for the deconvolution of the two main peaks of the spectra, therefore several options were tested and the most reproducible one was selected. This technique yielded crucial information on the molecular structure of the pore walls such as dimensions and the density of defects, from which molecular activation mechanisms could be proposed and cross-referenced with the other techniques.

Using all the available techniques in conjunction to analyse samples made in a variety of ways, a macroscopic activation mechanism, *i.e.* the development of the pore network on the particle size scale, was proposed and the effect of the synthesis parameters described. It was found that steam-activation, which rate was known to be temperature-dependent, produces a homogeneous pore network at 900 °C, provided the particle is small enough to minimize the radial activation gradient. At 700 °C, the reaction is about 50 times slower, which makes the radial activation gradient negligible, however the porosity was a lot more inhomogeneous with regions of the particle containing a significantly higher proportion of big pores and other regions containing a much higher density of metastable defects. These findings offer many options to customize the porosity and surface topology of the carbons. For example one could steam-activate small particles at 900 °C and then reactivate with KOH followed by recarbonization, to introduce significantly bigger pores in a well-connected pore network. There are also many other activating agents whose effect on the development of the porosity can be better understood using this multi-technique characterization approach.

Based mostly on NMR, simple saturation experiments were conducted on a series of samples with increasing BO, using LiCl, NaCl, and CsCl in a range of concentrations. A concentration-dependent $\Delta\delta$ was systematically observed for the first time. The conclusion of this study was that when spontaneously adsorbed, the ions are not homogeneously distributed within the pore network, but rather the big pores take up higher concentrations than the small pores. This has important repercussions on the general interpretation of NMR spectra in adsorption experiments, where in the past a smaller $\Delta\delta$ was automatically assigned to dynamics effects. The ability to synthesize carbons with pore networks containing regions with distinct average pore sizes should

also facilitates the quantification of concentration- and species-dependent adsorption properties.

The potential-driven adsorption of NaCl was also observed using a purpose-made electrochemical cell allowing to charge binder-free carbon electrodes ex-situ before recording NMR spectra under MAS conditions. In a first instance, a reproducible protocol was established, which was subsequently used to quantify the self-discharge dynamics as to better understand how this setup compares with in-situ charging protocols. Some unsuitable components and design features were identified and can be improved in the future, which should make this device a useful complement to static NMR in-situ experiments suffering from a lower resolution. The ex-situ and in-situ approaches will yield a lot more information when used together as the first allows to observe equilibrium states with enhanced resolution, while the second allows to observe the dynamics of the charging process.

Overall this work was driven by fundamental scientific questions, one project leading to another, and it was very exciting after a good three years to see all the pieces fall together nicely in a coherent representation of activated carbons.

Bibliography

- [1] L. Wei, G. Yushin, *Nano Energy* **2012**, *1*, 552–565.
- [2] M. Sevilla, R. Mokaya, *Energy Environ. Sci.* **2014**, *7*, 1250–1280.
- [3] S. Porada, R. Zhao, A. Van Der Wal, V. Presser, P. M. Biesheuvel, *Prog. Mater. Sci.* **2013**, *58*, 1388–1442.
- [4] M. Sevilla, A. B. Fuertes, *Energy Environ. Sci.* **2011**, *4*, 1765–1771.
- [5] H. Pan, J. Li, Y. P. Feng, *Nanoscale Res. Lett.* **2010**, *5*, 654–668.
- [6] I. Shown, A. Ganguly, L. C. Chen, K. H. Chen, *Energy Sci. Eng.* **2015**, *3*, 2–26.
- [7] K. Wang, H. Wu, Y. Meng, Z. Wei, *Small* **2014**, *10*, 14–31.
- [8] Y. Yin, K. Feng, C. Liu, S. Fan, *J. Phys. Chem. C* **2015**, *119*, 8488–8491.
- [9] U. N. Maiti, J. Lim, K. E. Lee, W. J. Lee, S. O. Kim, *Adv. Mater.* **2014**, *26*, 615–619.
- [10] H. Banda, S. Périé, B. Daffos, P. L. Taberna, L. Dubois, O. Crosnier, P. Simon, D. Lee, G. De Paëpe, F. Duclairoir, *ACS Nano* **2019**, *13*, 1443–1453.
- [11] F. Du, D. Yu, L. Dai, S. Ganguli, V. Varshney, A. K. Roy, *Chem. Mater.* **2011**, *23*, 4810–4816.
- [12] C. H. J. Kim, H. Zhang, J. Liu, *2D Mater.* **2015**, *2*, 024006.
- [13] L. Zhang, F. Zhang, X. Yang, G. Long, Y. Wu, T. Zhang, K. Leng, Y. Huang, Y. Ma, A. Yu, Y. Chen, *Sci. Rep.* **2013**, *3*, 1–9.
- [14] W. Gu, G. Yushin, *WIREs Energy Environ.* **2014**, *3*, 424–473.
- [15] S. Bernard, O. Beyssac, K. Benzerara, N. Findling, G. Tzvetkov, G. E. Brown, *Carbon* **2010**, *48*, 2506–2516.

- [16] Y. Eom, S. M. Son, Y. E. Kim, J. E. Lee, S. H. Hwang, H. G. Chae, *Carbon* **2019**, *150*, 142–152.
- [17] S. Sharma, C. N. Shyam Kumar, J. G. Korvink, C. Kübel, *Sci. Rep.* **2018**, *8*, 1–12.
- [18] A. K. Kercher, D. C. Nagle, *Carbon* **2003**, *41*, 15–27.
- [19] J. F. Long, K. W. Sykes, *Proc. R. Soc. Lond. A* **1948**, *193*, 377–399.
- [20] J. Gadsby, F. J. Long, P. Sleightholm, K. W. Sykes, *Proc. R. Soc. Lond. A* **1948**, *193*, 357–376.
- [21] J. Tanner, S. Bhattacharya, *Chem. Eng. J.* **2016**, *285*, 331–340.
- [22] Z. Huang, J. Zhang, Y. Zhao, H. Zhang, G. Yue, T. Suda, M. Narukawa, *Fuel Process. Technol.* **2010**, *91*, 843–847.
- [23] R. Zhang, Y. Chen, K. Lei, D. Liu, *Fuel* **2017**, *209*, 109–116.
- [24] R. C. Everson, H. W. J. P. Neomagus, H. Kasaini, D. Njapha, *Fuel* **2006**, *85*, 1076–1082.
- [25] K. Jurkiewicz, M. Pawlyta, A. Burian, *C* **2018**, *4*, 68–115.
- [26] E. Franklin, *Proc. R. Soc. London. Ser. A. Math. Phys. Sci.* **1951**, *209*, 196–218.
- [27] J. S. McDonald-Wharry, M. Manley-Harris, K. L. Pickering, *Energy and Fuels* **2016**, *30*, 7811–7826.
- [28] G. M. Jenkins, K. Kawamura, L. L. Ban, *Proc. R. Soc. Lond. A* **1972**, *327*, 501–517.
- [29] L. L. Ban, D. Crawford, H. Marsh, *J. Appl. Crystallogr.* **1975**, *8*, 415–420.
- [30] P. J. F. Harris, *Crit. Rev. Solid State Mater. Sci.* **2005**, *30*, 235–253.
- [31] L. Hawelek, A. Brodka, J. C. Dore, V. Honkimäki, A. Burian, *Diam. Relat. Mater.* **2008**, *17*, 1633–1638.
- [32] J. Baek, H. Lee, J. Roh, H. Lee, H. S. Kang, B. Kim, *Microporous Mesoporous*

- Mater.* **2016**, *219*, 258–264.
- [33] K. Jurkiewicz, S. Duber, A. Burian, *Int. J. Appl. Glas. Sci.* **2016**, *7*, 355–363.
- [34] T. X. Nguyen, N. Cohaut, J. S. Bae, S. K. Bhatia, *Langmuir* **2008**, *24*, 7912–7922.
- [35] A. Burian, A. Ratuszna, J. C. Dore, S. W. Howells, *Carbon* **1998**, *36*, 1613–1621.
- [36] J. C. Palmer, A. Llobet, S. H. Yeon, J. E. Fischer, Y. Shi, Y. Gogotsi, K. E. Gubbins, *Carbon* **2010**, *48*, 1116–1123.
- [37] C. de Tomas, I. Suarez-Martinez, F. Vallejos-Burgos, M. J. López, K. Kaneko, N. A. Marks, *Carbon* **2017**, *119*, 1–9.
- [38] C. Wang, J. K. Watson, E. Louw, J. P. Mathews, *Energy and Fuels* **2015**, *29*, 4814–4826.
- [39] V. M. Gun'Ko, O. P. Kozynchenko, S. R. Tennison, R. Leboda, J. Skubiszewska-Zięba, S. V. Mikhalovsky, *Carbon* **2012**, *50*, 3146–3153.
- [40] Z. Xing, Y. Qi, Z. Tian, J. Xu, Y. Yuan, C. Bommier, J. Lu, W. Tong, D. E. Jiang, X. Ji, *Chem. Mater.* **2017**, *29*, 7288–7295.
- [41] K. Fic, G. Lota, M. Meller, E. Frackowiak, *Energy Environ. Sci.* **2012**, *5*, 5842–5850.
- [42] Q. Gao, L. Demarconnay, E. Raymundo-Piñero, F. Béguin, *Energy Environ. Sci.* **2012**, *5*, 9611–9617.
- [43] S. Vaquero, J. Palma, M. Anderson, R. Marcilla, *Int. J. Electrochem. Sci.* **2013**, *8*, 10293–10307.
- [44] Z. Chang, Y. Yang, M. Li, X. Wang, Y. Wu, *J. Mater. Chem. A* **2014**, *2*, 10739–10755.
- [45] B. Dyatkin, V. Presser, M. Heon, M. R. Lukatskaya, M. Beidaghi, Y. Gogotsi, *ChemSusChem* **2013**, *6*, 2269–2280.

- [46] S. Porada, L. Borchardt, M. Oschatz, M. Bryjak, J. S. Atchison, K. J. Keesman, S. Kaskel, P. M. Biesheuvel, V. Presser, *Energy Environ. Sci.* **2013**, *6*, 3700–3712.
- [47] M. E. Suss, S. Porada, X. Sun, P. M. Biesheuvel, J. Yoon, V. Presser, *Energy Environ. Sci.* **2015**, *8*, 2296–2319.
- [48] C. D. Williams, P. Carbone, *Environ. Sci. Technol.* **2016**, *50*, 3875–3881.
- [49] L. A. Richards, A. I. Schäfer, B. S. Richards, B. Corry, *Phys. Chem. Chem. Phys.* **2012**, *14*, 11633–11638.
- [50] H. Liu, C. J. Jameson, S. Murad, *Mol. Simul.* **2008**, *34*, 169–175.
- [51] C. Song, B. Corry, *J. Phys. Chem. B* **2009**, *113*, 7642–7649.
- [52] L. A. Richards, A. I. Schäfer, B. S. Richards, B. Corry, *Small* **2012**, *8*, 1701–1709.
- [53] O. Beckstein, K. Tai, M. S. P. Sansom, *J. Am. Chem. Soc.* **2004**, *126*, 14694–14695.
- [54] S. Kondrat, P. Wu, R. Qiao, A. A. Kornyshev, *Nat. Mater.* **2014**, *13*, 387–393.
- [55] S. Kondrat, A. A. Kornyshev, *Nanoscale Horizons* **2016**, *1*, 45–52.
- [56] J. M. Griffin, A. C. Forse, H. Wang, N. M. Trease, P. L. Taberna, P. Simon, C. P. Grey, *Faraday Discuss.* **2014**, *176*, 49–68.
- [57] J. M. Griffin, A. C. Forse, C. P. Grey, *Solid State Nucl. Magn. Reson.* **2016**, *74–75*, 16–35.
- [58] R. K. Harris, T. V. Thompson, P. R. Norman, C. Pottage, *J. Chem. Soc. - Faraday Trans.* **1996**, *92*, 2615–2618.
- [59] R. K. Harris, T. V. Thompson, P. R. Norman, C. Pottage, *Carbon* **1999**, *37*, 1425–1430.
- [60] L. Borchardt, M. Oschatz, S. Paasch, S. Kaskel, E. Brunner, *Phys. Chem. Chem.*

- Phys.* **2013**, *15*, 15177–15184.
- [61] M. Deschamps, E. Gilbert, P. Azais, E. Raymundo-Piñero, M. R. Ammar, P. Simon, D. Massiot, F. Béguin, *Nat. Mater.* **2013**, *12*, 351–358.
- [62] P. von Ragué Schleyer, C. Maerker, A. Dransfeld, H. Jiao, N. J. R. Van Eikema Hommes, *J. Am. Chem. Soc.* **1996**, *118*, 6317–6318.
- [63] A. C. Forse, J. M. Griffin, H. Wang, N. M. Trease, V. Presser, Y. Gogotsi, P. Simon, C. P. Grey, *Phys. Chem. Chem. Phys.* **2013**, *15*, 7722–7730.
- [64] A. C. Forse, J. M. Griffin, V. Presser, Y. Gogotsi, C. P. Grey, *J. Phys. Chem. C* **2014**, *118*, 7508–7514.
- [65] A. C. Forse, C. Merlet, P. K. Allan, E. K. Humphreys, J. M. Griffin, M. Aslan, M. Zeiger, V. Presser, Y. Gogotsi, C. P. Grey, *Chem. Mater.* **2015**, *27*, 6848–6857.
- [66] C. Merlet, A. C. Forse, J. M. Griffin, D. Frenkel, C. P. Grey, *J. Chem. Phys.* **2015**, *142*, 094701.
- [67] N. Fulik, F. Hippauf, D. Leistenschneider, S. Paasch, S. Kaskel, E. Brunner, L. Borchardt, *Energy Storage Mater.* **2018**, *12*, 183–190.
- [68] I. P. P. Cansado, F. A. M. M. Gonçalves, J. M. V. Nabais, M. M. L. Ribeiro Carrott, P. J. M. Carrott, *Fuel Process. Technol.* **2009**, *90*, 232–236.
- [69] I. P. P. Cansado, F. A. M. M. Gonçalves, P. J. M. Carrott, M. M. L. Ribeiro Carrott, *Carbon* **2007**, *45*, 2454–2455.
- [70] T. P. McNicholas, A. Wang, K. O'Neill, R. J. Anderson, N. P. Stadie, A. Kleinhammes, P. Parilla, L. Simpson, C. C. Ahn, Y. Wang, Y. Wu, J. Liu, *J. Phys. Chem. C* **2010**, *114*, 13902–13908.
- [71] R. J. Anderson, T. P. McNicholas, A. Kleinhammes, A. Wang, J. Liu, Y. Wu, *J. Am. Chem. Soc.* **2010**, *132*, 8618–8626.

- [72] Y. Xing, Z. Luo, A. Kleinhammes, Y. Wu, *Carbon* **2014**, *77*, 1132–1139.
- [73] H. J. Wang, A. Kleinhammes, T. P. McNicholas, J. Liu, Y. Wu, *J. Phys. Chem. C* **2014**, *118*, 8474–8480.
- [74] Z. X. Luo, Y. Z. Xing, Y. C. Ling, A. Kleinhammes, Y. Wu, *Nat. Commun.* **2015**, *6*, 1–8.
- [75] Z. X. Luo, Y. Z. Xing, S. Liu, Y. C. Ling, A. Kleinhammes, Y. Wu, *J. Phys. Chem. Lett.* **2015**, *6*, 5022–5026.
- [76] Y. Song, Y. Chong, A. Raghavan, Y. Xing, Y. Ling, A. Kleinhammes, Y. Wu, *J. Phys. Chem. C* **2017**, *121*, 8504–8509.
- [77] J. T. Arnold, S. S. Dharmatti, M. E. Packard, *J. Chem. Phys.* **1951**, *19*, 507.
- [78] D. Massiot, F. Fayon, M. Deschamps, S. Cadars, P. Florian, V. Montouillout, N. Pellerin, J. Hiet, A. Rakhmatullin, C. Bessada, *Comptes Rendus Chim.* **2010**, *13*, 117–129.
- [79] A. E. Bennett, C. M. Rienstra, M. Auger, K. V. Lakshmi, R. G. Griffin, *J. Chem. Phys.* **1995**, *103*, 6951.
- [80] A. Pines, M. G. Gibby, J. S. Waugh, *J. Chem. Phys.* **1972**, *56*, 1776.
- [81] S. R. Hartmann, E. L. Hahn, *Phys. Rev.* **1962**, *128*, 2042–2053.
- [82] M. H. Levitt, *Spin Dynamics*, **2001**.
- [83] S. Hwang, J. Kärger, *Magn. Reson. Imaging* **2019**, *56*, 3–13.
- [84] F. Furtado, P. Galvosas, M. Gonalves, F. D. Kopinke, S. Naumov, F. Rodríguez-Reinoso, U. Roland, R. Valiullin, J. Kärger, *Microporous Mesoporous Mater.* **2011**, *141*, 184–191.
- [85] T. M. Alam, T. M. Osborn Popp, *Chem. Phys. Lett.* **2016**, *658*, 51–57.
- [86] A. C. Forse, J. M. Griffin, C. Merlet, J. Carretero-Gonzalez, A.-R. O. Raji, N. M. Trease, C. P. Grey, *Nat. Energy* **2017**, *2*, 1–16.

- [87] S. Macura, Y. Huang, D. Suter, R. R. Ernst, *J. Mag. Res* **1981**, *43*, 259–281.
- [88] A. D. Bain, *Prog. Nucl. Magn. Reson. Spectrosc.* **2003**, *43*, 63–103.
- [89] J. Silvestre-Albero, A. Silvestre-Albero, F. Rodríguez-Reinoso, M. Thommes, *Carbon* **2012**, *50*, 3128–3133.
- [90] R. V. R. A. Rios, J. Silvestre-Albero, A. Sepúlveda-Escribano, M. Molina-Sabio, F. Rodríguez-Reinoso, *J. Phys. Chem. C* **2007**, *111*, 3803–3805.
- [91] K. S. W. Sing, D. H. Everett, R. Haul, L. Moscou, R. A. Pierotti, J. Rouquérol, T. Siemieniewska, *Pure Appl. Chem.* **1982**, *54*, 2201–2218.
- [92] G. Horvath, *J. Chem. Eng. Japan* **1983**, *16*, 470–474.
- [93] N. D. Hutson, R. T. Yang, *Adsorption* **1997**, *3*, 189–195.
- [94] F. Stoeckli, *Russ. Chem. Bull.* **2001**, *50*, 2265–2272.
- [95] G. O. Wood, *Carbon* **2002**, *40*, 231–239.
- [96] P. A. Gauden, A. P. Terzyk, G. Rychlicki, P. Kowalczyk, M. S. Ćwiertnia, J. K. Garbacz, *J. Colloid Interface Sci.* **2004**, *273*, 39–63.
- [97] A. V. Neimark, Y. Lin, P. I. Ravikovitch, M. Thommes, *Carbon* **2009**, *47*, 1617–1628.
- [98] G. Y. Gor, M. Thommes, K. A. Cychosz, A. V. Neimark, *Carbon* **2012**, *50*, 1583–1590.
- [99] J. Landers, G. Y. Gor, A. V. Neimark, *Colloids Surfaces A Physicochem. Eng. Asp.* **2013**, *437*, 3–32.
- [100] J. E. Jones, *Proc. R. Soc. Lond. A* **1924**, *106*, 463–477.
- [101] W. A. Steele, *The Interactions of Gases with Solid Surfaces*, Oxford, **1974**.
- [102] J. Jagiello, J. Kenvin, J. P. Olivier, A. R. Lupini, C. I. Contescu, *Adsorpt. Sci. Technol.* **2011**, *29*, 769–780.
- [103] S. M. P. Lucena, C. A. S. Paiva, P. F. G. Silvino, D. C. S. Azevedo, C. L.

- Cavalcante, *Carbon* **2010**, *48*, 2554–2565.
- [104] M. V. López-Ramón, J. Jagiełło, T. J. Bandoz, N. A. Seaton, *Langmuir* **1997**, *13*, 4435–4446.
- [105] M. Kwiatkowski, V. Fierro, A. Celzard, *Adsorption* **2019**, *25*, 1673–1682.
- [106] I. Childres, L. Jauregui, W. Park, H. Caoa, Y. P. Chena, D. Němeček, G. J. Thomas, *New Dev. Phot. Mater. Res.* **2013**, 403–418.
- [107] A. Merlen, J. Buijnsters, C. Pardanaud, *Coatings* **2017**, *7*, 153.
- [108] A. . Ferrari, J. Robertson, *Phys. Rev. B - Condens. Matter Mater. Phys.* **2000**, *61*, 14095–14107.
- [109] L. G. Cançado, A. Jorio, E. H. M. Ferreira, F. Stavale, C. A. Achete, R. B. Capaz, M. V. O. Moutinho, A. Lombardo, T. S. Kulmala, A. C. Ferrari, *Nano Lett.* **2011**, *11*, 3190–3196.
- [110] G. A. Zickler, B. Smarsly, N. Gierlinger, H. Peterlik, O. Paris, *Carbon* **2006**, *44*, 3239–3246.
- [111] N. Shimodaira, A. Masui, *J. Appl. Phys.* **2002**, *92*, 902–909.
- [112] M. Inagaki, S. Somiya, in *Handb. Adv. Ceram. (Second Ed.*, Academic Press, Oxford, **2013**, pp. 25–60.
- [113] L. Cervini, N. Barrow, J. Griffin, *Johnson Matthey Technol. Rev.* **2019**, *64*, 152–164.
- [114] R. L. Vold, G. L. Hoatson, *J. Magn. Reson.* **2009**, *198*, 57–72.
- [115] C. Cadar, I. Ardelean, *Magn. Reson. Chem.* **2019**, *57*, 829–835.
- [116] I. N. Tsimpanogiannis, O. A. Moulτος, L. F. M. Franco, M. B. d. M. Spera, M. Erdős, I. G. Economou, *Mol. Simul.* **2019**, *45*, 425–453.
- [117] S. O. Diallo, *Phys. Rev. E - Stat. Nonlinear, Soft Matter Phys.* **2015**, *92*, 1–10.
- [118] M. Holz, S. R. Heil, A. Sacco, *Phys. Chem. Chem. Phys.* **2000**, *2*, 4740–4742.

- [119] Y. D. Fomin, V. N. Ryzhov, E. N. Tsiok, *J. Chem. Phys.* **2015**, *143*, 184702.
- [120] T. Shimoyama, K. Tashima, M. Ruike, *Colloids Surfaces A Physicochem. Eng. Asp.* **2017**, *533*, 255–266.
- [121] M. Fukano, T. Fujimori, J. Ségalini, E. Iwama, P. L. Taberna, T. Iiyama, T. Ohba, H. Kanoh, Y. Gogotsi, P. Simon, K. Kaneko, *J. Phys. Chem. C* **2013**, *117*, 5752–5757.
- [122] S. Bi, Y. Zhang, L. Cervini, T. Mo, J. M. Griffin, V. Presser, G. Feng, *Sustain. Energy Fuels* **2020**, *4*, 1285–1295.
- [123] C. J. Jafta, A. Petzold, S. Risse, D. Clemens, D. Wallacher, G. Goerigk, M. Ballauff, *Carbon* **2017**, *123*, 440–447.
- [124] L. Cervini, O. D. Lynes, G. R. Akien, A. Kerridge, N. S. Barrow, J. M. Griffin, *Energy Storage Mater.* **2019**, *21*, 335–346.
- [125] X. Hu, M. Radosz, K. A. Cychosz, M. Thommes, *Environ. Sci. Technol.* **2011**, *45*, 7068–7074.
- [126] A. Sadezky, H. Muckenhuber, H. Grothe, R. Niessner, U. Pöschl, *Carbon* **2005**, *43*, 1731–1742.
- [127] A. Sharma, T. Kyotani, A. Tomita, *Carbon* **2000**, *38*, 1977–1984.
- [128] H. M. Lee, D. C. Chung, S. C. Jung, K. H. An, S. J. Park, B. J. Kim, *Chem. Eng. J.* **2019**, *377*, 120836.
- [129] J. S. Roh, *Korean J. Mater. Res.* **2003**, *13*, 742–748.
- [130] K. Yang, J. Peng, H. Xia, L. Zhang, C. Srinivasakannan, S. Guo, *J. Taiwan Inst. Chem. Eng.* **2010**, *41*, 367–372.
- [131] Y. Du, C. Wang, H. Xin, D. Che, J. P. Mathews, *Carbon* **2019**, *141*, 226–237.
- [132] Y. Huang, Y. Liu, G. Zhao, J. Y. Chen, *J. Mater. Sci.* **2017**, *52*, 478–488.
- [133] P. Brender, R. Gadiou, J. C. Rietsch, P. Fioux, J. Dentzer, A. Ponche, C. Vix-

- Guterl, *Anal. Chem.* **2012**, *84*, 2147–2153.
- [134] S. Haydar, C. Moreno-Castilla, M. A. Ferro-García, F. Carrasco-Marín, J. Rivera-Utrilla, A. Perrard, J. P. Joly, *Carbon* **2000**, *38*, 1297–1308.
- [135] H. R. Thomas, S. P. Day, W. E. Woodruff, C. Vallés, R. J. Young, I. A. Kinloch, G. W. Morley, J. V Hanna, N. R. Wilson, J. P. Rourke, *Chem. Mater.* **2013**, *25*, 3580–3588.
- [136] Z. Zhu, G. Q. Lu, J. Finnerty, R. T. Yang, *Carbon* **2003**, *41*, 635–658.
- [137] J. Wang, S. Kaskel, *J. Mater. Chem.* **2012**, *22*, 23710–23725.
- [138] J. Romanos, M. Beckner, T. Rash, L. Firlej, B. Kuchta, P. Yu, G. Suppes, C. Wexler, P. Pfeifer, *Nanotechnology* **2012**, *23*, 015401.
- [139] S. M. P. Lucena, J. C. A. Oliveira, D. V Gonçalves, P. F. G. Silvino, *Carbon* **2017**, *119*, 378–385.
- [140] N. Shiratori, K. J. Lee, J. Miyawaki, S. H. Hong, I. Mochida, B. An, K. Yokogawa, J. Jang, S. H. Yoon, *Langmuir* **2009**, *25*, 7631–7637.
- [141] J. D. Halliday, R. E. Richards, R. . Sharp, *Proc. R. Soc. Lond. A. Math. Phys. Sci.* **1969**, *313*, 45–69.
- [142] W. J. DeWitte, L. Liu, E. Mei, J. L. Dye, A. I. Popov, *J. Solution Chem.* **1977**, *6*, 337–348.
- [143] A. C. Forse, C. Merlet, J. M. Griffin, C. P. Grey, *J. Am. Chem. Soc.* **2016**, *138*, 5731–5744.
- [144] J. M. Griffin, A. C. Forse, W. Y. Tsai, P. L. Taberna, P. Simon, C. P. Grey, *Nat. Mater.* **2015**, *14*, 1–16.
- [145] H. Wang, A. C. Forse, J. M. Griffin, N. M. Trease, L. Trognko, P. L. Taberna, P. Simon, C. P. Grey, *J. Am. Chem. Soc.* **2013**, *135*, 18968–18980.
- [146] M. Gerken, J. A. Boatz, A. Kornath, R. Haiges, S. Schneider, T. Schroer, K. O.

- Christe, *J. Fluor. Chem.* **2002**, *116*, 49–58.
- [147] L. A. Richards, B. S. Richards, B. Corry, A. I. Schäfer, *Environ. Sci. Technol.* **2013**, *47*, 1968–1976.
- [148] S. Kondrat, A. Kornyshev, *J. Phys. Chem. C* **2013**, *117*, 12399–12406.
- [149] J. M. Griffin, A. C. Forse, W. Y. Tsai, P. L. Taberna, P. Simon, C. P. Grey, *Nat. Mater.* **2015**, *14*, 812–819.
- [150] A. C. Forse, J. M. Griffin, C. Merlet, P. M. Bayley, H. Wang, P. Simon, C. P. Grey, *J. Am. Chem. Soc.* **2015**, *137*, 7231–7242.
- [151] A. C. Forse, J. M. Griffin, H. Wang, N. M. Trease, V. Presser, Y. Gogotsi, P. Simon, C. P. Grey, *Phys. Chem. Chem. Phys.* **2013**, *15*, 7722–7730.
- [152] M. Kaus, J. Kowal, D. U. Sauer, *Electrochim. Acta* **2010**, *55*, 7516–7523.
- [153] H. A. Andreas, *J. Electrochem. Soc.* **2015**, *162*, A5047–A5053.
- [154] I. S. Ike, I. Sigalas, S. Iyuke, *Phys. Chem. Chem. Phys.* **2015**, *18*, 661–680.
- [155] B. Wang, C. Wang, Q. Hu, L. Zhang, Z. Wang, *J. Energy Storage* **2020**, *30*, 101473.
- [156] J. Kowal, E. Avaroglu, F. Chamekh, A. Senfelds, T. Thien, D. Wijaya, D. U. Sauer, *J. Power Sources* **2011**, *196*, 573–579.
- [157] J. Black, H. A. Andreas, *Electrochim. Acta* **2009**, *54*, 3568–3574.
- [158] N. Ganfoud, A. Sene, M. Haefele, A. Marin-Laflèche, B. Daffos, P. L. Taberna, M. Salanne, P. Simon, B. Rotenberg, *Energy Storage Mater.* **2019**, *21*, 190–195.
- [159] J. M. Black, H. A. Andreas, *J. Phys. Chem. C* **2010**, *114*, 12030–12038.

Appendix

This Appendix gives the full python script created to simulate and plot FIDs and their Fourier transformed spectra to describe the effects of one unique spin, diffusing between two environments with their own Larmor frequencies. The variables are the frequencies and dwell times in each environment. The script is typically run with Geany and requires the math, matplotlib and numpy modules. The script should be copy pasted without modifying the formatting.

```
def exchange():
    import math
    import matplotlib.pyplot as plt
    import numpy

#Define parameters:
    omega1 = 30; omega2 = 50                                #Larmor
    frequencies, rad/ms or Hz or whatever
    T11 = 2                                                #T1 relaxation constant, ms

    A1= 1
                                                #Amplitude
    dwell1 = 0.1; dwell2 = 0.2                            #Dwell time in
    one env., ms
    res = 0.01
                                                #FID resolution, ms
    points1 = dwell1/res
        #Number of points in one env.
    points2 = dwell2/res
    points1 = int(points1)
    points2 = int(points2)

    shuttling= 100
    TD = shuttling*(points1+points2)
    TD= int(TD)

#Make abscisses axis:
```

```

abscisses =      [[i for i in range(TD)],
                  #points
                  [0 for i in range(TD)],
                  #time, ms
                  [[] for i in range(TD)]]
                  #environment
for i in range(1, TD):
    abscisses[1][i] = abscisses[1][i-1] + res

test = 0
switch = test + points1
env = 0
while test < TD:
    while abscisses[0][test] <= abscisses[0][switch-1]:
        if switch > TD:
            switch = TD-1
        abscisses[2][test] = env
        test = test + 1
        if test == TD:
            break
    if test == switch and env == 0:
        test = switch
        switch = test + points2
        env = 1
    if test == switch and env == 1:
        test = switch
        switch = test + points1
        env = 0

#Calculate angle (rad) made by spin in env. 1 and 2 without and with exchange:
angle1_no = list([0]*TD)
for i in abscisses[0]:
    angle1_no[i] = angle1_no[i-1] + res*omega1

angle1_ex = list([0]*TD)
for i in abscisses[0]:
    if abscisses[2][i] == 0:
        angle1_ex[i] = angle1_ex[i-1] + res*omega1
    if abscisses[2][i] == 1:
        angle1_ex[i] = angle1_ex[i-1] + res*omega2

#Calculate FIDs without and with exchange and sum:
fid1_no = list([0]*TD)
fid1_ex = list([0]*TD)
for i in abscisses[0]:
    fid1_no[i] = A1*math.exp(-abscisses[1][i]/T11)*math.cos(angle1_no[i])
    fid1_ex[i] = A1*math.exp(-abscisses[1][i]/T11)*math.cos(angle1_ex[i])

#Fourier transform the FIDs... manually:

```

```

#Make list of candidate frequencies with sublist of standard deviation for each fitted
FID:
N_freq= 600
res_fd = 2*(omega2 - omega1)/float(N_freq)
                                     #number of points has to be float, e.g. 20.0
freq_low = omega1 - (omega2 - omega1)/2
freq_high = omega2 + (omega2 - omega1)/2

def frange(freq_low, freq_high, res_fd):
    #function to sample points at "float" intervals
    while freq_low < freq_high:
        yield float(freq_low)
        freq_low = freq_low + res_fd

frequencies =      [[i for i in frange(freq_low, freq_high, res_fd)],
                    #frequencies to be tested, x axis of spectrum
                    [0 for i in frange(freq_low, freq_high,
res_fd)],
                    #integral of products for fid_tot_no, y
                    axis of spectrum
                    [0 for i in frange(freq_low, freq_high,
res_fd)]]
                    #integral of products for fid_tot_ex, y
                    axis of spectrum
#print(frequencies)

#Calculate FIDs for all candidate frequencies:
candidates = []
compare
freq = 0
#hypothetical fids to
while freq < len(frequencies[0]):
    candidates.append([0 for i in range(TD)])
    #print("Candidate " + str(freq) + " has frequency " +
str(frequencies[0][freq]) + " rad/ms, and is")
    #print(["+", ".join(["%.5f" % x for x in candidates[freq]])+""])
    point = 0
    while point < len(candidates[freq]):
        candidates[freq][point] =
math.cos(abscesses[1][point]*frequencies[0][freq])
        point = point + 1
    freq = freq + 1

#Calculate product between candidate signal and exp signal for each point:
product =      [],
calc fid_tot_no
#product between exp and
[]
#product between exp and calc fid_tot_ex
#print(product)
#print(len(frequencies[0]))
freq = 0
while freq < len(frequencies[0]):
    product[0].append([0 for i in range(TD)])

```

```

product[1].append([0 for i in range(TD)])
#print(product)
#print("calculating error of candidate", freq)
point = 0
while point < len(candidates[freq]):
    product[0][freq][point] =
candidates[freq][point]*fid1_no[point]
    product[1][freq][point] =
candidates[freq][point]*fid1_ex[point]
    point = point + 1
freq = freq + 1

#Calculate spectrum intensity for each frequencies, i.e. integral of products:
for i in range(N_freq):
    m=0
    while m < TD:
        frequencies[1][i] = frequencies[1][i] + product[0][i][m]
        frequencies[2][i] = frequencies[2][i] + product[1][i][m]
        m=m+1

#Spectra:
graph1 = 211
graph2 = 212

plt.figure(1)
plt.suptitle("freq: " + str(omega1) + " and " + str(omega2) + "; relax: " + str(T11)
+ "; dwell: " + str(dwell1) + " and " + str(dwell2) + """, fontsize = 18)
plt.subplot(graph1)
plt.title('Precession', fontsize = 16)
plt.plot(abscisses[1], angle1_no, color='blue', linewidth=2)
plt.plot(abscisses[1], angle1_ex, color='green', linewidth=2)
plt.xlabel('Acq time', fontsize=12)
plt.ylabel('Angle', fontsize=12)

plt.subplot(graph2)
plt.title('FID', fontsize = 16)
plt.plot(abscisses[1], fid1_no, color='blue', linewidth=2)
plt.plot(abscisses[1], fid1_ex, color='green', linewidth=2)
plt.xlabel('Acq time', fontsize=12)
plt.ylabel('Intensity', fontsize=12)

#fig.set_tight_layout(True)
plt.tight_layout(pad=1, w_pad=1, h_pad=1, rect=[0, 0, 1, 0.95])

plt.figure(2)
plt.suptitle("Purple: no exchange; green: exchange", fontsize = 18)
plt.subplot(graph1)
plt.title('FID', fontsize = 16)
plt.plot(abscisses[1], fid1_no, color='purple', linewidth=2)
plt.plot(abscisses[1], fid1_ex, color='green', linewidth=2)

```

```
plt.xlabel('Acq time', fontsize=12)
plt.ylabel('Intensity', fontsize=12)

plt.subplot(graph2)
plt.title("Spectra: freq: {" + str(omega1) + "," + str(omega2) + "}; dwell times: {"
+ str(dwell1) + "," + str(dwell2) + "}", fontsize = 16)

plt.plot(frequencies[0], frequencies[1], color='purple', linewidth=2)
plt.plot(frequencies[0], frequencies[2], color='green', linewidth=2)
plt.xlabel('Frequency', fontsize=12)
plt.ylabel('Intensity', fontsize=12)

#fig.set_tight_layout(True)
plt.tight_layout(pad=1, w_pad=1, h_pad=1, rect=[0, 0, 1, 0.95])
plt.show()
#sort figures by ex/no_ex ?

exchange()
```